ISBN 978-82-471-1771-2 (printed ver.)
ISBN 978-82-471-1773-6 (electronic ver.)
ISSN 1503-8181

Doctoral theses at NTNU, 2009:187

Mustafa Barri

Turbulent shear flows subject to system rotation

NTNU
Norwegian University of
Science and Technology

NTNU
Norwegian University of
Science and Technology
Thesis for the degree of
philosophiae doctor
Faculty of Engineering Science and Technology
Department of Energy and Process Engineering

Mustafa Barri
Doctoral Thesis

Doctoral theses at NTNU, 2009:187

NTNU

Mustafa Barri

Turbulent shear flows subject to system rotation

Thesis for the degree of philosophiae doctor

Trondheim, September 2009

Norwegian University of
Science and Technology
Faculty of Engineering Science and Technology
Department of Energy and Process Engineering

NTNU
Norwegian University of
Science and Technology

NTNU
Norwegian University of Science and Technology

Thesis for the degree of philosophiae doctor

Faculty of Engineering Science and Technology
Department of Energy and Process Engineering

ISBN 978-82-471-1771-2 (printed ver.)
ISBN 978-82-471-1773-6 (electronic ver.)
ISSN 1503-8181

Doctoral Theses at NTNU, 2009:187

Printed by Tapir Uttrykk

Turbulent shear flows subject to system rotation

by

Mustafa Barri

Sept. 2009
Doctoral Dissertation
NTNU Fluids Engineering Division
NO-7491 Trondheim, Norway

Typsatt i $\mathcal{AMS}$-LaTeX.

NTNU
Norwegian University of Science and Technology

Thesis for the degree of philosophiae doctor

Faculty of Engineering Science and Technology
Department of Energy and Process Engineering

ISBN 978-82-471-1771-2 (printed ver.)
ISBN 978-82-471-1773-6 (electronic ver.)

Thesis at NTNU, 2009:187

Dedication

This work is proudly dedicated to:

My father's soul (Allah bless him) and my great mother

My sisters/brothers and my wife Raghda

for their unconditional love and support all the time.

Trondheim 2009
Mustafa Barri

Turbulent shear flows subject to system rotation.

Mustafa Barri 2009
Fluids Engineering Division, EPT-NTNU
NO-7491 Trondheim, Norway.

Abstract

Turbulent flows in rotating frame-of-reference are of considerable interest in a variety of industrial, geophysical and astrophysical applications. In these flows, the system rotation induces additional body forces, i.e. centrifugal and Coriolis forces, acting on the turbulent flow, so that the momentum mechanism becomes more complicated. The present doctoral thesis concerns the system rotation influence on turbulent shear flows. To this end, direct numerical simulations (DNSs) have been performed in order to investigate the effect of system rotation on different turbulent flow configurations including plane Couette flow, sudden expansion flow and wake behind a flat plate. In addition, the PIV measurements for rotating plane channel and sudden expansion flows have been carried out in order to support the numerical simulations results.

A realistic turbulent inflow boundary condition is needed in order to perform direct numerical simulations for spatially developing flows subjected to system rotation such as rotating sudden expansion flows. The *cost effective* method is introduced based on a separate (precursor) simulation in order to establish fully turbulent inflow including wide ranges of length and time scales needed in the direct numerical simulations. On the other hand, the characteristic features of the rotating turbulent flows were investigated by means of three-dimensional flow visualization, two-point correlations and transport for the individual second-moments of the velocity and vorticity fluctuations.

Descriptors: Direct numerical simulations, system rotation, PIV measurements, plane Couette flow, sudden expansion flows, turbulent inflow conditions.

Contents

Preface

This thesis essentially considers the study of turbulent shear flows subjected to spanwise system rotation. The first part is a summary of the research presented in the papers included in the second part. The summary includes an introduction to the basic concept, a review of previous works and a brief presentation and discussion of the main results obtained. The second part consists of three different sections: parallel wall-bounded flows, turbulent inflow boundary condition and separated shear flows.

Throughout the present thesis, I am the major contributor to the eight papers of which I am the first author; i.e. Paper 1, Paper 2, Paper 3, Paper 5, Paper 6, and Papers 9–11. I performed the direct numerical simulations, post-processed and analysed the data, and interpreted the results. Besides Paper 3 I also wrote all these papers. My co-authors supervised the work and assisted in the analysis and interpretation of the findings and in the final writing process. The simulations reported in Paper 7, Paper 8 and Paper 12 were performed by the first author. I actively participated in the problem identification and definition, the analysis and interpretation of the results and the writing of the papers. As far as Paper 4 is concerned, I participated in the planning of the experimental set-up and I took part in the measurement campaign at LEGI in Grenoble in April–May 2007 and some preliminary data-processing.

The thesis is based on and contains the following papers.

Paper 1. Barri, M. & Andersson, H. I. 2007 Anomalous turbulence in rapidly rotating plane Couette flow. In *Advances in Turbulence XI* (ed. J.M.L.M. Palma & A. Silva Lopes), Springer-Verlag, pp. 100–102.

Paper 2. Barri, M., Holstad, A., Andersson, H. I. & Pettersen, B. 2007 On turbulent plane Couette flow with and without rotation. In 4^{th} *National Conference on Computational Mechanics* (ed. B. Skallerud & H. I. Andersson), Tapir Academic Press, pp. 103–111.

Paper 3. Barri, M. & Andersson, H. I. 2009 Computer experiments on rapidly rotating plane Couette flow. *Communications in Computational Physics*, In press.

Paper 4. Visscher, J., Andersson, H. I., Barri, M., Didelle., H., Viboud, S., Sous, D. & Sommeria, J. 2009 A new set-up for PIV measurements in rapidly rotating turbulent duct flows. *Experiments in Fluids*, Submitted.

Paper 5. Barri, M., El Khoury, G. K., Andersson, H. I. & Pettersen B. 2009 Inflow conditions for inhomogeneous turbulent flows. *International Journal for Numerical Methods in Fluids*, **60**, 227–235.

Paper 6. Barri, M., El Khoury, G. K., Andersson, H. I. & Pettersen B. 2009 DNS of backward-facing step flow with fully turbulent inflow. *International Journal for Numerical Methods in Fluids*, In press.

Paper 7. El Khoury, G. K., Barri, M., Andersson, H. I. & Pettersen B. 2009 Massive separation of turbulent Couette flow in one-sided expansion channel. *International Journal of Heat and Fluid Flow*, Invited paper from TSFP6; c.f. El Khoury *et al.* (2009).

Paper 8. El Khoury, G. K., Barri, M., Andersson, H. I. & Pettersen B. 2008 DNS of orifice flow with turbulent inflow conditions. In *Direct and Large-Eddy Simulations 7*, In press.

Paper 9. Barri, M., El Khoury, G. K., Andersson, H. I. & Pettersen B. 2009 Massive separation in rotating turbulent flows. In *Advances in Turbulence XII* (ed. Bruno Eckhardt), Springer-Verlag, pp. 625–628.

Paper 10. Barri, M. & Andersson, H. I. 2009 Turbulent flow in a sudden-expansion channel. Part I: Effects of anti-cyclonic system rotation. *Journal of Fluid Mechanics*, Submitted.

Paper 11. Barri, M. & Andersson, H. I. 2009 Turbulent flow in a sudden-expansion channel. Part II: Effects of cyclonic system rotation. *Journal of Fluid Mechanics*, To be submitted.

Paper 12. Khaledi, H. A., Barri, M. & Andersson, H. I. 2009 On the stabilizing effect of the Coriolis force on the turbulent wake of a normal flat plate. *Physics of Fluids*, In press.

Part 1

Summary

CHAPTER 1

Introduction

Turbulence is a very complex stochastic phenomenon which is not well understood. One striking features of turbulence in fluids is the wide range of length scales over which the velocity and pressure vary. Most of the kinetic energy of the turbulent motion is contained in the large scale motions. The energy cascades from these large scale structures to smaller structures by an inertial and essentially inviscid mechanism. This process continues, creating smaller and smaller structures which produces a hierarchy of eddies. Eventually this process create structures that are small enough that molecular diffusion becomes important and viscous dissipation of energy finally take place. These tiny scales are known as the Kolmogorov scales and are generally several orders of magnitudes smaller than the geometrical scales.

Although the Navier-Stokes equations constitute a complete mathematical model for the motion of fluids, numerical solutions of the Navier-Stokes equations can only be obtained for laminar flows in a straightforward manner. Only in rare cases when the scale range is fairly modest can the Navier-Stokes equations be accurately solved for turbulent flows. This approach is known as Direct Numerical Simulations (DNS) and is the only way to compute a turbulent flow from first principles without any modeling assumptions. The benefit of DNS is that all relevant scales of motion are resolved, with appropriate initial and boundary conditions for the specific flow problem considered. This makes it possible to study the physics of turbulence in details. It is important to say here, that computational simulations and experiments have their exclusive strengths and weakness and cannot replace one another, but if properly integrated, will strongly complement each other.

On the other hand, the turbulent flows in rotating frame of reference are of major practical concern, for instance in turbo-machinery and geophysical science. The Coriolis body force arising from the rotation frame has several important implications on the flow field. Not only the mean flow pattern altered by the presence of a Coriolis force, but the turbulence is also affected qualitatively as well as quantitatively. Depending on the orientation and the magnitude of the rotation vector, i.e. the angular velocity of the coordinate system, completely different flow phenomena may occur. The attention in the current thesis is to study the effect of spanwise system rotation on different turbulent shear flows. To this end, the vector rotation is taken either to be parallel or anti-parallel to the mean flow vorticity.

CHAPTER 2

Rotating flows

Fluid flows subjected to system rotation are of great concern in different real life applications. The knowledge gained throughout several decades is impressive and contributed to significant improvements in our way of thinking. Even though the vast majority of previous works on rotating flows were focused on parallel wall flows, the rotating shear layers and wakes start to be of special interest for the research community. Although the equations governing the flow are known, the complexity of the flow makes it impossible to find analytical solutions for even simple cases. Nowadays and due to the continuous development in computer resources, direct numerical simulations have provided physical insight into the phenomena of rotating turbulent flows.

2.1. Basic concepts

A rotating frame of reference is a special case of a non-inertial (accelerating) reference frame that is rotating relative to an inertial reference frame. In this frame the position of an object seems to be spontaneously changing its velocity with no apparent non-zero net force acting upon it. This completely violates the law of inertia and Newton's laws of motion, since these laws claim that the only way an object can change its velocity is if an actual non-zero net force is applied to the object.

In classical mechanics, an inertial force was described by the $19^{th}-$century French engineer Gustave-Gaspard Coriolis in 1835. Coriolis showed that, if the ordinary Newtonian laws of motion of bodies are to be used in a rotating frame of reference, extra acceleration terms must be included in the equations of motion. Therefore, if a mass particle is stationary in rotating system (Ω^F) at a distance (r) from the center of rotation, it appears to an observer taking part in the rotation, to be affected by a centrifugal force. Otherwise, if the particle is not stationary but moves (u_r) relative to the rotating system, it appears to be affected by an additional force (Coriolis force). In general, the relationship between the particle acceleration in inertial frame of reference a_f and rotating frame of reference a_r can be expressed as:

$$a_f = a_r + 2\Omega^F \times u_r + \Omega^F \times (\Omega^F \times r) \tag{2.1}$$

where the last two terms to the right hand side of the equation are the Coriolis and Centripetal acceleration, respectively. The cross product indicates that the Coriolis force is perpendicular both to the relative motion u_r and to the

rotational axis Ω^F. For this reason, and not only because the force is inertial, the Coriolis force does not do any work, i.e. it does not change the kinetic energy (speed) of the body, only the direction of its motion. The statement that the Coriolis force does not do any work should not be misunderstood to mean that it does not do anything. Like centrifugal force, viewed differently by observers in the rotating reference frame and outside of it, the Coriolis force is also a fictitious force. Keep in mind that what we see depends on where we are (our frame of reference).

2.2. Shear flows

There are numerous experimental and DNS studies of turbulent shear flows, with and without system rotation, see for instant Kim *et al.* (1987), Kristoffersen & Andersson (1993) and Lamballais *et al.* (1996) for plane channel flow, Bech *et al.* (1995), Bech & Andersson (1996, 1997) and Barri & Andersson (2009) for plane Couette flow and Cambon *et al.* (1994), Métais *et al.* (1995) and Khaledi *et al.* (2009a) for free shear layer and wake flow. In rotating sudden expansion flows it is importnant to refer the illuminating experimental work by Rothe & Johnston (1979). It is noteworthy to mention that the present doctoral thesis is only concerned with the system rotation around the spanwise direction where the axis of rotation is parallel or anti-parallel to the mean vorticity vector. Secondary instabilities associated with rotating three-dimensional mean flow (Ekman layer) are out of the scope of the current work. Therefore, two-dimensional mean flow will be considered.

Rotating flows are governed by the Navier-Stokes equations formulated in a rotating frame of reference which can be derived by applying Newton's laws of motion on a fluid element in a rotating system rotation using the acceleration expression in equation (2.1)

$$\frac{\partial u_i}{\partial x_i} = 0 \tag{2.2a}$$

$$\frac{\partial u_i}{\partial t} + u_j \frac{\partial u_i}{\partial x_j} = \frac{1}{\rho}\frac{\partial p^\star}{\partial x_i} + \nu \frac{\partial^2 u_i}{\partial x_j \partial x_j} + 2\varepsilon_{ijk} u_j \Omega_k^F \tag{2.2b}$$

where the effective pressure given by $p^\star = p - \frac{\rho}{2}(\varepsilon_{klm}\Omega_l^F r_m \varepsilon_{kpq}\Omega_p^F r_q)$ in which the first term p is the instantaneous pressure field and the second term is the centrifugal force. The last term in equation (2.2b) is the Coriolis force. If the rotation axis is along the spanwise direction then the system rotation $\Omega_k^F = \Omega^F \delta_{k3}$ where Ω^F is the rate of system rotation. The dimensionless form of equation (2.2) introduces two important non-dimensional numbers; Reynolds number (Re) and Rotation number (Ro) defined as:

$$Re = \frac{inertial\ force}{viscous\ force} = \frac{UL}{\nu} \tag{2.3a}$$

$$Ro = \frac{Coriolis\ force}{inertial\ force} = \frac{2\Omega^F L}{U} \tag{2.3b}$$

Here, U is a characteristic velocity, L is a characteristic length and ν is the kinematic viscosity. Care should be taken not to mix up the rotation number defined in equation (2.3b) with the Rossby number normally used in geophysical fluid dynamics.

The influence of the Coriolis force due to imposed system rotation depends both on the orientation and the magnitude of the background vorticity $2\Omega_i^F$ relative to the mean flow vorticity $\Omega_i = \varepsilon_{ijk}\partial U_k/\partial x_j$ in a rotating frame of reference. The local vorticity ratio $S \equiv 2\Omega_i^F/\Omega_i$ effectively distinguishes between different flow regimes. According to Bradshaw-Richardson number $B = S(S+1)$ the effect of rotation is *destabilizing* when $-1 < S < 0$ (i.e. $B < 0$) and *restabilization* of the flow may be expected when $S < -1$. On the other hand, the *stabilization* effect is always associated to $S > 0$. In plane channel flow, for instance, S changes sign where mean velocity peaks and the rotating channel flow is therefore simultaneously affected by *cyclonic* ($S > 0$) and *anti-cyclonic* ($S < 0$) rotation. Cambon *et al.* (1994) and Métais *et al.* (1995) indicated the stabilization effect in the cyclonic rotation regions in terms of reducing turbulence level and decreasing the momentum interchange. On the other hand, the destabilization effect associated with the increase in momentum interchange dominates the moderate anti-cyclonic rotation regions before it begins to restabilize at sufficiently high rotation rates.

Flow in a rotating system is susceptible to roll-cell instability (Taylor-Görtler vorticies), i.e. the rotational analogue to the centrifugal instability due to streamline curvature, which gives rise to an array of counter rotating cells of alternating sign aligned with the primary flow. The formation of pairs of counter-rotating longitudinal vorticies may occur both in laminar and turbulent flows.

2.2.1. *Channel flows*

Johnston *et al.* (1972) performed pioneering work in the field of rotating flows. They investigated the effect of spanwise rotation on fully developed turbulent plane channel flow. It was shown that the action of the Coriolis force due to system rotation changes not only the mean velocity distribution but also the turbulent fluctuations. The location of maximum mean velocity is shifted from the channel center towards the so-called *suction* side (cyclonic), whereas the turbulent agitation is enhanced at the opposite side of the channel, i.e. along *pressure* side (anticyclonic). Meanwhile, large-scale roll cells are generated due to Taylor-Görtler instability and shifted towards the pressure side as the rotation rate increases. Consequently, the cross-sectional secondary flow induced by the roll cells contributes to transporting the vorticity fluctuations and turbulent kinetic energy from the pressure side to the suction side. When the rotation rate increases further, turbulence level on the pressure side is reduced significantly, and the large-scale roll cells become much weaker and eventually disappear due to the thickening of the relaminarization region on the suction side. On the other hand, the mean velocity profile exhibits a linear range with

slope close to $2\Omega^F$, which makes the local vorticity ratio $S \approx -1$. This shows that the mean velocity profile has adjusted itself such that the mean flow vorticity Ω just counterbalances the imposed background vorticity $2\Omega^F$, i.e. the absolute vorticity in an inertial frame of reference is driven to zero. These essential observations have been confirmed and supplemented by more recent experimental studies by Nakabayashi & Kitoh (1996, 2005) and direct numerical simulations by Kristoffersen & Andersson (1993), Lamballais *et al.* (1996, 1998), Liu & Lu (2007) and Grundestam *et al.* (2008).

In contrast to the pressure-driven plane channel flow, the shear-driven plane Couette flow exhibits a monotonically increasing mean velocity from one wall to the other with obvious implication that entire flow field is either imposed to cyclonic or anticyclonic system rotation. This fact alone makes the rotating plane Couette flow an attractive prototype for explorations of rotational effects on rotating shear flows. In this context, the notion of *pressure* and *suction* sides should be discarded. In a computational study of turbulent plane Couette flow, Bech & Andersson (1996) observed that the roll cell instability was present in the anticyclonic rotating turbulent case. If the Couette flow was subjected to weak cyclonic rotation, no roll cells appeared and the turbulence was damped as compared with the turbulence level in non-rotating Couette flow. At certain anticyclonic rotaion rate the existence of pure turbulence is observed (see paper 3 in the present thesis), i.e. the rotation rate is sufficiently high to suppress the roll-cell instability but yet not high enough to quench the turbulence.

2.2.2. *Separated flows*

Similar to the channel flows, separated shear flows are also differently affected by system rotation. A rotating wake is exposed simultaneously to cyclonic and anticyclonic rotation, whereas a rotating mixing-layer is subjected only to cyclonic or anti-cyclonic rotation. An early flow visualization study of the mixing-layer emanating from the corner of a backward-facing step was performed by Rothe & Johnston (1979). They observed that the position at which the flow reattached to the channel wall downstream of the step was crucially dependent on the sense of rotation and the rotation rate. The reattachment length increased with increasing cyclonic rotation and diminished with higher anticyclonic rotation. In the later case, the turbulence in the shear layer was promoted and the excess mixing enhanced the spreading rate of the mixing layer. Cyclonic rotation, on the other hand, tended to damp the turbulence and the spanwise-oriented coherent flow structures were strengthened. The rotating mixing-layer was further investigated by Bidokhti & Tritton (1992) albeit in a rather different apparatus. They showed that the flow was stabilized at the cyclonic rotation whereas the flow was first destabilized and subsequently restabilized at the anticyclonic rotation. It is noteworthy to mention that the turbulence features of the shear layer emanating from the step edge in the non-rotating backward-facing step configuration shows similar behavior compared to the non-rotating mixing-layer (see paper 6 in the current thesis), while the

FIGURE 2.1. Instantaneous streamwise velocity field for turbulent flow over slits (see paper 8). The red iso-contours indicate positive velocity regions while the blue represent negative velocity (i.e. recirculation bubbles).

turbulence physics is totally different when it comes to the rotating cases. For instance, the anticyclonic rotating backward-facing step shows complex interactions between cyclonic and anticyclonic shear layers (see paper 10 in this thesis).

On the other hand, Métais *et al.* (1995) performed direct and large-eddy simulations of a planar mixing-layer and a planar wake flow subjected to system rotation. Their simulations confirmed the two-dimensionalization effect of cyclonic rotation and rapid anticyclonic rotation. At low rotation numbers, a destabilization was observed in the anticyclonic regime. Chabert d'Hiéres*et al.* (1990) showed that at moderate rotation rates, the cyclonic vorticies of the wake are reinforced while the anticyclonic ones are destroyed. Conversely, the wake is reorganized into a very regular two-dimensional Karman street of alternate vorticies at high rotation rates.

2.3. Turbulent inflow conditions

In order to perform direct numerical simulations for spatially developing flows (i.e. sudden expansion flows) subjected to system rotation for particular and non-homogeneous turbulent flows in general, realistic turbulent inflow is a crucial parameter since the influence of inlet conditions can be visible further downstream. In DNS, the inflow conditions should contain wide ranges of time and length scales which represent correctly the turbulent behavior consistent with the continuity condition and the momentum balance in equation (2.2). Several methods have been investigated previously in order to provide inflow data for spatially developing turbulent flows, see Kaltenbach *et al.* (1999) for instance. In paper 5, the *cost-effective* method is introduced in order to establish reliable fully turbulent inflow conditions for spatially developing flows. The method recycles a finite-length time series t_s of instantaneous velocity planes, extracted from a precursor simulation, at the inflow of the main simulation. A physical constraint has been introduced for t_s in order to ensure that the extracted velocity profiles contain wide ranges of length and time scales. Figure 2.1 shows the DNS results of slit flow using fully turbulent inflow conditions given by the cost-effective method. The same technique has been used also to simulate different non-homogeneous turbulent flows during the current PhD

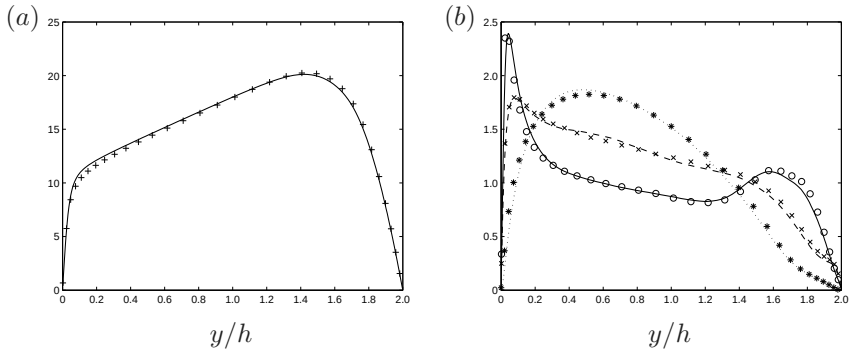

FIGURE 2.2. Rotating plane channel flow, $Ro = 0.5$. (a) U/u_τ and (b) u_{irms}/u_τ. The symbols denote DNS data from Kristoffersen & Andersson (1993).

work, especially the non-rotating (i.e. paper 6 & 7) and rotating (i.e. paper 10 & 11) sudden-expansion flows.

2.4. Simulation verifications

According to AIAA (1998), *verification* is the process of determining that a model implementation accurately represents the developers conceptual description of the model and the solution to the model. Verification ensures that there is little error between the true solution of the equations being solved and the approximate numerical solution. Indeed, several verification simulations are needed in the present PhD thesis in order to ensure that the quality of the work is comparable to the well-known results in the research field. For this purpose, several verification cases have been simulated throughout the thesis work using direct numerical simulations and the results have been compared with relevant experimental data or previous DNSs. For the moment, four different DNS verifications are needed:

1. Non-rotating turbulent channel.
2. Rotating turbulent channel.
3. Non-rotating sudden-expansion.
4. Rotating sudden-expansion.

For channel flows, DNS verifications for non-rotating turbulent plane channel and Couette flows are show in paper 6 and paper 3, respectively. On the other hand, figure 2.2 show DNS simulation for turbulent plane channel flow subjected to spanwise system rotation. The Reynolds number is defined to be similar to the famous work by Kim *et al.* (1987); $Re = U_b 2h/\nu \approx 5600$ based on the bulk velocity U_b and half the channel width h, where the rotation number is defined in the same manner as Kristoffersen & Andersson (1993), $Ro = 2\Omega^F h/U_b$. It is noteworthy to mention that the Reynolds number in the DNSs by Kristoffersen & Andersson (1993) is slightly higher than what had

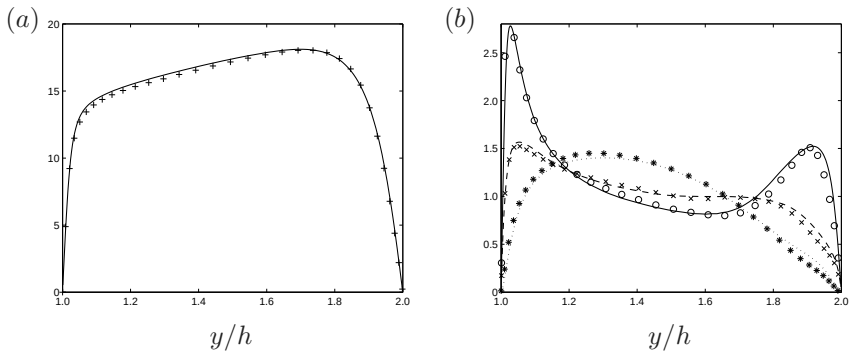

FIGURE 2.3. Sudden-expansion turbulent flow subjected to anticyclonic system rotation, $Ro = +0.2$ (see the definition for the Reynolds and rotation numbers in paper 10). Results are shown upstream of the sudden-expansion (step) at $x/h = 3$. (*a*) U/u_τ and (*b*) u_{irms}/u_τ. The symbols denote DNS data from Kristoffersen & Andersson (1993).

been used by Kim *et al.* (1987). The current simulation is compared with the DNS data from Kristoffersen & Andersson (1993) where nice agreement can be seen even if there is a small mismatch due to the difference in the Reynolds number.

The DNS verification for non-rotating sudden-expansion flow can be found in paper 6 where the fully turbulent flow over a backward-facing step is simulated. The results at the inlet section over the step are in excellent agreement with Kim *et al.* (1987) while the results down-stream of the step almost exactly match the experimental data by Kasagi & Matsunaga (1995). On the other hand the rotating sudden-expansion flow (backward-facing step) have been studied in papers 9–11 and unfortunately there are no data (experimental or DNS) available downstream of the step to compare with at the moment. For further details see papers 10 & 11 in the present thesis. Indeed, the turbulent flow upstream of the step can still be compared with the DNS by Kristoffersen & Andersson (1993). In figure 2.3 a comparison has been shown at the mid of the step ($x/h = 3$).

CHAPTER 3

Quick guide to papers content

A brief summary of each of the twelve papers will be presented in this chapter. The results presented in the attached papers basically concern the effect of system rotation on turbulent channel flows, turbulent sudden expansion flows and turbulent wake of a flat plate. Direct numerical simulation (DNS) was the major tool to study the system rotation effect in all previous mentioned cases. The first four papers focus on the effect of spanwise system rotation on parallel wall-bounded flows (Poiseuille & Couette). The next four papers investigate a realistic fully developed turbulent inflow technique for spatially developing shear flows. The last four papers describe the rotation effect on separated shear flows and turbulent wake. On the other hand, the PIV measurements for rotating Poiseuille and sudden expansion flows were of great help to understand the turbulent flow in rotating frame of reference. In paper 4, however, the PIV data for the clear channel is presented and unfortunately the data for obstructed channel are still in the post-processing stage.

Paper 1

Anomalous turbulence in rapidly rotating plane Couette flow.

M. Barri & H.I. Andersson

In this paper, the first numerical simulation in the present PhD work is performed. The aim was to implement the Coriolis force to the numerical code and compare the results with previous works on rotating channel flows. The system rotation effect on turbulent Couette flow was considered as a simple geometry case where the system rotation effect clearly observed. The focus was on high rotation number $Ro = 0.7$ which was believed to be a representative for the range $0.5 < Ro < 1.0$ since the mild and moderate rotation cases ($Ro \in [0, 0.5]$) have been studied by Bech & Andersson (1996, 1997), respectively. The elongated streamwise roll cells observed for $0 < Ro < 0.5$, did not occur at $Ro = 0.7$ and the turbulent flow is different in nature compare to the non-rotating case. Even though the computational domain is small and the grid resolution is coarse but still the basic effects of the system rotation are clear in the current simulation.

Paper 2

On turbulent plane Couette flow with and without rotation.

M. Barri, A. Holstad, H.I. Andersson & B. Pettersen

In the preceding paper, the effect of the domain size on the turbulent Couette flow is investigated through DNS. It is evident from the previous work on turbulent Couette flow by Komminaho *et al.* (1996) and Tsukahara *et al.* (2006) that a very large computational domain is necessary in order to obtain proper decay of the two-point correlations. Therefore, the domain size is increased by a factor of two in the streamwise direction and four times in the spanwise direction while the grid resolution was kept the same as in the previous work (paper 1). The two-point correlations fall of to almost zero over one half-width of the computational domain for both streamwise and spanwise directions indicating a suitable choice for the computational domain and the grid resolution.

Paper 3

Computer experiments on rapidly rotating plane Couette flow.

M. Barri & H.I. Andersson

This paper is a natural continuation of the previous papers where we studied the anti-cyclonic rotation ($Ro = 0.7$) effect on turbulent Couette flow using small domain and coarse grid resolution (paper 1) and suitable domain size and coarse grid (paper 2). Now, the grid resolution is significantly increased in order to resolve all the small scales by using DNS; the domain size in paper 2 is increased in the streamwise direction. The existence of pure turbulence is clear and no large roll cells can be observed since the rotation rate is sufficiently high to suppress Taylor-Görtler like instabilities but yet not high enough to quench the turbulence and relaminarize the flow field. The mean velocity profile exhibits a substantial linear range which extends over 80% of the cross-section. The slope of the velocity profile in the linear region is close to the imposed system vorticity, which makes the absolute mean vorticity to be zero.

Paper 4

A new set-up for PIV measurements in rapidly rotating turbulent duct flows.

J. Visscher, H.I. Andersson, M. Barri, H. Didelle, S. Viboud, D. Sous, & J. Sommeria

The present paper is focus on the PIV measurements of rotating turbulent duct flow at high aspect ratio. The Coriolis platform at the Laboratory of Geophysical and Industrial Fluid Flows (LEGI) in Grenoble-France has been used during the current study. With its 14m diameter, this is the largest turntable facility in the world. Wide range of rotation numbers for three different Reynolds numbers has been investigated. All the three components of the instantaneous velocity field have been measured in a plane spanning the channel from the pressure to the suction side. The general trend of the PIV data is in agreement

with the previous DNS for rotating channel flows by Kristoffersen & Andersson (1993). The side-wall effects which consist of weak secondary flow (Ekman layer) are negligible in general except at low rotation rates. Part of this work was presented at *ETMM* by Visscher *et al.* (2008).

Paper 5

Inflow conditions for inhomogeneous turbulent flows.

M. Barri, G.K. El Khoury, H.I. Andersson & B. Pettersen

A realistic turbulent inflow boundary condition is necessary to study separated shear flows such as the simplified geometry characterized by sudden expansion flow; backward facing step (BFS). The generation of a suitable fully developed turbulent inflow is the topic of this paper in order to be used to simulate inhomogeneous turbulent flows. A *cost-effective* method is introduced in this work where a finite-length time series t_s of instantaneous velocity planes is taken from a precursor simulation (fully developed plane channel flow). The velocity profiles are recycled at the inflow section of the actual simulation (spatially developing channel flow in the current paper) as many times as needed until a developed flow is obtained. A physical constraint is used for t_s in order to get a physical fully developed inflow containing wide ranges of time and length scales needed to perform DNS for inhomogeneous turbulent flows. The presented method gives good results in spatially developing channel flow compared to fully developed case where periodicity is used in the streamwise direction. However, the current method will be tested in several applications in papers 6, 7 and 8 for non-rotating flows and papers 9, 10 and 11 for rotating sudden expansion flows.

Paper 6

DNS of backward-facing step flow with fully turbulent inflow.

M. Barri, G.K. El Khoury, H.I. Andersson & B. Pettersen

The *cost-effective* method has been tested on spatially developing channel flow in paper 5. In the present paper, the same method is used to simulate fully developed channel flow over a backward facing step. The fully developed channel simulation is used as a precursor case and the saved velocity profiles are fed at the entrance of the backward facing step. The results at the inlet section over the step are in excellent agreement with Kim *et al.* (1987) while the results down-stream of the step almost exactly match the experimental data by Kasagi & Matsunaga (1995). This work is partially presented at *MekIt'09* by Barri *et al.* (2009).

Paper 7

Massive separation of turbulent Couette flow in a one-sided expansion channel.

G.K. El Khoury, M. Barri, H.I. Andersson & B. Pettersen

In paper 6, the pressure-driven flow over a backward facing step has been investigated. In the present paper the wall-driven flow over a backward facing step will be simulated. The *cost-effective* method is used in order to establish a reliable turbulent inflow and the precursor simulation is taken to be a fully developed plane Couette flow. In contrast with the pressure-driven backward facing step, the Reynolds number is changed after the expansion and even more, a fully redeveloped Couette flow cannot be reached in the far downstream of the step due to mass conservation. The Couette flow upstream of the step is redeveloped into a mixed Couette-Poiseuille flow in the recovery region. The turbulent flow over the step compares well with the DNS of fully developed Couette flow by Bech *et al.* (1995) whereas the flow in the recovery region shows similar trend to the Couette-Poiseuille simulations by Kuroda *et al.* (1995). This paper is an invited manuscript from *TSFP6*; c.f. El Khoury *et al.* (2009).

Paper 8

DNS of orifice flow with turbulent inflow conditions.

G.K. El Khoury, M. Barri, H.I. Andersson & B. Pettersen

The *cost-effective* method presented in paper 5 is used to establish fully turbulent inflow conditions for DNS of slits flow. A precursor simulation consisting of fully developed plane channel flow has been considered. Even though the geometry is symmetric in the wall-normal direction, the sudden expansion and contraction contribute to formulate asymmetric recirculation bubbles downstream of the slits. The previous DNS on the same topic carried out by Makino *et al.* (2008) where streamwise periodicity has been used. The current simulation indicates that the domain used by Makino *et al.* (2008) is significantly too short in the streamwise direction.

Paper 9

Massive separation in rotating turbulent flows.

M. Barri, G.K. El Khoury, H.I. Andersson & B. Pettersen

The present paper shows the primary DNS results for rotating sudden expansion flows using the simplified backward facing step geometry. Only anticyclonic rotation is considered in this work. Different rotation numbers have been considered with separate precursor case for each rotation number using the *cost-effective* method explained in paper 5. In addition to the separation shear layer extended from the step corner, the flow is separated after the expansion at the cyclonic (straight) wall due to stabilization effect.

Paper 10

Turbulent flow in a sudden-expansion channel. Part I: Effects of anti-cyclonic system rotation.

M. Barri & H.I. Andersson

Detailed investigations of turbulent flow in a simplified sudden expansion geometry (BFS) subjected to spanwise system rotation are covered in the present paper. The current DNSs are focused on anticyclonic system rotation. At certain rotation rate, the shear layer at the cyclonic side of the channel is separated after the expansion due to turbulence reduction induced by the system rotation. In contrast to the known behavior of cyclonic rotation regions where the turbulence level is reduced, the present simulations show significant amplification along the cyclonic side of the expansion region. The present abnormal amplification along the cyclonic region is due to strong interaction between the cyclonic and the anticyclonic shear layers. The recirculation region extended downstream of the step (anticyclonic bubble) is reduced in size at low and moderate system rotation before it starts to saturate at higher rotation rates. The recirculation region along the cyclonic wall continues to grow in size by increasing the rotation rate and no saturation has been observed in the current range of rotation numbers.

Paper 11

Turbulent flow in a sudden-expansion channel. Part II: Effects of cyclonic system rotation.

M. Barri & H.I. Andersson

In the current paper, the turbulent flow over backward facing step (BFS) under cyclonic system rotation is investigated. No separation has been observed along the straight wall (anticyclonic side). At low and moderate rotation rates, the recirculation bubble downstream of the step increased in size. Beyond a certain range of rotation rates the cyclonic recirculation region starts to reduce in size. The anticyclonic secondary recirculation region adjacent to the step corner almost quenched at low-moderate rotation rates before it start to be visible at higher system rotation.

Paper 12

On the stabilizing effect of the Coriolis force on the turbulent wake of a normal flat plate.

H.A. Khaledi, M. Barri & H.I. Andersson

The effect of system rotation on the turbulent Karman vortex street behind a flat plate using DNS is the topic of the present work. The Karman roller eddies either cyclonic or anti-cyclonic. At low and modest system rotation rate the turbulence at the cyclonic side of the wake is suppressed whereas the turbulence augmentation is enhanced at the anticyclonic side. Further increase in

the rotation rate suppresses the three-dimensional turbulence along the anticyclonic side of the wake and a nearly symmetric wake is observed with Strouhal number lower than the non-rotating wake. Part of this work is presented at *ETC12* by Khaledi *et al.* (2009b).

Acknowledgment

First and foremost I would like to thank my advisor Professor Helge I. Andersson for his trust, encouragement and inspiration throughout these three years. He is truly a guru to turn to with queries about mysteries of turbulent flows. His enthusiasm has inspired me to dig deeply into the problems I have faced during my research. For this and for never stopping to trying to make a better researcher out of me, I will always be indebted to him.

My gratefulness also goes to my co-supervisor Professor Bjørnar Pettersen, at the Marine Department−NTNU, for the collaboration and encouragement I received from him during my PhD work. I also thank Henri Didelle, Samuel Vibound, Damien Sous and Joël Sommeria at the Laboratory of Geophysical and Industrial Fluid Flows (LEGI), for hospitality and technical support during our stay in Grenobel. In addition, there are several people who have a great input in the research carried out in this thesis. I herein gratefully acknowledge the mutual collaboration and scholarly discussions I had with my articles co-authors: George El Khoury, Anders Holstad, Jan Visscher and Hatef Khaledi.

Special thanks goes to my colleagues, friends and previous co-workers. It is difficult to list all of them here but for instance I would like to mention: Adullah Al-Yafawi (State University of New York), Dr. Ashraf Al-Khateeb (University of Notre Dam), Prof. Reidar Kristoffersen (NTNU) and Dr. Luca Brandt (Royal Institue of Technology−Sweden). Thank you all for the encouragement and support during my research career.

I thank my great parents, my brothers and sisters for their immaterial support and caring. No words or expressions can formulate a real thank-you. Also, I would like to express my appreciation to my father-in-law, mother-in-law, brothers-in-law (Ashraf, Ahmad and Anas) and sisters-in-law (Lina and Nahla) for their continuous support.

Finally, I would like to express my heartfelt gratitude to my very much caring and loving wife for the never ending love and being always there. For her patience and the strength that she gave me by never stopping to believe in me, this thesis is as much hers as it is mine.

Tack Raghda for kjærlighet og støtte hele veien ♡

Bibliography

American Institute of Aeronautics and Astronautics 1998 Guide for the verification and validation of computational fluid dynamics simulations. *AIAA-G-077-1998*.

Barri, M. & Andersson, H. I. 2009 Computer experiments on rapidly rotating plane Couette flow. DOI:10.4208/cicp.2009.09.068

Barri, M., Andersson, H. I., El Khoury, G. K. & Pettersen, B. 2009 Massive separation in one-sided expansion channel. In 5^{th} *national conference on Computational Mechanics*(ed. B. Skallerud & H. I. Andersson), Tapir Academic Press, Trondheim-Norway, pp. 89–102.

Bech, K. H., Tillmark, N., Alfredsson, H. & Andersson, H. I. 1995 An investigation of turbulent plane Couette flow at low Reynolds numbers. *J. Fluid Mech.* **286**, 291–325.

Bech, K. H. & Andersson, H. I. 1996 Secondary flow in weakly rotating turbulent plane Couette flow. *J. Fluid Mech.* **317**, 195–214.

Bech, K. H. & Andersson, H. I. 1997 Turbulent plane Couette flow subject to strong system rotation. *J. Fluid Mech.* **347**, 289–314.

Bidokhti, A. A. & Tritton, D. J. 1992 The structure of a turbulent free shear layer in a rotating fluid. *J. Fluid Mech.* **241**, 469–502.

Cambon, C., Benoit, J.-P., Shao, L. & Jacquin, L. 1994 Stability analysis and large-eddy simulation of rotating turbulence with organized eddies. *J. Fluid Mech.* **278**, 175–200.

Chaber d'Hiéres, G., Davies, P. A. & Didelle, H. 1990 Experimental studies of lift and drag forces upon cylindrical obstacles in homogeneous, rapidly rotating fluids. *Dyn. Atmos. Oceans* **15**, 87–116.

El Khoury, G. K., Pettersen, B., Barri, M. & Andersson, H. I. 2009 Massive separation of turbulent Couette flow in a one-sided expansion channel. In 6^{th} *International Symposium on Turbulence and Shear Flow Phenomena*, Seoul-Korea, pp. 1217–1221.

Grundestam, O., Wallin, S. & Johansson, A. V. 2008 Direct numerical simulation of rotating turbulent channel flow. *J. Fluid Mech.* **598**, 177–199.

Johnston, J. P., Halleen, R. M. & Lezius, D. K. 1972 Effects of spanwise rotation on the structure of two-dimensional fully developed turbulent channel flow. *J. Fluid Mech.* **56**, 533–557.

Kaltenbach, H.-J., Fatica, M., Mittal, R., Lund, T. S. & Moin, P. 1999 Study

of flow in a planar asymmetric diffuser using large-eddy simulation. *J. Fluid Mech.* **390**, 151–158.

Kasagi, N. & Matsunaga, A. 1995 Three-dimensional particle-tracking velocimetry measurment of turbulent statistics and energy budget in a backward facing flow. *Int. J. Heat Fluid Flow* **16**, 477–485.

Khaledi, H. A., Barri, M. & Andersson, H. I. 2009a On the stabilizing effect of the Coriolis force on the turbulent wake of a normal flat plate. *Phys. Fluids*, In press.

Khaledi, H. A., Barri, M. & Andersson, H. I. 2009b Asymmetric vortex shedding in the turbulent wake of a flat plate in rotating fluid. In *Advances in Turbulence XII* (ed. Bruno Eckhardt), Springer-Verlag, pp. 301–304.

Kim, J., Moin, P. & Moser, R. 1987 Turbulence statistics in fully developed channel flow at low Reynolds number. *J. Fluid Mech.* **177**, 133–166.

Komminaho, J., Lundbladh, A. & Johansson, A. 1996 Very large structures in plane turbulent Couette flow. *J. Fluid Mech.* **320**, 259–285.

Kristoffersen, R. & Andersson, H. I. 1993 Direct simulations of low-Reynolds-number turbulent flow in a rotating channel. *J. Fluid Mech.* **256**, 163–197.

Kuroda, A., Kasagi, N. & Hirata, M. 1995 Direct numerical simulation of turbulent plane Couette-Poiseuille flows: effect of mean shear rate on the near-wall turbulence structures. *Turbulent Shear Flows 9*, Springer-Verlage, pp. 240–257.

Lamballais, E., Lesieur, M. & Métais, O. 1996 Effects of spanwise rotation on the vorticity stretching in transitional and turbulent channel flow. *Int. J. Heat Fluid Flow* **17**, 324–332.

Lamballais, E., Métais, O. & Lesieur, M. 1998 Spectral-dynamic model for large-eddy simulation of turbulent rotating channel flow. *Theoret. Comput. Fluid Dynamics* **12**, 149–177.

Liu, N.-S. & Lu, X.-Y. 2007 A numerical investigation of turbulent flows in a spanwise rotating channel. *Comput. Fluids* **36**, 282–298.

Makino, S., Iwamoto, K. & Kawamura, H. 2008 Turbulent structures and statistics in turbulent channel flow with two-dimensional slits. *Int. J. Heat Fluid Flow* **29**, 602–611.

Métais, O., Flores, C., Yanase, S., Riley, J. J. & Lesieur, M. 1995 Rotating free-shear flow. part2. numerical simulations. *J. Fluid Mech.* **293**, 47–80.

Nakabayashi, K. & Kitoh, O. 1996 Low Reynolds number fully developed two-dimensional turbulent channel flow with system rotation. *J. Fluid Mech.* **315**, 1–29.

Nakabayashi, K. & Kitoh, O. 2005 Turbulence characteristics of two-dimensional channel flow with system rotation. *J. Fluid Mech.* **528**, 355–377.

Rothe, P. H. & Johnston, J. P. 1979 Free shear layer behavior in rotating systems. *J. Fluids Eng.* **101**, 117–120.

Tsukahara, T., Kawamura, H. & Shingai, K. 2006 DNS of turbulent Couette flow with emphasis on the large-scale structure in the core region. *J. Turbulence* **7**, 19.

Visscher, J., Barri, M. & Andersson, H.I. 2008 Effects of rotation on clear and obstructed turbulent channel flows. In 7^{th} *International ERCOFTAC Symposium on Engineering Turbulence Modeling and Measurements*, Limassol-Cyprus, pp. 243–248.

Part 2

Papers

Part 2.1

Parallel wall-bounded flows

Paper 1

Anomalous turbulence in rapidly rotating plane Couette flow

Barri, M. & Andersson, H. I.

In *Advances in Turbulence XI, Proceedings of the 11th EUROMECH European Turbulence Conference, Springer–Verlag, pp.100–102, 2007.*

Anomalous turbulence in rapidly rotating plane Couette flow

Mustafa Barri and Helge I. Andersson

Department of Energy and Process Engineering,
Norwegian University of Science and Technology,
N-7491 Trondheim, Norway.
mustafa.barri@ntnu.no, helge.i.andersson@ntnu.no

Plane Couette flow offers a unique environment in which the effect of system rotation on wall-bounded shear flows can be studied. Depending on the magnitude and orientation of the imposed background vorticity Ω relative to the mean flow vorticity ω in the rotating frame-of-reference, a variety of different flow phenomena may occur. The ratio $S \equiv \Omega/\omega$ distinguishes between cyclonic ($S > 0$) and anti-cyclonic ($S < 0$) rotation. If $-1 < S < 0$, laminar Couette flow is *unstable* and counter-rotating roll cells occur, as recently observed in the experiments by Alfredsson & Tillmark.[1] Bech & Andersson[3,4] investigated turbulent Couette flow subjected to mild and moderately high anti-cyclonic rotation and observed distinct pairs of roll cells oriented in mean flow direction. Needless to say, these roll cells made a substantial contribution to the cross-sectional mixing and the wall-friction was higher than in the non-rotating case examined by Bech et al.[2]

The aim of the present study is to explore the turbulent flow field in a rapidly rotating Couette flow in the absence of roll cells. To this end we consider the shear-driven fluid motion between two infinite parallel planes separated a distance $2h$ in the y-direction. The turbulent flow is induced solely by the prescribed velocity difference $2U_w$ (in the x-direction) between the two planes. The Reynolds number is $Re \equiv U_w h/\nu = 1300$, i.e. well above 500 required for fully developed turbulence to persist.[1]

The relative importance of the imposed system rotation is given by the rotation number $Ro \equiv 2\Omega h/U_w$, which is a cross-sectional average of $-S$. While Bech & Andersson considered mild[3] and moderate[4] rotation with $Ro \in [0, 0.5]$, we will now focus on the high rotation number $Ro = 0.7$, which is believed to be representative for the range $0.5 < Ro < 1.0$. We therefore performed a direct numerical simulation of fully developed Couette flow, i.e. with periodic boundary conditions in the streamwise and spanwise directions. The size of the computational domain was $8\pi h \times 2h \times \frac{4}{3}\pi h$ and the first simulation reported here was made with a $64 \times 64 \times 64$ grid.

In accordance with our conjecture, rotational-induced roll cells, as observed for $Ro < 0.5$, did not occur at $Ro = 0.7$, as seen from the contour plots of the fluctuating velocity field in Fig. 1. The mean velocity variation $U(y)$ in Fig. 2a exhibits a substantial linear range which extends over 80% of the cross-section. Here, the slope $dU/dy \approx 2\Omega$ which makes $S = -1$. The extent of the Coriolis-dominated region is consistent with the criterion[5] that system rotation matters when $y > \delta_c$, where $\delta_c = u_\tau/\Omega$ is the Coriolis length scale. The tendency of a rotating flow to establish regions with zero vorticity in an inertial frame has been observed before both in Couette[4] and Poiseuille[5] flow. In the Couette flow, dU/dy cannot exceed U_w/h and $Ro = 1$ thus becomes an upper bound for which neutral stability $S = -1$ can be sustained.

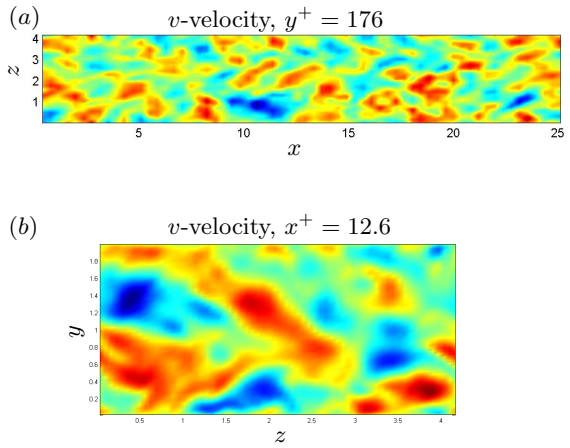

Fig. 1. Iso-contour plot of the instantaneous wall-normal velocity fluctuations. (a) (xz)-plane parallel with the walls; (b) Cross-sectional (yz)-plane.

The constancy of dU/dy in the Couette flow makes both contributions to the total mean shear stress $\mu dU/dy - \rho\overline{uv} = \tau_w \equiv \rho u_\tau^2$ constant in the core region, as seen in Fig. 2b. The rapidly rotating Couette flow therefore consists of a nearly homogeneous central region where rotational effects dominate and narrow regions adjacent to each wall where viscous effects prevail. The total production of turbulent kinetic energy can be expressed as:

$$\tilde{P} \equiv \frac{P}{U_w^3/h} = \left[\left(\frac{u_\tau}{U_w}\right)^2 - \frac{1}{Re}\frac{d\tilde{U}}{d\tilde{y}}\right]\frac{d\tilde{U}}{d\tilde{y}} \tag{1}$$

where $\tilde{U} = U/U_w$ and $\tilde{y} = y/h$ are dimensionless quantities. From equation (1) the dimensionless production $\tilde{P}$ in the core region is found to be 2.35×10^{-3}, which is nearly three times higher than the production rate found for $Ro =$

0.[2] It is particularly noteworthy that the turbulence exhibits an abnormal anisotropy with $v > w > u$, in contrast to the conventional anisotropy $u > w > v$ found in non-rotating shear flows. These anomalies will be further explored by means of structural information based on, e.g., λ_2-structures and quadrant analysis.

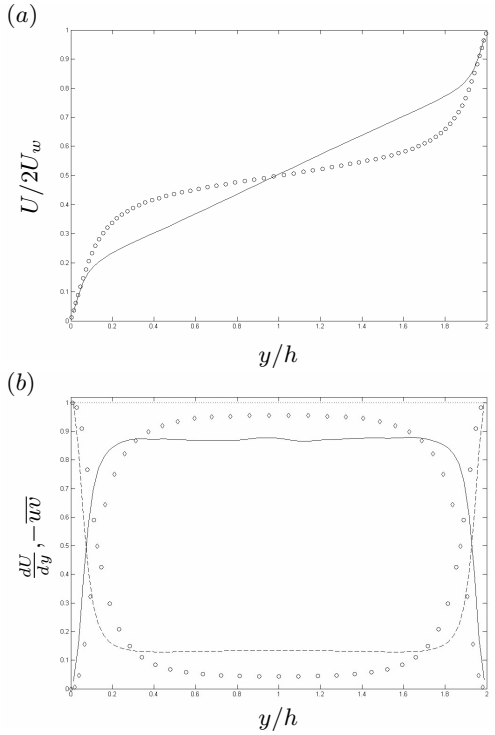

Fig. 2. Present results for $Ro = 0.7$ compared with DNS-data for $Ro = 0.0$ from Bech et al.[2] (diamonds). (a) Mean velocity profile $U(y)$, (b) Turbulent(—) and viscous(- - -) shear stresses.

References

1. P.H. Alfredsson & N. Tillmark: *Proc. IUTAM Symposium*, Springer 2005, pp. 173–193.
2. K.H. Bech, N. Tillmark, P.H. Alfredsson & H.I. Andersson: J. Fluid Mech. **286**, 291–325 (1995)
3. K.H. Bech & H.I. Andersson: J. Fluid Mech. **317**, 195–214 (1996)
4. K.H. Bech & H.I. Andersson: J. Fluid Mech. **347**, 289–314 (1997)
5. K. Nakabayashi & O. Kitoh: J. Fluid Mech. **315**, 1–29 (1996)

Paper 2

On turbulent plane Couette with and without rotation

Barri, M., Holstad, A., Andersson, H. I. &
Pettersen, B.

In *4th National Conference on Computational Mechanics, Tapir Academic Press, pp. 103–111, 2007.*

On turbulent plane Couette flow with and without rotation

Mustafa Barri, Anders Holstad, Helge I. Andersson and Bjørnar Pettersen
Faculty of Engineering Science
The Norwegian University of Science and Technology
mustafa.barri@ntnu.no, anders.holstad@ntnu.no, helge.i.andersson@ntnu.no,
bjornar.pettersen@ntnu.no

Summary. Turbulent plane Couette flow is studied by means of direct numerical simulations (DNSs) at a Reynolds number ($Re \equiv U_w h/\nu$) of 1300, where U_w is half of the wall relative speed and h is half of the channel height. The results show the need for long and wide enough computational domain in order to have good numerical simulations for the turbulent plane Couette flow, also show that the secondary vortex structure associated with pairs of streamwise counter-rotating roll cells disappears from the turbulent flow under high rotation number $Ro \equiv 2\Omega h/U_w = 0.7$,where Ω is the imposed angular vorticity.

Introduction

Plane Couette flow is a paradigm of shear flows because of its simple flow geometry and fundamental fluid mechanics characteristics where the effect of system rotation can be of great importance for engineering applications, notably within the turbomachinary industry.

Several studies have shown the existence of large-scale structures in numerically generated turbulent Couette flow[1-7]. The effect of the box size on the large-scale structures has been examined by Komminaho et al.[6] at Reynolds number of $Re = 750$ by comparing two-point velocity correlations for various computational box sizes. They concluded that a very large computational domain, indicating lengths of at least $28\pi h$ and $8\pi h$ in the streamwise and spanwise directions, was necessary in order to obtain proper decay of the two-point correlations. Tsukahara at al.[7] have also studied coherent structures in turbulent Couette flow at Reynolds numbers $Re = 750$ and $Re = 2150$ by comparing two-point correlations for various box sizes. They concluded that a box length of $89.6h - 128h$ was necessary if the large scale structures were to move freely.

Bech and Andersson[8,9] investigated turbulent Couette flow subjected to mild and moderately high anti-cyclonic rotation $Ro \in [0, 0.5]$, where the ratio of the imposed background vorticity Ω relative to the mean flow vorticity ω in the rotating frame of reference will be less than zero, and observed distinct pairs of roll cells oriented in the mean flow direction. As the rotation rate is increased turbulence is gradually enhanced on the pressure side and reduced on the suction side bringing asymmetric distributions of the mean flow and the Reynold stresses. At the same time, the large scale roll cells come forth as a result of Taylor-Görtler like instabilities and shifted towards the pressure side wall slowly as can be seen from Figure 1. If the rotation rate is further increased, turbulence on the pressure side is reduced after some critical rotation rate and the roll cells become much smaller and eventually disappear due to thickening of the relaminarized region on the suction side.

In this paper we study the turbulent structures in plane Couette flow with and without rotating the frame of reference, firstly we will focus on the non-rotating case and find an optimum long/wide computational box size, then we will study the rotating case using the optimal computational domain with high rotation number $Ro = 0.7$, which is believed to be representative for the range $0.5 < Ro < 1.0$. We consider the shear-driven fluid motion between two infinite parallel planes separated a distance $2h$ in the y-direction. The turbulent flow is induced by the

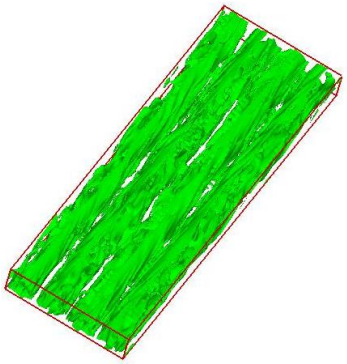

Figure 1: Iso-surface of streamwise velocity fluctuations for $Ro = 0.1$.

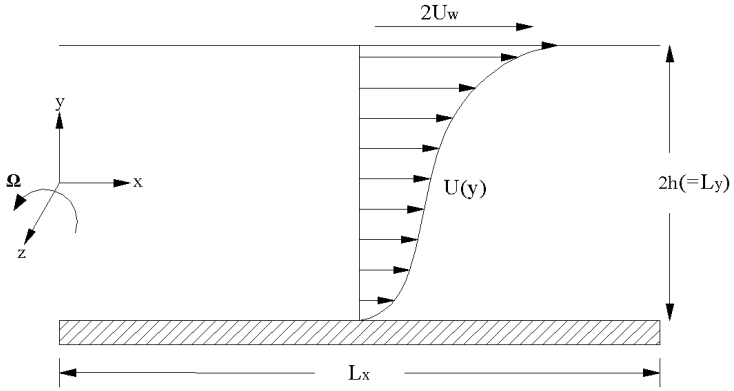

Figure 2: Mean velocity profile in turbulent plane Couette flow.

prescribed velocity difference $2U_w$ (in the x-direction) between the two planes as shown in Figure 2. The Reynolds number is $Re = 1300$, i.e. well above 500 required for fully developed turbulence to persist[13].

Numerical procedure

Numerical code

The unsteady Navier-Stokes equations for an incompressible Newtonian fluid with constantly rotating frame of reference can be written in their dimensionless form using Cartesian tensor notation:

$$\frac{\partial u_i}{\partial t} + u_j \frac{\partial u_i}{\partial x_j} = -\frac{\partial P_{eff}}{\partial x_i} + \frac{1}{Re}\frac{\partial^2 u_i}{\partial x_j^2} - \varepsilon_{ijk} Ro_j u_k, \tag{1}$$

$$\frac{\partial u_i}{\partial x_i} = 0, \tag{2}$$

where the rotational number $Ro = (0, 0, \frac{2\Omega h}{U_w})$ and ε_{ijk} is the alternating unit tensor. The last term on the right hand side of equation (1) represents the Coriolis force due to system rotation, while the centrifugal term is absorbed in the effective pressure term $P_{eff} = P_s - \frac{1}{8} Ro^2 r^2$, where P_s is the normalized static pressure and r denotes the dimensionless distance from the axis of rotation.

The given equations are integrated over a finite volume. The resulting equations are solved numerically on a staggered and non-uniform Cartesian grid by the parallel MPI computer code

MGLET[12]. Pressure is defined at the center of each grid cell and the velocity components at the interfaces. Velocity components and their derivatives are obtained by linear interpolation and central differences, respectively. The Coriolis force term enters the discritised momentum equation as a source term. As a result, the spatial discritisation is of second-order accuracy. Using Adams-Bashforth scheme for the explicit time integration of the momentum equations, a second-order accurate time step is achieved. This combination of central differencing and Adams-Bashforth time step is energy conserving for the non-dimensional convection equation and therefore appropriate for DNS. The Poisson equation for the pressure is solved by a full multi-grid method based on pointwise velocity-pressure iterations. The computational grid is divided into an arbitrary number of subgrids that are treated as dependent grid blocks in parallel processing.
No-slip boundary condition is used at the walls and periodic boundary conditions are employed in the streamwise and spanwise directions.

Computational domain and resolution

In order to choose a suitable computational box we studied different previous direct numerical simulations for plane Couette flow, as can be seen in Table 1. The computational box must be wide and long enough to get good accuracy. If the box size is smaller than the largest eddies these will artificially become infinitely long due to the periodic boundary conditions causing an overprediction of the two-point velocity correlations for large separation. On the other hand, if we choose a very large computational box then the computational cost will increase dramatically.
We will examine the influence of the box size on the two-point velocity correlation, so we choose two computational box sizes with the same spatial resolution ($\Delta x^+ = 16.6$ and $\Delta z^+ = 5.5$); Case 0 with small computational box size ($4\pi h \times 2h \times \frac{4}{3}\pi h$) and Case 1 with larger computational box size ($16\pi h \times 2h \times \frac{16}{3}\pi h$).

$Case$	$Year$	Re	$\sim Re_\tau$	L_x/h	L_z/h	$N_x \times N_y \times N_z$
Lee and Kim[1]	1991	3000	170	4π	$\frac{8}{3}\pi$	$128 \times 129 \times 192$
Kristoffersen *et al.*[11]	1993	1300	83.2	4π	2π	$96 \times 64 \times 64$
Bech *et al.*[5]	1995	1300	82.2	10π	4π	$256 \times 70 \times 256$
Hamilton *et al.*[15]	1995	400	32	1.75π	1.2π	$16 \times 33 \times 16$
Komminaho *et al.*[6]	1996	750	52	28π	8π	$340 \times 55 \times 170$
Papavassiliou and Hanratty[2]	1997	2660	150	4π	2π	$128 \times 65 \times 128$
Hu *et al.*[4]	2001	1300	82	192	48	$1024 \times 81 \times 512$
		3400	$--$	48	12	$512 \times 121 \times 256$
Debusschere and Rutland[3]	2004	3000	160	12	2	$231 \times 200 \times 64$
Tsukahara *et al.*[7]	2006	750	52	89.6	25.6	$1024 \times 96 \times 512$
		2150	126	128	12	$2048 \times 96 \times 256$
Holstad *et al.*[10]	2006	1300	84.6	16π	$\frac{16}{3}\pi$	$256 \times 64 \times 256$

Table 1: Direct numerical simulations of plane Couette flow.

Results

The simulation for the non-rotating case is started from an initial uniform streamwise velocity with superposed random fluctuations in all velocities. Constant time step size of $\Delta t = 0.001\frac{h}{u_\tau}$ which ensured that the maximum Courant number is small enough ($CFL = 0.2$) to guarantee a stable computation. After an initial transient period of about 100 time unit based on the wall shear stress and the channel height, statistics of first and second order are gathered for $T = 300\frac{h}{u_\tau}$ and averaged in the homogeneous directions. For the rotating case, we start with a fully developed non-rotating turbulent flow and impose the rotation effect gradually $Ro = 0.0 - 0.7$. The counter rotating roll cells appear at low rotation numbers and breakdown at high rotation numbers ($Ro = 0.7$).

The results are presented for three different DNS cases. Cases 0 and Case 1 are non-rotating turbulent plane Couette flows where we investigate the effect of the computational box size on the streamwise elongated structures. Case 2 is a rotating turbulent plane Couette flow with high rotation number $Ro = 0.7$, where we investigate the effect of Coriolis force. Both Case 0 and Case 1 has the same spatial resolution but different computational box size, where Case 2 is a coarser grid case with the same computational box size as Case 1, as we can see from table 2.

$Case$	Ro	Re	$\sim Re_\tau$	L_x/h	L_y/h	L_z/h	$N_x \times N_y \times N_z$	Δx^+	Δz^+
0	0	1300	84.9	4π	2	$\frac{4}{3}\pi$	$64 \times 64 \times 64$	16.6	5.5
1	0	1300	84.6	16π	2	$\frac{16}{3}\pi$	$256 \times 64 \times 256$	16.6	5.5
2	0.7	1300	75.8	16π	2	$\frac{16}{3}\pi$	$128 \times 64 \times 128$	29.8	9.9

Table 2: Parameters for the various simulation cases.

Non-rotating flow

As mentioned earlier, numerical simulations of plane Couette flow using periodic boundary conditions tend to develop large scale structures throughout the entire computational box. The effect of the computational box size can be most clearly observed on the two-point correlation of fluctuating velocities as shown in Figure 3 and 4 for the small domain (Case 0) and the larger domain (Case 1), respectively. The correlation functions are computed using time averaging and spatial averaging in the homogeneous streamwise and spanwise directions.

$$R_{uu}(x_i; \Delta x_i) = \frac{\overline{u(x_i)u(x_i + \Delta x_i)}}{u^2_{rms}(x_i)} \tag{3}$$

where the same expression can be used for the normal direction correlation R_{vv} and the spanwise correlation R_{ww}. It indicates that if the box size is too short then the correlations will not fall off to almost zero over half-width of the computational domain for streamwise and spanwise directions. For Case 0, the correlations neither fall off to zero both close to the wall, as shown in Figure $3(a)$, nor close to the center of the channel, as shown in Figure $3(b)$, which means that the computational domain for Case 0 is too small to prevent the enhancement of the large scales in the flow. For Case 1, the correlations fall off to almost zero over one half-width of the computational domain for both streamwise and spanwise directions, as shown close to the wall in Figure $4(a)$ and close to the mid of the channel in Figure $4(b)$, which indicates that

the computational domain for Case 1 is large enough to prevent the enhancement of the large scales in the flow (Optimal Case).

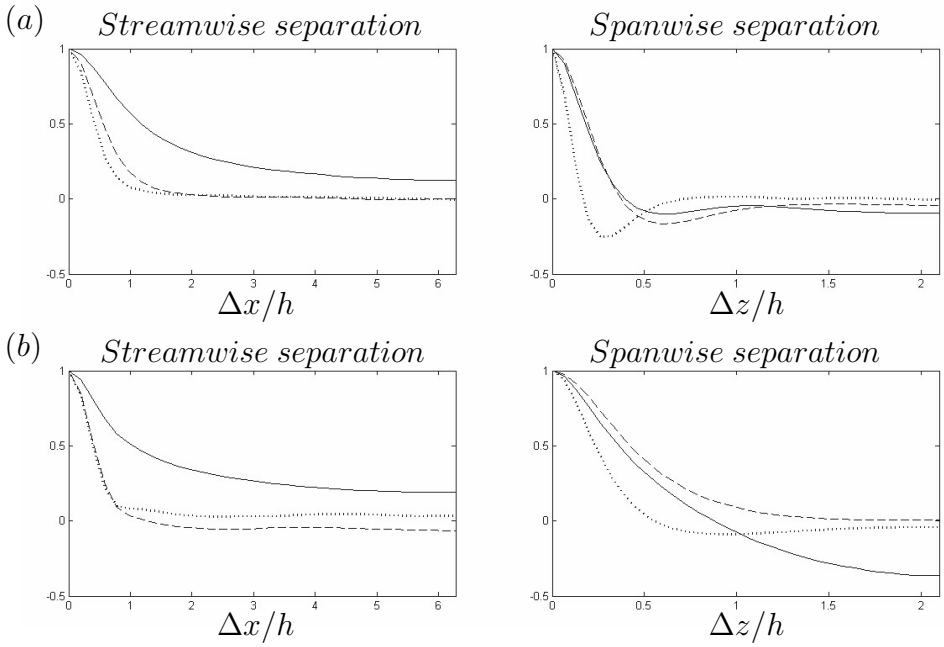

Figure 3: Streamwise and spanwise two-point correlation for Case 0. (a) $y^+ = 5$, (b) $y/h = 0.98$. R_{uu}; — , R_{vv}; .... , R_{ww}; - - - .

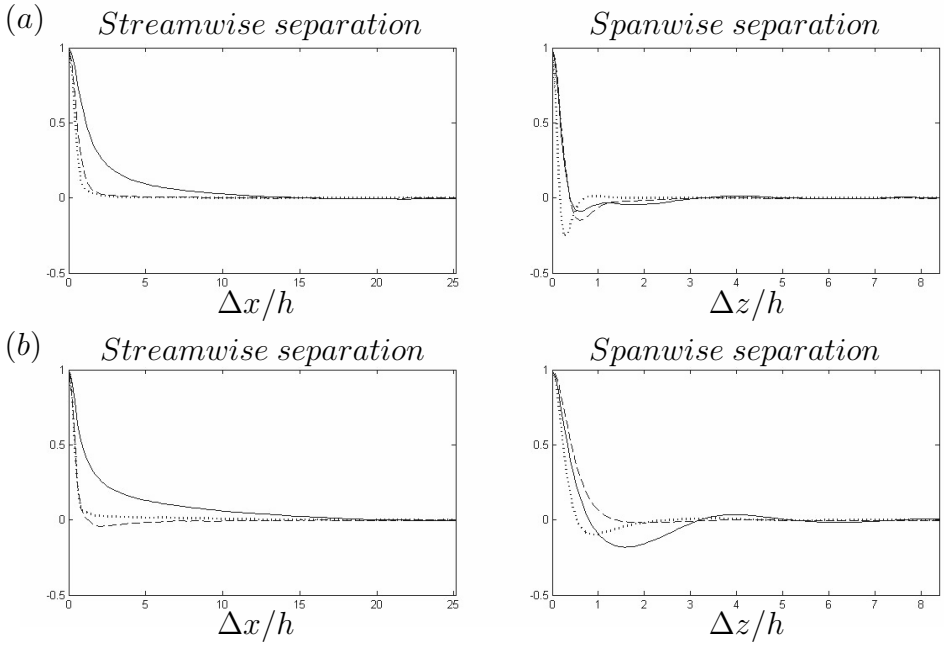

Figure 4: Streamwise and spanwise two-point correlation for Case 1. (a) $y^+ = 5$, (b) $y/h = 0.98$. R_{uu}; — , R_{vv}; .... , R_{ww}; - - - .

Rapidly-rotating flow

In Case 2, with high rotation number and the same computational domain as the Optimal Case, we notice the breakdown of the streamwise counter-rotating roll cells, as can be seen from the contour plots of the fluctuating velocity field in Figure 5. Figure 1 shows the counter-rotating roll cells at low rotation number and Figure 6 shows the breakdown effect at high rotation number.

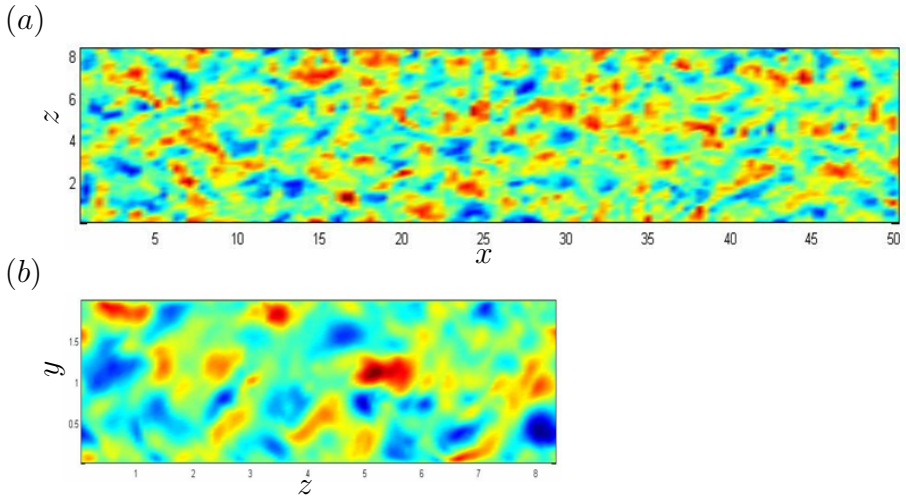

Figure 5: Iso-contour plot of the instantaneous wall-normal velocity fluctuations at the center of the channel. (a) (xz)-plane parallel with the walls; (b) Cross-sectional (yz)-plane.

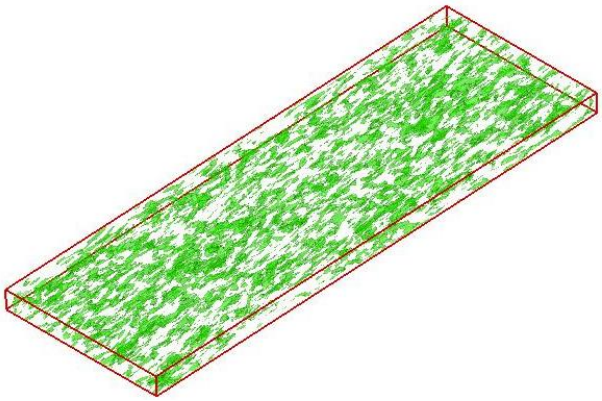

Figure 6: Iso-surface of streamwise velocity fluctuations for $Ro = 0.7$.

Figure $7(a)$ shows the change of the mean velocity profile $U(y)$ due to system rotation where a substantial linear range with slope $\sim 2\Omega$ extends over 80% of the cross section. The distribution of the Reynolds and total shear stress in Figure $7(b)$ is seen to be symmetric. The total shear stress is an indication that the flow has indeed reached a statistical-steady state. The constancy of dU/dy in the Couette flow makes both contributions to the total mean shear stress $\mu dU/dy - \rho\overline{uv} = \tau_w \equiv \rho u_\tau^2$ constant in the core region. The rapidly rotating Couette flow therefore consists of a nearly homogeneous central region where the rotational effects dominate and narrow regions adjacent to each wall where viscous effects prevail. The product of the turbulent shear stress and the viscous shear stress is equal to the turbulent production which has maximum where the curves intersects, i.e. at about $y/h = 0.1$.

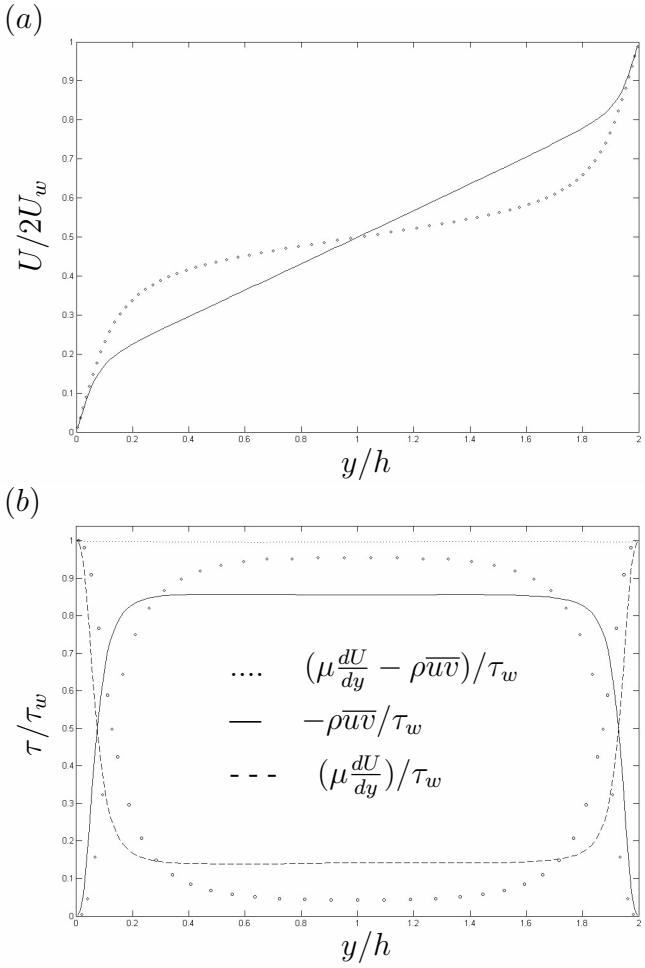

Figure 7: Present results for $Ro = 0.7$ compared with DNS-data for $Ro = 0.0$ from Bech et al.[5](diamonds). (a) Mean velocity profile $U(y)$, (b) Turbulent(—) and viscous(- - -) shear stresses.

Turbulence intensities for the three velocity components are shown in Figure 8, where the turbulence exhibits an abnormal anisotropy with $v > w > u$, in contrast to the conventional anisotropy $u > w > v$ found in non-rotating shear flows. The turbulence intensity of the wall normal velocity increases to almost a constant value through out the center of the channel and the streamwise turbulence intensity is almost constant in the core region, where on the other hand the spanwise turbulence intensity still vary in the center part of the channel. The highest intensity is found in the wall normal component which has a maximum $v_{rms}/u_\tau \approx 2.4$ around the center of the channel. Figure 9 shows the variation of the r.m.s vorticity fluctuations which have constant behavior through out 80% of the channel. The value of $\omega_{x_{rms}}$ in the core region is higher than $\omega_{y_{rms}}$ and $\omega_{z_{rms}}$. This is rather different from non-rotating shear flows, see for example Kim et al.[14]. The local near-wall minimum of $\omega_{x_{rms}}$ is an evidence of the presence of streamwise vortices[14], where the global minimum of 0.24 is at $y^+ \approx 5$ ($y/h \approx 0.07$). The maximum value of $\omega_{z_{rms}}$ approaches a value of 0.48 ($y/h \approx 0.006$) at the wall.

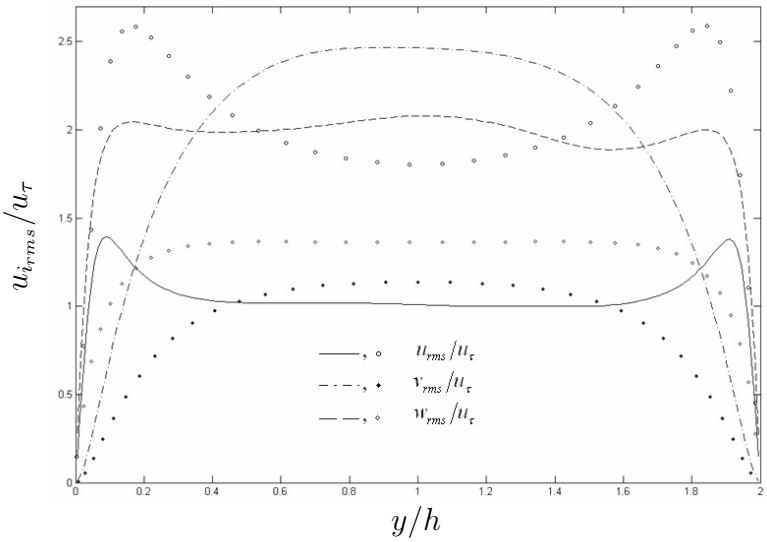

Figure 8: Root mean square of velocity fluctuations profiles scaled with the wall unit. $Ro = 0.7$ (lines) compared with DNS-data for $Ro = 0.0$ from Bech et al.[5](diamonds).

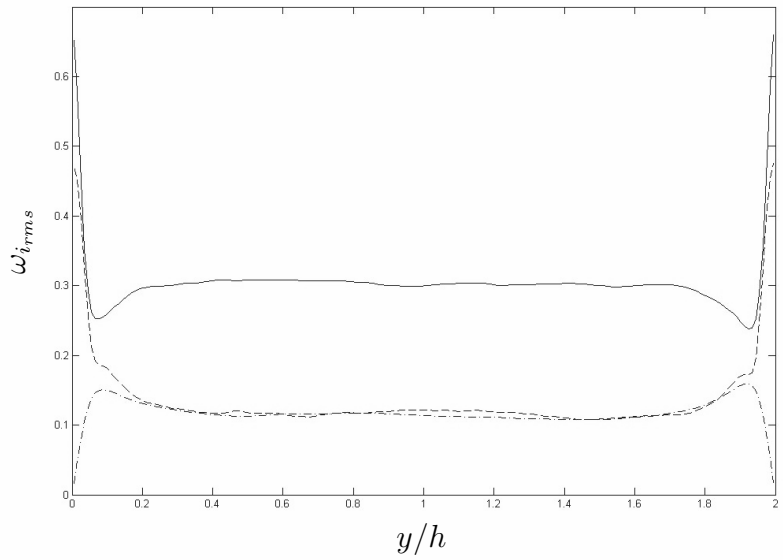

Figure 9: Root mean square of vorticity fluctuations normalized by the mean shear for $Ro = 0.7$. $\omega_{x_{rms}}$ (—), $\omega_{y_{rms}}$ (-.-), $\omega_{z_{rms}}$ (- - -).

Concluding remarks

DNSs of turbulent Couette flow were carried out with Re set at 1300 for both rotating and non-rotating the frame of reference. The cases of zero rotation number with different computational box size allow proper investigation of the streamwise large scale structures. We find a suitable long/wide enough computational box by calculating the two point correlation.
In the case of high rotation number, we use the same computational box which found to be suitable for the non-rotating case but with a coarser grid, where the Taylor-Görtler instabilities disappear from the flow.

The work reported herein was supported by the Norwegian Research Council through a research grant and computing time.

References

[1] M.J. Lee and J. Kim. The structure of turbulence in a simulated plane Couette flow, *Eighth Symposium on Turbulence Shear Flows, Munich*, **5-3**, 1991.

[2] D.V. Papavassiliou and T.J. Hanratty. Interpretation of large-scale structures observed in a turbulent plane Couette flow, *Int. J. Heat and Fluid Flow*, **vol.18**, 55–69, 1997.

[3] B. Debusschere and C.J. Rutland. Turbulent scalar transport mechanisms in plane channel and Couette flows, *Int. J. Heat and Mass Transfer*, **vol.47**, 1771–1781, 2004.

[4] Z. Hu, C.L. Morfey and N.D. Sandham. Sound radiation in turbulent channel flows, *J. Fluid Mech.*, **vol.475**, 269–302, 2003.

[5] K.H. Bech, N. Tillmark, P.H. Alfredsson and H.I. Andersson. An investigation of turbulent plane Couette flow at low Reynolds numbers, *J. Fluid Mech.*, **vol.286**, 291–325, 1995.

[6] J. Komminaho, A. Lundbladh and A. Johansson. Very large structures in plane turbulent Couette flow, *J. Fluid Mech.*, **vol.320**, 259–285, 1996.

[7] T. Tsukahara, H. Kawamura and K. Shingai. DNS of turbulent Couette flow with emphasis on the large-scale structure in the core region, *J. Turbulence*, **vol.7**(19), 2006.

[8] K.H. Bech and H.I. Andersson. Secondary flow in weakly rotating turbulent plane Couette flow, *J. Fluid Mech.*, **vol.317**, 195–214, 1996.

[9] K.H. Bech and H.I. Andersson. Turbulent plane Couette flow subject to strong system rotation, *J. Fluid Mech.*, **vol.347**, 289–314, 1997.

[10] A. Holstad, P.S. Johansson, H.I. Andersson and B. Pettersen. On the influence of domain size on POD modes in turbulent plane Couette flow, *Direct and Large-Eddy Simulation VI*, 763–770, Springer 2006.

[11] R. Kristoffersen, K.H. Bech and H.I. Andersson. Numerical study of turbulent plane Couette flow at low Reynolds number, *Advances in Turbulence IV*, 337–343, 1993.

[12] M. Manhart. A zonal grid algorithm for DNS of turbulent boundary layers, *Computers & Fluids*, **vol.33**, 435–461, 2004.

[13] P.H. Alfredsson and N. Tillmark. Instability, transition and turbulence in plane Couette flow with system rotation, *Proc. IUTAM Symposium*, 173–193, 2005.

[14] J. Kim, P. Moin and R. Moser. Turbulence statistics in fully developed channel flow at low Reynolds number, *J. Fluid Mech.*, **vol.117**, 133–166, 1987.

[15] J.M. Hamilton, J. Kim and F. Waleffe. Regeneration mechanisms of near-wall turbulence structures, *J. Fluid Mech.*, **vol.287**, 317–348, 1995.

Paper 3

Computer experiments on rapidly rotating plane Couette flow

Barri, M. & Andersson, H. I.

Accepted for publication in *Communications in Computational Physics*,
DOI: 10.4208/cicp.2009.09.068

Computer experiments on rapidly rotating plane Couette flow

Mustafa Barri* and Helge I. Andersson

Fluids Engineering Division, Department of Energy and Process Engineering, Norwegian University of Science and Technology (NTNU), 7491 Trondheim, Norway.

Received 23 April 2009; Accepted (in revised version) 17 July 2009

Abstract. The turbulence in plane Couette flow subjected to system rotation is investigated. The anti-cyclonic rotation rate is well above the range in which roll-cells occur and close to the upper bound, beyond which no stationary turbulent states of motion exist. The mean velocity profile exhibits a linear region over 80% of the cross-section, in which the mean absolute vorticity is driven to zero. Viscous effects still prevail in narrow regions next to the walls, whereas the quasi-homogeneous central core exhibits abnormal anisotropies of the Reynolds stress tensor, the vorticity tensor and the energy dissipation rate tensor. In spite of the distinctly higher turbulence level observed, a 13% drag reduction is found. This paradoxical finding is ascribed to configurational changes in the turbulence field brought about by the system rotation.

AMS subject classifications: 76M12, 76F10, 76F65, 76U05

Key words: Turbulence, plane Couette flow, system rotation, anti-cyclonic rotation, anisotropy tensor, zero absolute mean vorticity.

1 Introduction

Rotation might give rise to remarkable and profound alterations of shear flow turbulence. Ever since the illuminating experimental investigation of a rotating plane channel flow by Johnston *et al.* [20], it has been known that the action of the Coriolis force due to system rotation changes not only the mean velocity distribution but also the turbulent velocity fluctuations. The location of maximum mean velocity is shifted from the channel center towards the so-called '*suction*' side, and the mean velocity profile exhibits a linear region with slope close to twice the imposed rotation rate. The turbulence intensity is reduced or sometimes even suppressed near this '*suction*' side, whereas the turbulent agitation is enhanced at the opposite side of the channel, i.e. along '*pressure*' side. These essential

*Corresponding author. *Email addresses:* mustafa.barri@ntnu.no (M. Barri), helge.i.andersson@ntnu.no (H.I. Andersson)

observations have later been confirmed and supplemented by more recent experimental studies by Nakabayashi and Kitoh [30, 31] and direct numerical simulations by Kristoffersen and Andersson [22], Lamballais *et al.* [23, 24], Liu and Lu [26] and Grundestam *et al.* [13].

The influence of the Coriolis force due to imposed system rotation depends both on the orientation and the magnitude of the background vorticity $2\boldsymbol{\Omega}^F$ relative to the mean flow vorticity $\boldsymbol{\Omega} \equiv \nabla \times \boldsymbol{u}$ in a rotating frame-of-reference. In simple shear flows, like the two-dimensional channel flow, the mean vorticity vector $\boldsymbol{\Omega}$ is perpendicular to both the mean flow direction, say x, and to the wall-normal direction, say y. If the angular velocity vector $\boldsymbol{\Omega}^F$ of the rotating frame-of-reference is aligned with $\boldsymbol{\Omega}$, the local vorticity ratio $S \equiv 2\Omega^F/\Omega$ effectively distinguishes between different flow regimes. In the plane channel flow, for instance, S changes sign where the mean velocity peaks and the rotating channel flow is therefore simultaneously affected by cyclonic ($S > 0$) and anti-cyclonic ($S < 0$) rotation.

In contrast with the pressure-driven plane channel flow, the shear-driven plane Couette flow exhibits a monotonically increasing mean velocity from one wall to the other with the obvious implication that the entire flow field is either exposed to cyclonic or anti-cyclonic rotation. This fact alone makes the rotating plane Couette flow an attractive prototype for explorations of rotational effects on rotating shear flows. In this context, the notion of '*pressure*' and '*suction*' sides should be discarded. Hart [15] found that the *laminar* plane Couette flow is unstable with respect to inception of counter-rotating roll cells in the parameter range $-1 < S < 0$ and otherwise stable. In the *turbulent* flow regime, the mean flow vorticity Ω is no longer constant across the flow and S varies with the distance from the wall. Bech and Andersson [6] therefore introduced a rotation number defined in terms of the average mean flow vorticity Ω_{av}, i.e. $Ro \equiv -2\Omega^F/\Omega_{av}$. Here, Ω_{av} also equals the constant vorticity of the corresponding laminar Couette flow. Care should be taken not to mix up the rotation number defined above with the Rossby number routinely used in geophysical fluid dynamics.

In a computational study of turbulent plane Couette flow, Bech and Andersson [6] observed that the roll cell instability was present also in the turbulent case provided that the rotation is anti-cyclonic ($Ro = +0.01$). If the Couette flow, on the other hand, was subjected to weak cyclonic rotation with $Ro = -0.01$, no roll cells appeared and the turbulence was damped as compared with the turbulence level in non-rotating Couette flow. At the same time laboratory investigations by Tillmark and Alfredsson [37] and computer simulations by Komminaho *et al.* [21] showed that cyclonic rotation may completely suppress the turbulence.

While Bech and Andersson [6] were concerned about weak rotation with a rotation number $Ro = \pm 0.01$, the intermediate rotation numbers $Ro = 0.10, 0.20$ and 0.50 were considered in a subsequent study by Bech and Andersson [7]. The weak but yet distinct roll cells observed already at $Ro = +0.01$ became more regular and energetic at $Ro = +0.10$ and $+0.20$. At the highest rotation rate $Ro = +0.50$, however, a disordering of the counter-rotating vortices appeared. The overall turbulence level was substantially higher than

in the non-rotating flow and the resulting skin-friction was roughly 20% above that for $Ro = 0$.

Bech and Andersson [7] also attempted to simulate the anti-cyclonically rotating Couette flow with $Ro = +1.0$ and reported that the turbulent fluctuations were completely suppressed and the flow laminarized. This finding is consistent with the more recent observations by Alfredsson and Tillmark [1]. Their flow visualization studies revealed that the distinct roll cells observed at $Ro = +0.50$ were also distinguishable at $Ro = +0.75$. For rotation numbers above $+0.75$, however, they claim that the predominant cell structures have vanished and the elongation of the turbulent structures was significant. For $Ro > +1.0$ the turbulence was quenched, no roll cells were seen, and the flow was fully laminarized.

The central core region of a rotating Couette flow bears some resemblances with homogeneous shear flow subjected to system rotation. Rotating homogeneous shear flows have been considered both theoretically and numerically, including the computer simulations by Bartello *et al.* [5], Salhi and Cambon [35], Yanase *et al.* [40], Brethouwer [9] and Iida *et al.* [16]. Rotating homogeneous shear flows are known to be neutrally stable if the vorticity ratio $S = -1.0$ [11, 35]. This special case of anti-cyclonic rotation with $S = -1.0$, i.e. *zero absolute mean vorticity*, is particularly interesting. According to the Bradshaw-Richardson number $B = S(S+1)$, the case $S = -1$ should be neutrally stable (i.e. $B = 0$) just as the non-rotating case $S = 0$. Cambon *et al.* [11] convincingly demonstrated that although the zero absolute mean vorticity case should be equivalent to the $S = 0$ case according to the Bradshaw-Richardson stability criterion, the flow dynamics are indeed strikingly different. Comprehensive support of this view has subsequently been provided by Salhi and Cambon [35] and Brethouwer [9]. Yanase *et al.* [40] and Brethouwer [9] found that the flow field was dominated by very elongated and intense streamwise vortex tubes. Iida *et al.* [16] focused on $S = \pm 0.5$ with the view to investigate the tilting mechanism of the longitudinal vortex structures. Here, anti-cyclonic rotation $S = -1/2$ corresponds to *zero-tilting vorticity* and maximum destabilization ($B = -1/4$) according to Cambon *et al.* [11]. Iida *et al.* [16] examined the influence of spanwise system rotation on the vertical flow structures and observed that the spanwise tilting of the structures was reduced whereas their inclination with respect to the mean flow direction was increased.

It is well known that the rotating plane Couette flow can be considered as the narrow-gap limit of the Taylor-Couette (TC) flow, i.e. the fluid motion in the annular gap between two independently rotating circular cylinders; see e.g. Dubrulle *et al.* [12]. A wealth of stable flow regimes was observed in the TC apparatus of Andereck *et al.* [2], several of which exhibited toroidal Taylor vortices analogous to the roll cells observed by Bech and Andersson [7] and Alfredsson and Tillmark [1] in the rotating plane Couette flow. Townsend [38] assumed two different kinds of TC turbulence, one generated by the mean shear and the other due to the Taylor-vortices. In *featureless turbulence*, i.e. turbulence devoid of any sustained large-scale features, only the shear mechanism is retained. Such featureless turbulence was also observed in the Taylor-Couette flow by Andereck *et al.* [2]

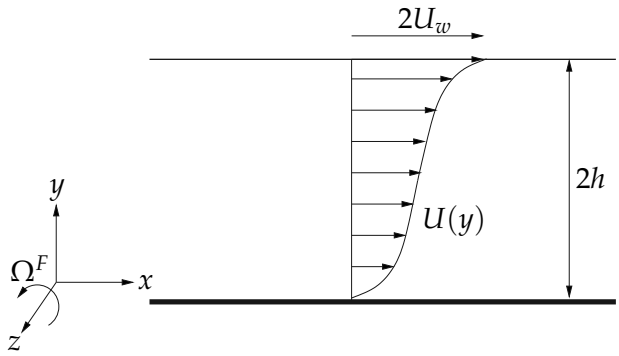

Figure 1: Schematic of spanwise rotating plane Couette flow. The system is rotating with constant angular velocity Ω^F about the spanwise $z-$axis.

in a certain parameter range.

The purpose of the present study is to identify, if possible, a plane Couette flow subjected to sufficiently strong anti-cyclonic rotation such that the roll-cell instability is completely suppressed but the turbulence still persists. If so, this particular flow configuration offers a unique environment in which the influence of the Coriolis force due to system rotation on shear flow turbulence can be studied in isolation, i.e. without being hampered by the simultaneous occurrence of roll cells. Unlike the featureless turbulence occurring in the Taylor-Couette flow, the plane Couette flow turbulence is unaffected by streamline curvature which inevitably affects the TC-flow, see e.g. Patel and Sotiropoulos [33].

First, the fully developed turbulent plane Couette flow in orthogonal-mode rotation is defined in Section 2 and some fundamental conservation laws in rotating frames-of-reference are provided. The basics of the direct numerical simulations performed are provided in Section 3. The primary flow statistics and Reynolds stress budgets are presented in Sections 4 and 5, respectively, while vortex dynamics and flow anisotropies are considered in Sections 6–7.

2 Orthogonally rotating plane Couette flow

2.1 Flow configuration and governing equations

Let us consider the turbulent Couette flow driven in the $x-$direction by the relative motion of two infinite parallel planes separated a distance $2h$ in the $y-$direction. The fluid motion is induced solely by the prescribed velocity difference $2U_w$ between the two planes (see figure 1). The flow is characterized by the Reynolds number $Re \equiv \rho U_w h/\mu$, where ρ and μ are the density and the dynamic viscosity of the incompressible fluid, respectively. The shear-driven Couette flow is rotated about the spanwise $z-$axis with

constant angular velocity $\mathbf{\Omega}^F = (0,0,\Omega^F)$. Since the average mean vorticity Ω_{av} is $-U_w/h$, the rotation number becomes:

$$Ro \equiv -2\Omega^F/\Omega_{av} = 2\Omega^F h/U_w \ . \tag{2.1}$$

The incompressible flow of a Newtonian fluid in a constantly rotating frame-of-reference is governed by the conservation equations for mass and momentum:

$$\nabla \cdot \boldsymbol{u} = 0 \tag{2.2a}$$

$$\frac{\partial \boldsymbol{u}}{\partial t} + \boldsymbol{u} \cdot \nabla \boldsymbol{u} = -\frac{1}{\rho}\nabla p + \nu \nabla^2 \boldsymbol{u} - 2\mathbf{\Omega}^F \times \boldsymbol{u} \tag{2.2b}$$

where ν is the kinematic viscosity μ/ρ. The last term on the right-hand side of equation (2.2*b*) is the Coriolis force due to system rotation, whereas centrifugal effects are absorbed in the effective pressure p. Since both U_w and Ω^F are prescribed constants, the time-dependent flow field will eventually evolve into a statistically steady state which is the subject of the present investigation.

2.2 Reynolds' decomposition

The instantaneous velocity components u_i and pressure p can be decomposed into mean (U_i, P) and fluctuating (u_i, p) parts to facilitate both the presentation and interpretation of the outcome of the simulation. In the absence of rotational-induced roll cells, the mean flow becomes unidirectional $(U,0,0)$ and the mean pressure P serves primarily to balance the wall-normal component of the Coriolis force:

$$\frac{1}{\rho}\frac{dP}{dy} = -2\Omega^F U - \frac{d}{dy}\overline{v^2} \ . \tag{2.3}$$

This balance results from the Reynolds-average of equation (2.2*b*) in the $y-$direction, provided that the flow is statistically homogenous in $(x,z)-$planes. If the corresponding mean momentum equation in the $x-$direction is integrated once in y, the constancy of the total mean shear stress:

$$\mu\frac{dU}{dy} - \rho\overline{uv} = \tau_w \equiv \rho u_\tau^2 \tag{2.4}$$

is obtained. Here, u_τ denotes the wall-friction velocity. It is noteworthy that the sum of the viscous and turbulent shear stresses remains constant throughout the flow field, irrespective of whether the flow is rotating or not. This is so because the mean flow U is only affected indirectly by the Coriolis force through the turbulent or Reynolds shear stress $-\rho\overline{uv}$. The latter is governed by the transport equation for the individual second-moments:

$$\frac{D\overline{u_i u_j}}{Dt} = P_{ij} + G_{ij} + D_{ij} + \Pi_{ij} - \varepsilon_{ij} \ . \tag{2.5}$$

The right-hand-side terms, which are responsible for production due to mean shear (P_{ij}), production due to rotation (G_{ij}), viscous and turbulent diffusion (D_{ij}), pressure-strain redistribution (Π_{ij}), and viscous energy dissipation (ε_{ij}), are defined in the Appendix.

The mean turbulent kinetic energy $k \equiv \frac{1}{2}\overline{u_i u_i}$ is a convenient scalar measure of the turbulent activity. The one-to-one relationship (2.4) between the viscous and turbulent shear stress components makes it possible to express the production of mean turbulent kinetic energy P_K in terms of only the mean shear rate:

$$P_K \equiv \frac{1}{2}P_{ii} = \frac{1}{2}P_{xx} = -\overline{uv}\frac{dU}{dy} = \frac{u_\tau^4}{\nu}\left(1-\frac{dU^+}{dy^+}\right)\frac{dU^+}{dy^+} \,. \tag{2.6}$$

Here, U^+ and y^+ are the inner or wall variables U/u_τ and yu_τ/ν, respectively. Maximum production is obtained where $dU^+/dy^+ = 1/2$, which according to equation (2.4) is the location at which the viscous and turbulent shear stress components are equal. Equation (2.6) for the production P_K of mean turbulent kinetic energy also shows that the production $P_K = 0$ as long as $dU^+/dy^+ = 1$, i.e. in the innermost viscous sublayer where the mean velocity varies linearly with the distance from the wall. This turns out to be an exact result for the plane Couette flow, whereas the same is only approximately correct in channel flows.

2.3 Mean vorticity and second-moments of vorticity fluctuations

The components of the instantaneous vorticity vector are decomposed in mean Ω_i and fluctuating ω_i parts in accordance with the Reynolds decomposition. In the present case where the steady mean flow is unidirectional and the turbulence statistics are homogeneous in $(x,z)-$planes and in time, the equation for the only non-vanishing mean vorticity component $\Omega_z = -dU/dy$ reduces to the ordinary differential equation:

$$0 = \frac{d}{dy}(\overline{w\omega_y} - \overline{v\omega_z}) + \nu\frac{d^2\Omega_z}{dy^2} \tag{2.7}$$

which can be integrated once to give:

$$0 = \overline{w\omega_y} - \overline{v\omega_z} + \nu\frac{d\Omega_z}{dy} \,. \tag{2.8}$$

Here, the constant of integration is zero since all the terms vanish identically at both walls. It is noteworthy that the vorticity $2\Omega^F$ due to the imposed system rotation does not appear explicitly in equation (2.7). This is so because we are concerned only with orthogonal mode rotation, i.e. the axis of rotation is aligned with the mean strain rate vector. This particular orientation of the imposed rotation does not contribute to stretching and/or tilting of the mean vorticity by mean strain.

Transport for the individual second-moments of the vorticity fluctuations can written symbolically as:

$$\frac{D\overline{\omega_i\omega_j}}{Dt} = T1_{ij} + T2_{ij} + S3_{ij} + S4_{ij} + S5_{ij} + V6_{ij} + V7_{ij} \tag{2.9}$$

where the terms on the right-hand side are given in the Appendix. The terms are numbered according to their order of appearance in Tennekes and Lumley [36] and Antonia and Kim [3]. Their enstrophy budgets are readily recovered as half the trace of equation (2.9). The capital letters are used to distinguish between transport (T), stretching (S) and viscous (V) terms. In the equation above, the system rotation appears explicitly only in the third stretching term $S5_{ij}$.

A striking difference between the second-moment equation for the velocity fluctuations (2.5) and that for the vorticity fluctuations (2.9) should be pointed out. While equation (2.5) simplifies considerably upon contraction of the indices since both $\Pi_{ii} = 0$ and $G_{ii} = 0$, none of the terms vanish when equation (2.9) is contracted to the enstrophy budget. In the present context, it is particularly noteworthy that the effect of system rotation remains in the stretching terms $S5_{ii}$ also after contraction. The enstrophy is therefore explicitly influenced by rotation, in contrast with the turbulent kinetic energy.

3 Computer simulations

A direct numerical simulation of a fully developed Couette flow at $Re = 1300$ and $Ro = 0.7$ has been performed. This Reynolds number is the same as that considered by Bech *et al.* [8] and Bech and Andersson [6,7], which is well above 500 as required for fully developed turbulence to persist [1]. The second-order accurate finite-volume code MGLET [28], was used for the numerical integration of the incompressible Navier-Stokes equations (2.2). The pressure is defined at the center of each grid cell and the velocity components at the interfaces. The velocity components and their derivatives are obtained by linear interpolation and central differences, respectively. An explicit second-order Adams-Bashforth scheme was employed for the time integration. Periodic boundary conditions were used in the two homogeneous directions and no-slip and impermeability conditions were imposed at both walls. The simulations were run on a parallel MPI computer.

The length and width of the computational domain were $L_x = 28\pi h$ and $L_z = 4\pi h$, and the number of grid points was $896 \times 240 \times 240$ in the $x-$, $y-$ and $z-$directions, respectively. This domain is nearly three times longer than that used by Bech *et al.* [8] and Bech and Andersson [6,7]. The resolution in wall-units achieved by this grid for $Ro = 0.7$ corresponded to $\Delta x^+ = 7.5$ and $\Delta z^+ = 4.0$ in the two homogeneous directions whereas Δy^+ varied from 0.15 to 1.14 in the wall-normal direction. Statistical averaging was made in the two homogeneous directions and over a time interval $30h/u_\tau$. Preliminary results obtained with a smaller domain and coarser mesh were presented by Barri and Andersson [4].

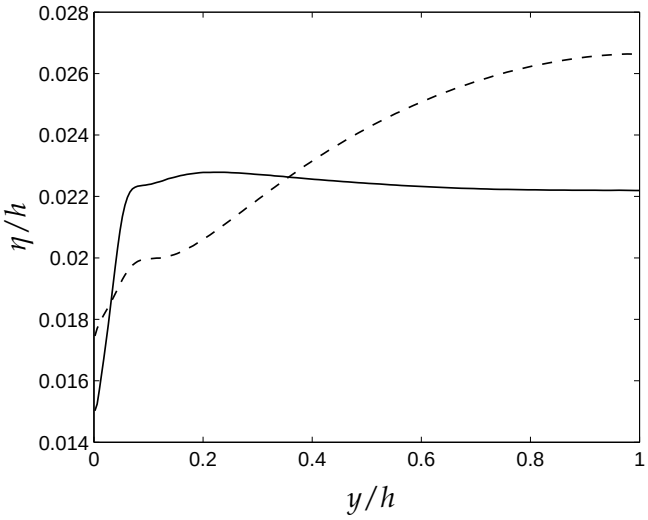

Figure 2: Kolmogorov length scale η/h for the rotating case Ro=0.7 (solid line) compared with the corresponding non-rotating Couette flow (broken line).

For comparative purposes, a new simulation of the non-rotating Couette flow at $Re=$ 1300 was performed using exactly the same computational domain and the same grid as for the $Ro=0.7$ case. In order to eliminate the potential role of domain size and grid resolution on the results, data from the new Ro=0 simulation will be used as the reference case throughout this paper to demonstrate the effects of system rotation. Comparisons with the DNS data of Bech *et al.* [8] will be provided only for the mean velocity and the Reynolds stress profiles in Section 4.

The Kolmogorov length scale $\eta=(\nu^3/\epsilon)^{1/4}$ is a measure of the order of magnitude of the size of the smallest turbulent eddies. In anticipation of small-scale isotropy, η is a scalar quantity. Figure 2 shows the Kolmogorov scale evaluated on the basis of the scalar dissipation rate ϵ of the turbulent kinetic energy. Since ϵ varies across the flow, also η varies with y/h. While η increases with the wall distance from $0.018h$ to $0.026h$ in the non-rotating case, η exhibits a surprisingly constant level of about $0.022h$ except in the innermost 10% of the rotating Couette channel. It is worthwhile to point out that if the Kolmogorov length scale η is expressed in wall units, i.e. $\eta^+=Re_\tau\eta/h$, we find that $\eta^+\approx 2$ which suggests that the grid resolution used in the present simulations is fully adequate.

In order to see whether or not counter-rotating roll cells, as observed both by Bech and Andersson [7] and Tillmark and Alfredsson [37] at relatively high anti-cylonic rotation rates, are embedded in the three-dimensional flow field, the two-point correlations $R_{ij}(r_k)$ are shown in figure 3, in which also results for the non-rotating case are included. The non-oscillatory behaviour of $R_{22}(r_z)$ and $R_{33}(r_z)$ and the rapid decay to zero of $R_{22}(r_x)$

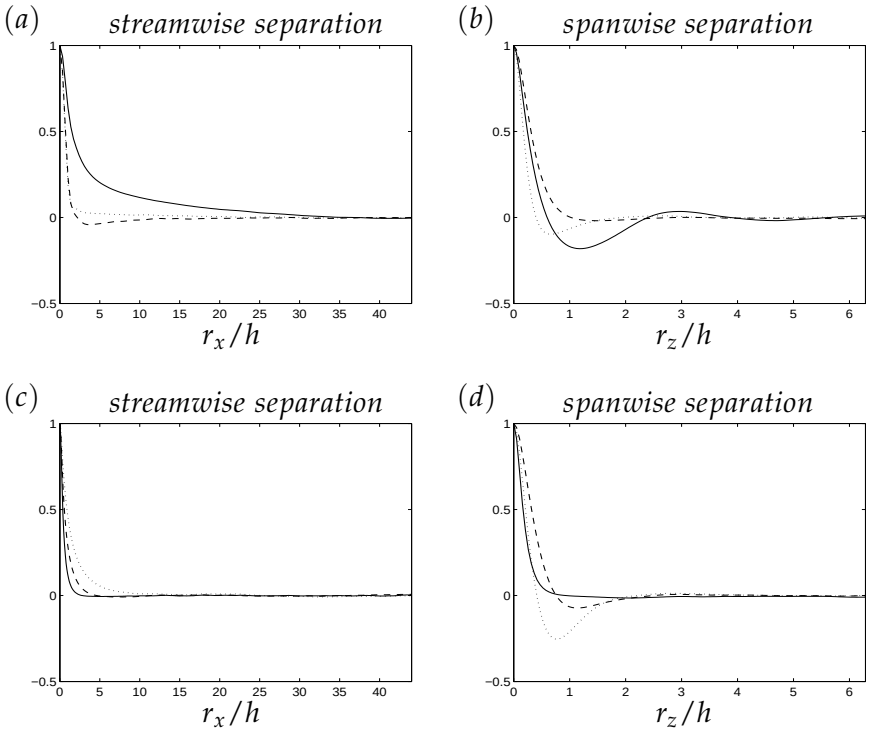

Figure 3: Two-point correlations near the center $(y/h=0.98)$ with (a), (c) streamwise and (b), (d) spanwise separations. Results without rotation $(Ro=0)$ are at the top and with rotation $(Ro=0.7)$ are at the bottom. —— R_{uu}; $\cdots$ R_{vv}; − − − R_{ww}.

and $R_{33}(r_x)$ assure that the present flow field with $Ro=0.7$ does not possess any counter-rotating roll cells.

While Alfredsson and Tillmark [1] observed elongated turbulent structures and weaker roll-cells of varying spanwise extent when the rotation number was increased from 0.50 to 0.75, the present DNS at $Ro=0.70$ showed no roll cells at all. The fact that the quenching of the roll-cells at high anti-cyclonic rotation rates occurred at a somewhat lower rotation number than in the laboratory channel might be due to the lower Reynolds number $(Re=790)$ in their study or more likely due to their finite-length channel width and the relatively low aspect ratio (about 5) which implies that side-wall effects may play a role.

The presence of extraordinarily long flow structures in plane Couette flow [21, 39] makes the required length L_x of the computational domain substantially larger than that needed in a channel flow simulation. The two-point correlations presented in figure 3 show that both the length L_x and the width L_z used herein are sufficient to accommodate the largest flow structures, both in the rotating and the non-rotating Couette flow. It is also noteworthy from figure $3(c)$ that the length scale of the wall-normal fluctuations is substantially larger than the length scale of the streamwise velocity fluctuations. This is

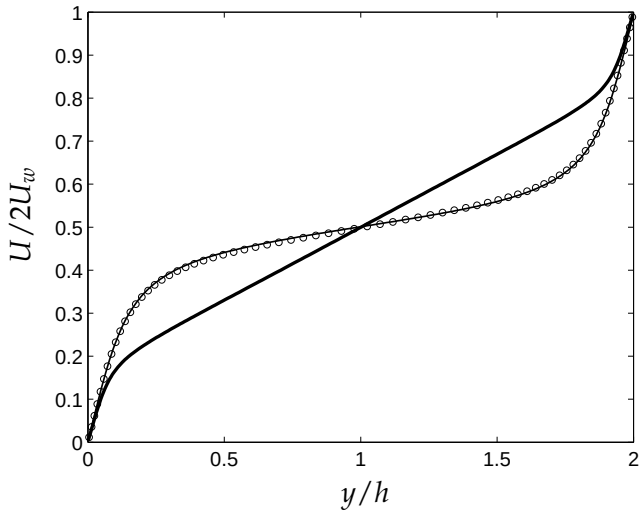

Figure 4: Mean velocity distribution $U(y)$ for $Ro=0.7$ (bold line) compared with the corresponding profile for non-rotating Couette flow (thin line) and DNS data from [8] for $Ro=0$ (symbols).

just the opposite of the situation in channel and Couette flow without rotation (see figure 3*a*) and is a first indication of the anomalies of rapidly rotating Couette flow.

4 Mean flow and velocity statistics

The shape of the mean velocity profile $U(y)$ in figure 4 is rather different from the typical $S-$shaped velocity distribution observed by Bech *et al.* [8] and others in non-rotating Couette flow. The DNS data from Bech *et al.* [8] are included here and in the two subsequent figures simply to demonstrate the close resemblance between the present simulation for $Ro=0$ and that of Bech *et al.* [8].

For the anti-cyclonically rotating Couette flow, the mean velocity profile exhibits a substantial linear range which extends over 80% of the cross-section. The slope dU/dy of the velocity profile in the linear region is close to $2\Omega^F$, which makes the local vorticity ratio $S \approx -1$. This shows that the mean velocity profile has adjusted itself such that the mean flow vorticity Ω just counterbalances the imposed anti-cyclonic background vorticity $2\Omega^F$, i.e. the absolute vorticity in an inertial frame-of-reference is driven to zero. This phenomenon has been observed before, both in rotating channel flows by Johnston *et al.* [20], Kristoffersen and Andersson [22], Lamballais *et al.* [23, 24] and Nakabayashi and Kitoh [30, 31] and in rotating Couette flows by Bech and Andersson [7].

The wall-friction velocity u_τ defined in equation (2.4) is obtained as a part of the numerical solution. Since the turbulent shear stress $-\rho\overline{uv}$ vanishes identically at the walls,

u_τ is determined by the wall-slope of the mean velocity profile. The Reynolds number $Re_\tau \equiv \rho u_\tau h/\mu$ based on the wall-friction velocity u_τ is an essential dimensionless parameter, which in the present case becomes ≈ 76.5. This is significantly lower than $Re_\tau = 82.02$ found for $Ro = 0$ and $Re_\tau = 82.2$ reported by Bech *et al.* [8] for non-rotating Couette flow at the same Reynolds number. This implies that a drag reduction of about 13% has been achieved by the imposed rotation. On the contrary, at the highest rotation number Ro=0.5 considered by Bech and Andersson [7] the wall-friction Reynolds number was Re_τ=91.0, i.e. a 21% increase in wall-friction.

The extent of the Coriolis-dominated region in figure 4 is consistent with the criterion proposed by Nakabayashi and Kitoh [30] that system rotation matters when $y > \delta_c$, where δ_c is the Coriolis length scale $\delta_c = u_\tau/\Omega^F$. In the present case, this criterion can be expressed as

$$\frac{y}{h} > \frac{2}{Ro}\frac{Re_\tau}{Re} \approx 0.2 \,. \tag{4.1}$$

The inequality (4.1) suggests that the region in which system rotation is a leading-order effect expands with increasing rotation Ro.

Nakabayashi and Kitoh [30] argued that the Coriolis force may penetrate deep into the near-wall layer. The role played by the Reynolds number is taken over by a new dimensionless parameter, namely the ratio between the viscous length scale ν/u_τ and the Coriolis length scale u_τ/Ω^F, i.e. $\nu\Omega^F/u_\tau^2$. This new dimensionless group can readily be expressed as a combination of the rotation number and the Reynolds number as:

$$\frac{\nu\Omega^F}{u_\tau^2} = \frac{1}{2} Ro Re Re_\tau^{-2} \,. \tag{4.2}$$

In the present case of a rapidly rotating Couette flow, this group is about 0.07. In the laboratory experiments of rotating channel flow reported by Nakabayashi and Kitoh [30,31] this parameter did not exceed 0.01, whereas Kristoffersen and Andersson [22] reached about 0.02 at their highest rotation rate. The case considered herein is therefore undoubtedly one of strong rotation. The present results support the relevance of the dimensional group in equation (4.2) as a distinguishing parameter in rotating shear flow. While Nakabayashi and Kitoh [30] introduced this parameter as the ratio between the viscous length scale and the Coriolis length scale, the parameter can equally well be identified as the ratio between the viscous time scale ν/u_τ^2 and the Coriolis time scale $1/\Omega^F$.

It is obvious that dU/dy cannot exceed U_w/h in the Couette flow and this intuitive constraint inevitably implies that $Ro = 1$ is an upper bound for which neutral stability $S = -1$ can be sustained. This is consistent with the upper bound on momentum transport in turbulent Couette flow derived by Busse [10]. He found that no state of turbulent motion can exist for

$$4Re \leq \frac{1708}{4ReRo} + 4ReRo \,. \tag{4.3}$$

This criterion for turbulence to exist can be recast into an explicit constraint on the rota-

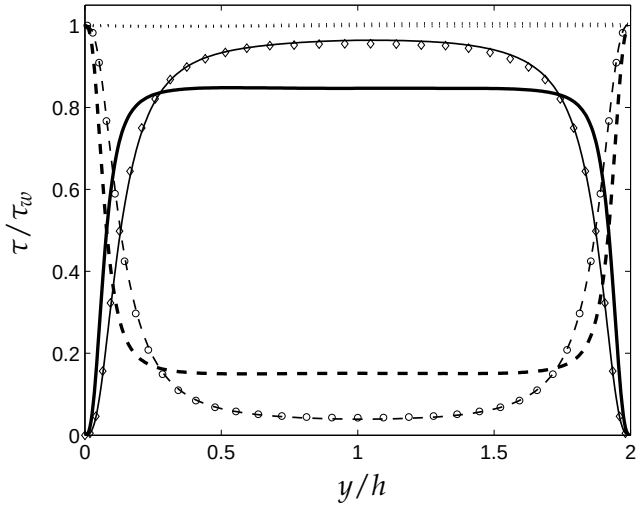

Figure 5: Variation of viscous and turbulent shear stress across the flow for $Ro=0.7$ (bold lines) compared with the corresponding data for non-rotating Couette flow (thin lines) and DNS data from [8] for $Ro=0$ (symbols). Viscous shear stress $\mu(dU/dy)/\tau_w$ (– – –; ○) and turbulent shear stress $-\rho\overline{uv}/\tau_w$ (——; ◇).

tion number:

$$Ro < \frac{1}{2}\left(1+\sqrt{1-4\frac{1708}{16}\frac{1}{Re^2}}\right) . \tag{4.4}$$

For $Re = 1300$, this formulae suggests that turbulence can be maintained only if $Ro < 0.9999$, i.e. fully consistent with our intuition-based conjecture that Ro cannot exceed unity. The recent flow visualizations of Alfredsson and Tillmark [1] indeed showed that the turbulence was suppressed and the flow relaminarized for rotation numbers beyond 1.0.

The partition between viscous and turbulent shear stresses is shown in figure 5. Due to the substantial linear portion of the mean velocity profile in figure 4, the viscous shear stress is constant over the entire center region and the stress magnitude is 3–4 times larger than in the non-rotating case. Let us recall that the viscous shear stress $\mu dU/dy$, when normalized by τ_w, is equal to dU^+/dy^+, i.e. the inner-variable mean shear rate. The slope of the mean velocity in outer variables, as in figure 4, is related to dU^+/dy^+ in figure 5 in accordance with:

$$\frac{d\widetilde{U}}{d\widetilde{y}} \equiv \frac{d(U/2U_w)}{d(y/h)}) = \frac{1}{2}Re^{-1}Re_\tau^2\frac{dU^+}{dy^+} . \tag{4.5}$$

The local vorticity ratio S can be deduced from either of the two, i.e.

$$S = -\frac{2\Omega^F}{dU/dy} = -\frac{1}{2}Ro\left(\frac{d\widetilde{U}}{d\widetilde{y}}\right)^{-1} = -RoReRe_\tau^{-2}\left(\frac{dU^+}{dy^+}\right)^{-1} . \tag{4.6}$$

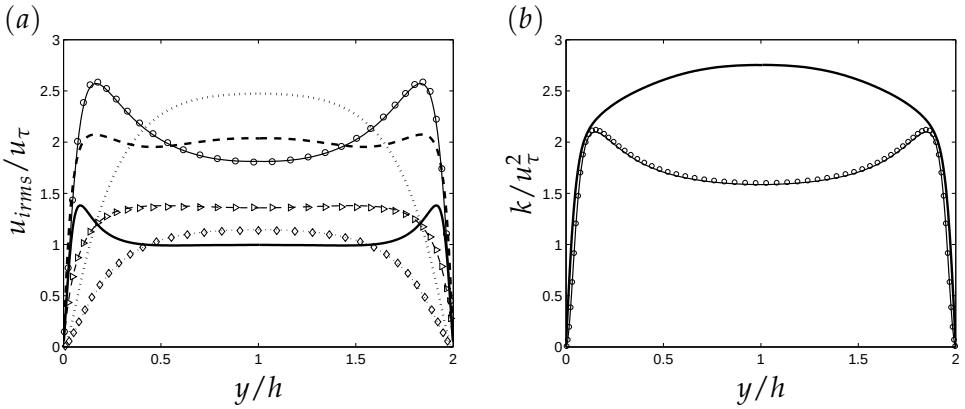

Figure 6: Variation of turbulence intensities and kinetic energy k across the flow for $Ro = 0.7$ (bold lines) and $Ro = 0$ (thin lines) compared with the corresponding data for non-rotating Couette flow (symbols) from [8]. The results are scaled with the corresponding friction velocities. (a) Turbulence intensities u_{rms} (——; ○), v_{rms} (···; ◇), w_{rms} (– – –; ▷); (b) Turbulent kinetic energy k for $Ro=0.7$ (bold line) and $Ro=0$ (thin line) compared with DNS data (○) from [8].

With dU^+/dy^+ approximately equal to 0.16 over nearly 80% of the cross-section in figure 5, the core region value of $S \approx -1.004$. In the substantial part of the cross-section where S is practically equal to -1.0, the absolute mean vorticity vanishes and the shear-Coriolis instability is neutral. A further elaboration on the consequences of this observation is postponed until Section 5.

The constancy of the total mean shear stress, as expressed in equation (2.4), therefore also makes the turbulent shear stress $-\rho\overline{uv}$ constant over about 80% of the cross section. The turbulent shear stress equals the viscous shear stress at about $y/h \approx 0.07$, which is significantly closer to the wall than in the non-rotating case where the two shear stresses equal at $y/h \approx 0.10$. This intersection point is exactly where the turbulent energy production attains its maximum value (see the discussion in §2.2). This observation therefore reflects that the imposition of rotation makes the near-wall layers thinner.

This suggestion is confirmed by the profiles of the turbulence intensities in figure $6(a)$, which show that the peak positions are indeed closer to the walls than for $Ro=0$. An even more striking observation is the reversal of the conventional anisotropy $u_{rms} > w_{rms} > v_{rms}$ in wall turbulence in general and in non-rotating Couette flow in particular. In the rapidly rotating Couette flow $v_{rms} > w_{rms} > u_{rms}$ over a substantial part of the flow. While the wall-normal velocity fluctuations v_{rms} are consistently smaller than the other velocity fluctuations for $Ro=0$, v_{rms} exceeds the streamwise fluctuations u_{rms} over the central 80% of the cross section and the spanwise fluctuations w_{rms} over more than 60% of the flow.

The dominance of the wall-normal velocity fluctuations affects the distribution of the mean turbulent kinetic energy k across the flow as shown in figure $6(b)$. The conventional near-wall peaks are totally absent and the maximum value of k is observed midway between the walls where also v_{rms} attains its maximum. The energy level is higher over the

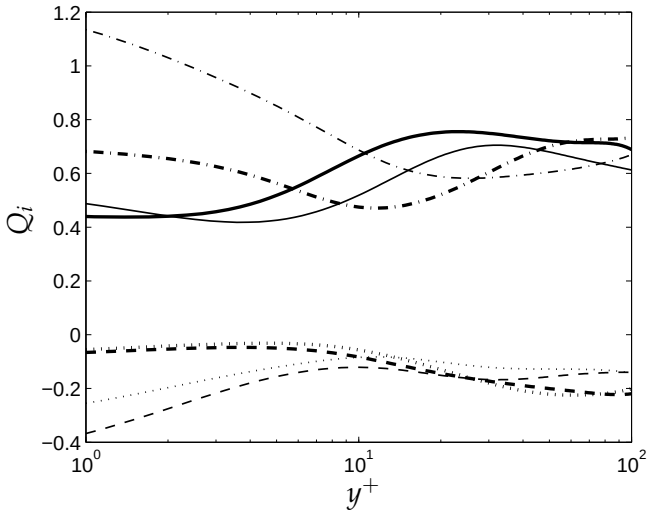

Figure 7: Fractional contributions to the turbulent shear stress $-\overline{uv}$ from the four quadrants. Data from the rotating Couette flow (bold lines) compared with the non-rotating case (thin lines). $--$ $Q1(u>0,v>0)$; —— $Q2(u<0,v>0)$; $\cdots$ $Q3(u<0,v<0)$; $-\cdot-$ $Q4(u>0,v<0)$.

entire core region and exceeds that of the non-rotating flow with about 75% at the center. The simultaneous observations of a higher turbulence level and reduced flow resistance can only be understood if the rotating turbulence is less efficient in wall-normal mixing (i.e. shear production) than conventional wall turbulence.

In spite of the above observation that the wall-normal fluctuations dominate over the streamwise fluctuations, the outcome of a quadrant analysis shown in figure 7 does not show any qualitative differences brought about by the system rotation. In both cases, the fourth quadrant ($Q4-$events) dominates very close to the wall whereas contributions from the second quadrant ($Q2$) are more influential further out. It is readily seen, however, that the position at which the two kind of events are of equal importance has shifted from $y^+ \approx 14$ in the non-rotating case to about $y^+ \approx 6$ for $Ro = 0.7$. It can also be noticed that the adverse contributions from the $Q1$ and $Q3$ events have been significantly reduced, especially near the wall. Although the $Q4-$dominance over the $Q2-$events still persists in the vicinity of the wall, the relative contribution from the $Q4-$events has been substantially reduced, thereby suggesting that the importance of the sweep events has diminished. It is noteworthy that a similar reduction of the fractional contribution of sweeping events relative to ejections was observed also at the anti-cyclonic side of the rotating Poiseuille flow both in the computer experiments by Kristoffersen and Andersson [22] and the laboratory experiments by Nakabayashi and Kitoh [31]. In that flow, however, the turbulent shear stress $-\rho\overline{uv}$ was increased due to the imposed system rotation, whereas the shear stress is lowered in the present flow. A particular feature of

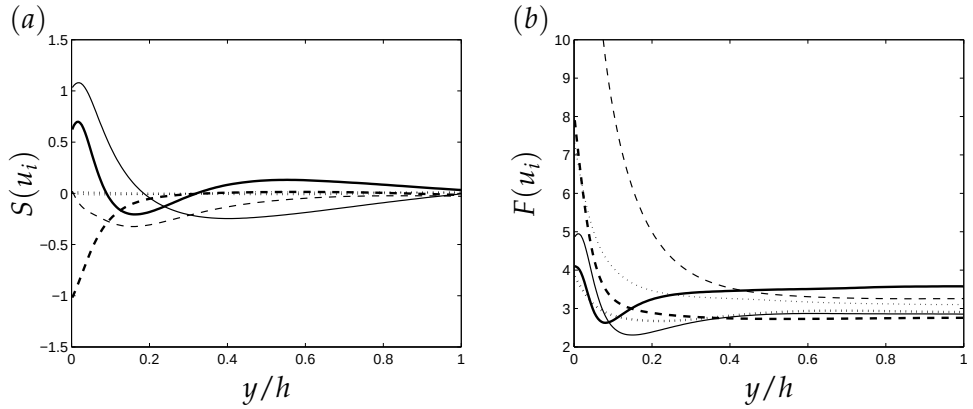

Figure 8: Higher-order moments of the velocity fluctuations u_i. (a) Skewness $S(u_i)$; (b) Flatness $F(u_i)$. Data from the rotating Couette flow (bold lines) compared with the non-rotating case (thin lines). —— u; − − − v; ⋯ w.

Couette flow turbulence is that an ejection ($Q2-$event) from the fixed wall appears as a sweeping event ($Q4$) when seen from the moving wall and vice versa.

For the sake of completeness, the skewness S and flatness F of the fluctuating velocity components are shown in figure 8. The skewness of u is positive in the core region and inevitably goes to zero at the center due to symmetry. This contrasts with the non-rotating case in which $S(u)$ is negative in the core. The latter is generally ascribed to the dominance of outbursts or ejections beyond $y^+ \approx 12$ whereas so-called sweeps are the major contributor to the turbulence production in the vicinity of the wall. The positive value of $S(u)$ in the core region of the rotating Couette flow must therefore imply that the conventional stress-producing mechanism has been suppressed. The flatness of u is substantially higher than 3.0 in the core region which suggests more frequent occurrences of extreme events than in a Gaussian distribution.

The skewness and flatness of the wall-normal velocity component v become roughly constant, i.e. $S(v) \approx 0$ and $F(v) \approx 2.8$, in the core region. In the immediate vicinity of the wall, the skewness of v has become negative with the wall-value $S(v) \approx -1$ rather than being close to zero as in the non-rotating case. This implies that extreme wall-ward motions, although possibly rare, are more frequent than extreme out-rushs. The violent wall-ward motions may furthermore be correlated with strong positive streamwise fluctuations and thus contribute to the Reynolds shear stress. This is in contrast with other wall-flows, notably plane Poiseuillle flow, where both $S(u)$ and $S(v)$ are positive in the vicinity of the wall and extreme $u-$motions are therefore not correlated with large $v-$motions.

The symmetry properties of the present flow imply that $S(w) = 0$. The skewness of w, as deduced from the simulated flow field, is essentially zero both in the rotating and non-rotating case and thereby confirms the adequacy of the sampling.

	$i=1,j=1$	$i=2,j=2$	$i=3,j=3$	$i=1,j=2$
P_{ij}	$+\,0.249$	————	————	$-\,0.919$
G_{ij}	$-\,0.264$	$+\,0.264$	————	$+\,0.794$
Π_{ij}	$+\,0.056$	$-\,0.176$	$+\,0.114$	$+\,0.102$
$-\varepsilon_{ij}$	$-\,0.040$	$-\,0.099$	$-\,0.103$	$+\,0.021$
Imbalance	$+\,0.001$	$-\,0.011$	$+\,0.011$	$-\,0.002$

Table 1: Core-region values of the leading terms in the second-moment budgets evaluated at the symmetry plane $y/h=1.0$ for $Ro=0.7$. All terms are scaled with u_τ^4/ν. The imbalance refers to the sum of the leading terms that are included in the table.

5 Energy considerations and Reynolds-stress budgets

The budgets of the individual components of the Reynolds stress tensor provide insight into the interactions between the large-scale turbulence and the mean flow. The budgets of the three diagonal components and the only non-zero off-diagonal Reynolds stress component are shown in figure 9.

In order to assist in the interpretation of the budgets, it might be helpful to consider the production terms due to mean shear and rotation. For unidirectional mean flow $U(y)$ rotating about the $z-$axis, we obtain:

$$P_{xx}+G_{xx}=-2\overline{uv}\frac{dU}{dy}+4\Omega^F\overline{uv}=(1+S)P_{xx}\approx 0 \tag{5.1a}$$

$$P_{yy}+G_{yy}=0-4\Omega^F\overline{uv}=-SP_{xx}\approx P_{xx} \tag{5.1b}$$

$$P_{xy}+G_{xy}=-\overline{v^2}\frac{dU}{dy}-2\Omega^F(\overline{u^2}-\overline{v^2})=\left[1+S\left(1-\frac{\overline{u^2}}{\overline{v^2}}\right)\right]P_{xy}\approx\frac{\overline{u^2}}{\overline{v^2}}P_{xy}=-\overline{u^2}\frac{dU}{dy}\,. \tag{5.1c}$$

Here, the rightmost part of the each of the above equations is valid only for $S\approx-1.0$. Data for the individual production terms in the core region, together with the pressure-strain rates and the dissipation rates, are provided in table 1.

It is well known that the mean shear only contributes to streamwise velocity fluctuations. The system rotation introduces source terms both in the streamwise and wall-normal directions, whereas the fluctuations in the direction of the axis of rotation are unaffected. It is particularly noteworthy that the rotational terms in equation (5.1) cancel out if the second-moment equation (2.5) is contracted to give an equation for the turbulent kinetic energy. This is intuitively evident since the instantaneous Coriolis force always acts perpendicular to the instantaneous velocity vector. The Coriolis force can therefore neither produce work nor directly alter the energy of the flow. The substantially higher mean turbulent kinetic energy in the rotating case (see figure 6*b*) must therefore be ascribed to indirect effects of system rotation. The weakly and moderately rotating Couette flow considered by Bech and Andersson [6,7] was affected by large-scale counter-rotating

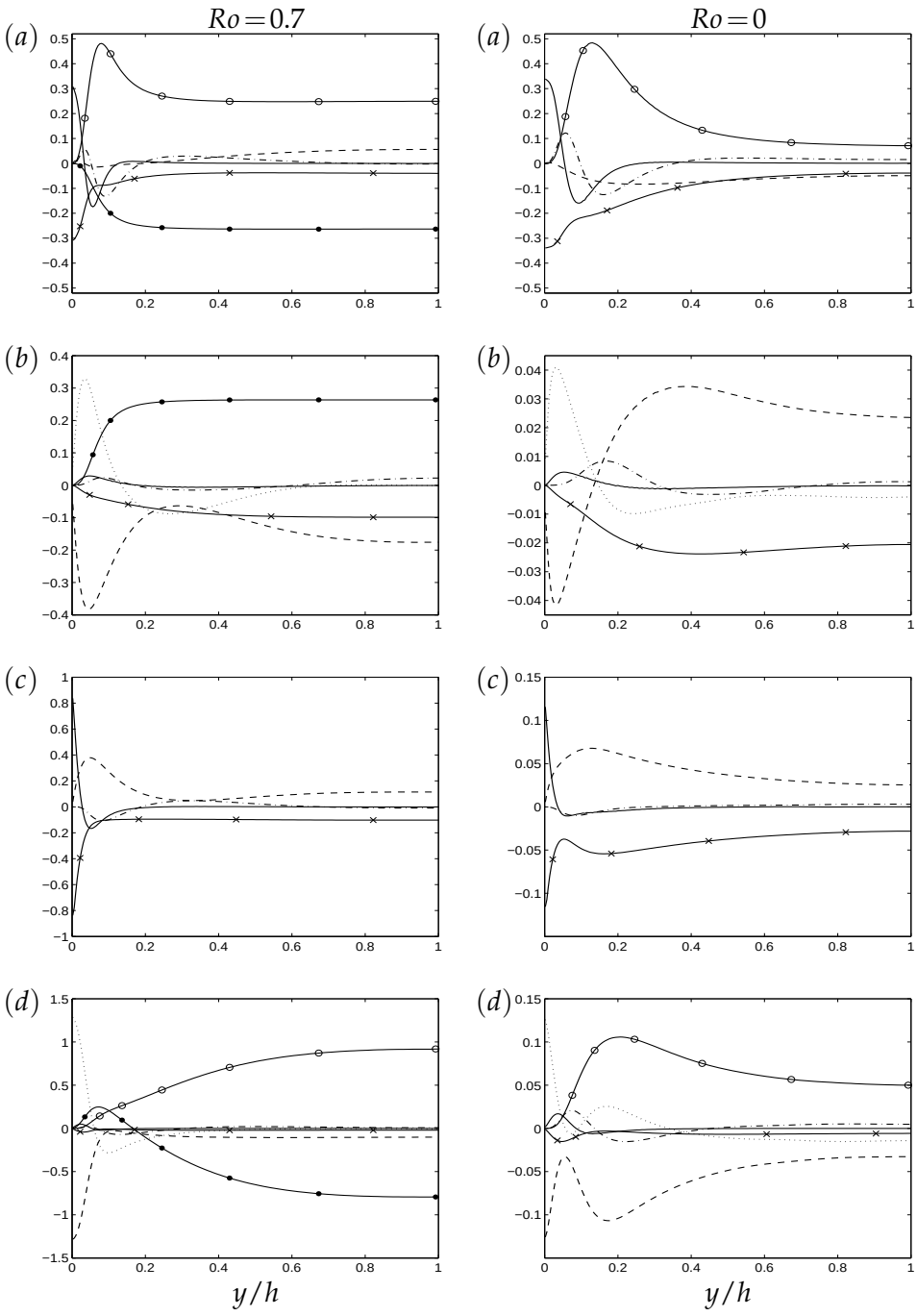

Figure 9: Budgets of the individual Reynolds stress components. The terms are scaled with u_τ^4/ν. Note the difference between the tick-marks along the ordinate axis. (a) uu; (b) vv; (c) ww; (d) $-uv$. (—○—) P_{ij}; (—●—) G_{ij}; (– · –) D_{ij}^T; (···) D_{ij}^P; (——) D_{ij}^V; (– – –) Π_{ij}; (—×—) $-\varepsilon_{ij}$.

roll cells, as was the rotating Poiseuille flow studied by Johnston *et al.* [20] and Kristoffersen and Andersson [22] and others. Such roll cells contribute substantially to the kinetic energy of the flow, whereas the present Couette flow is free of rotational-induced large-scale vortices. The excess kinetic energy level can therefore only be a result of an indirect influence of the Coriolis force on the turbulence structure.

The anisotropy and inhomogeneity of a turbulent flow field is caused by the production terms in equation (2.5). In the orthogonally rotating Couette flow, the only non-zero production terms are those given in equation (5.1) above. In non-rotating channel and Couette flow, the turbulence is produced by mean shear, i.e. $P_{xx} > 0$, whereas P_{yy} and P_{zz} both are zero.

Throughout the core region of the rapidly rotating Couette flow $S \approx -1$. This implies that the rotational turbulence production G_{xx} just outweighs the conventional mean shear production P_{xx} (see figure 9*a*) with the crucial implication that no energy is transferred from the mean flow into the streamwise velocity fluctuations. Instead, the correlation between the wall-normal Coriolis force and the wall-normal velocity fluctuations in equation (5.1*b*) becomes a significant source of $\overline{v^2}$, as seen in figure $9(b)$.

As far as the shear stress $-\rho\overline{uv}$ is concerned, the rotational production G_{xy} assists the mean shear production P_{xy} as long as the conventional shear flow anisotropy $\overline{u^2} > \overline{v^2}$ persists. In the presence of an abnormal anisotropy $\overline{v^2} > \overline{u^2}$, however, the situation is reversed and G_{xy} tends to reduce the turbulent shear stress, as can be observed from the budget for $-\rho\overline{uv}$ in figure $9(d)$. The overall implication is that the streamwise velocity fluctuations have taken over the role played by wall-normal fluctuations for $Ro = 0$, as demonstrated by equation (5.1*c*). It is noteworthy, however, that what is left in (5.1*c*) stems from interactions between streamwise velocity fluctuations and the wall-normal component of the instantaneous Coriolis force.

The rightmost parts of equation (5.1) apply in the core region of the rapidly rotating Couette flow where $S \approx -1.0$. In this region turbulent velocity fluctuations are contributed into the wall-normal direction by the action of the Coriolis force whereas no turbulence is produced in the streamwise and spanwise directions. Thus, in order for turbulence to prevail, a redistribution mechanism is required which transfers turbulent energy from the wall-normal direction into the two other coordinate directions. If no energy is fed into the streamwise direction, the correlation $\overline{uv}$ required for the turbulence production (5.1*b*) will vanish and the turbulence will eventually fade away. It is therefore speculated that the quenching of the turbulence in rapidly rotating Couette flow reported by Bech and Andersson [7] and Alfredsson and Tillmark [1] results from the attenuation of the crucial transfer mechanism between the directional components of the instantaneous velocity vector.

Outside of the core region, however, the local vorticity ratio S increases monotonically from -1 to -0.16 at the walls. Here, the wall-value of S is readily obtained from equation (4.6) with $dU^+/dy^+ = 1.0$. The simplifications introduced in the rightmost parts of equation (5.1) do no longer apply, which for instance implies that streamwise velocity

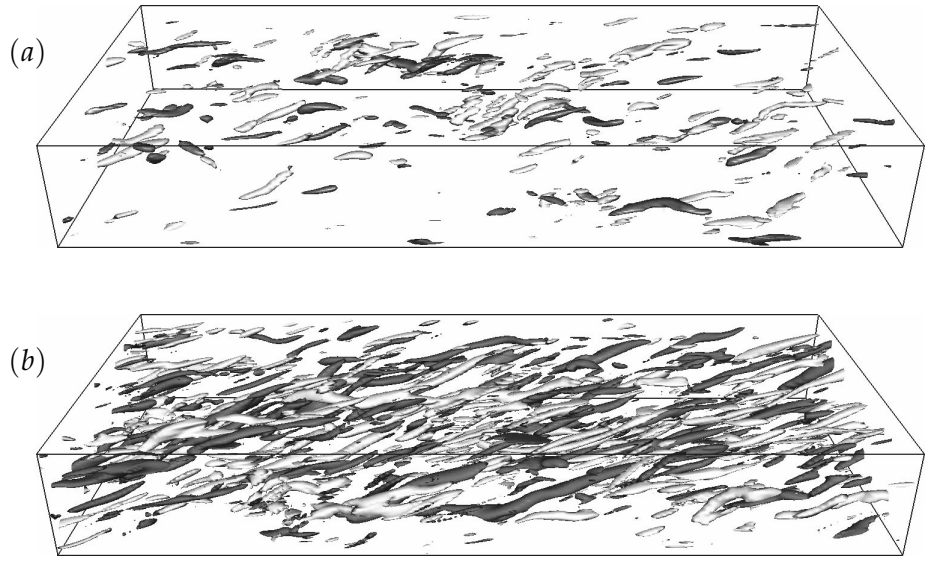

Figure 10: Instantaneous flow field visualised by means of iso-contours of $-\lambda_2\omega_x$. (a) $Ro=0$; (b) $Ro=0.7$. The contour level is the same in both parts of the figure. Positive and negative contour levels are distinguished by light and dark shading, respectively.

fluctuations produced by mean shear are only partially hampered by the rotational sink term near the walls, see e.g. figure $9(a)$.

The preceding discussion is valid only if the rotation is sufficiently fast, i.e. beyond the supercritical regime in which roll cells co-exist with the turbulence. The existence of a purely turbulent flow regime for anti-cyclonic rotation rates Ro above 0.5 and a roll-cell dominated regime for $0 < Ro < 0.5$ [6, 7] is analogous to the existence of two different flow regimes in the Taylor-Couette flow recently addressed by Dubrulle *et al.* [12]. The two conceptually different turbulent regimes for anti-cyclonic rotation contrast with the existence of only one turbulent flow regime in plane Couette flow subjected to cyclonic rotation.

6 Vorticity dynamics

The vorticity is an essential kinematic property of fluid motion, as illustrated by the snapshots of the flow field shown in figure 10. In order to focus on the streamwise vorticity, the instantaneous λ_2–field (to be defined in §6.2) has been pre-multiplied by ω_x before the iso-contours were plotted. It is evident from these plots that the streamwise vorticity has been substantially enhanced when the flow is subjected to strong anti-cyclonic rotation as in figure $10(b)$. Furthermore, we consider the distribution of $\theta = tan^{-1}(\omega_y/\omega_x)$, the inclination angle of the projection on the $(x,y)-$plane of the vorticity vector. Figure 11 shows the inclination angle θ close $(y^+ = 10)$ and far away $(y^+ = 50)$ from the wall

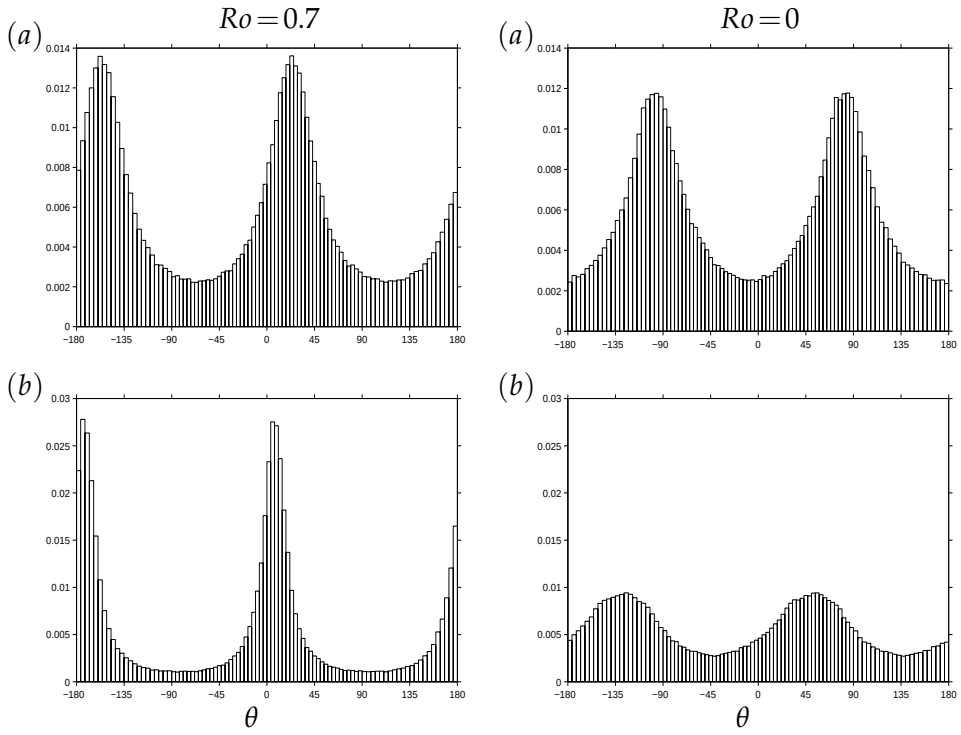

Figure 11: Probability distribution of the inclination angle θ. (a) $y^+=10$; (b) $y^+=50$.

for both rotating and non-rotating cases. The results indicate a distinct effect of system rotation on the flow structures not only in the core region $(\theta\approx 10)$ but even in the flow region close to the wall $(\theta\approx 25)$. These observations will be examined by means of vorticity statistics in the following subsections.

6.1 Mean vorticity and mean Lamb vector

It is evident from the mean velocity profile in figure 4 and the partition between viscous and turbulent shear stress components in figure 5 that the mean vorticity $\Omega_z=-dU/dy$ is constant and roughly equal to the background vorticity $2\Omega^F$ over about 80% of the cross-section. The integrated equation for the mean vorticity (2.8) is valid over the entire flow region. The constancy of Ω_z in the core region makes the viscous term in (2.8) vanish and leaves a balance between $\overline{w\omega_y}$ and $-\overline{v\omega_z}$. Such velocity-vorticity correlations are associated with the Lamb vector:

$$\boldsymbol{\lambda}=\boldsymbol{u}\times\boldsymbol{\omega}\ . \tag{6.1}$$

The above definition of the instantaneous Lamb vector is the same as that adopted by Orlandi [32] and Liu and Lu [26] while Moffatt and Tsinober [29] used the definition $\boldsymbol{\omega}\times\boldsymbol{u}$. The mean value $\boldsymbol{\Lambda}$ of the instantaneous Lamb vector $\boldsymbol{\lambda}$ lies entirely in the $(x,y)-$plane,

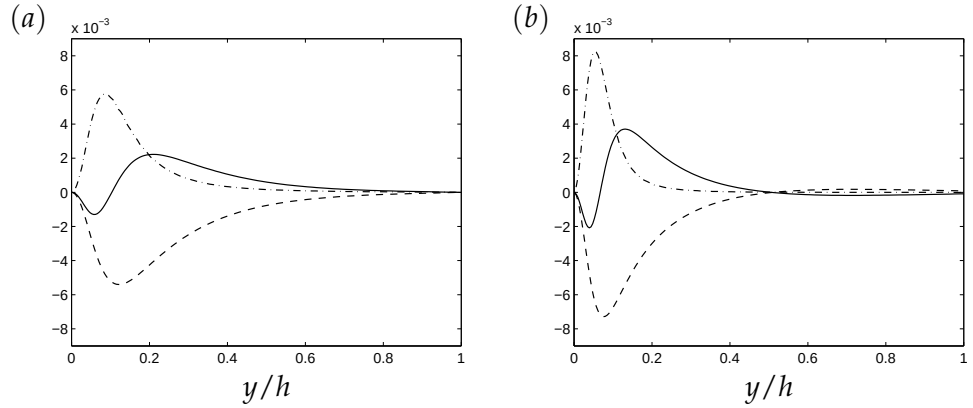

Figure 12: Individual terms (——) $\overline{w\omega_y}$; (– – –) $-\overline{v\omega_z}$; and (– · –) $\nu d\Omega_z/dy$ in the integrated mean vorticity equation (2.8). Notice that the sum $\overline{v\omega_z}-\overline{w\omega_y}$ equals Λ_x, i.e. the $x-$component of the mean Lamb vector in equation (6.2). (a) Non-rotating Couette flow; and (b) Anti-cyclonically rotating Couette flow with $Ro=0.7$.

i.e. $\Lambda_z=0$, due to symmetries. The two non-zero components are in the present case:

$$\Lambda_x=\overline{v\omega_z}-\overline{w\omega_y} \quad \text{and} \quad \Lambda_y=-U\Omega_z+\overline{w\omega_x}-\overline{u\omega_z}\,. \tag{6.2}$$

Here, the velocity-vorticity correlations which contribute to the streamwise component are recognized as the two first contributions to the integrated mean vorticity balance (2.8) which therefore can be stated as $\Lambda_x=\nu d\Omega_z/dy$. The mean vorticity Ω_z , which is negative across the entire flow, increases monotonically from its minimum value at $y=0$ to its maximum (but still negative) level in the core. The resulting $d\Omega_z/dy>0$ in the near-wall region is balanced by $-\Lambda_x$ in accordance with equation (2.8); see figure 12. The major contribution to the positive Λ_x in the near-wall region stems from the negative correlation between the spanwise velocity fluctuations and the wall-normal vorticity. It is noteworthy that Λ_x is roughly doubled in the presence of system rotation in the vicinity of the walls. This increase in the Lamb vector is in qualitiative agreement with the rotating Poiseuille flow simulations by Liu and Lu [26]. They reported a substantial enhancement of Λ_x near the pressure (i.e. anti-cylconic) side of their rotating channel, whereas Λ_x was nearly suppressed near the suction (i.e. cyclonic) side.

In the core region of the Couette flow where the mean vorticity is uniform, $d\Omega_z/dy\approx 0$ and the streamwise component of the mean Lamb vector vanishes, i.e. $\overline{v\omega_z}\approx\overline{w\omega_y}$. It is noteworthy from figure 12 that Λ_x is suppressed already at $y\approx 0.3h$ in the presence of system rotation. Since the Lamb vector is responsible for the energy cascade, this observation implies that the energy transfer from large to small scales is inhibited by the imposed rotation.

The role of the mean Lamb vector in the turbulence productions is readily revealed if the production of turbulent kinetic energy by mean shear in equation (2.6) is rewritten

as:

$$P_K = \frac{1}{2}P_{ii} = -\overline{u_i u_k}\frac{\partial U_i}{\partial x_k} = -\varepsilon_{ijk}\overline{\omega_j u_i}U_k - \frac{\partial \overline{u_i u_k}U_k}{\partial x_i} = -\Lambda_x U - \frac{dU\overline{uv}}{dy} \ . \tag{6.3}$$

Here, $\varepsilon_{ijk}\overline{\omega_j u_i}$ comprises the velocity-vorticity correlations involved in the $k-$component of the mean Lamb vector. The rightmost part of equation (6.3) shows that only the streamwise component of $\mathbf{\Lambda}$ contributes to the turbulent energy production in this particular flow. In the core region where the shear stress $-\overline{uv}$ remains constant and Λ_x vanishes, the more conventional expression (2.6) for the kinetic energy production is recovered. It can readily be inferred from the data in figure 12 that the consistently positive value of Λ_x is responsible for a loss of turbulent energy, i.e. transfer from large to small scales and ultimately dissipation. This loss is, however, more than outweighed by advection of large-scale energy.

The helicity density is defined as

$$h = \boldsymbol{u}\cdot\boldsymbol{\omega} \ . \tag{6.4}$$

The helicity h is related to the Lamb vector through the mathematical vector identity [34]:

$$h^2 + \boldsymbol{\lambda}^2 = |\boldsymbol{u}\cdot\boldsymbol{\omega}|^2 + |\boldsymbol{u}\times\boldsymbol{\omega}|^2 = |\boldsymbol{u}|^2|\boldsymbol{\omega}|^2 \ . \tag{6.5}$$

According to (6.4) helicity is a measure of the degree of alignment of the vorticity vector and the velocity vector. High levels of helicity are believed to hamper the energy cascade and therefore also the energy dissipation. In the present flow, however, the mean value of the helicity density defined in (6.4) vanishes identically due to the inherent symmetries associated with the statistical homogeneity in the spanwise direction.

6.2 Near-wall streaks and coherent flow structures

The wall-region of a non-rotating plane Couette flow resembles that in other simple wall-bounded flows, e.g. the plane Poiseuille flow. The presence of elongated streamwise streaks with a typical mean spacing Δ of about 100 wall units (i.e. ν/u_τ) are among the most characteristic features of wall turbulence. The particular spanwise separation which corresponds to the distinct minimum of the two-point correlation of u in figure 3 is a measure of the mean separation between low$-$ and high$-$speed motions. The mean streak spacing Δ is estimated as twice this distance. The results in figure 13 show that Δ^+ increases nearly linearly with the wall distance from about 100 in the immediate vicinity of the wall to about 150 at $y^+ = 30$ in the absence of rotation, i.e. just as in the non-rotating Poiseuille flow. In the presence of system rotation, a somewhat larger streak spacing Δ^+ is observed. This is opposite to the distinctly reduced streak spacing observed at the anti-cyclonic (pressure) side of the rotating Poiseuille flow considered by Kristoffersen and Andersson [22]. The enhanced streak density in that study was accompanied by a higher wall-friction velocity. In the present case, on the other hand, the increased streak separation is associated with a reduction in u_τ, i.e. fully consistent with the widely accepted belief that the streak density is closely related to the wall friction.

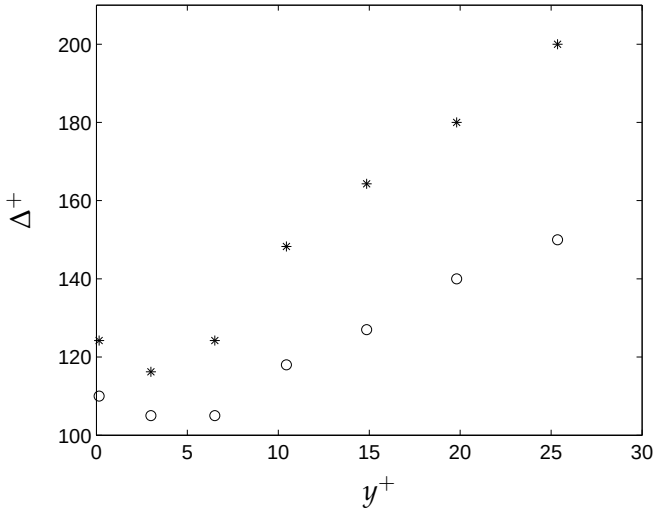

Figure 13: Variation of the mean streak spacing $\Delta^+ = \Delta \cdot u_\tau / \nu$ in the near-wall region for rotating ($*$) and non-rotating ($\circ$) Couette flow.

An efficient scalar quantity frequently used to identify regions of localized vortices in a flow field is λ_2 introduced by Jeong and Hussain [18] as the second largest eigenvalue of the tensor $s_{ik}s_{kj}+r_{ik}r_{kj}$ where s_{ij} and r_{ij} are the strain-rate and rotation-rate tensors, respectively. The distribution of the $rms-$value of λ_2 from the wall and towards the center is shown in figure 14. λ_{2rms} is normalized by u_τ^4/ν^2, i.e. the reciprocal of the viscous time scale ν/u_τ^2 squared. In the absence of rotation, the near-wall variation closely resembles that of plane Poiseuille flow with a peak located at about $y/h \approx 0.2$ or $y^+ \approx 16$. The peak level is, however, more than 50% higher in the Couette flow than in the Poiseiulle flow and the reduction of λ_{2rms} towards the centerline is by far more modest than in the channel flow. When the Couette flow is subjected to rapid anti-cyclonic rotation, however, λ_{2rms} increases monotonically all the way from the wall towards the center and the λ_2-level at the centerline is more than 3 times higher than without rotation. This is yet another manifestation of the anomaly of the flow dynamics in the core region.

6.3 Enstrophy and vorticity budgets

The root-mean-square values of the fluctuating vorticity components are shown in figure 15. The only resemblance with conventional wall-flow behaviour is that the wall-normal vorticity goes to zero at the wall simply as a result of the no-slip condition. While spanwise vorticity fluctuations $\overline{\omega_z^2}$ normally dominate in the near-wall region, see e.g. Antonia and Kim [3], the streamwise vorticity $\overline{\omega_x^2}$ is by far more intense in the present case. This

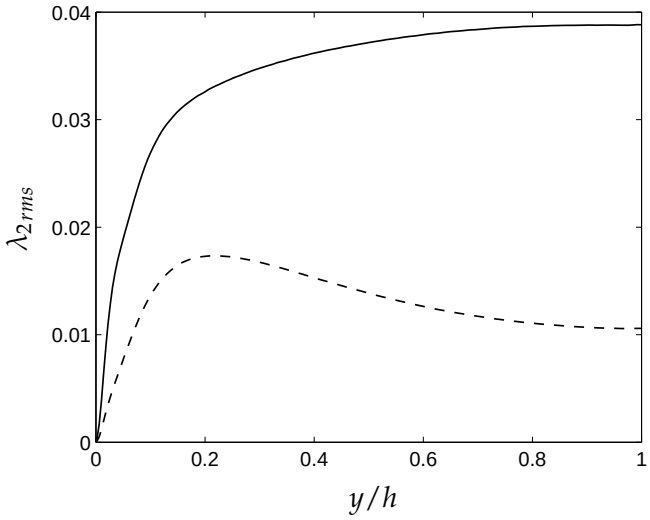

Figure 14: Variation of λ_{2rms} from the wall to the centerline for the rotating (solid line) and non-rotating (broken line) Couette flow. The data are scaled with u_τ^4/ν^2.

enhancement due to system rotation overshadows the characteristic near-wall peak of $\overline{\omega_x^2}$ which can be observed for $Ro = 0$. This peak has usually been associated with the presence of coherent streamwise-oriented vortices. A striking homogeneity of the fluctuating vorticity field is observed in the entire core region. Here, a distinct and anomalous anisotropy prevails with the streamwise vorticity fluctuations exceeding the two other components, which on the other hand turn out to be practically equal and thus reflects an axisymmetry of the vorticity field. This contrasts with the non-rotating case in which the vorticity field is close to an isotropic state in the core region.

Following Antonia and Kim [3], the behaviour of the individual vorticity components can be further explored by examining the dominating terms in the second-moment equation (2.9). They based their analysis on their equation (14) which appears as an equation for twice the scalar enstrophy due to the implicit summation over repeated indices i and j. Their equation (14) is consistent with the diagonal elements of present equation (2.9) for the individual second-moments provided that summation is only carried out for j whereas the conventional summation rule is not applied for the repeated index i which rather should be taken as either 1, 2 or 3. In the present context, the stretching term $S5_{ij}$ is of particular concern. Tennekes and Lumley [36] referred to this term as a mixed production term. This term plays a major role in the viscous sublayer in channel flows [3] where it peaks about $y^+ \approx 4$. In a rotating frame-of-reference, this is the only term in the second-moment vorticity budgets that explicitly includes the system rotation; see equation (A.13) in the Appendix.

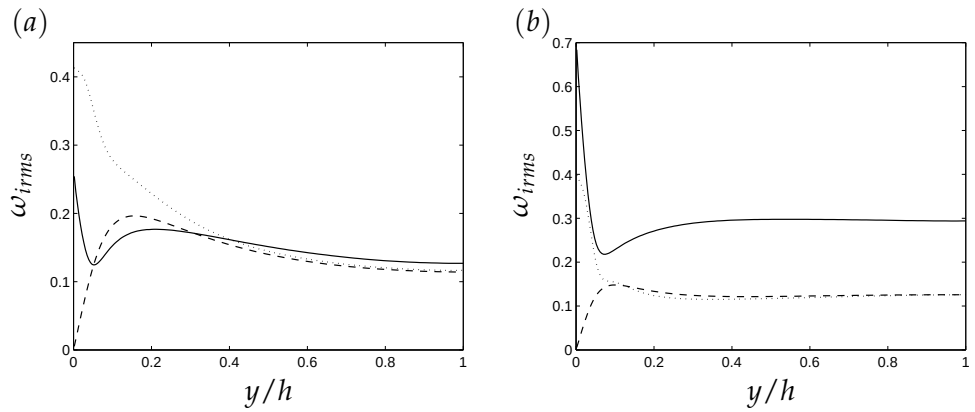

Figure 15: Root-mean-square vorticity fluctuations normalized by u_τ^2/ν. (a) Non-rotating Couette flow; and (b) Anti-cyclonically rotating Couette flow with $Ro=0.7$. —— $\omega_{x_{rms}}$; − − − $\omega_{y_{rms}}$; ⋯ $\omega_{z_{rms}}$.

	$i=j=1$	$i=j=2$	$i=j=3$	Enstrophy
$S3_{ij}\cdot 10^3$	-0.01	$+1.26$	$+1.90$	$+1.58$
$S4_{ij}\cdot 10^3$	$+6.60$	———	———	$+3.30$
$S5^{I}_{ij}\cdot 10^3$	-3.20	$+3.32$	-0.10	$+0.01$
$S5^{II}_{ij}\cdot 10^3$	$+3.20$	-3.34	$+0.10$	-0.02
$V7_{ij}\cdot 10^3$	-6.50	-1.34	-1.88	-4.86
Imbalance $\cdot 10^3$	$+0.09$	-0.10	$+0.02$	$+0.01$

Table 2: Core-region values of the leading terms in the second-moment vorticity budgets evaluated at the symmetry plane $y/h=1.0$ for $Ro=0.7$. All terms are scaled with $(u_\tau^2/\nu)^3$. The imbalance refers to the sum of the leading terms that are included in the table.

The vorticity budgets presented in figure 16 show that most of the terms in (2.9) contribute in the near-wall region, whereas a major simplification is observed further away from the walls. Several terms become of negligible importance in the core region and those that contribute remain constant over at least 60% of the cross-section (see table 2). The budget of the spanwise vorticity in figure $16(c)$, for instance, simplifies to a balance between stretching by fluctuating velocity gradients $S3_{zz}$ and viscous dissipation $V7_{zz}$. Such a balance prevails also in the central part of the plane channel flow examined by Antonia and Kim [3].

Most of the terms in the $\overline{\omega_y^2}$ –budget are vanishingly small in the absence of rotation, in particular in the core region. It is noteworthy that the present budget in figure $16(b)$ is rather different from the corresponding Poiseuille flow budget provided by Antonia and Kim [3] in their figure $8(b)$. They observed that two stretching terms $S4$ and $S5$ are the dominating sources of wall-normal vorticity fluctuations. In the present case,

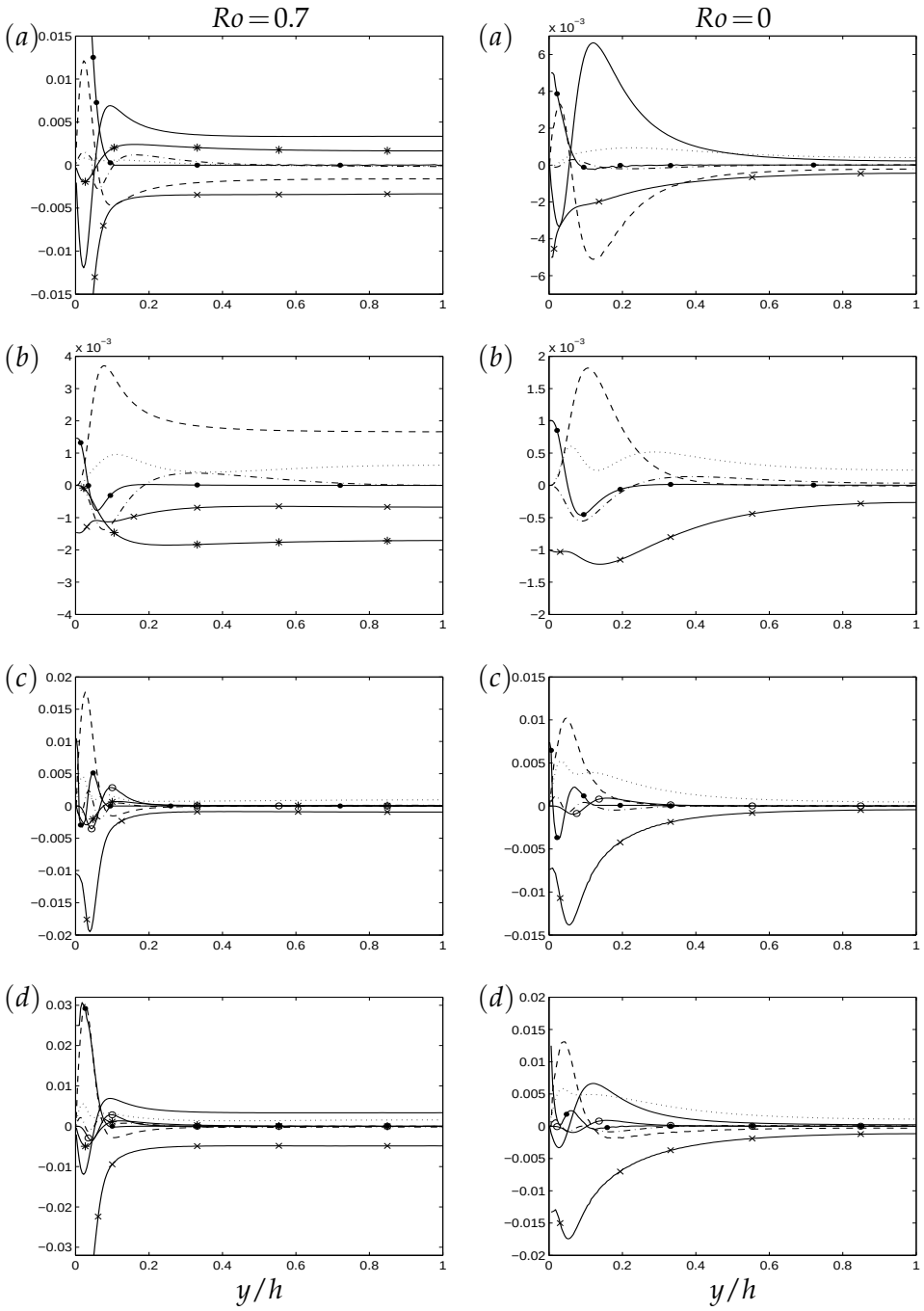

Figure 16: Budgets of (a) $\frac{1}{2}\overline{\omega_x^2}$, (b) $\frac{1}{2}\overline{\omega_y^2}$, (c) $\frac{1}{2}\overline{\omega_z^2}$ and (d) enstrophy $\frac{1}{2}\overline{\omega_i\omega_i}$. The individual terms are scaled with $(u_\tau^2/\nu)^3$. (—○—) $T1_{ij}$; (– · –) $T2_{ij}$; (···) $S3_{ij}$; (——) $S4_{ij}$; (– – –) $S5^I_{ij}$; (—∗—) $S5^{II}_{ij}$; (—●—) $V6_{ij}$; and (—×—) $V7_{ij}$.

however, $S4_{yy}$ is absent as it should be for symmetry reasons. In fact, $S4$ contributes only to streamwise vorticity fluctuations in unidirectional shear flows. With system rotation imposed, the important stretching term $S5_{yy}$ associated with the mean flow vorticity is outweighed by the stretching due to the imposed rotation in the entire core region. This leaves a balance between turbulent vortex stretching of vorticity fluctuations $S3_{yy}$ and viscous dissipation $V7_{yy}$, i.e. similarly as in the spanwise direction.

The streamwise vorticity fluctuations are the main contributor to the enstrophy $\frac{1}{2}\overline{\omega_i\omega_i}$ in the rapidly rotating Couette flow. According to the budget in figure $16(a)$, $S3_{xx}$ is reduced with rotation whereas $S4_{xx}$ is increased. Again, the stretching due to mean flow vorticity exactly balances the stretching due to rotation and thereby leaves a balance between the $S4_{xx}$ and $V7_{xx}$ in the core region. This contrasts with the non-rotating case in which $S3_{xx}$ is the major source term.

The enstrophy balance is readily obtained as the trace of equation (2.9), i.e. as the sum of the diagonal terms of the individual second-moments of the vorticity fluctuations. Let us recall from Section 2 that the rotational contribution to the stretching term $S5$ does not vanish when the indices are contracted in equation (2.9). However, in the nearly homogenous core region where the vorticity ratio $S{\approx}-1.0$, the two parts $S5^I_{ij}$ and $S5^{II}_{ij}$ due to mean flow stretching and rotational stretching, respectively, cancel out. The enstrophy budget in figure $16(d)$ is included here to enable a qualitative comparison with the results from the channel flow simulations by Lamballais *et al.* [23]. At the anti-cyclonic side of their rapidly rotating channel they observed a balance between stretching and viscous terms.

7 Turbulence anisotropies

To further examine the anisotropy of the rotating Couette flow, anisotropy invariant maps (AIM) are presented in figure 17. Here, these are derived on the basis of the anisotropy tensors:

$$a_{ij} \equiv \frac{\overline{u_iu_j}}{2k} - \frac{1}{3}\delta_{ij} \tag{7.1}$$

$$d_{ij} \equiv \frac{\varepsilon_{ij}}{2\varepsilon} - \frac{1}{3}\delta_{ij} \tag{7.2}$$

$$v_{ij} \equiv \frac{\overline{\omega_i\omega_j}}{2\omega^2} - \frac{1}{3}\delta_{ij}\,. \tag{7.3}$$

The socalled Lumley triangle is drawn in the (-II, III)–plane where II and III are the second and third invariant of the anisotropy tensor, see Lumley and Newman [27]. Figure $17(a)$ shows that the Reynolds stress anisotropy behaves rather differently in the rotating Couette flow. Instead of tending towards the one-component limit characterized by the dominance of streamwise fluctuations as in the non-rotating case, the path from the $2D$ limit in the immediate vicinity of the walls goes in the opposite direction. The anisotropy

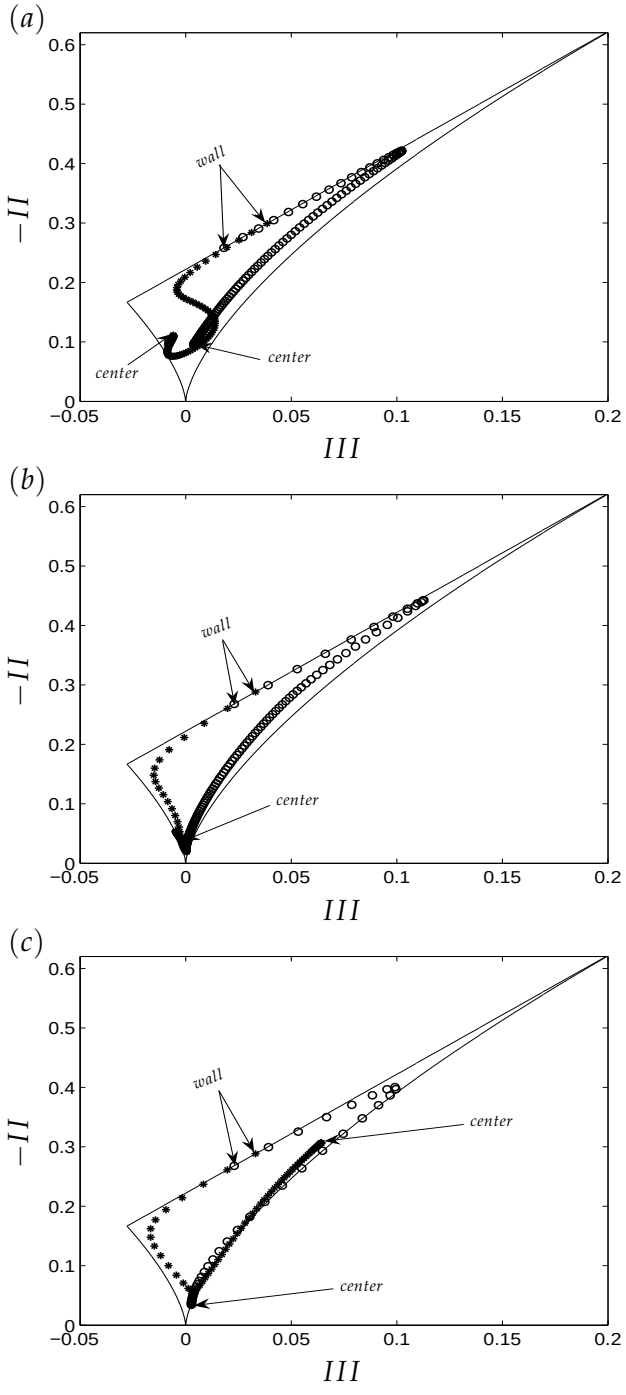

Figure 17: Anisotropy invariant maps. (a) Reynolds stress anisotropy a_{ij}; (b) dissipation rate anisotropy d_{ij}; (c) vorticity correlation anisotropy v_{ij}. Data for rotating ($*$) and non-rotating ($\circ$) Couette flow.

touches the boarder representing axisymmetric (rod-like) turbulence at $y^+ \approx 12$ and that of disk-like axisymmetry at $y^+ \approx 28$. Thereafter, i.e. in the quasi-homogeneous core, the anomalous anisotropy $v_{rms} > w_{rms} > u_{rms}$ prevails. The same Reynolds stress anisotropy has been observed also in rapidly rotating Poiseuille flow by Kristoffersen and Andersson [22] and Lamballais *et al.* [23], [24] as well as in homogeneous shear flows subjected to strong rotation by Salhi and Cambon [35]. The dissipation rate anisotropy d_{ij} in figure $17(b)$ follows a similar path as the Reynolds stress anisotropy a_{ij} in figure $17(a)$ and ends up with a similar anisotropy in the core region, but nearly touching the boarder signifying axisymmetric dissipation, i.e. $\varepsilon_{yy} \approx \varepsilon_{zz} > \varepsilon_{xx}$.

Also the anisotropies of the vorticity fluctuations behave similarly to the Reynolds-stress anisotropy in the near-wall region (cf figure $17c$), but stick to rod-like axisymmetry with $\overline{\omega_x^2}$ exceeding the two other directional vorticities throughout the core region. In the absence of rotation, however, the vorticiy fluctuations in the core region are close to an isotropic state, just as in the central region of a plane Poiseuille flow. The distinctly different path followed by v_{ij} in the rotating Couette flow reflects the anomalous anisotropy of the vorticity fluctuations. The excess streamwise vorticity fluctuations depart substantially from the nearly isotropic state observed in the non-rotating Couette flow. Both Yanase *et al.* [40] and Brethouwer [9] observed very elongated and intense streamwise vortex tubes in their simulations of rapidly rotating homogeneous shear flows with $S = -1.0$. The tabulated values of v_{ij} provided by Brethouwer [9] were attained after the simulation had evolved for a time $10(dU/dy)^{-1}$ and exhibit essentially the same vorticity anisotropy as in the core region of the present rotating Couette flow. Yanase *et al.* [40] further explored the temporal evolution of high-vorticity blobs via vortex sheets into tubular vortices.

In the absence of system rotation, the paths followed by the anisotropy tensors in the three AIM−maps in figure 17 exhibit roughly the same shapes. In the presence of strong system rotation, on the other hand, a_{ij}, d_{ij}, and v_{ij} follow rather different paths. It is particularly noteworthy that the anisotropy of the dissipation rate tensor behaves completely different from that of the vorticity correlation tensor in the quasi-homogeneous core region.

Inspired by the arguments put forward by Nakabayashi and Kitoh [30], one may conjecture that the impact of the system rotation on the individual flow structures depends on whether the eddy size is smaller or larger than the Coriolis length scale $\delta_c = u_\tau / \Omega^F$. This motivates an inspection of the component energy spectra of the rotating Couette flow. The spectra in figure 18 show that the dominating role of streamwise large-scale fluctuations has been taken over by wall-normal velocity fluctuations in the center of the flow. Due to the kinematic blocking enforced by the solid surface, however, enhancement of the wall-normal fluctuations is prohibited next to the wall. Instead, spanwise fluctuations have taken over the conventional role of the streamwise fluctuations in the near-wall region. The spectra at $y/h = 1.0$ show that the conventional stress anisotropy has been inverted due to the rotation as far as the large-eddy motion is concerned whereas the isotropy of the small-scale fluctuations is retained.

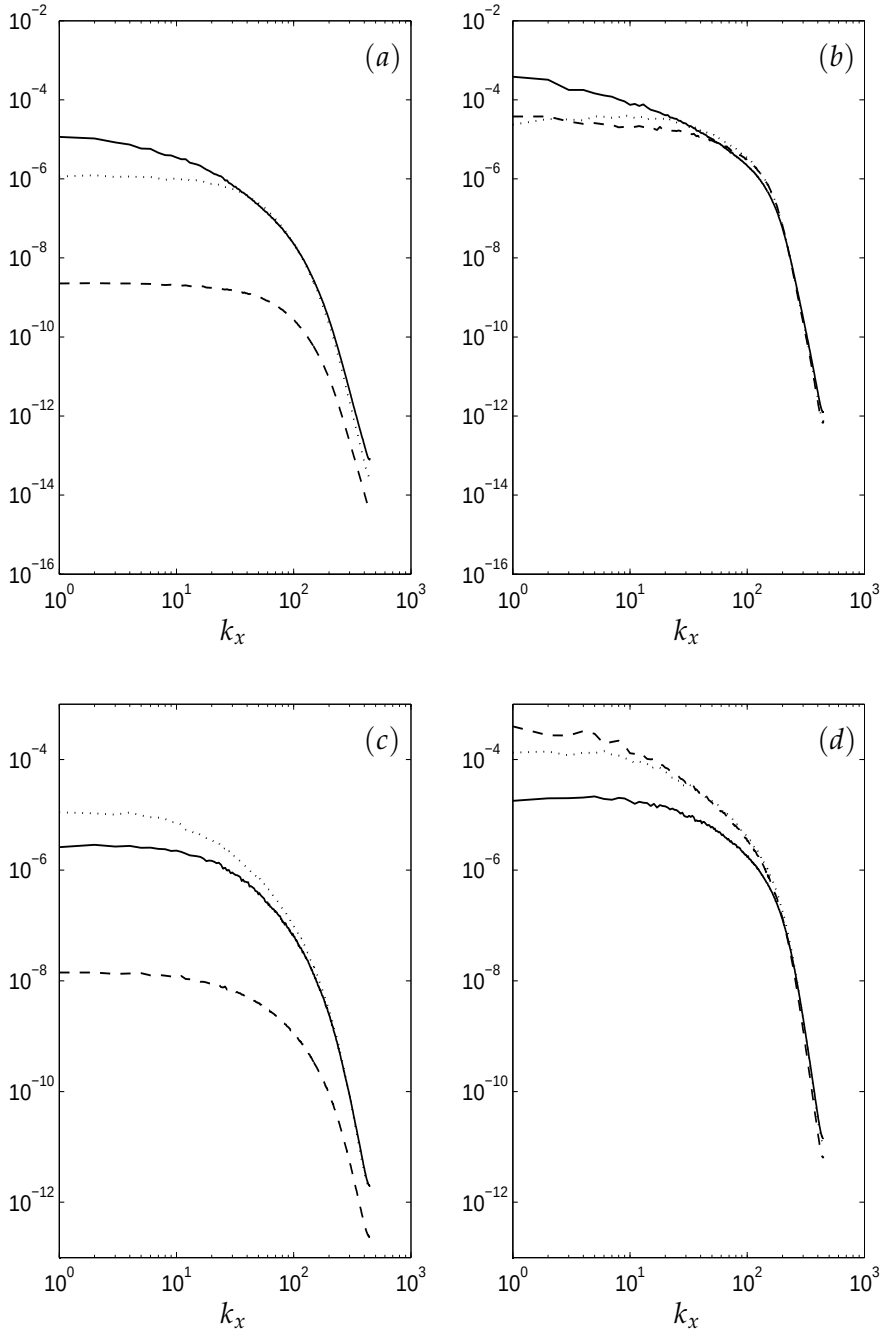

Figure 18: One-dimensional energy spectra $E_{ii}(k_x)$. (a), (c) Close to the wall at $y^+ \approx 5$; (b), (d) Near the center at $y/h = 0.98$. Results without rotation $(Ro = 0)$ at the top (a,b) and with rotation $(Ro = 0.7)$ at the bottom (c,d). —— E_{uu}; – – – E_{vv}; $\cdots$ E_{ww}.

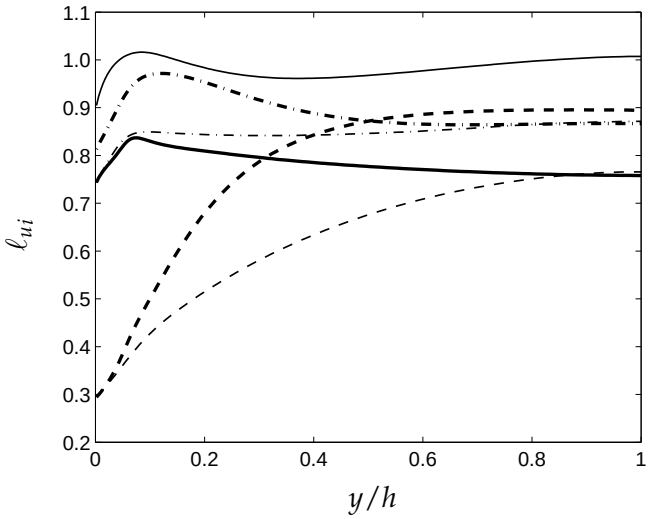

Figure 19: Taylor microscale in rotating (bold lines) and non-rotating (thin lines) plane Couette flow. —— ℓ_u; – – – ℓ_v; – · – ℓ_w.

The Taylor microscale ℓ_u is defined as:

$$\ell_u^2 = \frac{\overline{u^2}}{\overline{(\partial u/\partial x_j)^2}} \tag{7.4}$$

The directional index j of the derivative is subjected to summation such that ℓ_u becomes independent of the coordinate direction. Analogous definitions are used for ℓ_v and ℓ_w. The results in figure 19 show that both ℓ_u and ℓ_w are fairly constant across the flow, whereas ℓ_v increases monotonically from the wall to the center of the flow. This is due to the presence of the wall which imparts a substantial damping of wall-normal motions as compared to motions parallel with the walls. This general behaviour is therefore found irrespectively of whether the flow is rotating or not. It is interesting to observe that ℓ_v is some 15% larger in the core region in the presence of rotation than for $Ro = 0$. The Taylor microscale of the streamwise fluctuations is reduced whereas the microscale of the spanwise fluctuations is increased in the buffer region but otherwise unaffected by the rotation. The conventional scale anisotropy $\ell_u > \ell_w > \ell_v$, which reflects the conventional Reynolds stress anisotropy $u_{rms} > w_{rms} > v_{rms}$, has been inverted to $\ell_v > \ell_w > \ell_u$ in the core region for $Ro = 0.7$.

8 Concluding remarks

The plane Couette flow subjected to anti-cyclonic background rotation has been seen to develop a substantial nearly-homogeneous central core region in which the absolute mean vorticity vanishes entirely provided that the imposed system rotation is sufficiently fast. In spite of the presence of wall-layers bridging the core region with the solid walls, the core region has been found to share most of the characteristic features of the truly homogenous shear flow subjected to anti-cyclonic rotation provided that the imposed system rotation exactly outweighs the mean flow rotation.

A distinguishing feature of the present case is that the flow is statistically steady in time whereas a homogeneous shear flow is constantly evolving in time. Thus, while the mean velocity and turbulence statistics in the Couette flow become independent of time after a certain transient phase, the homogenous shear flow continuously evolves in time. In practice the computational grid often moves with the mean flow in the latter case. The inevitable skewing of the grid cells thus calls upon a re-meshing at regular time intervals [9, 16]. Another attractive feature of the present flow is the fact that the imposed system rotation vector is consistently anti-parallel with the mean flow vorticity vector and the flow field is everywhere exposed to anti-cyclonic rotation. This contrasts with the analogous rotating Poiseuille flow, in which one part of the flow is rotating cyclonically whereas another part is subjected to anti-cyclonic rotation.

The present results have for the first time demonstrated the existence of pure turbulence in an anti-cyclonically rotating plane Couette flow, i.e. the rotation rate is sufficiently high to suppress the roll-cell instability but yet not high enough to quench the turbulence. An intuition-based conjecture suggests that $Ro = 1.0$ is an upper bound beyond which turbulence cannot be sustained. The present flow case is therefore a prominent example of so-called featureless turbulence [2]. Since the resulting mean flow becomes unidirectional in the absence of roll cells, this flow case is particularly well suited for testing of turbulence closure models aimed to be used in conjunction with the Reynolds-averaged Navier-Stokes equations.

It is widely accepted that system rotation offers a challenge to any semi-phenomenological turbulence model; see e.g. Launder *et al.* [25], Johnston [19], Hamba [14] and Jakirlic *et al.* [17]. The present flow case should be attractive for the turbulence modeling community since the Reynolds-averaged Navier-Stokes equations and any accompanying one-point-closure model reduce to a coupled set of ODEs in the wall-normal direction. This favourable feature enables the elimination of all numerical inaccuracies and thus to pin-point any deficiencies in a model's ability to account for the effect of the Coriolis force on the turbulence field. This is only feasible in the absence of rotational-induced roll cells, i.e. in featureless turbulence as achieved for $Ro = 0.7$. Counter-rotating roll cells, which arise with moderate anti-cyclonic rotation ($Ro \leq 0.5$), inevitably contribute extra source terms to the transport equations for the second-moments of the velocity and the vorticity fluctuations, i.e. in equations (2.5) and (2.9), respectively. See, for instance, Pettersson Reif and Andersson [41].

A quasi-homogeneous central core spanned about 80% of the cross-section. Here, the mean velocity profile $U(y)$ increased linearly with a slope $\approx 2\Omega^F$ such that the local vorticity ratio $S \approx -1$. Throughout this extensive region of vanishing absolute vorticity, the turbulent shear stress remained constant and the normal stress components, the vorticity tensor and the energy dissipation rate tensor exhibited abnormal anisotropies. The core region was dominated by fluctuating streamwise vorticity primarily generated by the vortex stretching mechanism $S4_{xx} = \overline{\omega_x \omega_y} dU/dy$. A 13% drag reduction resulted from the configurational changes of the turbulence field. Nevertheless, the turbulent kinetic energy level turned out to be higher than in the absence of rotation.

The support for this work from the Research Council of Norway through a research grant (Contract no 171725/V30) and a grant of computing time (Programme for Supercomputing) is gratefully acknowledged. The authors also appreciate the grant of computing time provided by NTNU's Program in Computational Science and Visualization (BVV).

A Second-moment transport equations in a rotating frame-of-reference

The transport equation (2.5) for the individual components of the second-moments $\overline{u_i u_j}$ of the velocity fluctuations is written in quasi-symbolic form. The various terms on the right-hand side are defined in Cartesian tensor notation as follows:

$$P_{ij} \equiv -\overline{u_i u_k}\frac{\partial U_j}{\partial x_k} - \overline{u_j u_k}\frac{\partial U_i}{\partial x_k} \tag{A.1}$$

$$G_{ij} \equiv -2\Omega_k^F(\overline{u_j u_m}\varepsilon_{ikm} + \overline{u_i u_m}\varepsilon_{jkm}) \tag{A.2}$$

$$D_{ij} = D_{ij}^T + D_{ij}^P + D_{ij}^V \tag{A.3}$$

$$\Pi_{ij} \equiv \overline{\frac{p}{\rho}\left(\frac{\partial u_i}{\partial x_j} + \frac{\partial u_j}{\partial x_i}\right)} \tag{A.4}$$

$$\varepsilon_{ij} \equiv 2\nu\left(\overline{\frac{\partial u_i}{\partial x_k}\frac{\partial u_j}{\partial x_k}}\right) \tag{A.5}$$

where the different parts of the diffusion are given by

$$D_{ij}^T \equiv -\frac{\partial}{\partial x_k}(\overline{u_i u_j u_k}) \tag{A.6}$$

$$D_{ij}^P \equiv -\frac{1}{\rho}\frac{\partial}{\partial x_k}(\overline{p u_i}\delta_{jk} + \overline{p u_j}\delta_{ik}) \tag{A.7}$$

$$D_{ij}^V \equiv \nu\left(\frac{\partial^2 \overline{u_i u_j}}{\partial x_k \partial x_k}\right) \tag{A.8}$$

Here, ε_{ijk} is the permutation or *Levi-Civita* tensor. This organization of the terms in the second-moment transport equation follows Launder *et al.* [25]. The turbulent diffusion due to velocity (D_{ij}^T) and pressure (D_{ij}^P) fluctuations and the viscous diffusion (D_{ij}^V) are labeled collectively as a single diffusion term D_{ij}.

Similarily, the transport equation (2.9) for the individual components of the second-moments $\overline{\omega_i\omega_j}$ of the vorticity fluctuations was written in quasi-symbolic form, where the various terms on the right-hand side are defined as follows:

$$T1_{ij} \equiv -\overline{\omega_i u_k}\frac{\partial\Omega_j}{\partial x_k} - \overline{\omega_j u_k}\frac{\partial\Omega_i}{\partial x_k} \tag{A.9}$$

$$T2_{ij} \equiv -\overline{u_k\frac{\partial\omega_i\omega_j}{\partial x_k}} \tag{A.10}$$

$$S3_{ij} \equiv \overline{\omega_i\omega_k\frac{\partial u_j}{\partial x_k}} + \overline{\omega_j\omega_k\frac{\partial u_i}{\partial x_k}} \tag{A.11}$$

$$S4_{ij} \equiv \overline{\omega_j\omega_k}S_{ik} + \overline{\omega_i\omega_k}S_{jk} \tag{A.12}$$

$$S5_{ij} = S5_{ij}^I + S5_{ij}^{II} \equiv (\Omega_k + 2\Omega_k^F)(\overline{s_{ik}\omega_j} + \overline{s_{jk}\omega_i}) \tag{A.13}$$

$$V6_{ij} \equiv \nu\frac{\partial^2\overline{\omega_i\omega_j}}{\partial x_k\partial x_k} \tag{A.14}$$

$$V7_{ij} \equiv -2\nu\left(\overline{\frac{\partial\omega_i}{\partial x_k}\frac{\partial\omega_j}{\partial x_k}}\right) \tag{A.15}$$

Here, S_{ij} and s_{ij} denote the mean and fluctuating parts of the instantaneous strain-rate tensor. Notice that $\mathbf{\Omega}^F$ denotes the constant angular velocity of the steadily rotating frame-of-reference whereas $\frac{1}{2}\mathbf{\Omega}$ is the mean angular velocity associated with the fluid motion, i.e. half the mean vorticity $\nabla\times\boldsymbol{U}$. The stretching term $S5_{ij}$ has been split in two parts in order to distinguish between the roles played by mean fluid rotation $(S5^I)$ and system rotation $(S5^{II})$.

These expressions for the terms in the individual second-moment budgets of the fluctuating vorticity components in a rotating frame-of-reference are not available elsewhere. The above equations have been checked for consistency against the corresponding equation for the enstrophy provided by Lamballais *et al.* [23] and Lui and Lu [26]. By contraction of the indices i and j in the above terms their equation is recovered. The notion of transport (T), stretching (S), and viscous (V) terms follows Lamballais *et al.* [23], whereas the numbering refers to the order of the terms in Antonia and Kim [3], which in turn referred to equation (3.3.38) and the accompanying discussion in Tennekes and Lumley [36].

References

1. P. H. Alfredsson and N. Tillmark. Instability, transition and turbulence in plane Couette flow with system rotation. In Laminar Turbulent Transition and Finite Amplitude Solutions, editors, T. Mullin and R. R. Kerswell, pages 173-193, Springer-Verlag, 2005.
2. C. D. Andereck, S. S. Liu and H. L. Swinney. Flow regimes in a circular Couette system with independently rotating cylinders. J. Fluid Mech., 164 (1985), 155-183.
3. R. A. Antonia and J. Kim. Low-Reynolds-number effects on near-wall turbulence. J. Fluid Mech., 276 (1994), 61-80.
4. M. Barri and H. I. Andersson. Anomalous turbulence in rapidly rotating plane Couette flow. In Advances in Turbulence XI, edited by J. M. L. M. Palma and A. Silva Lopes, pages 100-102, Springer-Verlag, 2007.
5. P. Bartello, O. Métais and M. Lesieur. Coherent structures in rotating three-dimensional turbulence. J. Fluid Mech., 273 (1994), 1-29.
6. K. H. Bech and H. I. Andersson. Secondary flow in weakly rotating turbulent plane Couette flow. J. Fluid Mech., 317 (1996), 195-214.
7. K. H. Bech and H. I. Andersson. Turbulent plane Couette flow subject to strong system rotation. J. Fluid Mech., 347 (1997), 289-314.
8. K. H. Bech, N. Tillmark, P. H. Alfredsson and H. I. Andersson. An investigation of turbulent plane Couette flow at low Reynolds numbers. J. Fluid Mech., 286 (1995), 291-325.
9. G. Brethouwer. The effect of rotation on rapidly sheared homogeneous turbulence and passive scalar transport. Linear theory and direct numerical simulation. J. Fluid Mech., 542 (2005), 305-342.
10. F. H. Busse. Bounds on the momentum transport by turbulent shear flow in rotating systems. J. Fluid Mech., 583 (2007), 303-311.
11. C. Cambon, J.-P. Benoit, L. Shao and L. Jacquin. Stability analysis and large-eddy simulation of rotating turbulence with organized eddies. J. Fluid Mech., 278 (1994), 175-200.
12. B. Dubrulle, O. Dauchot, F. Daviaud, P.-Y. Longaretti, D. Richard and J.-P. Zahn. Stability and turbulent transport in Taylor-Couette flow from analysis of experimental data. Phys. Fluids, 17 (2005), 095103.
13. O. Grundestam, S. Wallin and A. V. Johansson. Direct numerical simulation of rotating turbulent channel flow. J. Fluid Mech., 598 (2008), 177-199.
14. F. Hamba. The mechanism of zero mean absolute vorticity state in rotating channel flow. Phys. Fluids, 18 (2006), 125104.
15. J. E. Hart. Instability and secondary motion in a rotating channel flow. J. Fluid Mech., 45 (1971), 341-351.
16. O. Iida, Y. Tsukamoto and Y. Nagano. The tilting mechanism of a longitudinal vortical structure in a homogenous shear flow with and without spanwise shear. Flow, Turbulence Combust., 81 (2008), 17-37.
17. S. Jakirlic, K. Hanjalic and C. Tropea. Modeling rotating and swirling turbulent flows: a perpetual challenge. AIAA J., 40 (2002), 1984-1996.
18. J. Jeong and F. Hussain. On the identification of a vortex. J. Fluid Mech., 285 (1995), 69-94.
19. J. P. Johnston. Effects of system rotation on turbulence structure: a review relevant to turbomachinery flows. Int. J. Rotating Machin., 4 (1998), 97-112.
20. J. P. Johnston, R. M. Halleen and D. K. Lezius. Effects of spanwise rotation on the structure of two-dimensional fully developed turbulent channel flow. J. Fluid Mech., 56 (1972), 533-557.
21. J. Komminaho, A. Lundblad and A. V. Johansson. Very large structures in plane turbulent

Couette flow. J. Fluid Mech., 320 (1996), 259-285.
22. R. Kristoffersen and H. I. Andersson. Direct simulations of low-Reynolds-number turbulent flow in a rotating channel. J. Fluid Mech., 256 (1993), 163-197.
23. E. Lamballais, M. Lesieur and O. Métais. Effects of spanwise rotation on the vorticity stretching in transitional and turbulent channel flow. Int. J. Heat Fluid Flow, 17 (1996), 324-332.
24. E. Lamballais, O. Métais and M. Lesieur. Spectral-dynamic model for large-eddy simulation of turbulent rotating channel flow. Theoret. Comput. Fluid Dynamics, 12 (1998), 149-177.
25. B. E. Launder, D. P. Tselepidakis and B. A Younis. A second-moment closure study of rotating channel flow. J. Fluid Mech., 183 (1987), 63-75.
26. N.-S. Liu and X.-Y. Lu. A numerical investigation of turbulent flows in a spanwise rotating channel. Comput. Fluids, 36 (2007), 282-298.
27. J. L. Lumley and G. R. Newman. The return to isotropy of homogeneous turbulence. J. Fluid Mech., 82 (1977), 161-178.
28. M. Manhart. A zonal grid algorithm for DNS of turbulent boundary layers. Comput. Fluids, 33 (2004), 435-461.
29. H. K. Moffatt and A. Tsinober. Helicity in laminar and turbulent flow. Ann. Rev. Fluid Mech., 24 (1992), 281-312.
30. K. Nakabayashi and O. Kitoh. Low Reynolds number fully developed two-dimensional turbulent channel flow with system rotation. J. Fluid Mech., 315 (1996), 1-29.
31. K. Nakabayashi and O. Kitoh. Turbulence characteristics of two-dimensional channel flow with system rotation. J. Fluid Mech., 528 (2005), 355-377.
32. P. Orlandi. Helicity fluctuations and turbulent energy production in rotating and non-rotating pipes. Phys. Fluids, 9 (1997), 2045-2056.
33. V. C. Patel and F. Sotiropoulos. Longitudinal curvature effects in turbulent boundary layers. Prog. Aerospace Sci., 33 (1997), 1-70.
34. M. M. Rogers and P. Moin. Helicity fluctuations in incompressible turbulent flows. Phys. Fluids, 30 (1987), 2662-2671.
35. A. Salhi and C. Cambon. An analysis of rotating shear flow using linear theory and DNS and LES results. J. Fluid Mech., 347 (1997), 171-195.
36. H. Tennekes and J. L. Lumley. A First Course in Turbulence. MIT Press, 1972.
37. N. Tillmark and P. H. Alfredsson. Experiments on rotating plane Couette flow. In Advances in Turbulence VI, pages 391-394, Kluwer Academic Publishers, 1996.
38. A. A. Townsend. Axisymmetric Couette flow at large Taylor numbers. J. Fluid Mech., 144 (1984), 329-362.
39. T. Tsukahara, H. Kawamura and K. Shingai. DNS of turbulent Couette flow with emphasis on the large-scale structure in the core region. J. Turbulence, 7 (2006), 19.
40. S. Yanase, M. Tanaka, S. Kida and G. Kawahara. Generation and sustenance mechanisms of coherent vortical structures in rotating shear turbulence of zero-mean-absolute vorticity. Fluid Dyn. Research, 35 (2004), 237-254.
41. B. A. Pettersson Reif and H. I. Andersson. Prediction of longitudinal roll cells in rotating plane turbulent Couette flow. Theoret. Comput. Fluid Dynamics, 14 (2000), 89-108.

Paper 4

A new set-up for PIV measurements in rapidly rotating turbulent duct flows

Visscher, J., Andersson, H. I., Barri, M., Didelle, H., Viboud, S., Sous, D. & Sommeria, J.

Submitted to *Experiments in Fluids.*

The present manuscript is an extended version of the draft paper titled as **Effects of rotation on clear and obstructed turbulent channel flows**. The paper was printed in the proceedings of *7th International ERCOFTAC Symposium on Engineering Turbulence Modeling and Measurements*, Limassol, Cyprus, pp. 243–248, 2008.

A new set-up for PIV measurements in rapidly rotating turbulent duct flows

Jan Visscher

Department of Marine Technology, Norwegian University of Science and Technology, Trondheim, Norway

phone: +47 735 51457; fax: +47 735 95528; email: jan.h.visscher@ntnu.no

Helge I. Andersson, Mustafa Barri

Department of Energy and Process Engineering, Norwegian University of Science and Technology, Trondheim, Norway

Henri Didelle, Samuel Viboud, Damien Sous, Joël Sommeria

Laboratoire Ecoulements Géophysiques et Industriels (LEGI), Universite Joseph Fourier, Grenoble, France

Abstract

A novel set-up designed for flow visualizations and turbulence measurements in rotating high-aspect-ratio ducts has been described. The 8*m* long duct was placed across a *13m* diameter turntable and the set-up enabled stereoscopic PIV-measurements over a wide range of rotation numbers $Ro \equiv 2\Omega H/U \leq 0.80$. Measurements of all three components of the instantaneous velocity vector were made in a plane spanning the channel from the pressure to the suction side. The important turbulence statistics, such as all components of the Reynolds stress tensor and the spanwise component of the vorticity field, were obtained. The overall observation was that the Coriolis force due to the imposed system rotation damped the turbulence level along the suction side whereas an augmentation of the turbulent agitation was found at the pressure side of the rotating channel.

1. Introduction

Rotating flows are encountered both in geophysical and industrial fluid mechanics. The influence of the Coriolis body force on fluid motion exhibits a number of generic features which may occur irrespective of the particular field of application. Internal flows in rotating ducts and channels, however, are typically found in engineering applications, notably in rotating machinery, e.g. cyclone separators, pumps and turbines. An excellent review, with an intentional application-oriented bias, was provided by Johnston (1998). The first of the four distinct situations covered by the review is the fully-developed flow in long rotating channels. This particular flow configuration is also the subject of the present study.

Background rotation is known to alter not only the mean fluid motion but also the turbulence field is affected qualitatively as well as quantitatively (Kristoffersen & Andersson 1993). Depending on both the orientation and magnitude of the rotation vector Ω, i.e. the angular velocity of the rotating device, completely different flow phenomena may occur. In a rectangular duct which rotates about a spanwise axis, the background rotation results in a transverse pressure-gradient intended to balance the Coriolis force which acts normal both to the axis of rotation and to the primary flow direction. This gives rise to the notion of *suction* and *pressure* sides frequently used in the turbomachinery vocabulary. This terminology corresponds to *cyclonic* and *anti-cyclonic* flow conditions, respectively, in geophysical fluid dynamics.

In the present article we report on a novel set-up which enables detailed investigations of fully-developed flows in rectangular ducts over a wide range of rotation rates. Our interest is in high-aspect-ratio ducts such that the flow field in the mid-plane is two-dimensional. We are therefore neither addressing the flow in low-aspect-ratio rotating ducts nor in shorter ducts in which turbulent boundary layers develop along the duct walls.

2. Background

2.1 Controlling parameters

Let us consider the flow through a long duct with a rectangular cross-section with height D and width H. Besides the aspect ratio $AR \equiv D/H$, the flow is determined by the Reynolds number Re and the rotation number Ro defined as

$$Re \equiv U_b H/\nu; \quad Ro \equiv 2\Omega H/U_b. \tag{1}$$

Here, $U_b = Q/A$ is the bulk or average velocity over the cross-sectional area $A = DH$, ν is the kinematic viscosity of the fluid and Ω is the constant angular velocity with which the duct is rotating. For convenience, we assume that the duct is rotating about an axis aligned with the side walls (D) of the duct such that the geometric length scale perpendicular both to the bulk flow direction and the axis of rotation is the duct width H.

In geophysical fluid dynamics, the Rossby number $U_b/2\Omega H$, i.e. the reciprocal rotation number, is used instead of Ro. The Ekman number

$$Ek \equiv \nu/\Omega H^2 = 2Re^{-1}\cdot Ro^{-1} \tag{2}$$

is used to estimate the thickness of the Ekman layers that form on the sidewalls perpendicular to the axis of rotation. The alternative dimensionless group

$$\Omega\nu/U_b^2 = \tfrac{1}{2}Ro\cdot Re^{-1} = (\tfrac{1}{2}Ro)^2\cdot Ek \tag{3}$$

has sometimes been used in industrial fluid dynamics, but then with the bulk velocity U_b replaced by the friction velocity (Watmuff et al. 1985; Nakabayashi & Kitoh 1996).

2.2 Secondary flows and aspect ratio considerations

It is well known that turbulent flow in a rectangular duct is slightly affected by secondary corner vortices in the cross-sectional plane. These secondary motions are driven by gradients of the Reynolds stress tensor components and are absent in a duct with circular cross-section. In a rotating duct, two other kinds of secondary flows may occur. The mean pres-

sure gradient set up to balance the Coriolis force in the direction perpendicular to the primary flow gives rise to secondary flows along the end walls. This fluid motion is driven from the pressure side to the suction side by the spanwise pressure gradient. Finally, a rotational instability, analogous to the more well-known centrifugal instability in Taylor-Couette flow, may occasionally induce pairs of counter-rotating roll cells aligned with the primary flow direction.

In rotating duct flows, the turbulence-driven corner vortices can be assumed to be of negligible importance. For high-aspect-ratio ducts, i.e. AR $\geq$ 4, the secondary flow caused by the end walls does not penetrate to the mid-plane of the duct. The flow at the duct mid-plane can therefore be considered as nominally two-dimensional. In a recent computational study, Julien et al. (2008) found that despite being very small, the presence of the secondary flow at the end walls has a global impact on the mid-plane mean velocity profile even for AR = 22. They therefore argued that distinctions should be made between the two-dimensional central core of high-aspect-ratio 3D duct flow and the fictitious 2D plane Poiseuille or channel flow.

2.3 Earlier experiments in high-aspect-ratio ducts

Experimental studies of fully developed turbulent flow in rotating rectangular ducts are scarce; see Table 1. Here, we define a high-aspect-ratio duct as having aspect ratio D/H $\geq$ 4:1 (height:width). Measurements in the entrance region of such ducts, with the view to examine the boundary layer development, are not considered herein. Likewise, flows in low-aspect-ratio ducts are not dealt with either since the overall flow pattern is rather dependent on the aspect ratio; see e.g. the exposition based on large-eddy simulations by Murata & Mochizuki (1999). For this reason, also flows in rotating square ducts are discarded in this brief overview.

Following some pioneering investigations at MIT, e.g. Moore (1967), Johnston et al. (1972) and Johnston (1973) presented results from an extensive laboratory investigation which included both fascinating flow visualizations and pitot-tube mean velocity measurements in a rotating water channel. They observed that the turbulence level was enhanced along the pressure side and correspondingly reduced along the suction side of their 7:1 aspect ratio duct. A nearly total suppression of the turbulence was found for the lower Reynolds number cases at relatively high rotation rates. They also observed the development of large-scale roll cells near the pressure side.

Nakabayashi & Kitoh (1996, 2005) investigated the turbulent flow in the rectangular test section of a rotating air tunnel. By means of hot-wire anemometry accurate mean flow measurements (Nakabayashi & Kitoh 1996) and turbulence statistics (Nakabayashi & Kitoh 2005) were provided. The velocity fluctuations in the streamwise and wall-normal directions were measured by a single X-probe, whereas the velocity component aligned with the axis of rotation was not reported. With air as the working medium, they were unable to reach rotation numbers above 0.11.

More recently, Maciel et al. (2003) designed a similar rotating apparatus aimed to rotate up to 4 revolutions per second (240 r.p.m.). A rotation number as high as 2.0 can then be reached at relatively low Reynolds numbers. Mean velocity profiles and r.m.s. values of the streamwise velocity fluctuations obtained with a single hot-wire probe were reported for some different rotation rates with Ro up to 0.44 (see Table 1).

TABLE 1 Experiments of rotating fully developed high-aspect-ratio duct flow

Author(s)	Year	Aspect ratio	L/H	Re	Max{Ro}	Max{Ω} (r.p.m.)	
Moore	1967	7.33 : 1	96	12 700 21 900	0.0710 0.0414		Pitot
Johnston et al.	1972	7.14 : 1	38.3	11 500 ≤36 000	0.42 0.2	14	Pitot
Nakabayashi & Kitoh	1996 2005	8 : 1	180 *	1 700 – 10 000	0.1094	≈ 197	HWA – 2C
Maciel et al.	2003	11 : 1	59 *	6 000	0.44	40	HWA - 1C
Present	2009	5 : 1	80 *	5 600 22 400	0.8 0.2	2	PIV - 3C

* Here, L denotes the distance from the channel entrance to the first measurement plane

2.4 Conflicting constraints

The entries in Table 1 witness some of the conflicting constraints met in the design of a rotating duct experiment. First of all, a relatively long duct is required in order to assure that the flow is fully developed, i.e. independent of the axial position, at the measurement stations. Rules-of-thumb do exist for the hydrodynamic entrance length in fixed ducts and suggest that a turbulent flow at Reynolds number 20 000 is fully developed 25H downstream. No such design criterion is available for flows in rotating ducts. In practice, however, the need to rotate the duct imposes a severe constraint on its length L, irrespective of whether the duct is rotating about a vertical or a horizontal axis.

Due to the occurrence of secondary flows of various kinds, cf §2.2, the choice of aspect ratio substantially affects the cross-sectional flow pattern and to some extent also the axial flow. Ideally, it would have been interesting to carry out experiments in a rotating plane channel, i.e. infinitely high aspect ratio, in order to eliminate the end-wall effects. In a recent RANS-based computational study, Julien et al. (2008) found that noticeable end-wall effects persisted in the mid-plane even at an aspect ratio as high as 22:1. They therefore concluded that although the flow in a 3D duct is essentially two-dimensional in the central region, the flow field is nevertheless different from that in an idealized AR = ∞ case. It is definitively advantageous from a constructional point of view to avoid an excessively high aspect ratio to facilitate the stiffness of the construction as well as to reduce its weight. For this reason we adopted a moderately high aspect ratio of 5:1 in the present study, which is sufficient to assure two-dimensionality of the flow in the mid-plane (see e.g. Murata & Mochizuki 1999).

Due to the large difference in the viscosities between air and water, the velocity of an air stream needs to be faster by a factor of $\nu_{air}/\nu_{water} \approx 15$ than that of a water flow in order to achieve the same Reynolds number in a given duct. According to the definition of the

rotation number in eq. (1), an air-filled duct should thus be rotated 15 times faster than the same duct filled with water to achieve the same Ro. Higher rotation numbers are therefore more easily reached with water as the flowing medium.

In order to increase the Reynolds number for the flow of a given fluid in a given duct, the bulk velocity and thus the flow rate need to be increased. This will inevitably reduce the maximum attainable rotation number. In a given set-up the highest rotation numbers are therefore reached at the lowest Reynolds numbers.

3 Set-up and measuring system

3.1 Test duct

The test duct is 8m long and has a rectangular cross-section with height 0.50m (D) and width 0.10m (H), i.e. aspect ratio 5:1. The duct consists of five different sections, three of which are 2.0 m long and the two others are 1.0 m each; see Figure 1. The first of the shorter sections is equipped with a set of screens and a 40 cm long honeycomb with 1cm wide hexagonal cells in order to quench any large-scale flow structures and homogenize the flow field over the cross-section. Between the honeycomb and the test section a 4 m long clear inflow section is situated to establish fully developed, homogenous inflow. Four of the duct sections are made of PVC, whereas the one-meter long test section is made of Plexiglas to enable visual inspection of the flow, as well as flow visualizations and the PIV measurements.

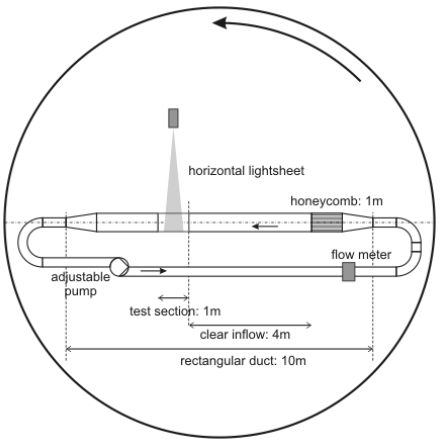

Fig. 1: Experimental setup seen from above

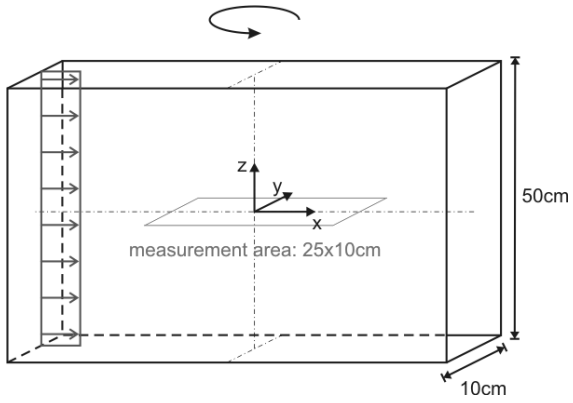

Fig. 2: Details of the 1m long test section

The flow is driven through the flow circuit by a *Rotaflow* pump (*CCM Sulzer*) with a capacity of more than 180 m^3/h or 50 liter/s. In practice, however, the experiments required not more than half of the available pumping capacity. Upstream and downstream of the 10 m long rectangular test duct, the flow circuit is made up of circular pipe sections with internal diameter 0.10 m. Plane diffuser sections connect the circular pipe to the rectangular section. Each diffuser is 1 m long and has a spread angle of 53.1º. In order to eliminate any swirling motion created in the pipe bends and also to avoid undesired flow

separation, four flat plates are mounted inside the diffuser such that each diffuser section in reality comprises five diffuser channels.

3.2 PIV system and instrumentation

The PIV system consists of a *Spectra Physics Millenia Pro* 6W continuous-wave Laser and two *Dalsa 1M60P* CCD cameras with a resolution of 1024 by 1024 pixels and a maximum image rate of 60 Hz. The light sheet is created in the center of the test section by a synchronized oscillating mirror to maintain full laser brightness over the entire field of view. It illuminates a horizontal area in the xy-plane with 30 cm extent in the streamwise x-direction by sweeping the beam forth and back within one camera frame length. The two cameras are mounted over the duct at a view angle of 30 degrees to enable stereoscopic view. Camera synchronization and data acquisition is done on a PC with 4 GB memory and a RAID system using *acquix*, an open source software package which was developed by laboratory team members. Images could be recorded at rates up to 10 Hz, while series of at least 500 images were acquired in one run. *Orgasol* polyamide particles of 30 μm in diameter were used as seeding material.

The images were processed using *CivX*, an open source cross-correlation program which is controlled through the *Matlab* user interface *UVmat*. The effective field of view covered the width of the channel (i.e. 10 cm) and 20 cm in streamwise direction; see Figure 2. The vector fields of all three velocity components u, v and w were obtained from correlation regions of 21 by 31 pixels, which correspond to 4 by 6 mm, and sampled on a 100 by 50 mesh, leading to a final vector resolution of 1/1mm.

3.3 The "Coriolis" platform

The entire setup, i.e. flow circuit, PIV system, instrumentation and data processing system, was placed on the "Coriolis" platform at the Laboratory of Geophysical and Industrial Fluid Flows in Grenoble (France). With its 14m diameter, this is the largest turntable in the world. The axis of rotation is vertical with an accuracy of ±3·10-6 rad and the rotation period T can be set between 28 s and 1000 s with an accuracy of 0.01%. The maximum rotation speed Ω is thus about 2 rpm or $\approx$ 0.21 rad/s. The test duct was positioned transversely on the platform through its center, as shown in Figure 1, such that the test (Plexiglas) section started about 1 meter from the axis of rotation.

Unlike all earlier rotating duct flow experiments, the present set-up enables not only the flow circuit but also all accessories and even the researchers to stay on the rotating platform. This eliminates the need for transmission of water, power, control and data signals from the laboratory frame to the rotating rig. Visual inspections of the illuminated flow field can easily be made by the researcher onboard the platform.

4 Results

The measurements comprised a variety of parameter combinations, as shown in Table 2. The empty entries in the test matrix are due to the conflicting constraints which make high rotation numbers out of reach at the higher Reynolds numbers; see the discussion in section 2.4. The lowest Reynolds number $Re_H = 5\,600$ matches that in the DNS study by Kristoffersen & Andersson (1993). The higher Reynolds numbers are roughly comparable

with Reynolds numbers considered in the pioneering experimental investigations by Moore (1967) and Johnston et al. (1972). Only results from the lowest Reynolds number will be presented in the following with focus on how the flow is becoming increasingly asymmetric with increasing system rotation. The sense of rotation was always anti-clockwise as indicated in Figure 1 (i.e. $\Omega \geq 0$ in the coordinate system defined in Figure 2), which implies that the pressure side wall is at y = -5cm while the suction side is at y = +5cm in the subsequent figures.

4.1 Instantaneous flow

Examples of the instantaneous velocity fields in the non-rotating and a rapidly rotating case are shown in Figure 3. To enhance the visability, only every fourth result vector is shown in both streamwise and wall-normal direction. Note that the backflow close to the upper wall visible in Figure 3b) and d) is only an effect of the subtraction of the bulk velocity in order to emphasize the large-eddy structure. The flow field appears to be by far more regular, i.e. less chaotic, along the suction side (the upper half of the visualized plane) in the rotating case (Fig. 3d) as compared with the non-rotating case (Fig. 3b). The large-scale eddies that are visible for Ro = 0 are almost absent for Ro = 0.6.

TABLE 2 The test matrix showing the different parameter combinations considered. The entries in the matrix denote the rotation period $T = 2\pi/\Omega$ in seconds. The superscript # indicates that the parameter combination matches a case simulated by Kristoffersen & Andersson (1993).

Ro	Re = 5 600	Re = 11 200	Re = 22 400
	$Q = 10m^3/h$	$Q = 20m^3/h$	$Q = 40m^3/h$
0	∞	∞	∞
0.10	$224.4^{\#}$	112.2	56.1
0.20	$112.2^{\#}$	56.1	28.05
0.40	$56.1^{\#}$	28.05	------
0.60	37.4	------	------
0.80	28.05	------	------

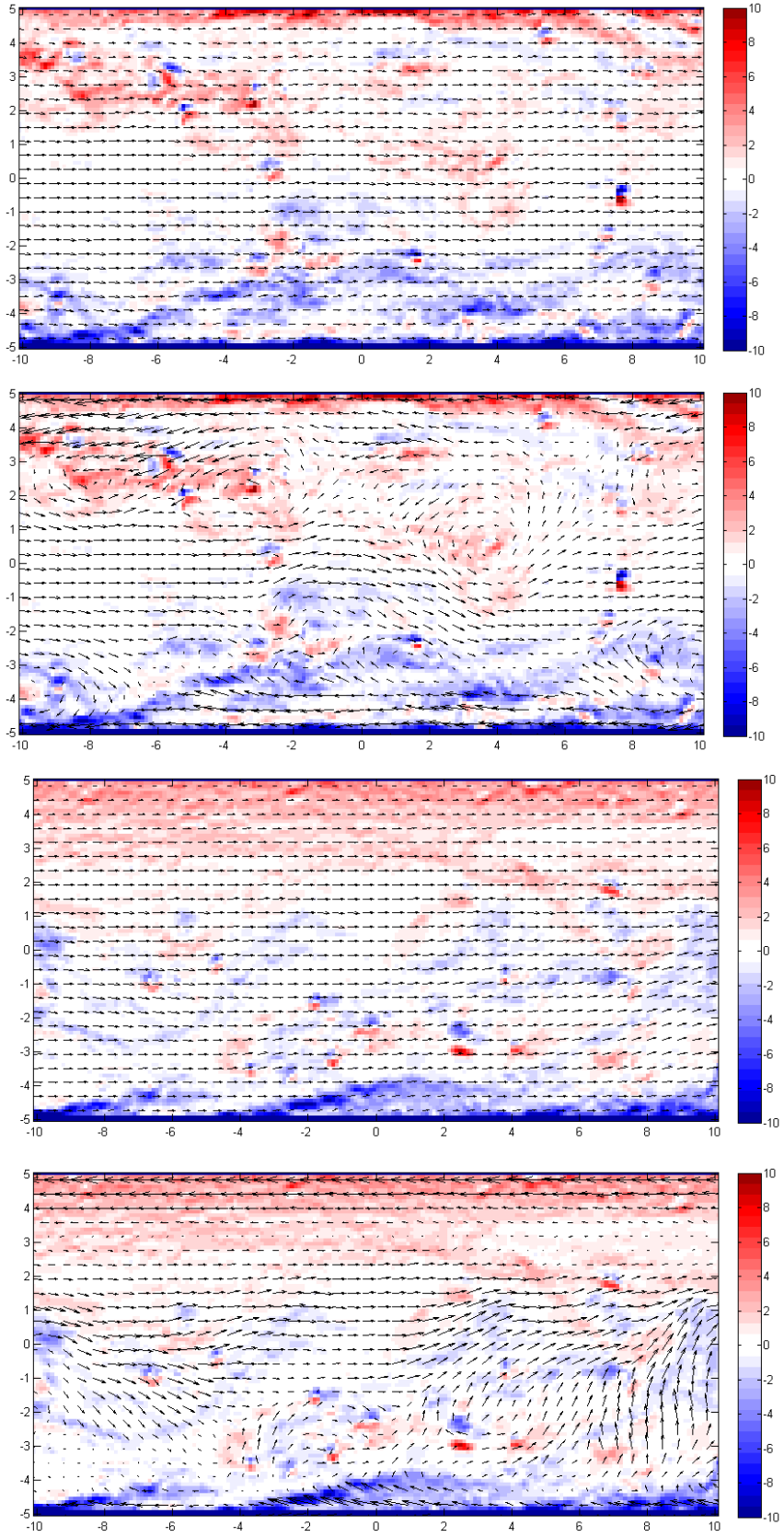

Figure 3: Instantaneous velocity field u (arrows) and spanwise vorticity ω_z (colour contours) for Re = 5.600 in the (x, y)-plane. The bulk velocity U_b has been subtracted from the streamwise velocity component to highlight the turbulent eddies in every second frame. From top to bottom: a) Ro = 0; b) Ro = 0, u-U_b; c) Ro = 0.60; d) Ro = 0.60, u-U_b.

4.2 Mean flow

The cross-stream variations of the mean velocity components U, V, and W are presented in this section. The profiles shown are obtained by averaging the instantaneous pointwise data first in time and afterwards in the homogeneous x-direction. The statistics are thus based on at least 500 realizations in time and 100 realizations in space. The homogeneity of the flow in the streamwise direction is demonstrated by Figures 4 and 5, which show pointwise time-averaged data. Both the streamwise velocity $\langle u \rangle$ and the accompanying fluctuations $\langle u'^2 \rangle$ suggest that the flow field is practically fully developed, i.e. homogeneous in x.

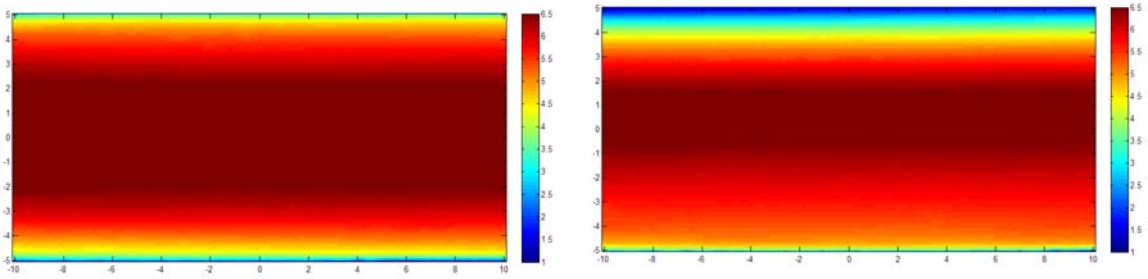

Fig. 4: Pointwise time-average $\langle u \rangle$ of the streamwise velocity component at Re=5 600 in the (x, y)-plane. Left: Ro = 0, right: Ro = 0.60

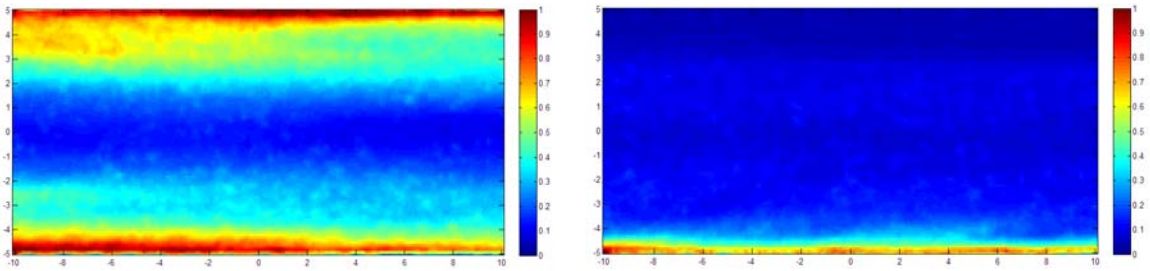

Fig. 5: Pointwise time-average of the streamwise Reynolds stress $\langle u'^2 \rangle$ at Re = 5 600 in the (x, y)-plane. Left: Ro = 0, right: Ro = 0.60

Figure 6 shows the three components of the mean velocity vector for Re = 5 600 at rotation numbers in the range from Ro = 0 to Ro = 0.80. For this Reynolds number the flow rate Q was fixed to $10 m^3$ per hour, which gives a bulk velocity $U_b \approx 5.6$cm/s. With anticlockwise rotation $\Omega \geq 0$ the pressure side wall is at y = -5cm while the suction side is at y = +5cm in the figure.

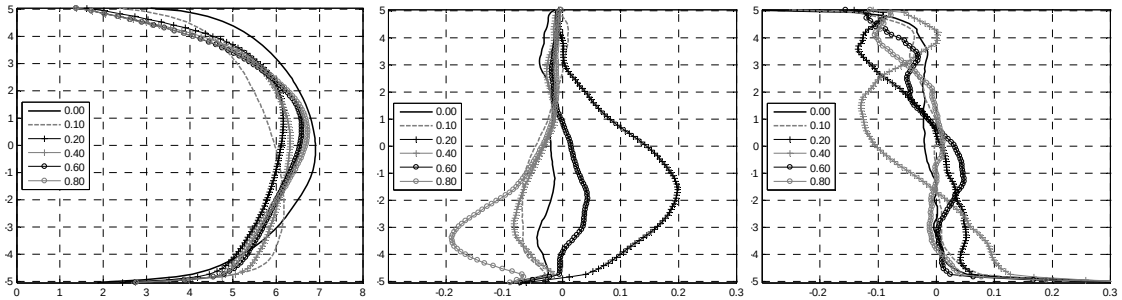

Figure 6: Mean velocity components in cm/s for multiple rotation numbers at Re = 5 600. Left: streamwise U(y); Middle: wall-normal V(y); Right: spanwise W(y).

Without rotation, the streamwise mean velocity component U(y) varies almost symmetrically around the mid-plane y = 0 while the wall-normal component V(y) and the spanwise W(y) both are smaller than 1% of the bulk velocity. With system rotation imposed, U(y) becomes asymmetric with the location of maximum velocity shifted from the centerline towards the suction side, i.e. towards positive y-values. For the higher rotation numbers $Ro \geq 0.4$, the velocity profiles become linear over a certain interval near the pressure side, fully consistent with earlier experiments (Johnston et al. 1972) and simulations (Kristoffersen & Andersson 1993). The unsteady RANS calculations reported by Julien et al. (2008) demonstrated that the central portion of the flow in high-aspect-ratio rectangular ducts is different from the flow in a plane channel with infinitely high aspect ratio. The offset location of the maximum of the mean velocity profile U(y) is larger in a plane channel ($AR = \infty$) than in a high rectangular duct with aspect ratio AR = 11. This somewhat surprising observation results from the non-negligible influence of the weak secondary flows driven by the side-wall Ekman layers.

The results for the lowest rotation number considered, i.e. Ro = 0.10, showed a behaviour rather different from the results at the other rotation numbers (cf. the mean velocity profiles in Figure 6a). After a thorough examination of the entire data set for this particular rotation number, we concluded that this modest rate of rotation acts primarily on the mean flow, which appears to be very sensitive to aspect ratio and inflow conditions. Since the scales of the secondary flow field are substantially larger than the scales of the turbulence, it is conjectured that the major effect of rotation at this Ro is through alterations of the mean flow field. At the higher rotation numbers, on the other hand, the local or direct effect of rotation on the turbulence dominates. Since we are interested in this direct effect, we discard the case of low rotation in the analysis of the turbulence. Data for Ro = 0.10 will therefore not be included in the remaining figures.

For some other non-zero rotation numbers, the two mean velocity components normal to the bulk flow attain small but yet non-vanishing values. The results for Ro = 0.2, for instance, suggest a modest cross-flow V in the positive y-direction near the pressure side, i.e. directed from the pressure to the suction side. A downward flow ($W < 0$) occurs near the suction side. These secondary flow components are visualized in Figure 7, which reveals a surprisingly regular flow pattern which is likely to be associated with rotational-induced roll cells. Such roll cell patterns depend on the Reynolds number, the rotation number, and the duct aspect ratio. The roll cells are nevertheless not persistent; neither in space nor in time (see the discussion in Kristoffersen & Andersson 1993). They may therefore contribute differently in the different cases considered in this study. Surely, their effect on the otherwise unidirectional mean flow U(y) cannot be ignored.

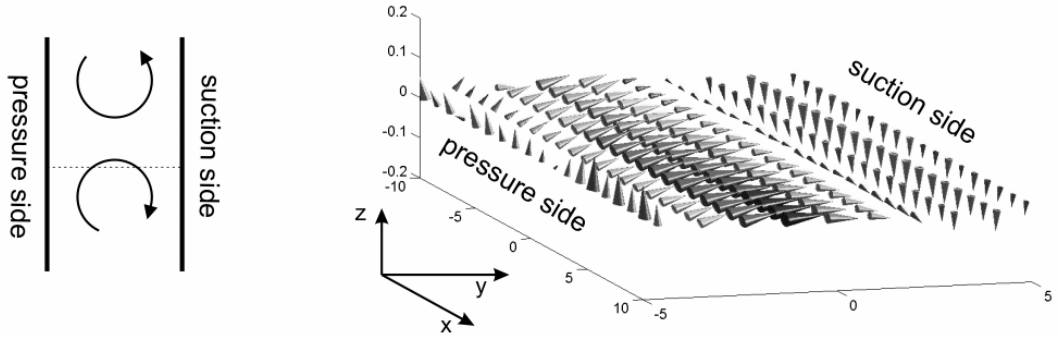

Figure 7. Secondary mean flow in the measurement area indicated in figure 2. The glyphs show the direction and magnitude of the V and W components for Re = 5 600 and Ro = 0.2. The sketch to the left shows a pair of counter-rotating roll cells with the measurement plane indicated by the dotted line.

4.3 Reynolds stresses

The three normal Reynolds stress components are presented in Figure 8 for the same rotation numbers as in Figure 6, except that data for Ro = 0.10 are excluded. The square-root of a diagonal component of the Reynolds stress tensor is, in fact, the turbulence intensity, i.e. the root-mean-square value of the fluctuating velocity component in that direction. The data for the non-rotating case varies symmetrically around y = 0, whereas the profiles for the rotating cases become increasingly asymmetric with increasing rotation rates. The peak value of the wall-normal velocity fluctuations near the pressure side increases gradually with Ro in accordance with the DNS data of Kristoffersen & Andersson (1993). The PIV-data, however, show a tendency of saturation at the highest rotation number Ro = 0.8. The more than twofold increase of $\langle v'^2 \rangle$ can readily be ascribed to the Coriolis term $-4\Omega\langle u'v' \rangle$ due to rotation in the balance equation for this Reynolds stress component. With $\Omega > 0$ this term is positive near the pressure side where $\langle u'v' \rangle$ is negative, see e.g. Kristoffersen & Andersson (1993). The same term is also responsible for the damping of wall-normal fluctuations along the suction side. Here, this Coriolis term becomes negative and therefore acts as a sink term in the v'-budget. In fact, v' is dramatically reduced already at Ro = 0.20 and the wall-normal fluctuations are entirely quenched for even higher rotation numbers.

The influence of rotation on the velocity fluctuations u' and w' is not as clear-cut as on v'. However, the reduction and eventual suppression of the wall-normal velocity fluctuations near the suction side leads to an overall reduction of the turbulent agitation that is seen in all three velocity components. It should be emphasized that the spanwise velocity fluctuations w' are aligned with the axis of rotation and the spanwise fluctuations can therefore not be directly affected by the Coriolis force. The damping of $\langle w'^2 \rangle$ observed in Figure 8c is therefore an indirect effect of system rotation. A detailed discussion on these phenomena was provided by Andersson & Kristoffersen (1995) on the basis of their DNS data.

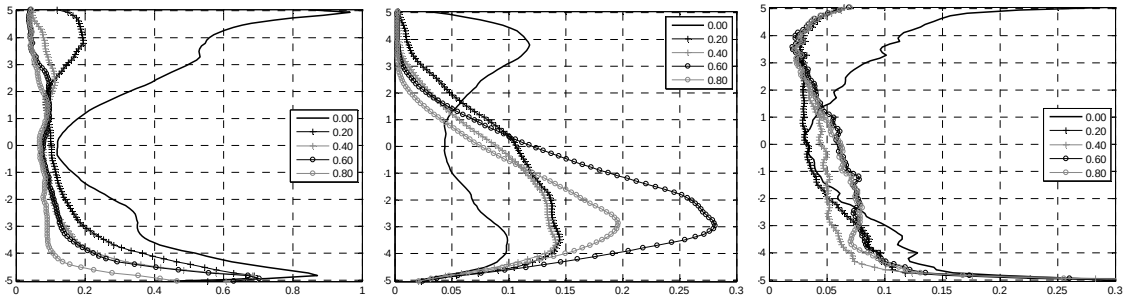

Figure 8: Normal Reynolds stress components at Re = 5 600 and various rotation numbers.
Left: streamwise $\langle u'^2 \rangle$; Middle: wall-normal $\langle v'^2 \rangle$; Right: spanwise $\langle w'^2 \rangle$.

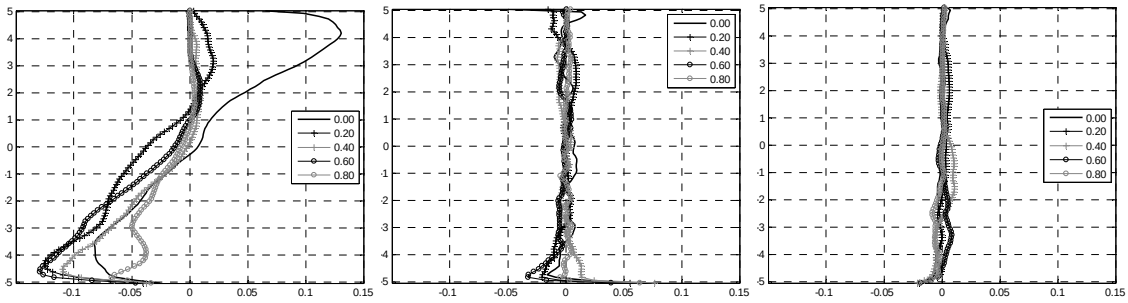

Figure 9: Reynolds shear stresses componets at Re = 5 600 and various rotation numbers. Left: shear stress $\langle u'v' \rangle$; Middle: shear stress $\langle u'w' \rangle$; Right: shear stress $\langle v'w' \rangle$.

The three off-diagonal components of the Reynolds stress tensor are presented in Figure 9. In the non-rotating channel the nearly anti-symmetric profile of the primary shear stress $\langle u'v' \rangle$ exhibits the well-known shape in conventional plane Poiseuille flow with a linear variation over more than 80% of the cross-section. The friction velocity u_τ can readily be estimated from the intersections of the extrapolated $\langle u'v' \rangle$-profile with the walls to be ca 0.37 cm/s. According to the DNS data of Kristoffersen & Andersson (1993), the bulk velocity $U_b \approx 15.1\, u_\tau$, from which we obtain $U_b \approx 5.55$ cm/s in the present case. This value is consistent with the imposed flow rate Q (giving $U_b = 5.6$ cm/s).

The shear stress is substantially reduced near the suction side at Ro = 0.2 and vanishes entirely for the higher rotation rates $Ro \geq 0.4$. This is a direct consequence of the suppression of the wall-normal fluctuations v'. The associated damping of the Reynolds shear stress $\langle u'v' \rangle$ results in quenching of the turbulence. The largest shift of the zero-crossing towards the suction side is found for Ro = 0.2, whereas the DNS data at the same Reynolds number indicated at monotonically increasing shift with increasing rotation numbers. Nakabayashi & Kitoh (1996) argued that the presence of secondary motions tended to distort the shear stress profile such that significant deviations from the conventional linear profile could be observed, notably near the pressure side where counter-rotating roll cells were believed to be present.

The two other off-diagonal components of the Reynolds-stress tensor should vanish identically in a perfectly unidirectional mean flow. Here, the shear stress components $\langle u'w' \rangle$ and $\langle v'w' \rangle$ are seen to be satisfactorily small.

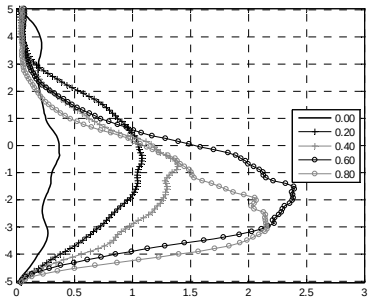

Figure 10: Normal stress ratio $\langle v'^2\rangle/\langle u'^2\rangle$ at Re = 5 600

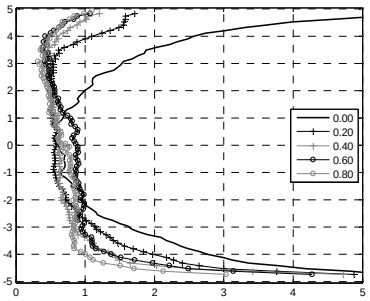

Figure 11: Mean spanwise vorticity fluctuations $\langle(\partial u/\partial y-\partial v/\partial x)'^2\rangle$ at Re = 5 600

The ratio between the wall-normal <v'v'> and streamwise <u'u'> Reynolds-stress components is shown in Figure 10. In a non-rotating channel flow this ratio is consistently smaller than unity simply because the production of turbulence contributes only to streamwise velocity fluctuations and the two other velocity components receive their energy through pressure-strain interactions. When the duct is subjected to rotation, additional stress generation mechanisms are involved which stem from interactions between the instantaneous flow field and the instantaneous Coriolis force. As we have already seen from the data in Figure 6, the most prominent effect of these extra rotational production terms is the enhancement of the wall-normal velocity fluctuations along the unstable pressure side and the corresponding reduction and even suppression of v' near the stabilized suction side. When the wall-normal stress component is compared with the streamwise stress component, this effect becomes particularly pronounced. With increasing rotation rates, <v'v'>/<u'u'> exhibits a fourfold increase from about 0.5 to above 2.0 on the pressure side of the duct, fully consistent with the increase reported by Andersson & Kristoffersen (1995). This reversal of the Reynolds stress anisotropy is one of the most striking features of rapidly rotating shear flows and has probably been observed experimentally for the first time herein. It is particularly noteworthy that this reversal of the conventional Reynolds stress anisotropy occurs already Ro = 0.2, both in the present experiments and in the earlier DNS study (Andersson & Kristoffersen 1995).

Many phenomena observed in rotating flows are more easily explained in terms of the vorticity of the flow rather than in view of the velocity field. The spanwise component of the vorticity can be deduced from the PIV data in the (x, y)-plane. In the present flow, the mean vorticity in the z-direction is essential dU/dy, i.e. the y-derivative of the streamwise mean velocity U(y) shown in Figure 6a, and the two other components of the mean vorticity vector are essentially zero. The vorticity fluctuations have been unattainable in the earlier experimental investigations of rotating channel flows (see Table 1). The PIV system used in the present study, however, provides field data rather than point measurements. The instantaneous vorticity fluctuations in the spanwise direction, i.e.

$$\omega_z' = \frac{\partial v'}{\partial x} - \frac{\partial u'}{\partial y} \tag{4}$$

can be deduced from the PIV data in a post-processing step; see the instantaneous contours in Figure 3. The two other components of the fluctuating vorticity vector are not

accessible from our data with the present orientation of the measurement area (see Fig. 2). Nevertheless, ω_z which is the component perpendicular to the plane of mean shear (dU/dy) and aligned with the axis of rotation, is the most relevant of the three vorticity components.

The variation of $\omega_{z,\,rms}$ across the channel is shown in Figure 11. For the non-rotating channel, the $\omega_{z,\,rms}$ profile is nearly symmetric about the mid-plane y = 0 with the highest vorticity levels at the walls and the lowest value in the channel center. The spanwise vorticity is substantially reduced near the suction side for rotation number Ro = 0.2 and even further reduced at the higher rotation rates. The spanwise vorticity is also reduced near the pressure side of the rotating channel, but not as much as the reduction observed at the suction side. In the core region, a roughly constant plateau is established with only a modest level of spanwise vorticity fluctuations. This plateau roughly coincides with the region of a linearly increasing mean velocity in Figure 6a, i.e. constancy of the mean vorticity dU/dy. These observations are in keeping with the DNS results obtained by Lamballais et al. (1996) and Liu & Lu (2007). From their numerically simulated flow fields, they also observed that the streamwise vorticity fluctuations dominated over the two other vorticity components along the pressure side of the duct when the flow was subjected to strong system rotation.

5 Concluding remarks

In the new set-up we were able to reach higher rotation numbers than those reported in earlier experimental studies of fully-developed duct flows. By means of stereoscopic PIV, all three velocity components were measured for the first time for a variety of different rotation numbers and at four different Reynolds numbers. Only results for the lowest Re = 5 600 have been included in the present paper. It is anticipated that the most pronounced effects of rotation are occurring at the lowest Reynolds number, as suggested by the alternative dimensionless parameter in eq. (3).

The present study is the first ever reporting field measurements of the instantaneous flow field. On the basis of the field data, the vorticity intensity in the spanwise direction could be deduced.

The data for the mean flow components showed that the flow was essentially unidirectional, albeit being somewhat affected by modest secondary circulations in the cross-sectional plane. The rotational-induced secondary flow field was beyond our control and most likely of varying importance for different rotation numbers. The almost vanishing off-diagonal components <u'w'> and <v'w'> of the Reynolds stress tensor supports the assumption that the flow field is almost fully developed in the test section, i.e. independent of the streamwise location. All data examined so far are consistent with earlier experimental findings and results from DNS.

The modular construction of the rectangular duct enables internal obstructions to be inserted. This attractive feature will enable investigations of massively separated flow fields downstream of the obstruction.

Acknowledgements

We appreciate the constructive discussions with Dr B.A. Pettersson Reif at The Norwegian Defence Research Establishment (FFI) in the planning stage of this project. The work described in this publication was supported by the European Community's Sixth Framework Programme through the grant to the budget of the Integrated Infrastructure Initiative HYDRALAB III, Contract no. 022441 (RII3) and by the Research Council of Norway through a research grant Contract no. 171725/V30 which includes a PhD research fellowship (M. Barri).

References

Andersson HI, Kristoffersen R (1995) Turbulence statistics of rotating channel flow. Turbulent Shear Flows 9. Selected Papers, Springer Verlag, Berlin, pp. 53-70

Johnston JP (1973) The suppression of shear layer turbulence in rotating systems. ASME J Fluids Eng 95:229-236

Johnston JP (1998) Effects of system rotation on turbulence structure: A review relevant to turbomachinery flows. Int J Rotating Machinery 4:97-112

Johnston JP, Halleen RM, Lezius DK (1972) Effects of spanwise rotation on the structure of two-dimensional fully developed turbulent channel flow. J Fluid Mech 56:533-557

Julien S, Dumas G, Torriano F, Maciel Y (2008) Secondary flow and roll cells interaction in high-aspect-ratio rotating turbulent duct flows. Int J Comp Fluid Dynamics 22:19-28

Kristoffersen R, Andersson HI (1993) Direct simulations of low-Reynolds-number turbulent flow in a rotating channel. J Fluid Mech 256:163-197

Lamballais E, Lesieur, M, Métais, O (1996) Effects of spanwise rotation on the vorticity stretching in transitional and turbulent channel flow. Int J Heat Fluid Flow 17:324-332

Liu N-S, Lu X-Y (2007) A numerical investigation of turbulent flows in a spanwise rotating channel. Comput Fluids 36:282-298

Maciel Y, Picard D, Yan G, Dumas G, Gleyzes C (2003) Fully developed turbulent channel flow subject to system rotation. 33rd AIAA Fluid Dynamics Conference, Paper AIAA-2003-4153

Moore J (1967) Effects of Coriolis on turbulent flow in rotating rectangular channels. MIT Gas Turbine Lab. Rep. 89.

Moore JG, Moore J (2006) Functional Reynolds Stress Modeling. Pocahontas Press, Blacksburg, Virginia

Murata A, Mochizuki S (1999) Effect of cross-sectional aspect ratio on turbulent heat transfer in an orthogonally rotating rectangular smooth duct. Int J Heat Mass Transfer 42:3803-3814

Nakabayashi K, Kitoh O (1996) Low Reynolds number fully developed two-dimensional turbulent channel flow with system rotation. J Fluid Mech 315:1-29

Nakabayashi K, Kitoh O (2005) Turbulence characteristics of two-dimensional channel flow with system rotation. J Fluid Mech 528:355-377

Watmuff JH, Witt HT, Joubert PN (1985) Developing turbulent boundary layers with system rotation. J Fluid Mech 157:405-448.

Part 2.2

Turbulent inflow boundary conditions

Paper 5

Inflow conditions for inhomogeneous turbulent flows

Barri, M., El Khoury, G. K., Andersson, H. I. & Pettersen, B.

International Journal for Numerical Methods in Fluids, **60***, 227–235, 2009.*

Is not included due to copyright

Paper 6

DNS of backward-facing step flow with fully turbulent inflow

Barri, M., El Khoury, G. K., Andersson, H. I. & Pettersen, B.

Accepted for publication in *International Journal for Numerical Methods in Fluids, DOI: 10.1002/fld.2176*

The present manuscript is an extended version of the paper titled as **Massive separation in one-sided expansion channel**. The paper was printed in the proceedings of *5th National Conference on Computational Mechanics*, Trondheim, Norway, pp. 89–102, 2009.

Is not included due to copyright

Paper 7

Massive separation of turbulent Couette flow in one-sided expansion channel

El Khoury, G. K., Barri, M., Andersson, H. I. & Pettersen, B.

International Journal of Heat and Fluid Flow.

Submitted for inclusion in a special issue of selected papers from *6th International Symposium on Turbulence and Shear Flow Phenomena,* Seoul, Korea, June 22–24, 2009. This manuscript is a substantially extend version of the paper with the same title that was printed in the conference proceedings (pp. 1217–1221).

Massive separation of turbulent Couette flow in a one-sided expansion channel

George K. El Khoury[*,a,1], Mustafa Barri[b], Helge I. Andersson[b], Bjørnar Pettersen[a]

[a] *Department of Marine Technology, The Norwegian University of Science and Technology, Trondheim, NO-7491, Norway*
[b] *Department of Energy and Process Engineering, The Norwegian University of Science and Technology, Trondheim, NO-7491, Norway*

Abstract

Direct numerical simulation has been performed to study wall-driven flow over a backward-facing step at Reynolds number $Re = 5200$ based on the step height h and the upper-wall velocity U_w. The flow configuration consisted of a step with height equal to that of the upstream channel yielding an expansion ratio 2: 1. Instantaneous enstrophy contours revealed the formation of Kelvin-Helmholtz instabilities downstream of the step. Intense velocity and vorticity fluctuations were generated in the shear-layer formed between the bulk flow and the massive recirculation zone in the lee of the step. Extraordinarily high turbulence levels persisted in the center region even $7.5h$ downstream of the step, i.e. where the separated shear-layer reattached to the wall. A fully redeveloped Couette flow cannot be reached in the downstream part of the channel due to mass conservation. The local wall pressure coefficient gave evidence of an adverse pressure gradient in the recovery region where a Couette-Poiseuille flow type prevailed.

Key words: Couette flow, Separation, DNS, Backward-facing step

[*]Corresponding author
Email address: george@ntnu.no (George K. El Khoury)
[1]Present address: Department of Marine Technology, The Norwegian University of Science and Technology, NO-7491, Trondheim, Norway. Tel: +47 735 96114.

1. Introduction

Turbulent flow over a backward-facing step (BFS) is a simplified case of the general family of separated flows with widespread industrial applications. Although its geometry is simple, the flow physics is still complex. Typical prototypes of BFS flows are the boundary layer, the plane channel and the Couette flow cases, see e.g. Eaton & Johnston (1981). A common feature of these flows is the existence of a shear-layer emanating from the step corner and reattaching further downstream leading to the formation of a recirculation bubble. The presence of the internal shear-layer and the massive recirculation zone gives rise to complex flow dynamics which for instance affect the turbulence production and Reynolds stress anisotropy.

The understanding of the flow over a backward-facing step was initially acquired by experiments and two-dimensional numerical simulations. The early studies were performed by Abbot & Kline (1962) and Goldstein *et al.* (1970). This type of flow is characterized by the channel expansion ratio ER and the upstream Reynolds number. Armaly *et al.* (1983) conducted experiments on air flow over a backward-facing step with an expansion ratio of $2:1$ and provided information on the relationship between the Reynolds number and the reattachment length X_R. The authors covered a wide range of Reynolds numbers from about 50 to 6000 and found that X_R tends to increase with the increase of Re in the laminar flow regime and decrease in the transitional one while X_R remains relatively constant in the fully-developed turbulent state. The findings of Kuehn (1980), Durst & Tropea (1981), Ötügen (1991), and Ra & Chang (1990), on the other hand, showed that the reattachment length increases with the expansion ratio ER.

Owing to the rapid developments in high-performance computing, three-dimensional numerical simulations of turbulent flow over a backward-facing step have been performed since the late $1980's$. Friedrich & Arnal (1990) studied high Reynolds number turbulent backward-facing step flow using the large-eddy simulation (LES) technique. This technique was also used by Neto *et al.* (1993) who performed numerical investigation of the coherent vortices in turbulence behind a backward-facing step. Later, Le *et al.* (1997) provided an extensive DNS study of turbulent boundary layer flow over a backward-facing step with an expansion ratio of $6{:}\,5$ and reported a reattachment length equal to 6 step heights. Since the BFS problem is not homogeneous in the streamwise direction, proper inflow conditions are to be employed in order to provide a realistic fully turbulent flow at the input. Several methods

of different complexity have been used by researchers in the past years to generate suitable inflow conditions. In the boundary layer backward-facing step flow, Le *et al.* (1997) imposed a mean velocity profile for a flat plate turbulent boundary at the input (Spalart (1988)) whereas Meri & Wengle (2002) utilized a time-dependent inflow condition from a precursor Poiseuille flow simulation to perform DNS and LES of pressure-driven backward-facing step flow. A recent DNS study on the same flow problem was performed by Barri *et al.* (2009b) where the authors used a cost-effective method to generate the inflow conditions. This technique was proposed by the same authors in an earlier study on numerical simulation of plane channel flow (see Barri *et al.* (2009a)) and consists of recycling finite-length time series (ts) of instantaneous velocity planes at the input. These profiles were taken from a precursor simulation and a physical constraint was introduced on ts to be of order of the large-eddy-turnover-time. The authors kept the inflow time series discontinuous and showed that this discontinuity in the inflow signal vanishes due to the nonlinear interactions of the turbulent flow.

Due to the principle of mass conservation, the Reynolds number in pressure-driven plane channel flow with a sudden one-sided expansion remains the same downstream of the step as in the upstream part of the channel. In a BFS Couette flow, on the other hand, the Reynolds number becomes higher downstream of the step. It is well known that the shear-driven turbulent Couette flows (see e.g. Bech *et al.* (1995)) exhibit a number of characteristic features which make them distinguishingly different from the pressure-driven Poiseuille flow, notably the monotonically increasing mean velocity profile. The only investigation of BFS Couette flow we are aware of is the recent experimental study by Morinishi (2007). He considered a configuration with the step height h equal to half of the upstream channel height, i.e. with an expansion ratio 3:2. The Reynolds number based on the wall-friction velocity at the input was fixed to 300. This configuration (i.e. fixed ER and $Re_{\tau i}$) allowed the author to investigate the effect of the non-dimensional pressure gradient β_o. By varying β_o, Morinishi (2007) set up conditions for the following fully-developed upstream flows: the pure Poiseuille flow, the mixed Couette-Poiseuille flow and the pure Couette flow. For the three cases, the reattachment lengths were almost identical and approximately $6.5h$ and $2h$ for the primary and secondary recirculation regions, respectively.

In the present study we perform direct numerical simulation (DNS) of turbulent Couette flow over a BFS. This will enable us to gather accurate mean flow and turbulence statistics throughout the flow domain, as well as to

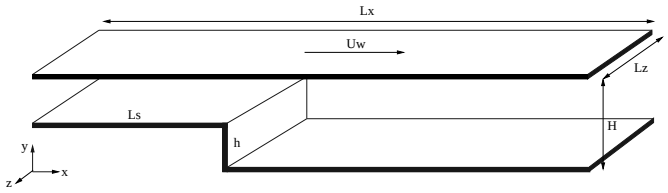

Figure 1: Flow configuration and coordinate system (not to scale).

explore in detail the instantaneous vortex topology in the shear-layer and the recirculation bubble as well as in the re-development zone. We intentionally considered a BFS configuration where the flow upstream of the step is the same as that studied by Bech *et al.* (1995).

2. Flow configuration and governing equations

Figure 1 shows a schematic view of the Couette backward-facing step flow which is composed of a step of height h and an upper-wall moving with velocity U_w. Of particular relevance in backward-facing step flows is the expansion ratio ER. This dimensionless parameter is defined as the ratio between the downstream and upstream channel heights, i.e. $ER = H/(H-h)$. In the present study we consider a flow configuration where the step height is equal to that of the upstream channel, i.e. $H = 2h$. This gives an expansion ratio of $2:1$.

The governing equations are the time-dependent, incompressible Navier-Stokes equations for a viscous fluid expressed in non-dimensional form:

$$\nabla \cdot \mathbf{u} = 0, \tag{1}$$

$$\frac{\partial \mathbf{u}}{\partial t} + (\mathbf{u} \cdot \nabla)\mathbf{u} = -\nabla p + \frac{1}{Re}\nabla^2 \mathbf{u}. \tag{2}$$

Here, the variables have been non-dimensionalized by h and U_w and the Reynolds number based on the step height and upper-wall velocity, $Re = U_w h/\nu$, is 5200.

3. Numerical approach

The computational domain has a length of $L_x = 39h$ in the streamwise $x-$direction including an inlet section $L_s = 15h$, $H = 2h$ in the wall-

	L_s^*	L_z^*	Δx^+	Δy^+	Δz^+
Bech	5π	2π	10.1	$(0.7, 3.9)$	4
Inlet	4.8π	3π	$(4.8, 14.8)$	$(0.083, 2.4)$	8.2

Table 1: Computational parameters at the inlet section with the corresponding reference case Bech *et al.* (1995). (The symbol $*$ denotes a division by the channel height in the inlet section $(H - h)$)

normal $y-$direction, and $L_z = 9.43h$ in the spanwise $z-$direction. A total of $(672 \times 384 \times 192)$ grid points are used in x, y and z, respectively. In order to adequately resolve the turbulence scales in the separation region and the vicinity of the walls, a non-uniform mesh distribution is used in the streamwise and wall-normal directions. Thus for a viscous length scale of $l_i = \nu/u_{\tau i}$, based on the wall-friction velocity at the input $u_{\tau i} = 0.032U_w$, the first grid point next to the walls is at $y^+ \approx 0.083$ while the largest grid spacing is about $\Delta y^+ \approx 2.4$ (measured in wall units). For the streamwise direction, the minimum grid spacing $\Delta x^+ \approx 4.8$ is at the step corner and maximum at the beginning and the end of the domain with $\Delta x^+ \approx 14.8$. A uniform mesh is used in the spanwise z-direction with $\Delta z^+ \approx 8.2$. The grid specification in the inlet section is given in table 1 together with that of Bech *et al.* (1995).

No-slip boundary conditions are imposed on the solid surfaces in the domain. The flow in the spanwise direction is assumed to be statistically homogeneous and periodic boundary conditions are imposed. A realistic fully turbulent flow is generated at the input by recycling finite-length time series of the instantaneous velocity planes. This technique was first used by Barri *et al.* (2009a) in a numerical simulation of plane channel flow. For the outflow condition, we solve the convective equation $\partial \mathbf{u}/\partial \mathbf{t} + U_c \partial \mathbf{u}/\partial x = 0$ at the exit plane. This type of boundary condition was used in previous numerical simulations by Lowery & Reynolds (1986) for a mixing-layer and Le *et al.* (1997) for turbulent flow over a backward-facing step and is considered suitable for vortical structures moving out of the domain.

The DNS code used to numerically solve the governing equations 1 and 2 is MGLET (see Manhart (2004)). MGLET is a finite-volume code in which the Navier-Stokes equations are discretized on a staggered Cartesian mesh with non-equidistant grid-spacing. The discretization is second-order accurate in space. A second-order explicit Adams-Bashforth scheme is used for the time integration. The Poisson equation for the pressure is solved using a multi-grid

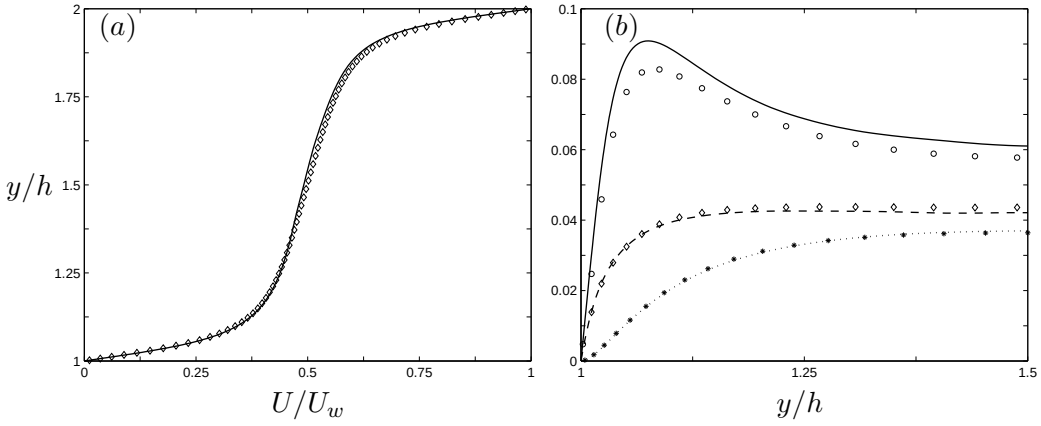

Figure 2: (a) Mean velocity profile at $x/h = 7$. (b) Turbulent intensities at $x/h = 7$: ———, streamwise direction; · · · · · · ·, wall-normal direction; – – – –, spanwise direction. The symbols denote data from Bech *et al.* (1995).

algorithm.

The simulations were started from an arbitrary flow field and thereafter let to evolve to a statistically steady state. The time step used was $\Delta t = 0.001h/U_w$. Statistics were gathered for $396h/U_w$ after the flow field first had evolved into a statistically steady state.

Direct numerical simulation of plane Couette flow has been performed in several studies. Before the statistical results of the simulation in the downstream part of the channel are presented, it is interesting to compare some primary statistics obtained in the inlet section with the fully-developed Couette flow data from Bech *et al.* (1995) for the same Reynolds number. This is to ensure that the finite-length time series of velocities recycled at the input provided realistic fully-developed turbulence in the upstream section.

In figure 2a, the mean velocity profile is plotted at $x/h = 7$ and is nearly indistinguishable from that of Bech *et al.* (1995). The computed turbulent intensities (the root-mean-square of the velocity fluctuations) are shown in figure 2b. The agreement between the two simulations is very good for the wall-normal and streamwise components while the streamwise component exhibits a higher turbulence level.

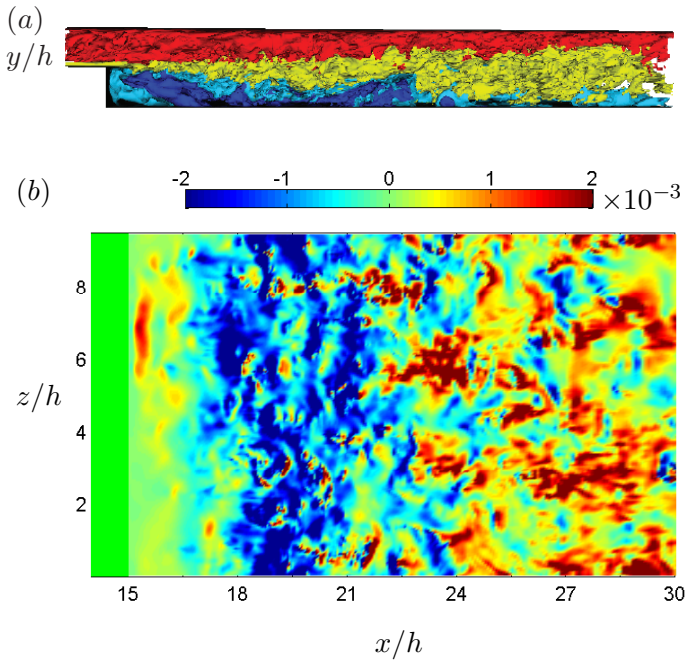

Figure 3: Instantaneous streamwise velocity. (a) Contour levels: red 0.5, yellow 0.2, light blue 0.01, dark blue -0.03; (b) top view at $y^+ = 0.083$.

4. Flow Structures

In this section, we focus on the instantaneous features of turbulent Couette flow over a backward-facing step. The various plots of the velocity and vorticity fields presented in this section have been non-dimensionalized by U_w and U_w/h, respectively.

4.1. Velocity

A snapshot of the flow field is shown in figure 3 where a three-dimensional side view of the iso-surfaces of the streamwise velocity is plotted in figure 3a, and a plane parallel to the bottom wall at $y^+ \approx 0.083$ is shown in figure 3b. An overall picture of the separation scenario can be deduced from the figure. Starting from the inlet, the incoming flow separates at the sharp step edge and reattaches further downstream leading to the formation of a primary recirculation region. Patches of positive fluid velocity ($u \approx 0.01$) are observed in the region with backward motion ($u < 0$) and adjacent to

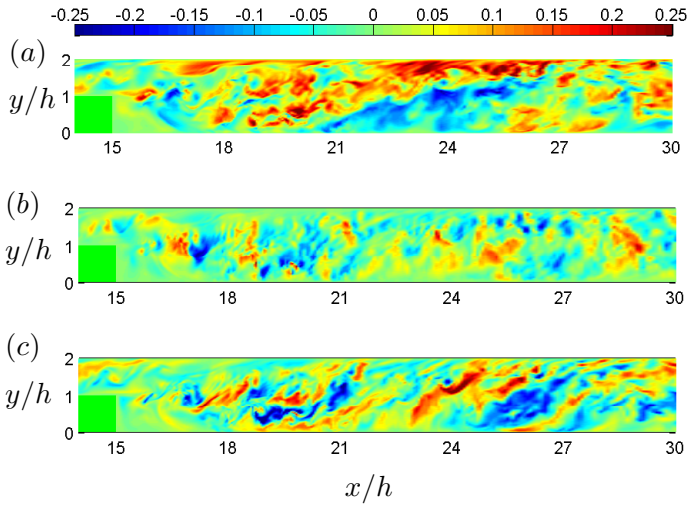

Figure 4: Instantaneous velocity fluctuations in an (x, y)-plane at $z = L_z/2$. (a) Streamwise component; (b) wall-normal component; (c) spanwise component.

the step thereby identifying a secondary recirculation region. The interface between the two streams with different velocities leads to a complex three-dimensional flow structure. Figure 3b provides a qualitative impression on the three-dimensional flow pattern close to the lower-wall. Around $x/h \approx 22$, it is readily observed that the reattachment location is not confined to a fixed streamwise position but rather consists of irregular bursts of fluid formed by the shear-layer at the moment it strikes the bottom plane. Downstream the reattachment, the flow sustains its irregular pattern as it is convected towards the recovery region. Meanwhile, the primary recirculation region shows large structures that are aligned in the spanwise direction with spots of positive fluid velocity observed in-between. These spots are forced to decay quickly due to the surrounding pressure gradients.

A cross-sectional view of the individual velocity fluctuations is shown in figure 4. These quantities are defined as the difference between the instantaneous velocity field $\widetilde{u}_i(x, y, z, t)$ and its time-spanwise average $U_i(x, y)$. The results show that fluctuations reach around 20% of the wall velocity U_w in the shear-layer and the primary recirculation zone indicating strong spanwise motions in these regions. The alternating positive-negative pattern observed

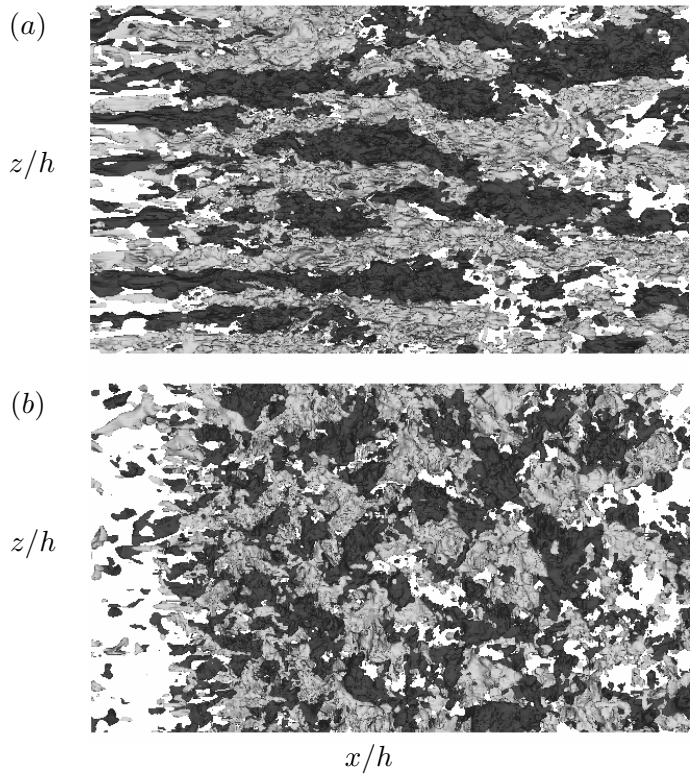

Figure 5: Top view of iso-surfaces of positive (light gray) and negative (dark gray) velocity fluctuations, $x/h \in [15, 30]$, $y/h \in [0, 1.5]$ and z/h covers the whole spanwise length. (a) Streamwise component; (b) spanwise component.

for v downstream of the step indicates the presence of spanwise vortices. In figure 4c, the pseudocolors of w show large elongated structures that are inclined in the streamwise direction and persist towards the recovery region almost filling the entire wall gap.

In figure 5, we display a top view of iso-surfaces of positive and negative streamwise and spanwise fluctuations. Note that the iso-surfaces of w correspond to the instantaneous spanwise velocity since there is no mean flow in the $z-$direction. The flow clearly features streaks above the step in figure 5a. These streaky structures grow in width downstream of the step and remain discernible even $15h$ downstream of the corner. In the same region, the iso-surfaces of w show lumps of positive and negative values.

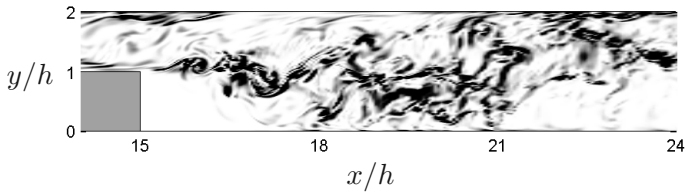

Figure 6: Instantaneous enstrophy contours in an (x, y)-plane at $z = L_z/2$.

4.2. Vorticity

Transverse vortices are a commonly observed feature in backward-facing step flows where the underlying mechanism in the formation of such vortical structures downstream of the step is a Kelvin-Helmholtz instability. These instabilities arise from the interaction between the shear-layer and the recirculating region near the step. This interface between the high- and low-speed fluid region, being unstable, leads to such a vortex formation. In order to see whether or not K-H vortices are embedded in the present flow field, the instantaneous iso-surfaces of enstrophy are plotted in an $(x, y)-$plane in figure 6. There is an apparent roll-up of the shear layer behind the step edge where the unsteady K-H vortices are generated and break up into numerous small high-intensity vortices as they are transported downstream.

All turbulent flows exhibit high levels of vorticity fluctuations. The instantaneous vorticity $\widetilde{\omega_i}$ is decomposed into a mean vorticity Ω_i and vorticity fluctuations ω_i: $\widetilde{\omega_i} = \Omega_i + \omega_i$, $\overline{\omega_i} = 0$. The present mean flow is statistically two-dimensional and entirely in the (x, y)-plane. Then Ω_x and Ω_y are zero, so that the only non-zero mean vorticity component is Ω_z. Pseudocolors of vorticity fluctuations are shown in figure 7. In contrast with the rather different patterns of the streamwise, wall-normal and spanwise velocity components in figure 4, the topology of the three components of the fluctuating vorticity vector in figure 7 is rather similar. Since the fluctuating vorticity field is associated with small-scale eddies, the vorticity field is only modestly affected by the anisotropic geometric constraints which enforce a substantial anisotropy on the velocity fluctuations.

A cross-stream view of the vortical structures from $x/h = 15$ is shown in figure 8a. These structures are extracted by using the $-\lambda_2$ definition proposed by Jeong & Hussain (1995) in which a vortex core is identified as a connected region of negative λ_2. Here, λ_2 corresponds to the second largest

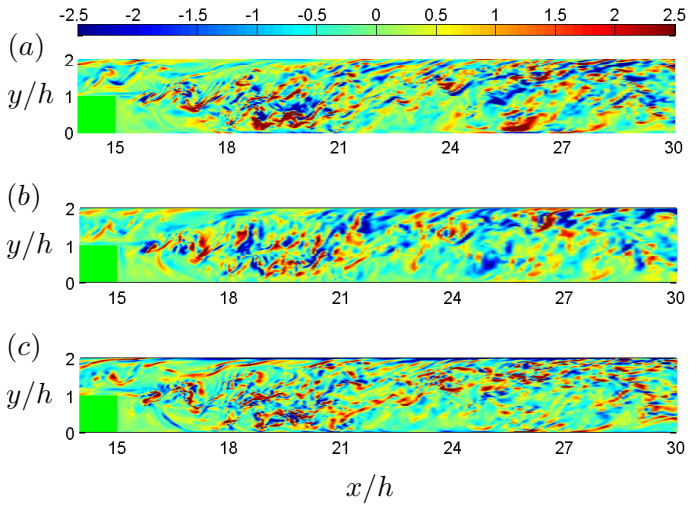

Figure 7: Instantaneous vorticity fluctuations in an (x, y)-plane at $z = L_z/2$. (a) Streamwise component; (b) wall-normal component; (c) spanwise component.

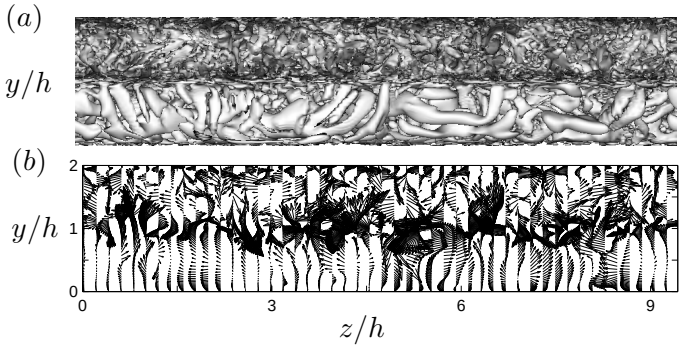

Figure 8: (a) Cross-stream view of $-\lambda_2$ structures taken from $x/h = 15$. (b) Cross-stream plane at $x/h = 16$. The velocity vectors represent spanwise and wall-normal velocities.

eigen value of the tensor $S_{ij}S_{ij} + \Omega_{ij}\Omega_{ij}$ where S_{ij} and Ω_{ij} represent the symmetric and antisymmetric parts of the velocity gradient tensor, respectively. In the secondary recirculation region large elongated structures are observed in contrast to the upper part of the channel that is filled with numerous small

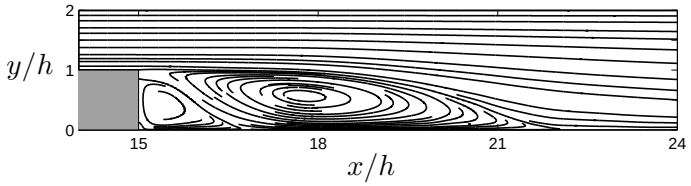

Figure 9: Streamlines of the mean flow.

high-intensity vortices. To obtain a more detailed view on the flow in this region, the instantaneous flow in a vertical plane is shown in figure 8b at a distance h from the step. The highest turbulent activity is in the shear-layer which is composed of streamwise vortices, whereas in the secondary recirculation region the flow shows strong spanwise motions.

5. Mean flow and turbulence statistics

5.1. Mean statistics

From pressure-driven BFS flows it is known that the unsteady behaviour of the shear-layer causes the reattachment line to fluctuate around a mean value X_R, see e.g. Friedrich & Arnal (1990). The streamline pattern of the mean flow in figure 9 shows a large primary separation bubble which extends about $7.5h$ downstream of the step. A secondary bubble of length $1.78h$ can be observed adjacent to the corner. The skin friction coefficient, defined as $C_f = \tau_w/\frac{1}{2}\rho u_{\tau i}^2$, is shown in figure 10 and confirms that a secondary separation bubble with anti-clockwise flow ($C_f > 0$) is embedded within the primary separation bubble with clockwise motion ($C_f < 0$). This flow pattern is consistent with the findings of Morinishi (2007) who reported that reattachment occurred at $X_R = 6.63h \pm 1.4h$ and the secondary bubble was at $1.88h \pm 0.4h$. Downstream of $x/h = 30$, C_f is almost constant along both walls with the wall-friction along the moving surface being about 10 times higher than at the lower surface. This suggests a substantial asymmetry of the mean velocity field.

The local wall pressure coefficient is defined as

$$C_p = \frac{P - P_o}{\frac{1}{2}\rho u_{\tau i}^2} \tag{3}$$

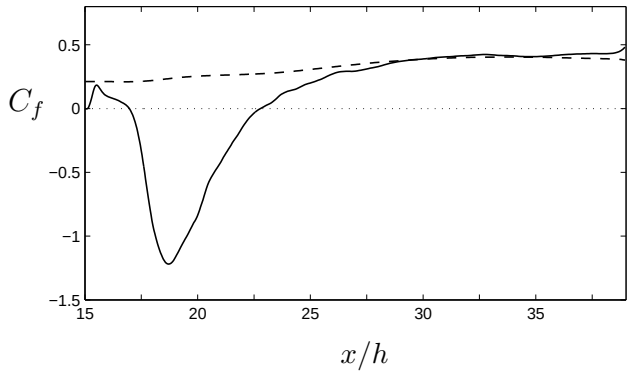

Figure 10: Skin friction coefficient variation downstream the step: ———, lower-wall; – – – –, upper-wall (divided by a factor of 10).

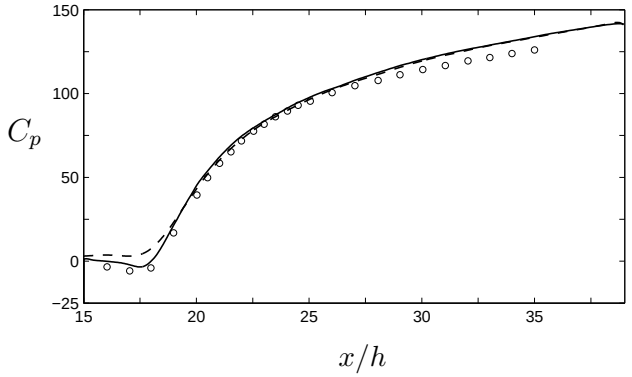

Figure 11: Pressure coefficient variation downstream the step: ———, lower-wall; – – – –, upper-wall. The symbols denote lower-wall data from Morinishi (2007), case $C300$.

where P_o is a reference pressure taken at $x/h = 0$. In figure 11, C_p is shown together with the corresponding values from Morinishi (2007) for Couette flow over a backward-facing step. The agreement between the computational and experimental results is very good. The local wall pressure coefficient exhibits a local minimum close to the position of maximum backflow (i.e. beneath the core of the primary separation bubble). Downstream of $x/h = 30$, an almost linear variation of C_p is observed for the two cases. This implies that the streamwise mean pressure gradient has become independent of x,

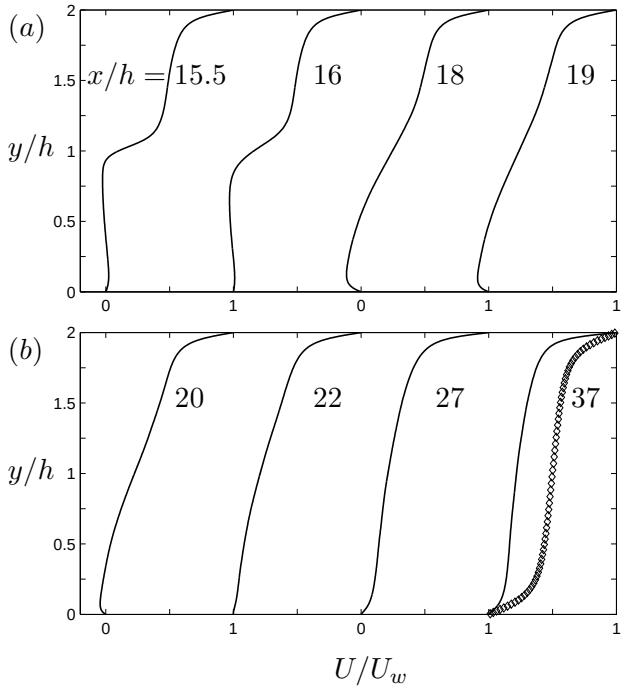

Figure 12: Mean streamwise velocity profiles. (a) Recirculation region; (b) recirculation, reattachment and recovery regions.

in keeping with the measurements of Morinishi (2007), and the flow field can be considered as being nearly fully-developed in the downstream part of the computational domain. This is also consistent with the constancy of C_f observed in figure 10.

The mean velocity profiles are presented in figures 12 and 13 for the streamwise and wall-normal components at different representative locations: inside the secondary bubble, through the primary recirculation, downstream of the reattachment and in the recovery region. In the recirculation region the strongest backflow is observed beneath the core of the primary bubble, whereas the secondary separation region shows a weak mean-streamwise motion. Although the characteristic S-shape of the mean velocity profile $U(x, y)$ has been retained at $x/h = 27$, the profile is yet far from being anti-symmetric. Midway between the walls U is still roughly half of $U_w/2$ which should be reached in the case a fully redeveloped Couette flow. However,

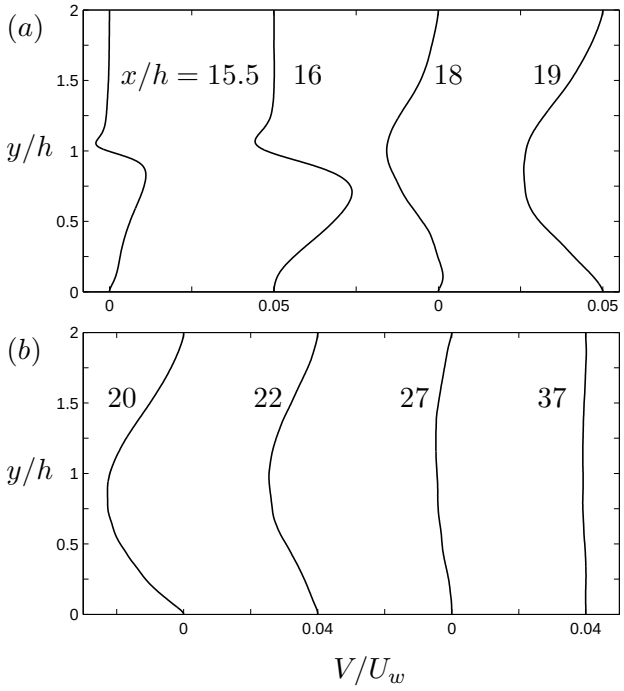

Figure 13: Mean wall-normal velocity profiles. (a) Recirculation region; (b) recirculation, reattachment and recovery regions.

irrespective of the length of the domain that can be used in the downstream part of the channel, an anti-symmetric profile corresponding to a fully redeveloped Couette flow will not be reached. This is due to the principle of mass conservation. It follows that since the height of the domain after the step is twice that of the inlet section and the mean velocity profile of Couette flow is monotonically increasing to a constant value of U_w, the flow cannot adjust itself to an anti-symmetric S-profile shape and at the same time maintain a constant flow rate.

An examination of the mean wall-normal velocity profiles presented in figure 13 show that the flow emanating from the step corner exhibits an upward motion in the lower half of the channel and a downward flow above $y/h \approx 1$. This pattern is sustained up till $x/h \approx 18$, where afterwards a relatively high downward motion is solely observed in the remaining part of the recirculation zone. Downstream of the reattachment region, the mean

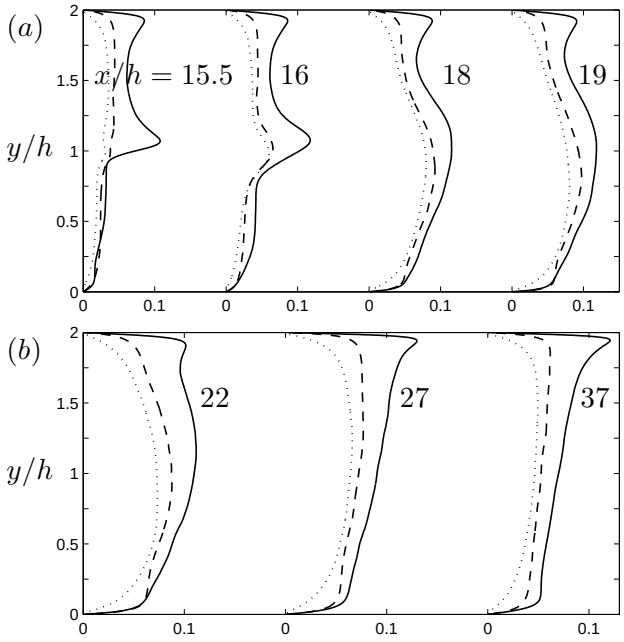

Figure 14: Turbulent intensities scaled with the maximum mean velocity at the input: ———, streamwise direction; · · · · · · ·, wall-normal direction; – – – –, spanwise direction. (a) Recirculation region; (b) reattachment and recovery regions.

wall-normal velocity is attenuated.

5.2. Turbulence intensities and Reynolds shear stress

The turbulence intensities and the Reynolds shear stress are shown in figures 14 and 15 at different streamwise locations downstream the step. The $r.m.s$ values and $-\overline{uv}$ exhibit a high turbulence level immediately downstream of the corner of the step at $y/h \approx 1$. This localized high-turbulence zone, mainly for u_{rms}, is obviously caused by the locally high mean-shear-rate in the shear-layer emanating from the step edge. As the flow progresses downstream, the streamwise turbulence intensity peaks are broaden and attenuated while the turbulence levels of the spanwise and wall-normal components increase. Downstream the reattachment and in the recovery region, the asymmetry in u_{rms} persists where a substantially higher longitudinal turbulence intensity is observed near the moving wall that is almost twice that seen near the stationary wall. Apart from the secondary recirculation region

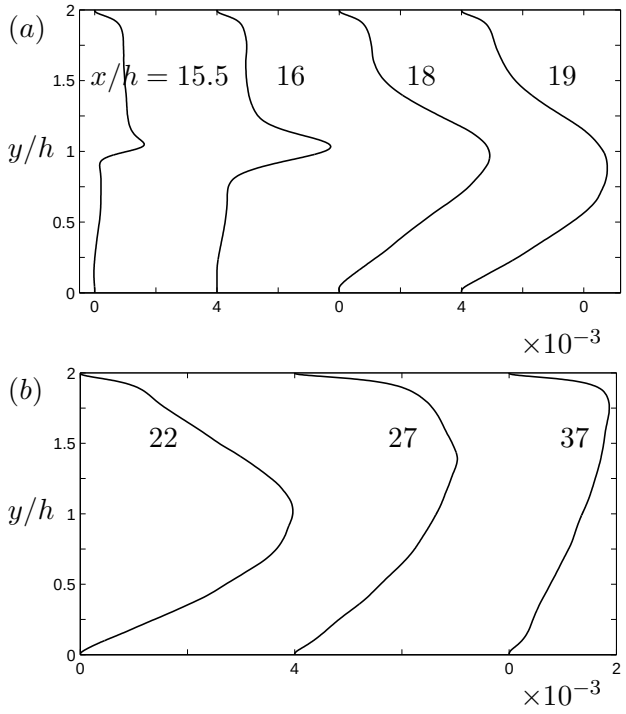

Figure 15: Reynolds shear stress $-\overline{uv}/U_w^2$. (a) Recirculation region; (b) reattachment and recovery regions.

where $w_{rms} > u_{rms} > v_{rms}$, the turbulence exhibits everywhere the usual shear-flow anisotropy with the streamwise intensity being the most significant. The flow anisotropy was not accessible with the I-type hot-wire used in Morinishi's (2007) measurements since only u_{rms} could be obtained.

The profiles of $-\overline{uv}$ show that the Reynolds shear stress is positive almost throughout the whole domain. The distinct positive peak of $-\overline{uv}$ is typical of a turbulent mixing-layer. The peak broadens with downstream distance but remains discernible above the reattachment point at about $7h$ downstream of the step. Further downstream, the $-\overline{uv}$-profile fails to attain the symmetric shape which characterizes a pure Couette flow; see e.g. Bech & Andersson (1996). The profile at $x/h = 37$, i.e. 22 step heights downstream of the step, shows that the Reynolds shear stress is substantially higher near the moving wall than along the fixed wall.

5.3. Reynolds stress budget

In this section, the Reynolds stress budget is presented at a distance h from the step and in a wall-normal region confined within the shear-layer (i.e. $0.5 < y/h < 1.5$). The transport equation for the Reynolds stress tensor is:

$$\frac{D}{Dt}(\overline{u_i u_j}) = P_{ij} - \epsilon_{ij} + \Pi_{ij} + G_{ij} + D_{ij} + T_{ij} \tag{4}$$

Where the production, dissipation, pressure-strain, pressure diffusion, molecular diffusion and turbulent diffusion are defined as:

$$P_{ij} = -\overline{u_i u_k}\frac{\partial U_j}{\partial x_k} - \overline{u_j u_k}\frac{\partial U_i}{\partial x_k} \tag{5a}$$

$$\epsilon_{ij} = 2\nu\overline{\frac{\partial u_i}{\partial x_k}\frac{\partial u_j}{\partial x_k}} \tag{5b}$$

$$\Pi_{ij} = \frac{1}{\rho}\left(\overline{p\frac{\partial u_i}{\partial x_j} + p\frac{\partial u_j}{\partial x_i}}\right) \tag{5c}$$

$$G_{ij} = -\frac{1}{\rho}\left(\frac{\partial}{\partial x_i}\overline{pu_j} + \frac{\partial}{\partial x_j}\overline{pu_i}\right) \tag{5d}$$

$$D_{ij} = \nu\frac{\partial^2}{\partial x_k^2}\overline{u_i u_j} \tag{5e}$$

$$T_{ij} = -\frac{\partial}{\partial x_k}\overline{u_i u_j u_k} \tag{5f}$$

The budget for $\overline{uu}$ in figure 16a is largely dominated by production and pressure-strain where a large peak of positive production is observed close to the position of maximum u_{rms} (i.e. $y/h \approx 1$). Meanwhile, the profiles of the molecular diffusion in figure 16 show that the contribution of D_{ij} is negligible everywhere and thereby turbulent and pressure diffusion play the role of transporting energy across the shear-layer. For the normal stresses, T_{ij} carries energy away from the position of maximum production.

Since there is only modest production of $\overline{v^2}$ as can be inferred from figures 16b, the primary source of energy is from Π_{ij} which serves to redistribute energy between the normal stresses. Across the shear-layer, $\overline{vv}$ and $\overline{ww}$ act as receiving components taking energy from $\overline{uu}$. Moreover, the maximum

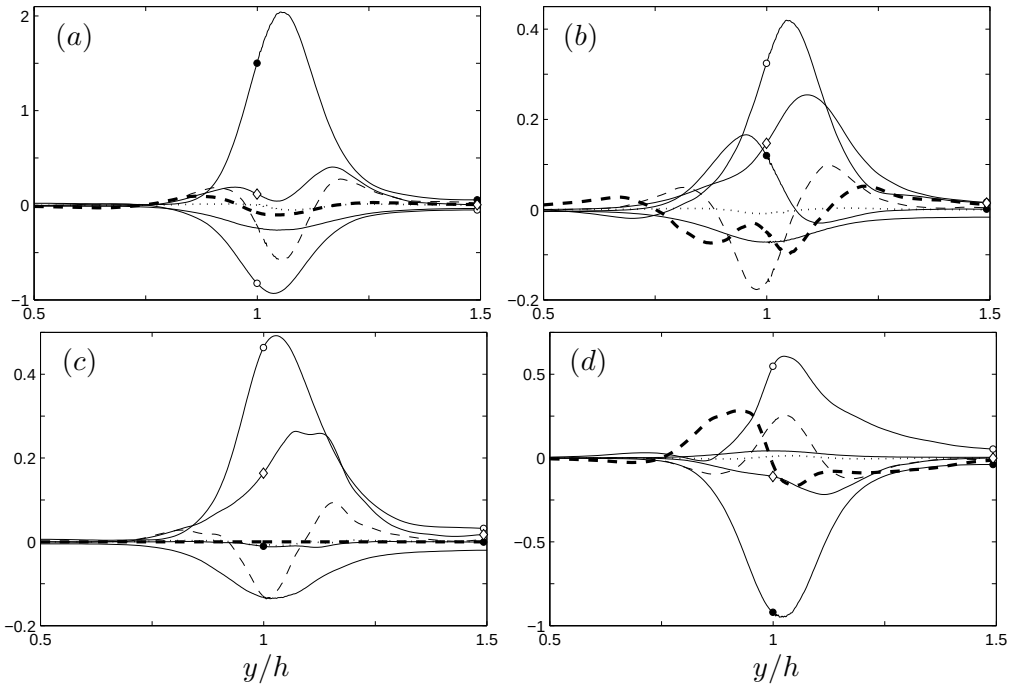

Figure 16: Reynolds stress budget normalized by $u_{\tau i}^4/\nu$ at $x/h = 16$. —●—, P_{ij}; ———, $-\epsilon_{ij}$; —○— , Π_{ij}; --------, G_{ij}; · · · · · · · , D_{ij}; – – – –, T_{ij}; —◇—, $U_k\partial(\overline{u_i u_j})/\partial x_k$. (a) $\overline{uu}$; (b) $\overline{vv}$; (c) $\overline{ww}$; (d) $\overline{uv}$.

rate of energy transfer is reported at the peak production for the streamwise normal stress.

As in the budget of $\overline{uu}$, the equation for $\overline{uv}$ is largely dominated by production and pressure-strain where a large peak of negative production is observed around $y/h = 1$. The expression for this production term is

$$P_{12} = -\overline{uv}\frac{\partial U}{\partial x} - \overline{vv}\frac{\partial U}{\partial y} - \overline{uu}\frac{\partial V}{\partial x} - \overline{uv}\frac{\partial V}{\partial y} \tag{6}$$

Since the mean flow is statistically two-dimensional, the first and fourth terms of equation 6 add up to zero due to mass conservation. This implies that the change of sign of P_{12} depends solely on the gradients of the mean streamwise and wall-normal velocities. $\partial U/\partial y$ being dominant over all the other mean gradient terms in this region, then equation 6 reduces to $P_{12} \approx -\overline{vv}\partial U/\partial y$. The production of the Reynolds shear stress is thus governed by

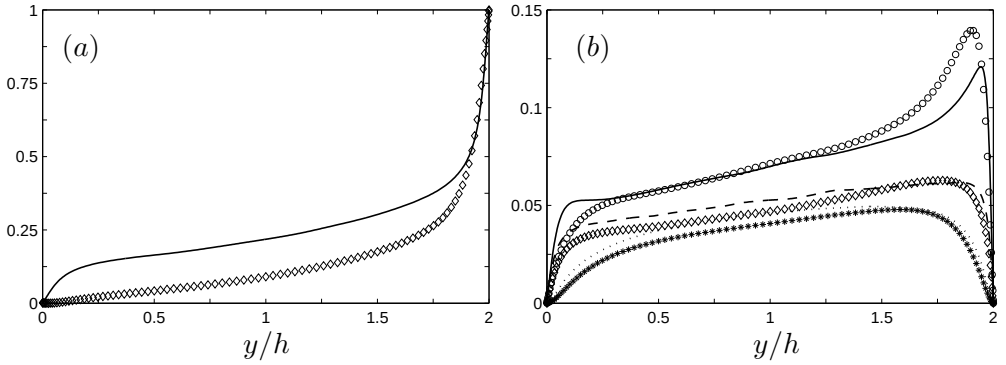

Figure 17: (a) Mean velocity profile U/U_w at $x/h = 37$. (b) Turbulent intensities at $x/h = 37$: ———, ∘, streamwise direction; · · · · · · ·, ∗, wall-normal direction; – – – –, ⋄, spanwise direction. The symbols denote DNS data from Kuroda *et al.* (1995).

$\partial U/\partial y$ and thereby the change of sign of P_{12} occurs when $\partial U/\partial y$ is equal to zero, and peak production is attained where $\partial U/\partial y$ exhibits a local maximum in the shear-layer.

The turbulent diffusion contributes to the increase of $\overline{uv}$ in the central region whereas pressure diffusion transports $\overline{uv}$ downwards from the upper part of the shear-layer. Meanwhile, viscous dissipation is negligible almost everywhere in this case. The nearly negligible viscous dissipation is consistent with the observation made by Bech & Andersson (1996) in a fully-developed Couette flow. This is because ϵ_{12} consists of relatively weakly correlated velocity gradients. Although the convection term $U_k\partial(\overline{u_iu_j})/\partial x_k$ is almost negligible for the terms dominated by production (i.e. $\overline{uu}$ and $\overline{uv}$), it shows significant positive values in the shear-layer for the wall-normal and spanwise components.

5.4. Recovery region

The two-dimensional mean flow has developed to an essentially unidirectional flow in the downstream part of the computational domain, i.e. beyond $x/h \approx 30$ or 15 step heights h downstream of the sudden expansion. It is noteworthy that the upstream pure Couette flow redeveloped into a mixed Couette-Poiseuille flow in contrast to the classical pressure-driven backward-facing step flow where an upstream Poiseuille flow inevitably redevelops to another pure Poiseuille flow far downstream of the step. In the present case,

Case	$U_w H/2\nu$	$c \times \partial P/\partial x$	$u_{\tau t} H/2\nu$	$u_{\tau b} H/2\nu$
Kuroda	3000	1.33×10^{-3}	154	17.7
Present	5200	1.2×10^{-3}	233.8	77

Table 2: Simulation parameters from Kuroda *et al.* (1995) case $CP3$, and present simulation at $x/h = 37$. Here, $c = -H/2\rho U_w^2$.

however, an adverse pressure gradient is established with the view to assure global mass conservation. The resulting mixed Couette-Poiseuille flow exhibits major asymmetries in the turbulence field with a substantially reduced turbulence level along the stationary wall, and the flow field closely resembles the Couette-Poiseuille flow simulations reported by Kuroda *et al.* (1995).

Kuroda *et al.* (1995) conducted direct numerical simulations of fully-developed turbulent plane Couette-Poiseuille flow to study the effect of the mean-shear rate on the near-wall turbulent flow field. Four cases were considered by the authors in which the mean-shear rate was varied by changing the wall velocity and the streamwise pressure gradient. Of particular relevance to our study is case $CP3$ in Kuroda *et al.* (1995).

Owing to the asymmetry of the Couette-Poiseuille flow, the wall shear stresses on the lower and upper-wall are generally different. For the current simulation, the corresponding local Reynolds numbers based on the wall friction velocities and the non-dimensionalized pressure gradient are provided in table 2 together with simulation parameters from Kuroda *et al.* (1995). The mean velocity profile and turbulent intensities presented in figure 17 compare surprisingly well with the DNS data of Kuroda *et al.* (1995), especially near the upper-wall.

5.5. Vorticity and λ_2 statistics

Profiles of the root-mean-square vorticity normalized by $u_{\tau i}^2/\nu$ are shown in figures 18. While the secondary recirculation region show low levels, the effect of mean-shear motion is clearly observed from $y/h \approx 0.75$ in the form of increasing vorticity fluctuations. This increase is sustained till midway between the walls where the three components attain their local maxima in the shear-layer, and then followed by a decrease towards a local minimum around $y/h \approx 1.5$. Two step heights further downstream, the primary recirculation region shows higher fluctuation levels than the secondary one while

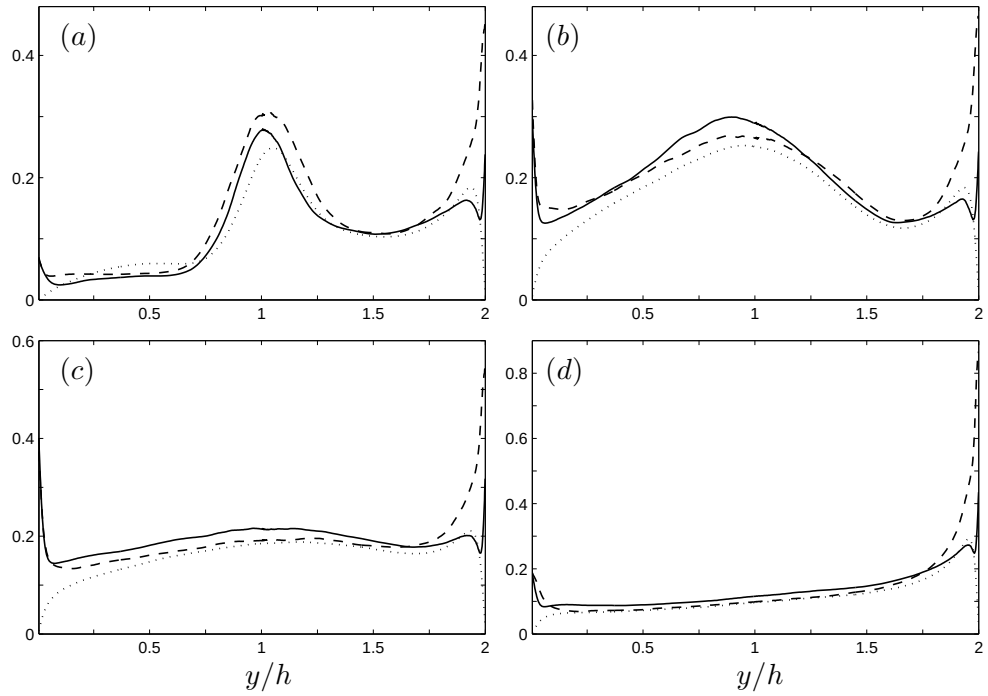

Figure 18: Wall-normal distribution of the root-mean-square vorticity fluctuations normalized by $u_{\tau i}^2/\nu$: ———, streamwise direction; $\cdots\cdots$, wall-normal direction; – – – –, spanwise direction. (a) $x/h = 16$; (b) $x/h = 18$; (c) $x/h = 22$; (d) $x/h = 37$.

in the shear-layer $(\overline{\omega_x{}^2})^{1/2}$ is amplified and $(\overline{\omega_z{}^2})^{1/2}$ is attenuated. In a direct numerical simulation of a self-similar mixing-layer, Rogers & Moser (1993) reported an axisymmetric anisotropy in the free planar shear-layer. In the present case, however, the results show that the vorticity is almost isotropic in the shear-layer. Near the upper-wall, the distributions of $(\overline{\omega_i{}^2})^{1/2}$ are very anisotropic as in the case of plane Couette flow whereas at the stationary one a different anisotropy is observed with $(\overline{\omega_x{}^2})^{1/2}$ and $(\overline{\omega_z{}^2})^{1/2}$ being almost equal and attaining higher values than $(\overline{\omega_y{}^2})^{1/2}$. It is noteworthy that the flow exhibits the same anisotropy further downstream.

Figure 19 shows the cross-correlation between $-\lambda_2$ and the three components of the vorticity fluctuation vector in the recirculation and recovery regions. The main tendency at both $x-$stations is that the cross-correlation between $-\lambda_2$ and ω_x is higher than that between $-\lambda_2$, ω_y and ω_z. This indi-

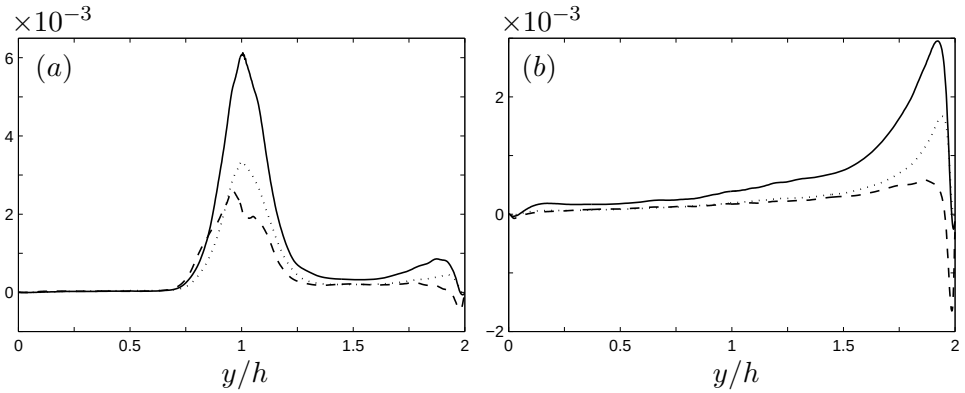

Figure 19: Wall-normal distritubtion of the dimensionless cross-correlation of $-\lambda_2$ with ω_i normalized by $u_{\tau i}^6/\nu^3$: ———, $\overline{-\lambda_2\omega_x}$; · · · · · · ·, $\overline{-\lambda_2\omega_y}$; – – – –, $\overline{-\lambda_2\omega_z}$. (a) $x/h = 16$; (b) $x/h = 37$.

cates that the coherent vortices are predominantly aligned in the streamwise direction.

6. Conclusions

A direct numerical simulation of turbulent Couette flow over a backward-facing step has been performed at a relatively low Reynolds number. The mean reattachment length of the shear layer was found to be $7.5h$. In the recirculation zone a large negative skin friction coefficient was observed beneath the core of the primary separation bubble.

The streaky near-wall structures formed along the step persisted several step heights downstream of the step. High and anisotropic turbulence levels were produced in the shear layer emanating from the corner. Although advection by the mean flow as well as turbulent diffusion were of some importance in the vicinity of the step, the mean-shear production was the primary source of turbulent energy. As in other turbulent shear flows, the energy arose as streamwise velocity fluctuations and was subsequently transferred into wall-normal and spanwise fluctuations by means of pressure-strain interactions.

Even though the wall-normal mean velocity V vanished far downstream of the step, the streamwise velocity U did not retain the characteristic S-shape typical of a pure Couette flow. This phenomenon is ascribed to the principle

of global mass conservation, which can be fulfilled only if an adverse mean pressure gradient is established in the recovery region. This is indeed what was observed. In the resulting asymmetric mean flow, the wall friction was roughly 10 times higher along the moving wall than at the steady surface. The resulting flow field was thus by far less vigorous along the stepped wall and this was reflected in the low levels of velocity and vorticity fluctuations.

7. Acknowledgements

We are grateful to the audience at the $6th$ International Symposium on Turbulence and Shear Flow Phenomena in Seoul (June 2009) for the constructive comments and valuable feedback on the presentation of this work by the first author.

PhD research fellowships for the first and second authors were provided by the Norwegian University of Science and Technology (NTNU) and the Research Council of Norway, respectively.

Computing time was granted by the Research Council of Norway (Programme for Supercomputing) and by the Research Programme in Computational Science and Visualization (BVV) at NTNU.

References

Abbot, D.E., Kline, S.J., 1962. Experimental investigations of subsonic turbulent flow over single and double backward-facing steps. Trans. A.S.M.E. D: J. Basic Engng. 84, 317–325.

Armaly, B.F., Durst, F., Pereira, J.C.F., Schönung, B., 1983. Experimental and theoretical investigation of backward-facing step flow. J. Fluids Mech. 127, 473–496.

Barri, M., El Khoury, G.K., Andersson, H.I., Pettersen, B., 2009a. Inflow conditions for inhomogeneous turbulent flows. Int. J. Numer. Meth. Fluids 60, 227–235.

Barri, M., El Khoury, G.K., Andersson, H.I., Pettersen, B., 2009b. DNS of backward-facing step flow with fully turbulent inflow. Int. J. Numer. Meth. Fluids (in print).

Bech, K.H., Tillmark, N., Alfredsson, H., Andersson, H.I., 1995. An investigation of turbulent plane Couette flow at low Reynolds numbers. J. Fluids Mech. 286, 291–325.

Bech, K.H., Andersson, H.I., 1996. Structure of Reynolds shear stress in the central region of plane Couette flow . Fluid Dynamics Research 18, 65–79.

Durst, F., Tropea, C., 1981. Turbulent backward-facing step flows in two-dimensional ducts and channels. Proc. Third Intl Symp. on Turbulent Shear Flows 18.1–18.5.

Eaton, J.K., Johnston, J. P., 1981. A review of research on subsonic turbulent flow reattachment. AIAA Journal 19, 1093–1100.

Friedrich, R., Arnal, M., 1990. Analysing turbulent backward-facing step flow with the lowpass-filtered Navier-Stokes equations. J. Wind Eng. Ind. Aerodyn. 35, 101–128.

Goldstein, R.J., Eriksen, V.L., Olson R.M., Eckert E.R.G., 1970. Laminar separation reattachment, and transition of flow over a downstream-facing step. Trans. A.S.M.E. D: J. Basic Engng. 92, 732–741.

Jeong, J., Hussian, F., 1995. On the identification of a vortex. J. Fluids Mech. 285, 69–94.

Kuehn, D.M., 1980. Some effects of adverse pressure gradient on the incompressible reattaching flow over a rearward-step. AIAA Journal 18, 343–344.

Kuroda, A., Kasagi, N., Hirata, M. 1995. Direct numerical simulation of turbulent plane Couette-Poiseuille flows: effect of mean shear rate on the near-wall turbulence structures. Turbulent Shear Flows 9, Springer-Verlag, Berlin, 240–257.

Le, H., Moin, P., Kim, J., 1997. Direct numerical simulation of turbulent flow over a backward-facing step. J. Fluid Mech. 330, 349–374.

Lowery, P.S., Reynolds, W.C., 1986. Numerical simulation of a spatially-developing, forced, plane mixing layer. Rep. TF-26. Thermosciences Division, Dept. of Mech. Engng. Stanford University.

Manhart, M., 2004. A zonal algorithm for DNS of turbulent boundary layers. Computers and Fluids 33, 435–461.

Meri, A., Wengle, H., 2002. DNS and LES of turbulent backward-facing step flow using 2nd- and 4th-order discretization. Advances in LES of Complex Flows, Friedrich, R., Rodi, W., (eds.) Kluwer Academic Publishers 65, 99-114.

Morinishi, Y., 2007. Backward-facing step flow between step-side stationary and moving walls. Proc. 5th International Symposium on Turbulence and Shear Flow Phenomena, Munich, 673–676.

Neto, S.A., Grand, D., Métais, O., Lesieur, M., 1993. A numerical investigation of the coherent vortices in turbulence behind a backward-facing step. J. Fluid Mech. 256, 1–25.

Ötügen, M.V., 1991. Expansion ratio effects on the separated shear layer and reattachment downstream of a backward-facing step. Exps. Fluids 10, 273–280.

Ra, S.H., Chang, P.K., 1990. Effects of pressure gradient on reattaching flow downstream of a rearward-facing step. J. Aircraft 27, 93–95.

Rogers, M.M., Moser, R.D., 1993. Direct simulation of a self similar turbulent mixing layer. Phys. Fluids 6, 903–923.

Spalart, P.R., 1988. Direct simulation of a turbulent boundary layer up to $Re_\theta = 1410$. J. Fluids Mech. 187, 61–98.

Paper 8

DNS of orifice flow with turbulent inflow conditions

El Khoury, G. K., Barri, M., Andersson, H. I. & Pettersen, B.

In *Direct and Large-Eddy Simulations 7, Trieste, Italy, Sept. 8–10, 2008.* (to be published by Springer)

Is not included due to copyright

Part 2.3

Separated shear flows

Paper 9

Massive separation in rotating turbulent flows

Barri, M., El Khoury, G. K., Andersson, H. I. & Pettersen, B.

In *Advances in Turbulence XII, Proceedings of the 12th EUROMECH European Turbulence Conference, Springer–Verlag, pp.625–628, 2009.*

Is not included due to copyright

Paper 10

Turbulent flow in a sudden-expansion channel. Part I: Effects of anti-cyclonic system rotation

Barri, M. & Andersson, H. I.

Submitted to *Journal of Fluid Mechanics.*

Turbulent flow in a sudden-expansion channel. Part I: Effects of anti-cyclonic system rotation

MUSTAFA BARRI AND HELGE I. ANDERSSON

Fluids Engineering Division, Department of Energy and Process Engineering
Norwegian University of Science and Technology (NTNU), 7491 Trondheim, Norway

(Received 5 September 2009)

The effects of rotation on the turbulent flow in a sudden-expansion channel are investigated by means of direct numerical simulations. The backward-facing step configuration is rotated anti-cyclonically about a spanwise axis. The upstream flow is a fully-developed plane Poiseuille flow subjected to orthogonal-mode rotation, which subsequently detaches from the step corner and eventually re-attaches further downstream. The size of the resulting separation bubble with recirculating flow diminishes monotonically with increasing rotation rates and the reattachment distance is reduced from about 7 to 3 step heights. This is ascribed to the augmentation of the cross-stream turbulence intensity in the shear-layer formed between the bulk flow and the recirculating eddy due to the destabilizing influence of the Coriolis force. The spanwise-oriented vortex cells or roller-eddies found in non-rotating shear-layers were disrupted by the enhanced turbulence. The flow along the planar wall is subjected to an adverse pressure gradient induced by the sudden expansion. The stabilizing influence of the system rotation in this cyclonic shear layer tends to damp the turbulence, the flow becomes susceptible to flow separation, and a substantial cyclonic recirculation bubble is observed at the highest rotation rates. The resulting meandering of the bulk flow is associated with interactions between the anti-cyclonic shear layer at the stepped side and the cyclonic shear flow along the planar surface. These give rise to enhanced turbulence levels at the cyclonic side in spite of the otherwise stabilizing influence of the Coriolis force. Exceptionally high velocity fluctuations in the spanwise direction are observed in the vicinity of re-attachment behind the step and ascribed to longitudinal Taylor-Görtler-like roll cells which extend into the backflow region.

1. Introduction

Turbulent flows in a rotating frame-of-reference are of considerable interest in a variety of industrial, geophysical and astrophysical applications. Ocean currents, atmospheric boundary layers and engineering flows in rotating turbomachinery such as turbines, pumps and cyclone separators are among the widely observed areas where the Coriolis effect gives rise to remarkable alterations of flow turbulence.

Wall-bounded shear flows (plane Poiseuille and Couette flows) subjected to system rotation have been extensively investigated through the previous few decades by means of laboratory experiments and computer simulations. The illuminating experimental investigation of rotating plane channel flow by Johnston *et al.* (1972) was confirmed and supplemented by more recent experimental studies by by Nakabayashi & Kitoh (1996, 2005) and direct numerical simulations by Kristoffersen & Andersson (1993), Lamballais *et al.* (1996, 1998), Liu & Lu (2007) and Grundestam *et al.* (2008). These, and other studies, showed that the influence of the Coriolis force due to imposed system rotation depends both on the orientation and the magnitude of the background vorticity $2\boldsymbol{\Omega}^F$ relative to the mean flow vorticity $\boldsymbol{\Omega} \equiv \nabla \times \boldsymbol{U}$ in a rotating frame-of-reference. In simple shear flows, the mean vorticity vector $\boldsymbol{\Omega}$, is perpendicular to both the mean flow direction and to the wall-normal direction. If the angular velocity vector $\boldsymbol{\Omega}^F$ of the rotating frame-of-reference is aligned with $\boldsymbol{\Omega}$, the local vorticity ratio $S \equiv 2\Omega^F/\Omega$ effectively distinguishes between different flow regimes. In the plane channel flow, for instance, S changes sign where the mean velocity peaks and the rotating channel flow is therefore simultaneously affected by *cyclonic* ($S > 0$) and *anti-cyclonic* ($S < 0$) rotation. In rotating plane channel flow, the turbulence is damped (stabilized) at the cyclonic side with increasing the rotation rate whereas the turbulence agitation is enhanced (destabilized) at the anticyclonic side and re-damped (restabilized) at high rotation rates. Rotating plane channel flows are inevitably exposed simultaneously to cyclonic and anticyclonic rotation. On the other hand, the rotating plane Couette flow is either exposed entirely to cyclonic or anticyclonic rotation. Barri & Andersson (2009) reported that the distinct secondary flows observed by Bech & Andersson (1997) were quenched and the turbulence damped when a plane Couette flow was subjected to strong anti-cyclonic system rotation.

In homogeneous shear flows subject to anti-cyclonic rotation, the special case consisting of $S = -1.0$, i.e. *zero absolute mean vorticity*, is particularly interesting. According to the Bradshaw-Richardson number $B = S(S+1)$, the case $S = -1$ should be neutrally stable (i.e. $B = 0$) just as the non-rotating case $S = 0$. Cambon *et al.* (1994) convincingly demonstrated that although the zero absolute mean vorticity case $S = -1$ should be equivalent to the $S = 0$ case according to the Bradshaw-Richardson stability criterion, the flow dynamics are indeed strikingly different. Comprehensive support of this view has subsequently been provided by Salhi & Cambon (1997) and Brethouwer (2005). Yanase *et al.* (2004) and Brethouwer (2005) found that the flow field was dominated by very elongated and intense streamwise vortex tubes. Iida *et al.* (2008) focused on $S = \pm 0.5$ with the view to investigate the tilting mechanism of the longitudinal vortex structures. Here, anti-cyclonic rotation $S = -1/2$ corresponds to *zero-tilting vorticity* and maximum destabilization ($B = -1/4$) according to Cambon *et al.* (1994). Iida *et al.* (2008) examined the influence of spanwise system rotation on the vertical flow structures and observed that the spanwise tilting of the structures was reduced whereas their inclination with respect to the mean flow direction was increased.

Similar to the wall-bounded shear flows, free shear flows are also differently affected by system rotation. A rotating wake is exposed simultaneously to cyclonic and anticyclonic

rotation, whereas a rotating mixing-layer is subjected only to cyclonic or anticyclonic rotation. An early flow visualisation study of the mixing-layer emanating from the corner of a backward-facing step was performed by Rothe & Johnston (1979). They observed that the position at which the flow reattached to the channel wall downstream of the step, i.e. the reattachment point, was crucially dependent on the sense of rotation and the rotation rate. In short, the reattachment length increased with increasing cyclonic rotation and diminished with higher anti-cyclonic rotation. In the latter case, the turbulence in the shear layer was promoted and the mixing enhanced the spreading rate of the mixing layer. Cyclonic rotation, on the other hand, tended to damp the turbulence and the spanwise-oriented coherent flow structures were strengthened. The rotating mixing-layer was further investigated by Bidokhti & Tritton (1992) albeit in a rather different apparatus. They showed that the flow was stabilized when the imposed system vorticity was parallel with the mean shear vorticity vector (i.e. in the cyclonic regime) whereas the flow was first destabilized and subsequently restabilized when the system rotation vector was anti-parallel to the vorticity vector (i.e. anti-cyclonic rotation). Measurements of the Reynolds-stress components at higher rotation rates indicated that the destabilization occurred in an early stage of the mixing-layer development and subsequent two-dimensionalization took place further downstream. They also confirmed the existence of a roller-eddy pattern (Kelvin-Helmholtz rollers) in all cyclonic cases whereas the flow was completely disrupted by the destabilization at even weak anticyclonic rotation. Bidokhti & Tritton (1992) pointed out that since Kelvin-Helmholtz rollers are essentially two-dimensional, they will not be suppressed by stabilizing, i.e. cyclonic, rotation. What will suppressed are the three-dimensional motions that lead to distortions of the large eddies. They therefore anticipated that the stabilizing rotation tends to make the roller eddies more robust.

Métais *et al.* (1995) performed direct and large-eddy simulations of a planar mixing-layer and a planar wake flow subjected to solid-body rotation. Their simulations were concerned with the time evolution from an initial mean flow profile (a hyperbolic-tangent form for the mixing-layer and a Gaussian profile for the wake) and periodicity was assumed in the streamwise direction. They superimposed both quasi-two-dimensional and three-dimensional perturbations separately on the basic shear flow and studied the effect of different rotation numbers on cyclonic and anti-cyclonic shear flow regimes. Their simulations confirmed the two-dimensionalization effect of cyclonic rotation and rapid anti-cyclonic rotation.

System rotation effects on simple turbulent shear flows are now reasonably well understood. The aim of the present study is to explore the effects of rotation on a topologically more complex flow, i.e. a wall-bounded flow with detachment, re-attachment and massive recirculation. To this end, the plane backward-facing step flow will be considered. This flow configuration is probably the most frequently studied separated-flow configuration due to its geometrical simplicity and yet complex flow dynamics. The majority of investigations have been concerned with an upstream boundary layer flow which detaches from the plane surface at the step corner and re-attaches further downstream, see e.g. Le *et al.* (1997).

Here, however, we will consider a fully-developed turbulent rotating channel flow which separates from the lower wall at the step corner, as illustrated in figure 1. A free shear-layer will form between the jet-like flow coming from the upstream channel and the so-called 'dead water' zone in the lee of the step. This shear layer is first nearly parallel with the walls and only modestly effected by the stepped surface downstream of the expansion. However, somewhat downstream the shear-layer curves sharply downwards and eventually impinges on the lower wall. A part of the fluid is deflected upstream by an adverse pressure gradient and forms a substantial recirculation zone, whereas the bulk flow proceeds in the downstream direction and a new shear-layer develops beyond the reattachment point. The shear-layer which, together with the corner, circumcises the 'dead water' zone is qualitatively different from a plane mixing-layer in many respects and exhibits significantly higher turbulence on the low-speed side. The shear-layer is substantially affected both by the adverse pressure gradient and the mean streamline curvature. Today it is widely accepted that the notion of a 'dead water' zone is misleading since the magnitude of the backflow is not at all negligible. Depending on the expansion ratio and the Reynolds number, the region between detachment and reattachment may even contain a smaller corner recirculation zone between the step surface and the primary recirculation bubble. This corner eddy re-circulates oppositely to the main recirculation. At relatively low Reynolds numbers, i.e. in the high-Re laminar and transitional regimes, the flow may also detach and reattach at the upper planar wall. This pressure-induced flow separation leads to a slender recirculation zone which, to the best of our knowledge, has never been observed under fully turbulent flow conditions.

In the present investigation we consider the turbulent flow over a backward-facing step subjected to anti-cyclonic rotation, i.e. the flow along the stepped wall, in the free shear-layer and downstream of reattachment is anti-cyclonic whereas the flow along the opposite planar surface is cyclonic. The primary recirculation bubble will also be anti-cyclonic whereas the secondary corner-eddy, if any, recirculates cyclonically. The aim is to examine how the free shear layer downstream of the corner is affected by rotation and whether or not a secondary cyclonic eddy will form in between the primary recirculation bubble and the step. The results will be compared with the experimental data for the reattachment distance by Rothe & Johnston (1979) obtained by means of flow visualizations. The turbulence is known to be damped along the cyclonic side of a rotating channel and one may therefore speculate whether the rotational damping renders the shear-layer susceptible to flow separation. A particular feature of the backward-facing step configuration is that the effective rotation is higher downstream of the step than in the upstream part although the effective bulk flow Reynolds number remains the same. This may possibly give rise to some unexpected flow phenomena.

2. Orthogonally rotating turbulent flow over a backward-facing step

2.1. *Flow configuration and governing equations*

Let us consider the turbulent flow in an infinitely long planar channel geometry with a one-sided sudden expansion, i.e. the so-called *backward-facing step* configuration depicted

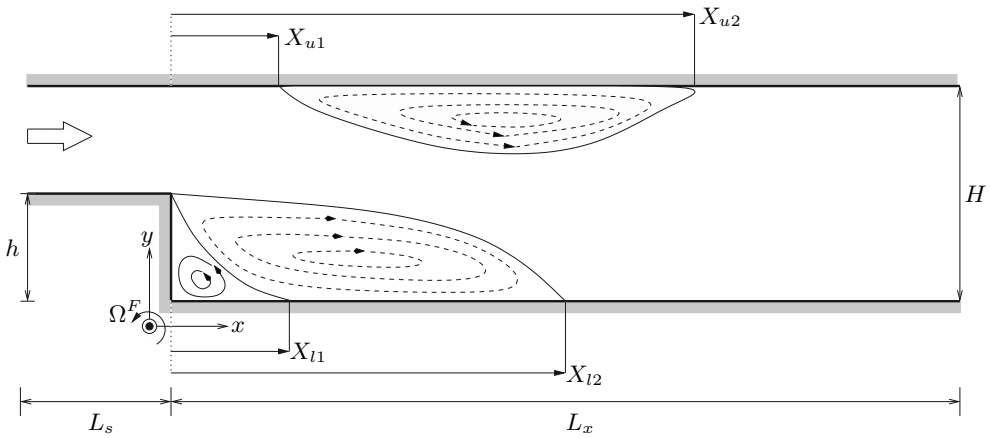

FIGURE 1. Schematic of spanwise rotating sudden-expansion flow (BFS). The system is rotating with constant angular velocity Ω^F about the spanwise $z-$axis.

in figure 1. The step height is denoted by h, whereas the upstream and downstream heights of the channel are $(H-h)$ and H, respectively. The spanwise width of the channel is denoted by W. The aspect ratio of the upstream channel is thus $AR = W/(H-h)$ and the expansion ratio is $ER = H/(H-h)$. The entire flow configuration is fixed with respect to a Cartesian coordinate system which rotates with a constant angular velocity Ω^F about the $z-$axis. The origin of the rotating coordinate system is positioned at the step with the $x-$axis pointing in the direction of the upstream mean flow and the $y-$axis perpendicular to the stepped wall downstream of the expansion.

The flow in this set-up depends on several distinguishing of parameters: (a) the geometrical parameters AR and ER; (b) the state of the upstream flow; and (c) the rate of system rotation. In the present study an infinitely wide channel, i.e. $AR = \infty$, will be considered and end-wall effects are therefore completely eliminated. The expansion ratio ER is taken as 2 in order to enable comparisons with the experimental data of Rothe & Johnston (1979). The upstream flow is that of a fully-developed rotating channel flow at a Reynolds number Re of about 5600 where $Re = \rho U_b(H-h)/\mu$ is based on the upstream bulk flow velocity U_b and the upstream channel height (see section 3 for further details). Here, ρ and μ are the density and the dynamic viscosity of the incompressible fluid. For the particular expansion ratio $ER = 2$, the step height h equals the height $(H-h)$ of the upstream channel. The step Reynold number $Re_h = \rho U_b h/\mu$ is therefore identically equal to Re in this case.

The amount of system rotation is expressed in terms of the upstream rotation number $Ro = \Omega^F(H-h)/U_{bo}$, where U_{bo} denotes the upstream bulk velocity in the absence of rotation. This definition of the rotation number is essentially the same as that in Rothe & Johnston (1979) and twice the rotation number used by Kristoffersen & Andersson (1993). In the present study, Ro serves only as a dimensionless measure of the amount of the imposed system rotation, i.e. the angular velocity Ω^F is normalized with the time scale $(H-h)/U_{bo}$ of the bulk flow. Only anti-cyclonic rotation, i.e. $\Omega^F > 0$, will be

	$i=1,j=1$	$i=2,j=2$	$i=3,j=3$	$i=1,j=2$
P_{ij}	$-2(\overline{uu}\frac{\partial U}{\partial x}+\overline{uv}\frac{\partial U}{\partial y})$	$-2(\overline{uv}\frac{\partial V}{\partial x}+\overline{vv}\frac{\partial V}{\partial y})$	0	$-(\overline{uu}\frac{\partial V}{\partial x}+\overline{vv}\frac{\partial U}{\partial y})^{\S}$
G_{ij}	$4\Omega^F\overline{uv}$	$-4\Omega^F\overline{uv}$	0	$-2\Omega^F(\overline{uu}-\overline{vv})$

TABLE 1. Production terms in two-dimensional mean flow.

§ *The contribution* $-\overline{uv}(\frac{\partial U}{\partial x}+\frac{\partial V}{\partial y})$ *to* P_{xy} *vanishes identically due to mass conservation.*

considered in the present article whereas results for cyclonic rotation will be published in a companion paper.

The incompressible flow of a Newtonian fluid in a constantly rotating frame-of-reference is governed by the conservation equations for mass and momentum:

$$\nabla\cdot\boldsymbol{u}=0 \tag{2.1a}$$

$$\frac{\partial\boldsymbol{u}}{\partial t}+\boldsymbol{u}\cdot\nabla\boldsymbol{u}=-\frac{1}{\rho}\nabla p+\nu\nabla^2\boldsymbol{u}-2\boldsymbol{\Omega}^F\times\boldsymbol{u} \tag{2.1b}$$

where ν is the kinematic viscosity μ/ρ. The last term on the right-hand side of equation (2.1b) is the Coriolis force due to system rotation, whereas centrifugal effects are absorbed in the effective pressure p.

2.2. *Reynolds' decomposition*

The instantaneous velocity components u_i and pressure p can be decomposed into mean (U_i,P) and fluctuating (u_i,p) parts to facilitate both the presentation and interpretation of the outcome of the simulations. The mean flow becomes two-dimensional $(U,V,0)$ and the mean pressure P serves to drive the flow through the stepped channel configuration and at the same time to balance the wall-normal component of the Coriolis force. In contrast with rotating parallel shear flows, the streamwise component of the Coriolis force $2\Omega^F V$ makes a significant contribution in the expansion zone.

The transport equation for the individual second-moments can be written as follows:

$$\frac{D\overline{u_iu_j}}{Dt}=P_{ij}+G_{ij}+D_{ij}+\Pi_{ij}-\varepsilon_{ij} \tag{2.2}$$

The right-hand-side terms, which are responsible for production due to mean shear (P_{ij}), production due to rotation (G_{ij}), viscous and turbulent diffusion (D_{ij}), pressure-strain redistribution (Π_{ij}), and viscous energy dissipation (ε_{ij}), are defined in the Appendix. For a two-dimensional mean flow in the $(x,y)-$plane the production terms due to mean shear and system rotation are detailed in Table 1.

The mean turbulent kinetic energy $k=\frac{1}{2}\overline{u_iu_i}$ is a convenient scalar measure of the turbulent activity. From the rotational production terms in Table 1, we readily find that

the source of kinetic energy becomes:

$$P_K \equiv \frac{1}{2}P_{ii} = \left(\overline{uu} - \overline{vv}\right)\frac{\partial V}{\partial y} - \overline{uv}\left(\frac{\partial V}{\partial x} + \frac{\partial U}{\partial y}\right) \tag{2.3}$$

Here, mean flow continuity $\partial U/\partial x = -\partial V/\partial y$ has been utilized.

In parallel shear flows where $V = 0$ the only turbulence-generating term is the last one. The terms involving V can be considered as additional production terms associated with streamline curvature. These terms inevitably vanish both upstream and far downstream of the channel expansion. It is particularly noteworthy that the rotational production of kinetic energy $G_K = \frac{1}{2}G_{ii}$ is identically zero. This fact does by no means imply that the turbulent flow remains unaffected by the system rotation.

2.3. *Mean vorticity and second-moments of vorticity fluctuations*

The components of the instantaneous vorticity vector are decomposed in mean Ω_i and fluctuating ω_i parts in accordance with the Reynolds decomposition. In the present case where the steady mean flow is two-dimensional and the turbulence statistics are homogeneous in spanwise direction and in time, the equation for the only non-vanishing mean vorticity component $\Omega_z = \partial V/\partial x - \partial U/\partial y$ reduces to:

$$\frac{\partial}{\partial x}(\overline{w\omega_x} - \overline{u\omega_z} - U\Omega_z) + \nu\frac{\partial^2\Omega_z}{\partial x^2} = \frac{\partial}{\partial y}(\overline{v\omega_z} - \overline{w\omega_y} + V\Omega_z) - \nu\frac{\partial^2\Omega_z}{\partial y^2} \tag{2.4}$$

It is noteworthy that the vorticity $2\Omega^F$ due to the imposed system rotation does not appear explicitly in equation (2.4). This is so because we are concerned only with orthogonal mode rotation. This particular orientation of the imposed rotation does not contribute to stretching and/or tilting of the mean vorticity by mean strain.

Transport for the individual second-moments of the vorticity fluctuations can written symbolically as:

$$\frac{D\overline{\omega_i\omega_j}}{Dt} = T1_{ij} + T2_{ij} + S3_{ij} + S4_{ij} + S5_{ij} + V6_{ij} + V7_{ij} \tag{2.5}$$

where the terms on the right-hand side are given in the Appendix. The terms are numbered according to their order of appearance in Tennekes & Lumley (1972) and Antonia & Kim (1994). The enstrophy budget is readily recovered as half the trace of equation (2.5). The capital letters are used to distinguish between transport (T), stretching (S) and viscous (V) terms. In the equation above, the system rotation appears explicitly only in the third stretching term $S5_{ij}$.

A striking difference between the second-moment equation for the velocity fluctuations (2.2) and that for the vorticity fluctuations (2.5) should be pointed out. While equation (2.2) simplifies considerably upon contraction of the indices since both $\Pi_{ii} = 0$ and $G_{ii} = 0$, none of the terms vanish when equation (2.5) is contracted to the enstrophy budget. In the present context, it is particularly noteworthy that the effect of system rotation remains in the stretching terms $S5_{ii}$ also after contraction. The enstrophy is therefore explicitly influenced by rotation, in contrast with the turbulent kinetic energy.

3. Computer simulations

Direct numerical simulations of turbulent flow over a backward-facing step were performed for a wide range of upstream rotation numbers (Ro = 0, 0.05, 0.10, 0.20 and 0.40). The highest rotation number is well above the highest rotation number $Ro = 0.25$ considered by Kristoffersen & Andersson (1993) in their fully-developed channel flow simulations. The upstream bulk Reynolds number $Re \approx 5600$ in the present simulations is only marginally below the Reynolds number ≈ 5900 in the simulations by Kristoffersen & Andersson (1993).

In order to assure well-defined upstream conditions, the flow upstream of the step is that of an infinitely long channel subjected to spanwise rotation. Besides the rotation number Ro, that flow is determined uniquely by the wall-friction Reynolds number $Re_\tau = \rho u_\tau (H-h)/\mu$, where u_τ can be considered as the *global* skin-friction velocity required to balance the driving streamwise gradient of the mean pressure P, i.e.

$$\rho u_\tau^2 = -\frac{\partial P}{\partial x}(H-h)/2 \tag{3.1}$$

Irrespective of the rotation number considered in the present study, Re_τ was kept equal to 360, i.e. exactly the same value as in the plane Poiseuille flow simulations of Kim *et al.* (1987) and marginally lower than $Re_\tau = 388$ in the rotating channel flow simulations by Kristoffersen & Andersson (1993). To facilitate comparisons between the different cases (to be presented in the subsequent sections), the results will be made dimensionless either by means of u_τ or U_{bo}. Even though the shape of mean velocity profile varies substantially with Ro, the bulk velocity U_b did not change by more than 4% in the parameter range considered by Kristoffersen & Andersson (1993). U_{bo} rather than U_b has therefore been adopted as an appropriate velocity scale of the mean motion for all cases.

The simulations were performed with the second-order accurate finite-volume code MGLET; see Manhart (2004). Coriolis body force terms were implemented into the discretized momentum equations. The three-dimensional governing equations (2.1) were integrated forward in time until a statistically steady state was reached. The results for the non-rotating case $Ro = 0$ compared perfectly well with the accurate PIV data provided by Kasagi & Matsunaga (1995) from an $ER = 1.5$ set-up at a slightly lower step Reynolds number Re_h. Both mean velocity profiles and turbulent statistics in the separated zone, near reattachment, and in the recovery region were compared by Barri *et al.* (2009b).

3.1. *Computational domain and grid resolution*

The length of the computational domain was $L_x + L_s = 32h + 6h = 38h$ in streamwise direction, $L_y = H = 2h$ in the wall-normal direction and $L_z = 6.28h$ in the spanwise direction. The upstream length L_s before the sudden expansion was taken as $6h$. The grid resolution was kept the same for all different simulation cases where the number of grid points was $864 \times 256 \times 200$ in the $x-$, $y-$ and $z-$directions, respectively. A non-uniform mesh has been used in the streamwise direction with $\Delta x^+ = 3.6$ close to the step edge and 15.4 at the outlet section. The multi-block grid in the wall-normal direction with $\Delta y^+ = 0.7$ (close to the walls and at $y/h = 1$) and 2.4 (at $y/h = 0.5$ and 1.5) aimed to

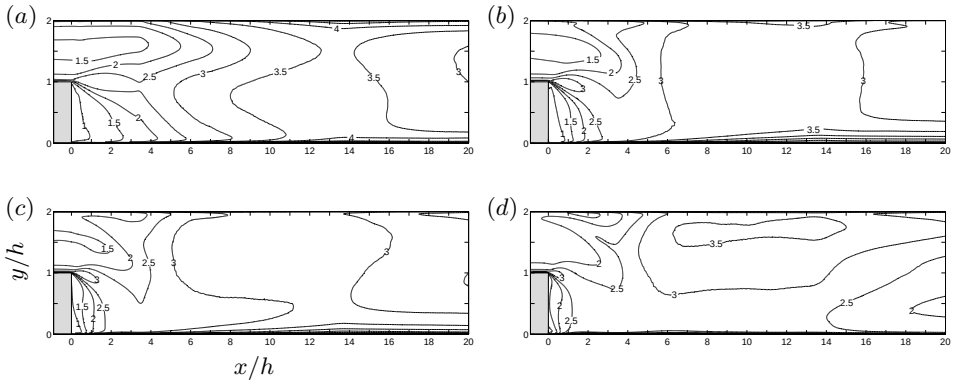

FIGURE 2. Ratio between largest local mesh size and Kolmogorov length scale Δ/η. (*a*) $Ro = 0.0$, (*b*) $Ro = 0.1$, (*c*) $Ro = 0.2$ and (*d*) $Ro = 0.4$.

resolve the turbulence scales in the regions close to the walls and especially in the shear-layer regions downstream of the expansion, whereas a uniform grid spacing $\Delta z^+ = 8.6$ is used in the homogeneous spanwise direction. The superscript $^+$ denotes scaling with the viscous length ν/u_τ, where u_τ is the global wall-friction velocity defined in equation (3.1).

Statistical averaging was made in the homogeneous spanwise direction and over a time interval $120h/u_\tau$. In order to eliminate the potential role of domain size and grid resolution on the results, the computational domain, expansion ratio and the number of grid points were kept to be the same for all different simulations.

The Kolmogorov length scale $\eta = (\nu^3/\epsilon)^{1/4}$ is a measure of the order of magnitude of the size of the smallest turbulent eddies. Figure 2 shows the local grid resolution ratio Δ/η evaluated on the basis of the largest local-mesh size in the three-dimensional grid $\Delta(x, y) = max(\Delta x, \Delta y, \Delta z)$ and the Kolmogorov length scale η. Here, ϵ has been evaluated as $\frac{1}{2}\varepsilon_{ii}$ from the simulated flow field along with other statistical quantities. Since the dissipation rate of the turbulent kinetic energy ϵ varies across the flow both in streamwise and wall-normal directions, also η varies with x/h and y/h. The coarsest grid resolution is found to be $\Delta/\eta \approx 4$ close to the walls downstream of the reattachment region and reduced towards the recirculation region and upstream of the step. Although the flow field is substantially affected by rotation, we are inclined to conclude that all essential scales of turbulence have been resolved for all *Ro* considered.

3.2. *Boundary conditions*

No-slip and impermeability conditions are imposed on the solid surfaces of the computational domain. For the computational cells within the step, the so called "*blanking*" technique is used, i.e., velocity components are set to zero whereas the pressure is set to an infinitely large number. The same boundary conditions are used for both the intermediate and the final divergence-free velocity field at each time step. Periodic boundary conditions are imposed in the homogeneous spanwise direction.

A dynamic inflow field was obtained by recycling a finite-length time series of instan-

taneous velocity planes taken from separate, i.e. precursor, simulations of fully-developed Poiseuille flow subjected to rotation about a spanwise axis. Barri *et al.* (2009a) advocated this as a cost-effective method to generate reliable inflow conditions for DNS of flows that are inhomogeneous in the streamwise direction and therefore prohibit the use of conventional inflow-outflow periodicity. The present precursor simulations closely resembled the earlier simulations by Kristoffersen & Andersson (1993) albeit at a slightly different Reynolds number. The duration t_s of each finite-length time series was $2h/u_\tau$, which is twice as long as recommended by Barri *et al.* (2009a) to assure representative inflow conditions comprising a wide range of time and length scales. Separate precursor simulations were run for each of the five rotation numbers.

As outflow conditions, we used the convective boundary condition for the velocity components $\partial\mathbf{u}/\partial t + U_e\partial\mathbf{u}/\partial x = 0$ where the convective velocity U_e was taken to be the mean streamwise velocity at the outflow plane. A small correction (of order of 0.01% of U_e) was applied to ensure global mass conservation. On the other hand, since a constant exit pressure results is a very reflective boundary condition, we forced the total normal stress to zero at the outlet section as a pressure boundary condition $-p + 2\mu\partial u/\partial x = 0$. This type of outflow boundary conditions were used in previous numerical simulations by Gartling (1990) for laminar backward-facing step flow and by Orlanski (1976) for a spatially growing K-H instability. Provided that the exit boundary is sufficiently downstream of the step, the influence of the streamwise component of the mean Coriolis force has become vanishingly small and can therefore be ignored.

4. Mean flow pattern and primary turbulence statistics

The purpose of this section is to show the dramatic alterations in the mean-flow pattern and the turbulence field which arise due to the imposed system rotation. The attention is focused on the flow just downstream of the expansion, which encompasses the shear layer which develops from the sharp corner as well as the zones with separated and reattaching flow. Although the computational domain extended $L_x = 32h$ downstream of the expansion, results in the far downstream will generally not be shown.

The mean flow and the turbulence statistics depend on both streamwise and cross-stream positions but are independent of z due to spanwise homogeneity. Upstream of the step, i.e. for $x < 0$, the flow field closely resembles that of an infinitely long channel in spanwise rotation, as considered by Kristoffersen & Andersson (1993).

Throughout the presentation and discussion of the results, positive rotation rates $\Omega^F > 0$ (i.e. counterclockwise rotation in figure 1) will be referred to as *anti-cyclonic* since the system rotation is opposing the mean flow rotation along the stepped wall upstream of the sudden expansion, i.e. the local vorticity ratio $S < 0$.

4.1. *Mean flow pattern*

The streamline patterns deduced from $U(x, y)$ and $V(x, y)$ are shown in figure 3 for the five different cases considered. Without rotation, the flow separated from the corner reattaches at $X_{l2} = 7.1$ and a clockwise recirculating eddy can be observed in figure $3(a)$. Upstream of this primary recirculating flow, a secondary counterclockwise bubble

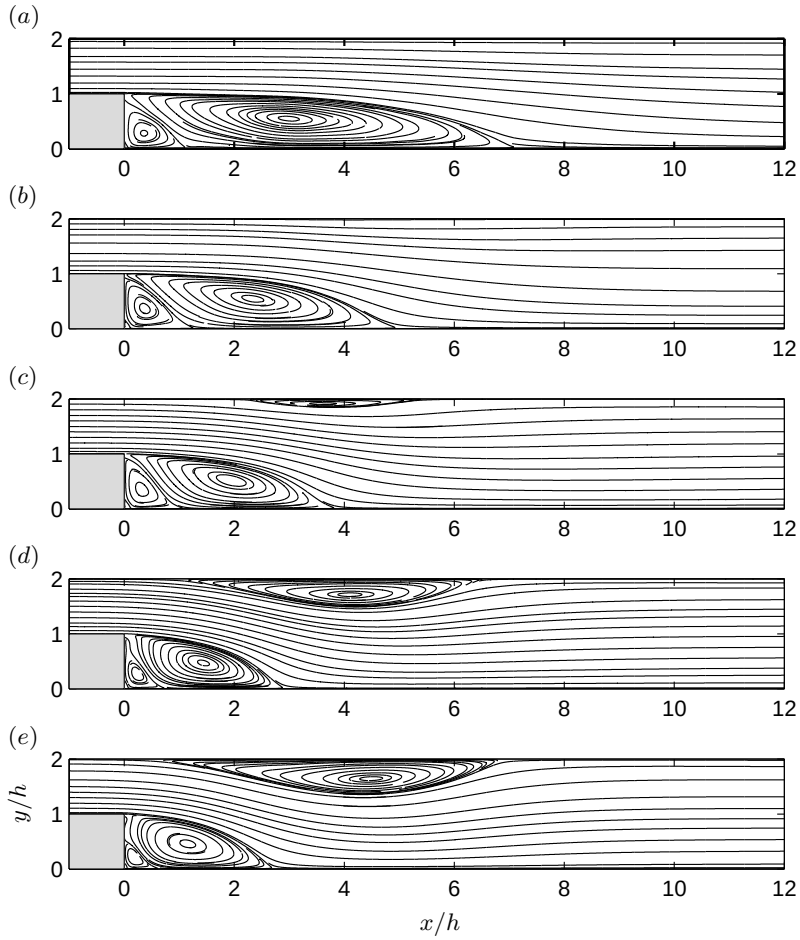

FIGURE 3. Streamlines at different rotation numbers. Counter clockwise sense of rotation. The computational domain extended another $20h$ downstream, i.e. to $x/h = 32$. (*a*) $Ro = 0.0$, (*b*) $Ro = 0.05$, (*c*) $Ro = 0.1$, (*d*) $Ro = 0.2$ and (*e*) $Ro = 0.4$.

extends $X_{l1} = 1.1$ from the concave corner. No recirculating flow can be discerned along the upper wall, in contrast to observations sometimes made in laminar and transitional BFS flows.

Anti-cyclonic system rotation severely affects the streamline pattern downstream of the expansion. The reattachment point X_{l2} of the separated shear layer reduces substantially with increasing Ro, but the monotonic reduction seems to saturate slightly below $3h$. The size of the secondary bubble is similarly reduced with increasing rotation. The position X_{l1} at which the reversed flow (i.e. backflow) within the primary bubble separates, is more than halved for $Ro = 0.4$.

A particularly striking effect of the imposed system rotation is the separation bubble which occurs at the upper wall already at $Ro = 0.10$ and achieves a substantial size at even higher rotation. The existence of this bubble acts a partial blockage at the

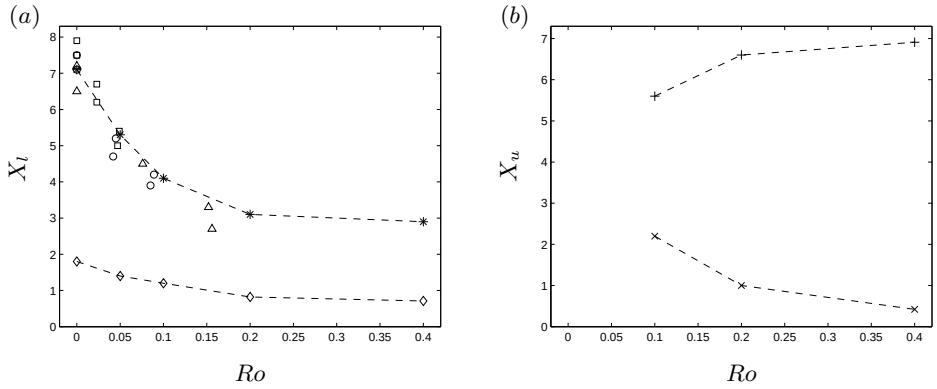

FIGURE 4. Positions of mean flow separation and reattachment, as defined in figure 1. (a) X_l and (b) X_u. $\triangle$, $\circ$ and $\square$ are experimental data from Rothe & Johnston (1979) for Reynolds numbers 3000, 5500 and 10000, respectively. $-\diamond-$ X_{l1}, $-*-$ X_{l2}, $-\times-$ X_{u1} and $-+-$ X_{u2}.

otherwise planar surface and inevitably directs the mean flow towards the stepped wall. Rothe & Johnston (1979) focused their attention on the free-shear layer behaviour and its reattachment downstream of the step and they did not report any flow separation at the opposite wall. The flow adjacent to the upper straight wall is exposed to an adverse pressure gradient shortly downstream of the location of the step, even for $Ro = 0$. Flow separation does, however, not occur in the non-rotating case. It is therefore likely that the turbulence level is reduced along the straight wall when rotation is imposed and the flow therefore becomes more vulnerable with respect to the adverse pressure gradient.

For the sake of the interpretation of the results, it should be emphasized that the primary recirculating flow is anti-cyclonic whereas the secondary bubble as well as the recirculation flow at the upper wall are cyclonic. The mean local Coriolis force is therefore directed inwards in the primary separation bubble and outwards in the two others. This distinction may possibly affect the turbulence within the recirculation zones.

The locations of the various reattachment and separation points in the five different flow cases are summarized in figure 4. The monotonically decreasing trend of X_{l2} is fully consistent with the data from the flow visualization experiments by Rothe & Johnston (1979). Their experiments were performed in rotating water channels with different aspect ratios and at some different Reynolds numbers. Here, only their data from the highest aspect ratio channel $AR = 15$ are used for comparison in figure 4(a). Some of their data points stem from flow visualisation by dye injection and others by hydrogen bubbles. Their facility did not allow rotation numbers above ~ 0.17. The length of the separation bubble at the upper wall, i.e. $X_{u2} - X_{u1}$, shows no tendency to saturate and one may speculate whether this bubble will become even longer for rotation rates above those considered here.

Mean velocity profiles $U(x, y)$ are presented in figure 5 at some characteristic streamwise locations. The strongest backflow ($U < 0$) is observed in the core of the primary recirculation bubble. When the cyclonic bubble emerges at the upper wall for $Ro \geq 0.10$, the backflow in the bubble increases as the rotation rate is further increased and eventu-

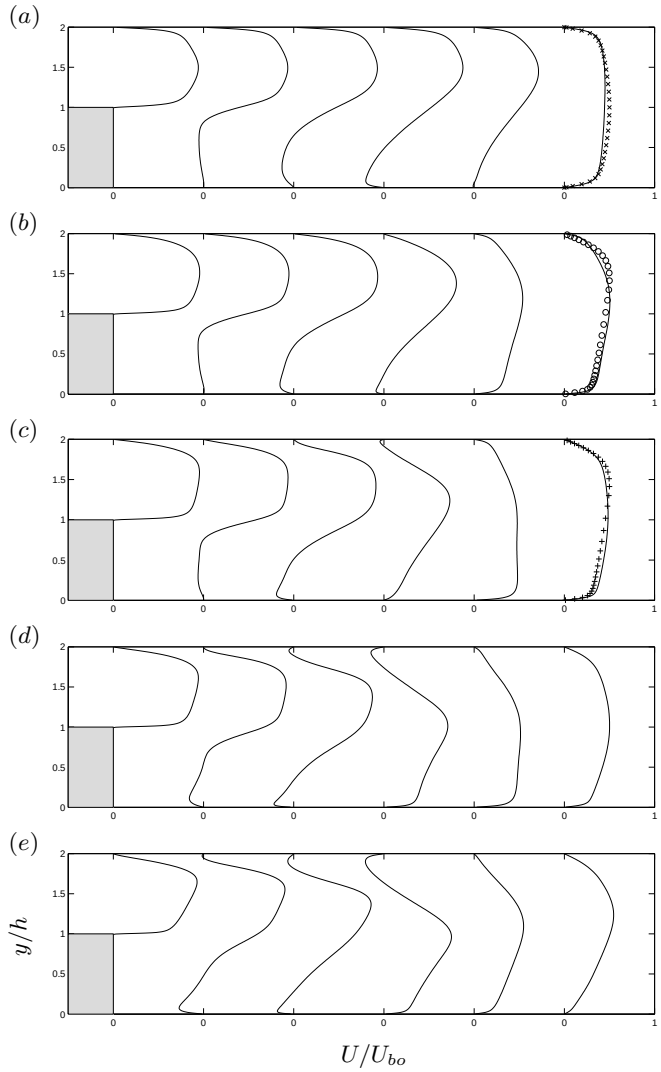

FIGURE 5. Mean streamwise velocity distribution at different streamwise locations $x/h = 0, 1, 2, 4, 7$ and 24. (*a*) $Ro = 0.0$, (*b*) $Ro = 0.05$, (*c*) $Ro = 0.1$, (*d*) $Ro = 0.2$ and (*e*) $Ro = 0.4$. $\times$ is DNS data for non-rotating plane Poiseuille flow from Kim *et al.* (1987), $\circ$ and $+$ are DNS data from Kristoffersen & Andersson (1993) for $Ro = 0.2$ and 0.5, respectively.

ally becomes comparable with the reversed flow in the primary bubble, i.e. of the order of 10% of U_b. In comparison, the velocity in the smaller secondary recirculation zone is considerably smaller and hardly distinguishable at $x/h = 1$ in figure 5(a, b).

It is noteworthy that the local channel Reynolds number in the downstream part of the channel remains the same as in the upstream channel since the local bulk velocity is related to the upstream bulk velocity U_b as $U_b(H - h)/H$. Similarly, the local channel rotation number becomes $\Omega^F H^2/U_b(H - h)$ when expressed in terms of the local channel height H and the downstream bulk velocity. The downstream channel rotation number

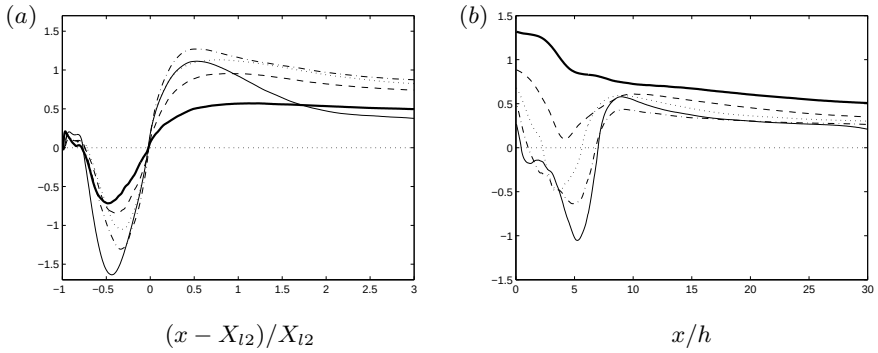

FIGURE 6. Variations of the skin friction coefficient C_f. (a) stepped wall and (b) straight wall. (bold line) $Ro = 0.0$, – – – $Ro = 0.05$, $\cdots$ $Ro = 0.1$, – · – $Ro = 0.2$, —— $Ro = 0.4$.

is therefore 4 times greater than the upstream Ro in the present case with $ER = 2$. Stronger effects of system rotation should therefore be expected downstream of the step.

The strong effects of rotation can be observed from the mean velocity profiles $24h$ downstream of the step. In the non-rotating case the profile compares surprisingly well with the fully-developed flow profile from the DNS of Kim *et al.* (1987). For the two lowest rotation numbers $Ro = 0.05$ and 0.10, comparisons are made with the profiles of Kristoffersen & Andersson (1993) for $Ro = 0.20$ and 0.50, respectively (data for $Ro = 0.40$ is not available). The mean velocity profiles seem to have re-developed nearly into those of a fully-developed rotating channel. These observations are consistent with the almost parallel streamlines downstream of $x = 10h$ in figure 3. By a closer examination of the non-rotating case, Barri *et al.* (2009b) reported that although the mean velocity field $U(x, y)$ was practically re-developed at $x = 24h$, the second-moment turbulence statistics were still re-developing and the profiles of the individual Reynolds stress components exhibited distinct asymmetries.

The variation of the local skin-friction coefficient $C_f = \tau_w(x)/\rho u_\tau^2$ downstream of the expansion is shown in figure 6. Here, $\tau_w(x)$ is the wall-shear stress and u_τ is defined in equation (3.1). The multiple zero-crossings of C_f confirm the existence of the primary ($C_f < 0$) and secondary ($C_f > 0$) separation bubbles at the lower wall and also the recirculation zone at the upper wall with $C_f < 0$. The magnitude of the negative peak value increases monotonically with Ro. This observation is directly linked to the gradually increasing backflow with rotation rate and suggests that the backflow is substantially stronger for $Ro = 0.4$ than in the non-rotating. This is also the case at the upper wall where $C_f < -1.0$ signifies a rather strong flow reversal.

A closer examination of the data along the upper wall shows that the flow is already at the verge of separation for $Ro = 0.05$ since C_f is only marginally positive about $x = 4h$. It is also noteworthy that the results for $Ro = 0.4$ exhibits a distinctly bimodal shape with a local minimum near $x = 1h$ and an absolute minimum at about $x = 5h$. This suggests a tendency towards two smaller rather than one large recirculation zone.

The inspection of the instantaneous skin-friction pattern in figure 7 for $Ro = 0.4$ shows that pockets of forward flow (empty spots) are embedded also in between the mean

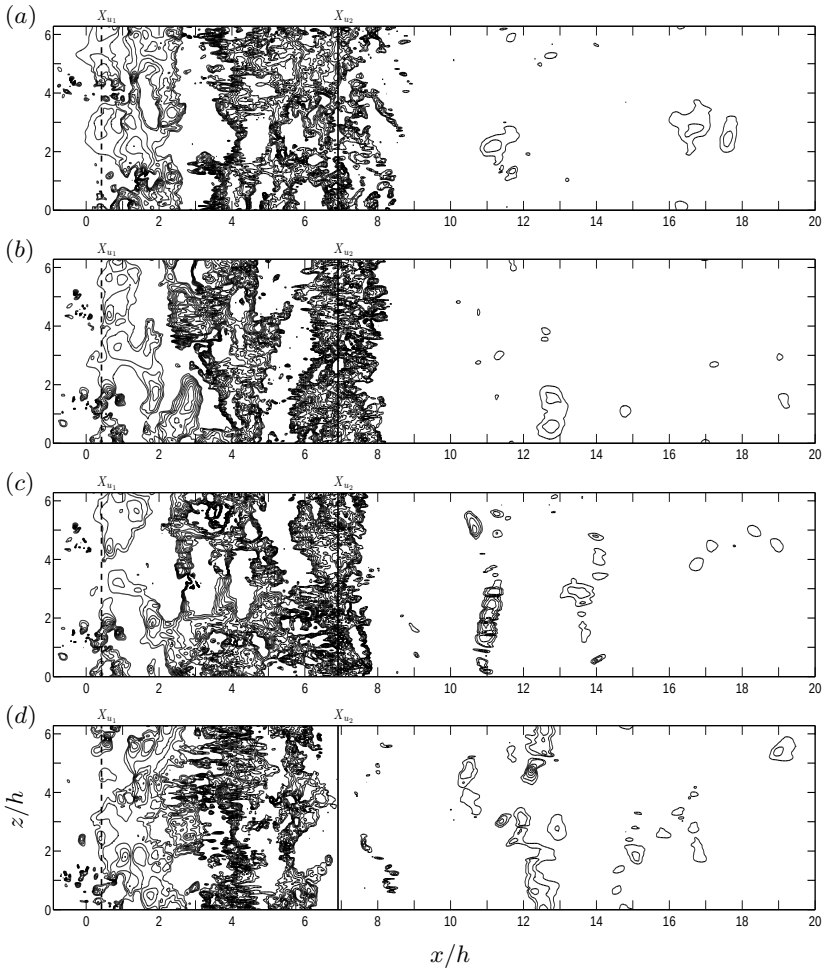

FIGURE 7. Contour plots of instantaneous skin friction at the straight upper-wall for $Ro = 0.4$. The contours identify regions with backflow. The straight lines are the mean separation point X_{u1} and mean reattachment point X_{u2}. (*a*) $t = 10h/u_\tau$, (*b*) $t = 11h/u_\tau$, (*c*) $t = 12h/u_\tau$ and (*d*) $t = 13h/u_\tau$.

separation X_{u1} and mean reattachment X_{u2} where the mean flow is in the upstream direction ($U < 0$). The snapshot in figure 7(*d*) is closest to the mean flow pattern, whereas the flow in the three preceding snapshots, separated h/u_τ in time, indicates the presence of two or even three smaller eddies.

The local skin-friction coefficient gradually approaches a constant level in the re-development zone. However, a complete recovery has not been attained even at $x = 30h$. A nearly complete symmetry between the two sides has been reached in the non-rotating case. C_f at the cyclonic side of the channel shows a monotonic decrease with increasing rotation, whereas the skin-friction along the anti-cyclonic side of the downstream channel first increases with Ro and ultimately for $Ro = 0.4$ becomes lower than in the

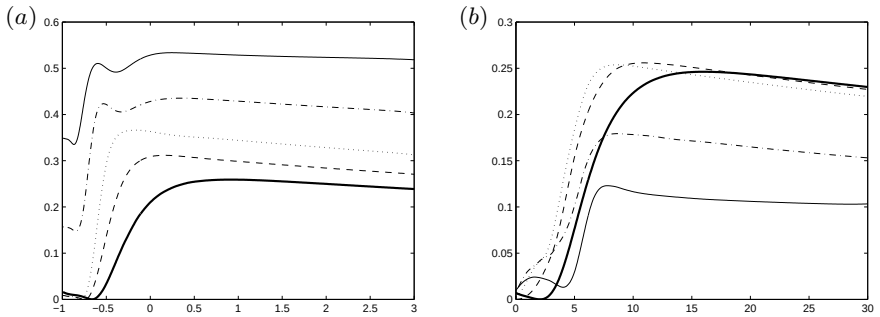

FIGURE 8. Variations of the pressure coefficient $\widetilde{C_p}$. (a) stepped wall and (b) straight wall. (bold line) $Ro = 0.0$, – – – $Ro = 0.05$, $\cdots$ $Ro = 0.1$, – · – $Ro = 0.2$, —— $Ro = 0.4$.

non-rotating channel. This behaviour is apparently due to the complex non-linear effects of the Coriolis force on the turbulent flow field.

The local wall pressure coefficient is defined as $\widetilde{C_p} = (C_p - C_{p_{min}})/(1 - C_{p_{min}})$, where $C_p = (P - P_o)/\frac{1}{2}\rho U_{bo}^2$ and $C_{p_{min}}$ is the minimum value of C_p. The reference pressure P_o and the bulk velocity U_{bo} are taken at the inflow section of the non-rotating case. In figure 8, C_p exhibits a local minimum close to the position of maximum backflow, i.e. beneath the core of the primary anti-cyclonic separation bubble. The pressure then recovers and attains a local maximum somewhat downstream of reattachment. Broadly the same trend is seen at both sides of the channel and irrespective of the rotation number. Downstream of the recovery region, the mean pressure is the same along both walls and exhibits a linear variation with streamwise location x. This reflects that the constant and favourable streamwise pressure gradient required to drive the flow further downstream has been established. It is noteworthy that the adverse pressure gradient in the recovery region at the cyclonic wall seems to be independent of the rotation number. The reason why the flow separates only for $Ro > 0.05$ can therefore not be explained by alterations in the mean flow field.

The results in figure 8(a) show that the pressure coefficient along the anti-cyclonic wall increases monotonically with the rate of system rotation whereas the wall pressure at the cyclonic side tends to decrease with Ro. This is due to the mean pressure gradient in the wall-normal direction established to balance the $y-$component of the mean Coriolis force:

$$\frac{\partial P}{\partial y} \approx -2\Omega^F U \tag{4.1}$$

The above force balance is simply the leading terms in the $y-$component of the Reynolds-averaged version of the instantaneous Navier-Stokes equations (2.1b). Positive rotation thus gives rise to a negative pressure gradient. In fluid machinery vocabulary, the cyclonic and anti-cyclonic sides are therefore referred to as the *suction* and *pressure* sides; see e.g. Johnston (1998).

The local mean vorticity ratio $S \equiv 2\Omega^F/\Omega_z$ where $\Omega_z = \partial V/\partial x - \partial U/\partial y$, exhibits a

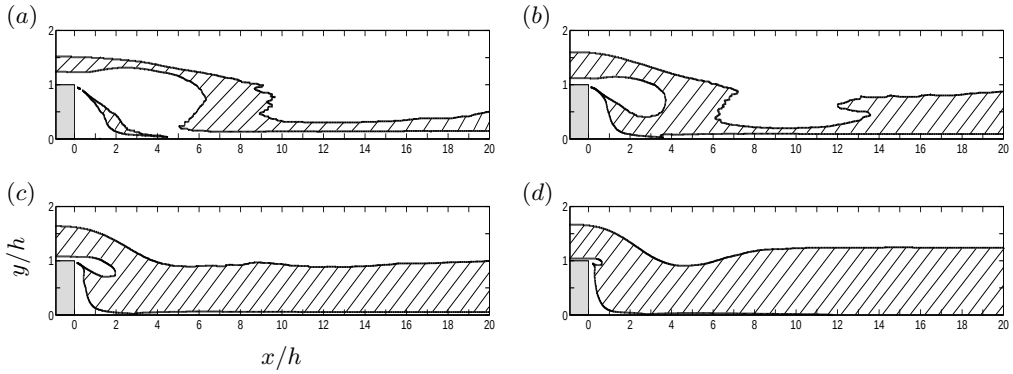

FIGURE 9. Zero absolute vorticity region ($S = -1 \pm 0.01$). (a) $Ro = 0.05$, (b) $Ro = 0.1$, (c) $Ro = 0.2$ and (d) $Ro = 0.4$.

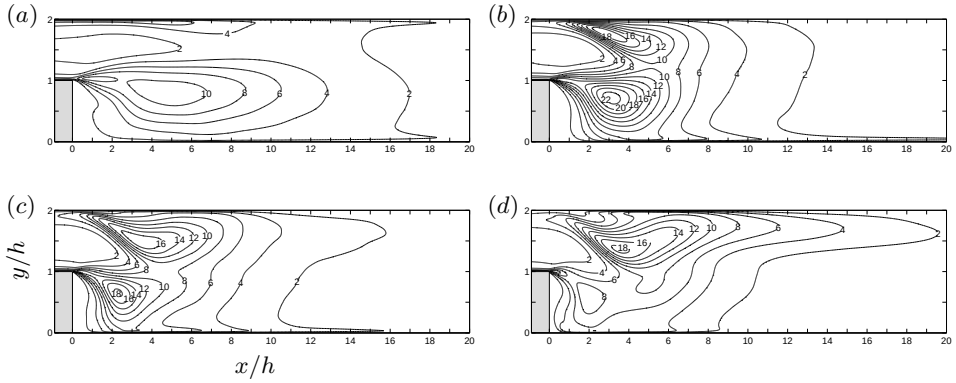

FIGURE 10. Streamwise Reynolds stress $\overline{uu}$ scaled with u_τ^2. (a) $Ro = 0.0$, (b) $Ro = 0.1$, (c) $Ro = 0.2$ and (d) $Ro = 0.4$.

wide region with a value of -1, as shown in figure 9. The mean flow vorticity Ω_z opposes the system rotation $2\Omega^F$ when $S < 0$, i.e. anti-cyclonic rotation. The absolute vorticity in an inertial frame-of-reference is driven to zero when $S = -1$. This phenomenon has been observed before, both in rotating channel flows by Johnston *et al.* (1972), Kristoffersen & Andersson (1993), Nakabayashi & Kitoh (1996, 2005) and Barri & Andersson (2009) and in rotating free shear flows by Métais *et al.* (1995). The region of zero absolute vorticity $S = -1 \pm 0.01$ is increasing by turning the system rotation to higher levels as shown in figure 9. At low-moderate rotation rates Métais *et al.* (1995) reported a zero absolute vorticity throughout the free shear layer. This is in contrast with the current observations where the anti-cyclonic shear layer is outside the region of $S \approx -1$, except for the highest rotation rate $Ro = 0.4$.

4.2. *Primary turbulence characteristics*

The second-moments of the velocity fluctuations, i.e. $\overline{u_i u_j}$, are adequate measures of the turbulent flow field of which the trace is twice the mean turbulent kinetic energy usually denoted by k. The flow under consideration is statistically homogeneous in the spanwise

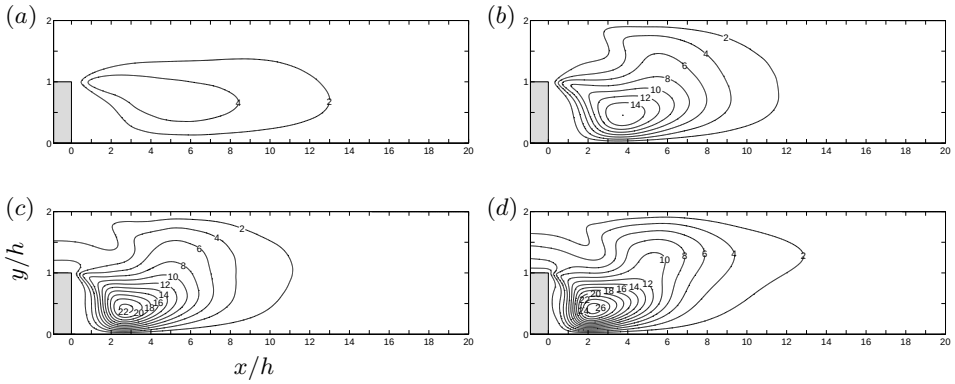

FIGURE 11. Wall-normal Reynolds stress $\overline{vv}$ scaled with u_τ^2. (*a*) $Ro = 0.0$, (*b*) $Ro = 0.1$, (*c*) $Ro = 0.2$ and (*d*) $Ro = 0.4$.

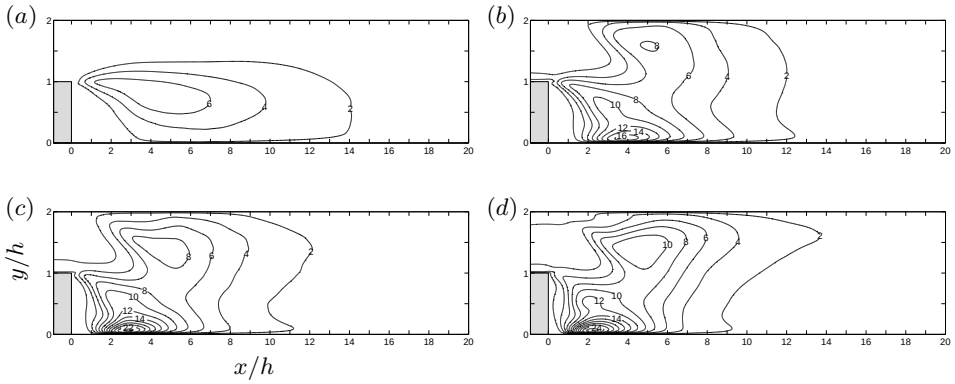

FIGURE 12. Spanwise Reynolds stress $\overline{ww}$ scaled with u_τ^2. (*a*) $Ro = 0.0$, (*b*) $Ro = 0.1$, (*c*) $Ro = 0.2$ and (*d*) $Ro = 0.4$.

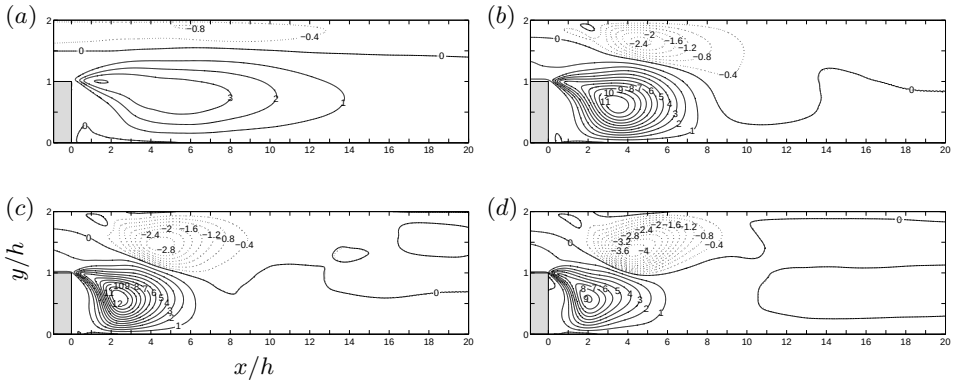

FIGURE 13. Reynolds shear stress $-\overline{uv}$ scaled with u_τ^2. (*a*) $Ro = 0.0$, (*b*) $Ro = 0.1$, (*c*) $Ro = 0.2$ and (*d*) $Ro = 0.4$.

direction and $\overline{u_1 u_2} = \overline{uv}$ is therefore the only non-zero off-diagonal component of the second-moment tensor. The different second-moments are shown in figures 10−13. Even though the turbulent kinetic energy is not directly affected by the imposed rotation, both the turbulence level and the anisotropy of the turbulence are severely changed.

The streamwise fluctuations $\overline{uu}$ in the anti-cyclonic mixing-layer just downstream of the step is substantially higher for $Ro = 0.1$ than in the non-rotating case. At higher rotation rates, the velocity fluctuations are slightly reduced at $Ro = 0.2$ whereas a substantial reduction occurs for $Ro = 0.4$. The exceptionally high levels of streamwise fluctuations observed for $Ro = 0.1$ and 0.2 cannot be explained by the rotational term $G_{xx} = 4\Omega^F \overline{uv}$ which acts as a sink since u and v are negatively correlated. The remarkable enhancement of streamwise fluctuations in the separating cyclonic shear layer at the upper wall, however, can be directly ascribed to $G_{xx} = 4\Omega^F \overline{uv}$ since $\overline{uv} > 0$ in this layer.

The wall-normal fluctuations shown in figure 11 increase monotonically with Ro in the primary anti-cyclonic separation bubble downstream of the step. This enhancement can directly be associated with the Coriolis term $G_{yy} = -4\Omega^F \overline{uv}$ which acts as a gradually increasing source term. The explanation of the more modest increase of $\overline{vv}$ along the upper cyclonic wall must be sought elsewhere since G_{yy} acts as a sink here. Even the velocity fluctuations in the spanwise direction are affected by the rotation, as seen in figure 12. However, neither the mean shear nor the Coriolis force tend to alter this velocity component (both P_{zz} and G_{zz} are zero) and the changes in $\overline{ww}$ in figure 12 are therefore due to other mechanisms. Pressure-strain interactions are known to be a primary source of spanwise velocity fluctuations in parallel shear flows. The excessively high level of $\overline{ww}$ in the vicinity of the wall about $3h$ downstream of the step cannot be explained in this way.

The Reynolds shear stress $-\overline{uv}$ in figure 13 changes sign across the stepped channel just as in a planar channel flow. Then the sign-change is brought about by the sign of the mean shear rate $\partial U/\partial y$. Now the magnitude of $-\overline{uv}$ increases with higher rotation rates both along the cyclonic and the anti-cyclonic sides. This increase seems to be correlated with the wall-normal velocity fluctuations, with the exception of the decrease of $-\overline{uv}$ in the primary recirculation bubble when the rotation rate is further increased from $Ro = 0.2$ to $Ro = 0.4$. The higher levels of the wall-normal fluctuations will tend to promote the mean shear production P_{xy} along both sides, whereas the Coriolis production $G_{xy} = -2\Omega^F(\overline{uu} - \overline{vv})$ makes a positive contribution to $-\overline{uv}$ along the anti-cyclonic side but tends to oppose the mean-shear production in the cyclonic shear layer whenever $\overline{uu} > \overline{vv}$.

The unexpected and extraordinarily high level of $\overline{ww}$ observed below the center of the primary recirculation bubble in figure 12 requires a closer inspection of the instantaneous flow field in this particular area. Two snap shots separated h/u_τ in time reveals a distinctly streaky pattern with elongated regions of either positive or negative w as can be seen in figure 14. The alternating positive and negative regions outweighs when the flow field is averaged in the spanwise direction, but nevertheless give rise to excessively high levels of $\overline{ww}$. The accompanying cross-flow in the $(y, z)-$plane $3h$ downstream of the step in figure 15 shows roughly circular cells of size of the order h with either clock-

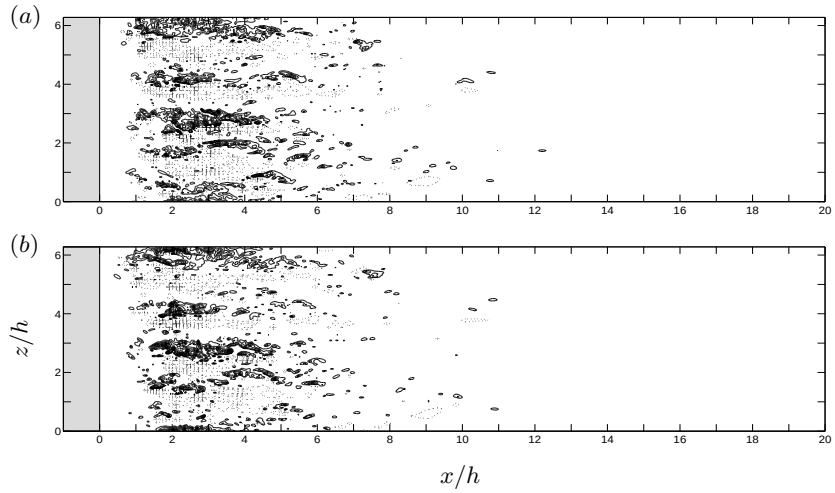

FIGURE 14. Contour plots of instantaneous spanwise velocity fluctuations (w/u_τ) for $Ro = 0.4$ close to the stepped wall. (a) $t = 10h/u_\tau$ and (b) $t = 11h/u_\tau$.

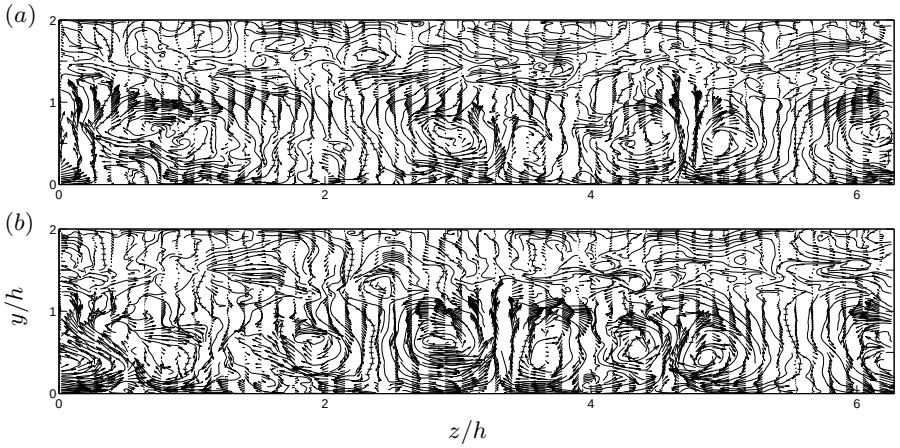

FIGURE 15. Instantaneous velocity vectors together with tangent lines projected into the $(y, z)-$plane at $x/h = 3$ for $Ro = 0.4$. (a) $t = 10h/u_\tau$ and (b) $t = 11h/u_\tau$.

wise or anticlockwise rotation. The cells seem to occur in pairs and resemble the roll cells observed earlier in fully developed rotating Poiseuille flow by Johnston *et al.* (1972) and Kristoffersen & Andersson (1993) and in rotating Couette flow by Bech & Andersson (1997). These cells are the rotational analogue of the Taylor-Görtler vortices arising from a centrifugal instability caused by streamline curvature. It should be recalled that the reattachment point X_{l2} of the primary bubble is at about $2.9h$, which means that the upstream halves of the present roll cells are in a region with predominantly reversed flow, whereas their downstream part extends $1 - 2h$ downstream of reattachment where the streamwise motion is in the positive direction. Such counter-rotating vortex cells have probably never been seen before in a region with mean-flow reversal.

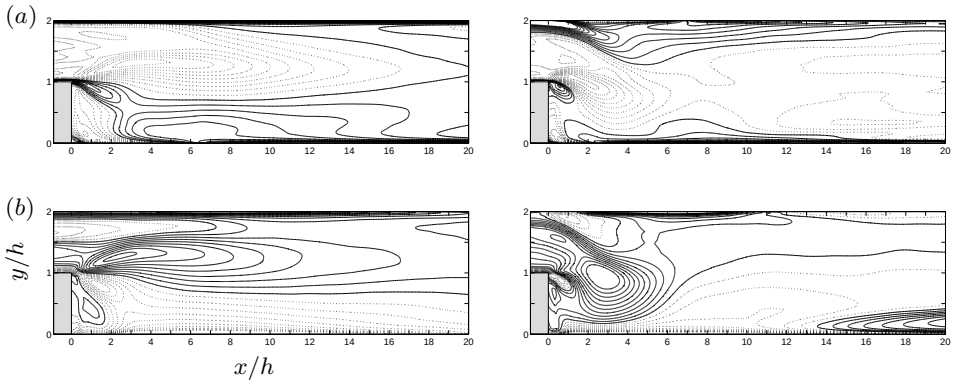

FIGURE 16. Third-order moment of the velocity fluctuations u_i for $Ro = 0.0$ (left) and $Ro = 0.4$ (right). (*a*) $S(u)$ and (*b*) $S(v)$. The contour level is 0.1 and the dotted lines represent negative values. The values for $S(w)$ are identically zero due to flow symmetry.

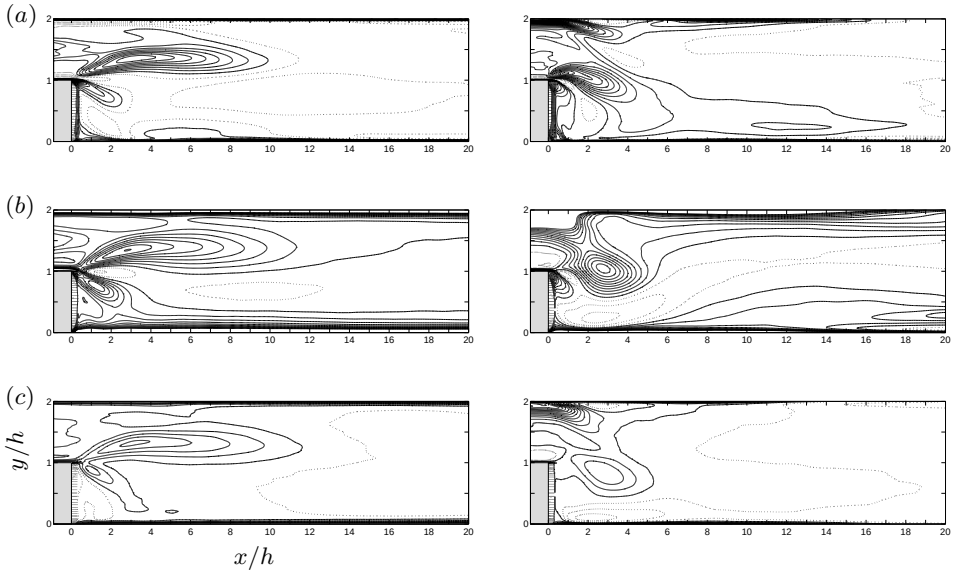

FIGURE 17. Fourth-order moment of the velocity fluctuations u_i for $Ro = 0.0$ (left) and $Ro = 0.4$ (right). (*a*) $F(u)$, (*b*) $F(v)$ and (*c*) $F(w)$. Contour increment of 0.1 is used and the solid contours indicate $F(u_i) > 3$ regions while $F(u_i) < 3$ areas are shown as dotted contours.

For the sake of completeness, the skewness S and the flatness F of the fluctuating velocity components are shown in figures 16 and 17, respectively. Both $S(u)$ and $S(v)$ have opposite signs in the two halves of the shear layer in the absence of rotation, but the skewness contours are not at all anti-symmetric as they would be in a free mixing-layer. The lack of symmetry between the upper and lower sides of the present shear layer is even more pronounced by the flatness. Large regions of high flatness are observed in the upper half of the shear layer. The skewness and flatness are substantially affected by the imposed system rotation. A wide zone with distinctly non-Gaussian turbulence ($S(v) > 0$

and $F(v) > 3$) is observed above the primary recirculation bubble. The particularly high levels of the flatness factors just upstream of the separation point at the upper wall reflect the intermittent nature of the flow in this region.

5. Energy considerations and second-moment budgets

The budgets of the individual components of the Reynolds stress tensor provide insight into the interactions between the large-scale turbulence and the mean flow. The major contributions to the budgets of the Reynolds stress components at the highest rotation rate are shown in figures 18-21. In order to assist in the interpretation of the budgets, it might be helpful to consider the production terms due to mean shear and rotation. The different production components for two-dimensional mean flow rotating about the spanwise $z-$axis are shown in Table 1.

It is well known that the mean shear only contributes to streamwise and wall-normal velocity fluctuations in two-dimensional flows. The system rotation introduces source terms both in the streamwise and wall-normal directions, whereas the fluctuations in the direction of the axis of rotation are directly unaffected. It is particularly noteworthy that the rotational terms in Table 1 cancel out if the second-moment equation (2.2) is contracted to give an equation for the turbulent kinetic energy. This is intuitively evident since the instantaneous Coriolis force always acts perpendicular to the instantaneous velocity vector. The Coriolis force can therefore neither produce work nor directly alter the energy of the flow.

The mean shear production P_{xx} is positive in both shear layers whereas the Coriolis production G_{xx} inevitably attains the same sign as $\overline{uv}$, cf figure 13(d). The system rotation thus tends to increase $\overline{uu}$ in the cyclonic shear layer and reduce $\overline{uu}$ in the anticyclonic shear layer. As already noticed, however, the streamwise velocity fluctuations are substantially enhanced for $Ro = 0.10$ and $Ro = 0.20$ in figure 10. Let us therefore rearrange the terms responsible for the production of streamwise fluctuations as:

$$P_{xx} + G_{xx} = -2\overline{uv}(S+1)\frac{\partial U}{\partial y} - 2\overline{uu}\frac{\partial U}{\partial x} + 2\overline{uv}S\frac{\partial V}{\partial x} \tag{5.1}$$

Here, S is the local vorticity ratio which is zero in the absence of rotation. In the anticyclonic regions with $S \approx -1$, the leading part of the Coriolis term outweighs the primary mean shear production and the first part to the right in equation (5.1) vanishes. The remaining two terms in (5.1) are associated with the non-parallel streamlines and contributes therefore only in the expansion region where the mean flow components U and V vary with x.

The mean shear production P_{yy} of wall-normal fluctuations is zero except in regions with streamwise variations of the mean flow. Downstream of the step, where the mean flow is bent towards the stepped surface, the negative $\partial V/\partial y$ contributes to a modest mean shear production of $\overline{vv}$. The rotational generation of wall-normal fluctuations is by far more influential and is the cause of the exceptionally high levels of $\overline{vv}$ at the anticyclonic side in figure 11. The adverse effect along the cyclonic side is not reflected in the data displayed in figure 11. In fact, it seems that the role of the rotational production

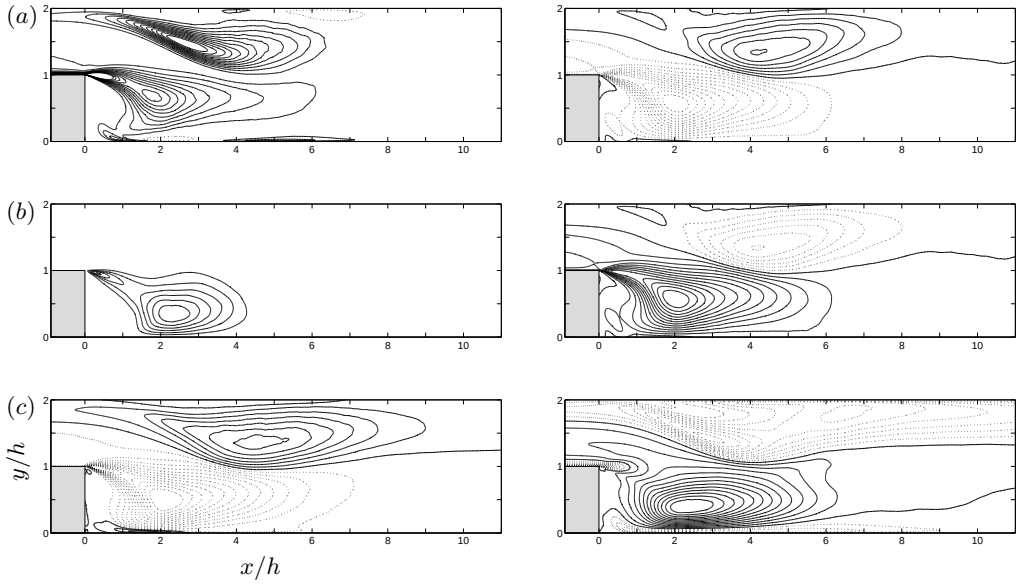

FIGURE 18. Mean shear production term P_{ij} (left) and rotational production term G_{ij} (right) for $Ro = 0.4$. The terms are scaled with u_τ^4/ν and contour increment of 0.1 is used. (a) streamwise production, (b) wall-normal production and (c) shear production.

in the cyclonic shear layer is to increase streamwise fluctuations rather than to damp wall-normal velocity fluctuations.

The aforementioned inability of the Coriolis force to directly affect the turbulent kinetic energy is demonstrated by figure 18 which shows that $G_{yy} = -G_{xx}$. Thus, with $G_{zz} = 0$, we also have $G_{ii} = 0$.

The primary source of mean shear production of $\overline{uv}$, i.e. $-\overline{vv}\partial U/\partial y$, changes sign at the inflection point of the mean velocity profiles shown in figure 5. The rotational production G_{xy}, on the other hand, remains negative at positive rotation rates as long as the conventional turbulence anisotropy $\overline{uu} > \overline{vv}$ persists. In the present case of strong rotation, however, the positive contours in figure 18(c) show that an anomalous anisotropy with $\overline{vv} > \overline{uu}$ has developed in the anti-cyclonic region.

The sources of the shear stress $-\overline{uv}$ can be rewritten in terms of the local vorticity ratio S as:

$$-P_{xy} - G_{xy} = \left[(S+1)\overline{vv} - S\overline{uu}\right]\frac{\partial U}{\partial y} + \left[(S+1)\overline{uu} - S\overline{vv}\right]\frac{\partial V}{\partial x} \approx \overline{uu}\frac{\partial U}{\partial y} - \overline{vv}\frac{\partial V}{\partial x} \quad (5.2)$$

The first part of this equation is generally valid for all two-dimensional mean flows subjected to spanwise rotation, whereas the rightmost side shows the outcome in zones with vanishing absolute vorticity, i.e. $S = -1$. Here, the major term left over stems from interactions between streamwise velocity fluctuations and the wall-normal component of the Coriolis force. The reduction of $-\overline{uv}$ at the highest rotation number in figure 13 is probably an outcome of the reversal of the turbulent anisotropy which makes $-G_{xy}$ negative rather than positive. The streamwise turbulence intensity required to maintain a

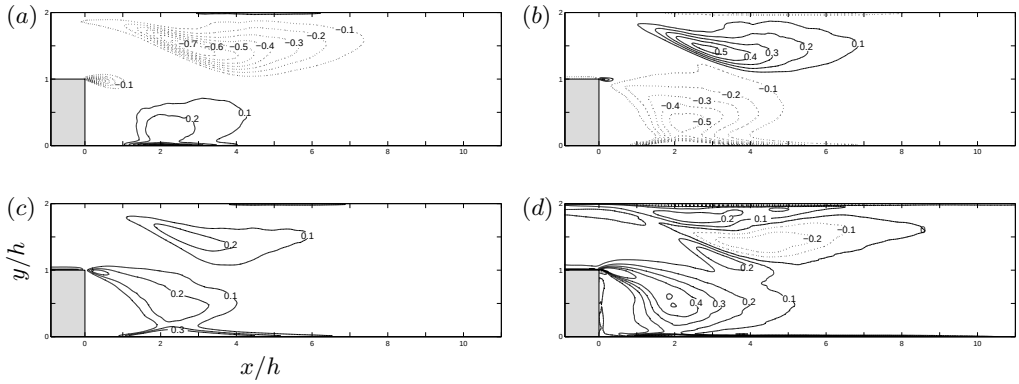

FIGURE 19. Pressure-strain term Π_{ij} for $Ro = 0.4$ scaled with u_τ^4/ν. Contour increment of 0.1 is used. (a) Π_{xx}, (b) Π_{yy}, (c) Π_{zz} and (d) Π_{xy}.

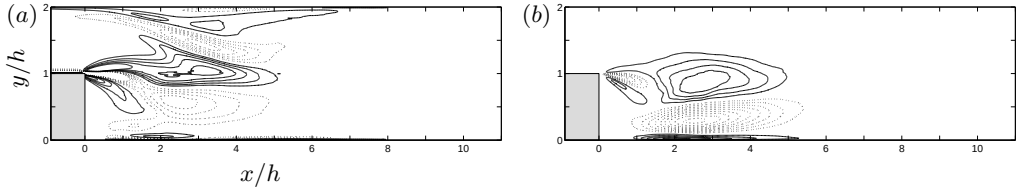

FIGURE 20. Turbulent diffusion term D_{ij}^T for $Ro = 0.4$ scaled with u_τ^4/ν. Contour increment of 0.1 is used. (a) D_{xx}^T and (b) D_{yy}^T. The other two components are almost negligible.

significant production of $-\overline{uv}$ through $\overline{uu}\partial U/\partial y$ is at the same time considerably reduced due to the cancellation of the primary source terms in (5.1) when $S = -1$.

The pressure-strain interaction terms Π_{ij} are known to play an important role in shear-flow turbulence. For example, Π_{zz} is the only source of spanwise fluctuations in a planar mean flow since both production terms are identically zero. Normally, turbulent energy is being transferred from the mean flow direction to the two other components of the fluctuating velocity vector, i.e. $\Pi_{xx} < 0$ whereas Π_{yy} and Πzz are positive. This is indeed the situation also in the cyclonic shear layer along the upper wall in the present case, as shown in figure 19. In the anti-cyclonic shear layer, on the contrary, the situation is reversed and energy is transferred from the wall-normal component ($\Pi_{yy} < 0$) and fed into the two other components by roughly equal amounts, as shown in figure 19.

The off-diagonal component Π_{xy} presented in figure 19(d) is positive in the anti-cyclonic shear layer and negative in the cyclonic shear layer and thus tends to assist the shear stress $-\overline{uv}$ in these areas. Similar tendency was observed in the anti-cyclonically rotating plane Couette flow by Barri & Andersson (2009). It is anyhow noteworthy that the magnitude of Π_{xy} is only roughly $1/3^{rd}$ of the mean-shear and rotation terms, whereas Π_{xy} is known to be the leading sink term in the budget in non-rotating shear flows.

The turbulent diffusion D_{ij}^T represents a spatial redistribution of turbulence caused by triple-correlations of the fluctuating velocity components. D_{xx}^T in figure 20(a) is responsible for a diffusive transport of streamwise fluctuations away from both the shear layers

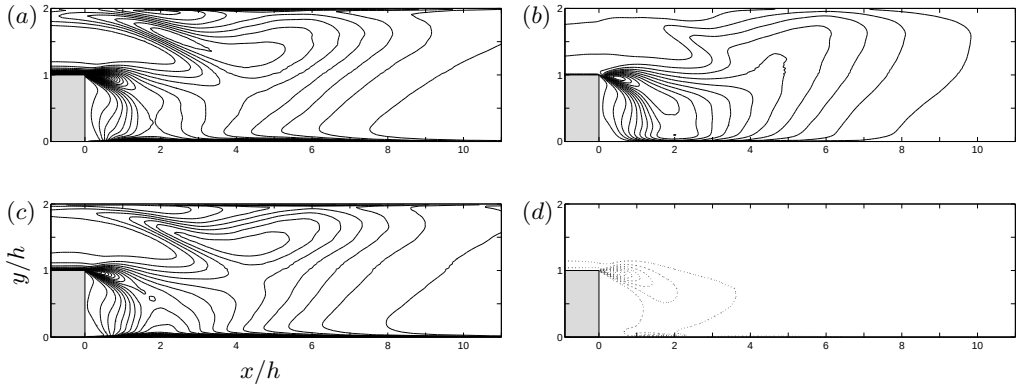

FIGURE 21. Viscous dissipation term ε_{ij} for $Ro = 0.4$ scaled with u_τ^4/ν. Contour increment of 0.1 is used. (*a*) ε_{xx}, (*b*) ε_{yy}, (*c*) ε_{zz} and (*d*) ε_{xy}.

and towards the central flow. Wall-normal fluctuations are on the other hand transported primarily against the gradient of $\overline{v^3}$ and thus away from the peak position of $S(v)$ in figure 16(*b*), i.e. towards the area just above the reattachment point.

The distribution of the non-zero components of the dissipation rate tensor ε_{ij} is presented in figure 21. Locally high levels of all of the diagonal components of ε_{ij} can be observed in the anti-cyclonic mixing zone just downstream of the step corner and even the off-diagonal component ε_{xy} attains an appreciable level in the vicinity of the step. In the cyclonic shear layer, which separates from the upper wall at this high rotation rate, fairly high levels of ε_{xx} and ε_{yy} can be seen. The slope of the isocontours in the downstream part of figure 21 simply reflects that the dissipation rate along the cyclonic side exceeds that at the anti-cyclonic side. This is consistent with the relatively higher turbulence levels along the cyclonic wall downstream of $x \sim 5h$.

6. Vorticity dynamics

The vorticity is an essential kinematic property of fluid motion, as illustrated by the snapshots of the flow field at different Ro shown in figure 22. A time sequence for $Ro-0.4$ shown in figure 23 in order to explain the significant increase in turbulence levels in the cyclonic region. The complex interaction between the cyclonic and anti-cyclonic shear layers is the main mechanism of transferring energy. During interaction the cyclonic recirculation bubble is splitted to mainly two smaller bubbles which interact and merge during the absence of shear layer interactions. Another important source of energy transfer is between the reattachment region of the anti-cyclonic shear layer and the smaller cyclonic bubble established far downstream.

An efficient scalar quantity frequently used to identify regions of localized vortices in a flow field is λ_2 introduced by Jeong & Hussain (1995) as the second largest eigenvalue of the tensor $s_{ik}s_{kj} + r_{ik}r_{kj}$ where s_{ij} and r_{ij} are the strain-rate and rotation-rate tensors, respectively. The distribution of the $rms-$value of λ_2 from the wall and towards the

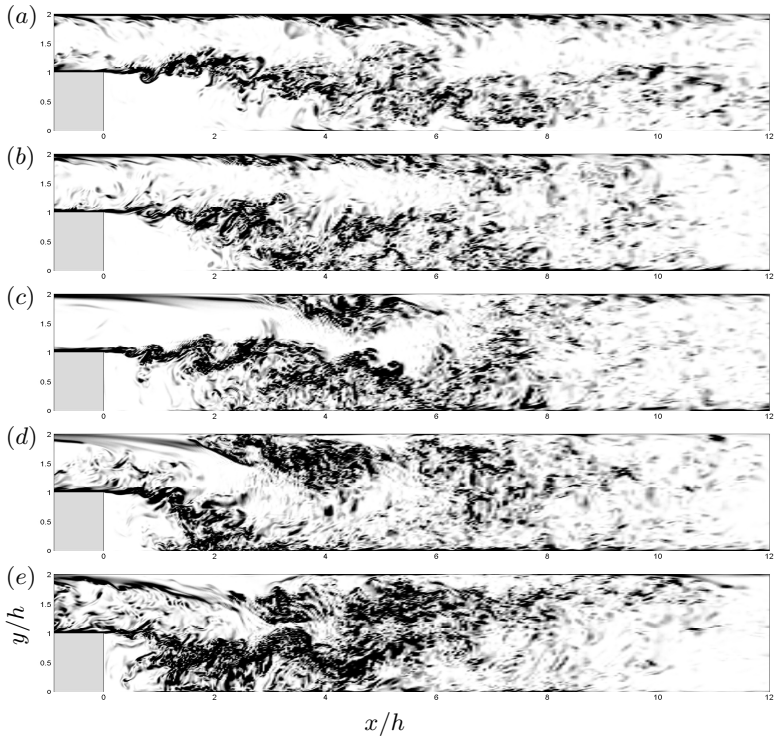

FIGURE 22. Contour plots of instantaneous enstrophy fluctuations $\omega_i\omega_i$ at the center of the channel at $t = 14h/u_\tau$. Dark contours indicate high energy regions. (*a*) $Ro = 0.0$, (*b*) $Ro = 0.05$, (*c*) $Ro = 0.1$, (*d*) $Ro = 0.2$ and (*e*) $Ro = 0.4$.

center is shown in figure 24. λ_{2rms} is normalized by u_τ^4/ν^2, i.e. the reciprocal of the viscous time scale ν/u_τ^2 squared.

6.1. *Mean vorticity and mean Lamb vector*

In contrast with rotating channel flows, the anti-cyclonically rotating backward-facing step does not exhibit a region with linear variation of the mean velocity profiles where the slope $\partial U/\partial y$ of the velocity profiles is close to $2\Omega^F$. This is due to the fact that the mean vortcity is $\Omega_z = \partial V/\partial x - \partial U/\partial y$ in the present case. For $Ro = 0.4$, the maximum value for $(\partial V/\partial x)/(\partial U/\partial y)$ is about 0.3 and found to be in the anti-cyclonic shear layer. This shows that the mean velocity profiles cannot adjust itself to have a linear slope even though the mean flow vorticity Ω_z just counterbalances the imposed anti-cyclonic background vorticity $2\Omega^F$, i.e. the absolute vorticity in an inertial frame-of-reference is driven to zero.

The velocity-vorticity correlations present in the mean vorticity equation (2.4) are associated with the Lamb vector:

$$\boldsymbol{\lambda} = \boldsymbol{u} \times \boldsymbol{\omega} \tag{6.1}$$

The above definition of the instantaneous Lamb vector is the same as that adopted by Orlandi (1997) and Liu & Lu (2007). The mean value $\boldsymbol{\Lambda}$ of the instantaneous Lamb

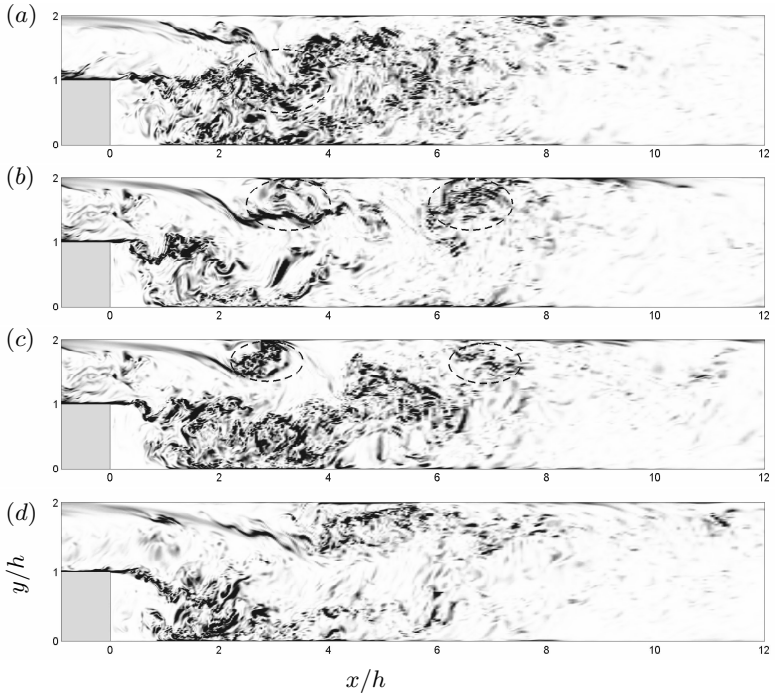

FIGURE 23. Time sequence of instantaneous enstrophy fluctuations $\omega_i\omega_i$ at the center of the channel for $Ro = 0.4$. (*a*) $t = 10h/u_\tau$, (*b*) $t = 11h/u_\tau$, (*c*) $t = 12h/u_\tau$ and (*d*) $t = 13h/u_\tau$.

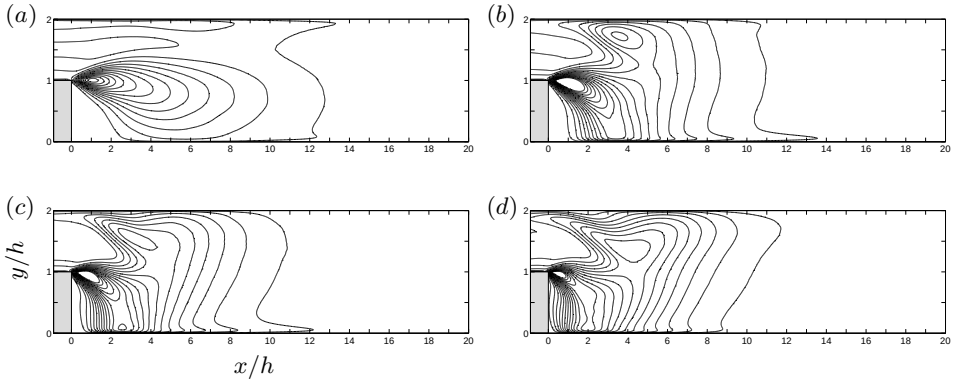

FIGURE 24. Variations of λ_{2rms} scaled with u_τ^4/ν^2. Contour increment of 0.003 is used. (*a*) $Ro = 0.0$, (*b*) $Ro = 0.1$, (*c*) $Ro = 0.2$ and (*d*) $Ro = 0.4$.

vector $\boldsymbol{\lambda}$ lies entirely in the $(x, y)-$plane, i.e. $\Lambda_z = 0$, due to symmetries. The two non-zero components are in the present case:

$$\Lambda_x = \overline{v\omega_z} - \overline{w\omega_y} + V\Omega_z \quad \text{and} \quad \Lambda_y = \overline{w\omega_x} - \overline{u\omega_z} - U\Omega_z \tag{6.2}$$

This representation for the Lamb vector allow us to re-write the mean vorticity equation (2.4) as follow:

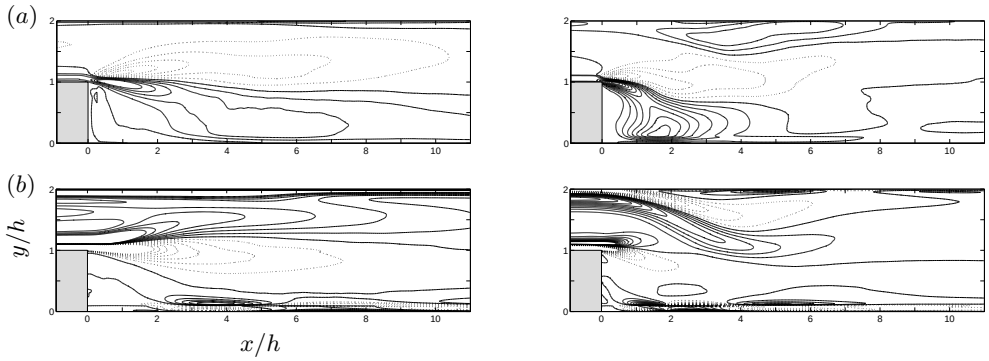

FIGURE 25. Individual terms in the mean vorticity equation (6.3). (a) Λ_x and (b) $\frac{\partial}{\partial y}(\Lambda_x - \nu\frac{\partial \Omega_z}{\partial y})$. $Ro = 0.0$ is to the left and $Ro = 0.4$ is to the right. Contour level is 0.001.

$$\frac{\partial}{\partial x}(\Lambda_y + \nu\frac{\partial \Omega_z}{\partial x}) = \frac{\partial}{\partial y}(\Lambda_x - \nu\frac{\partial \Omega_z}{\partial y}) \tag{6.3}$$

For unidirectional mean flows equation (6.3) simplifies and can be integrated once to give:

$$\Lambda_x = -\nu\frac{d^2U}{dy^2} \tag{6.4}$$

The $x-$component of the mean Lamb vector is shown in figure 25(a). Λ_x is substantially higher in the rotating flow than in absence of rotation. Fairly high positive levels are observed in the cyclonic recirculation bubble at the planar surface and even higher positive values are obtained in the primary separation bubble at the anti-cyclonic wall. This suggests that the interaction between the large scales $\mathbf{u}$ and the small-scale turbulence ω is enhanced when the flow is subjected to system rotation. The viscous term to the left in eq. 6.3 is negligible almost everywhere. The deviation of the right-hand side from zero is associated with the non-parallel streamlines in the vicinity of the step. The contour plot of the right-hand side of eq. 6.3 in figure 25(b) shows that the simplified balance (6.4) is not at all fulfilled in the neighborhood of step, i.e. for $x < 10h$.

6.2. *Enstrophy and vorticity budgets*

The root-mean-square values of the fluctuating vorticity components are shown in figure 26. The only resemblance with conventional wall-flow behaviour is that the wall-normal vorticity goes to zero at the wall simply as a result of the no-slip condition. While spanwise vorticity fluctuations $\overline{\omega_z^2}$ normally dominates in the near-wall region, see e.g. Antonia & Kim (1994), the streamwise vorticity $\overline{\omega_x^2}$ is by far more intense in the anti-cyclonic region. A distinct and anomalous anisotropy prevails with $\overline{\omega_x^2} > \overline{\omega_z^2} > \overline{\omega_y^2}$ in the anti-cyclonic region, while an axisymmetric turbulence ($\overline{\omega_x^2} \approx \overline{\omega_z^2} > \overline{\omega_y^2}$) has been noticed in the cyclonic region. The anisotropy of the vorticity tensor resembles that downstream of the step in the non-rotating simulation.

Following Antonia & Kim (1994), the behaviour of the individual vorticity components

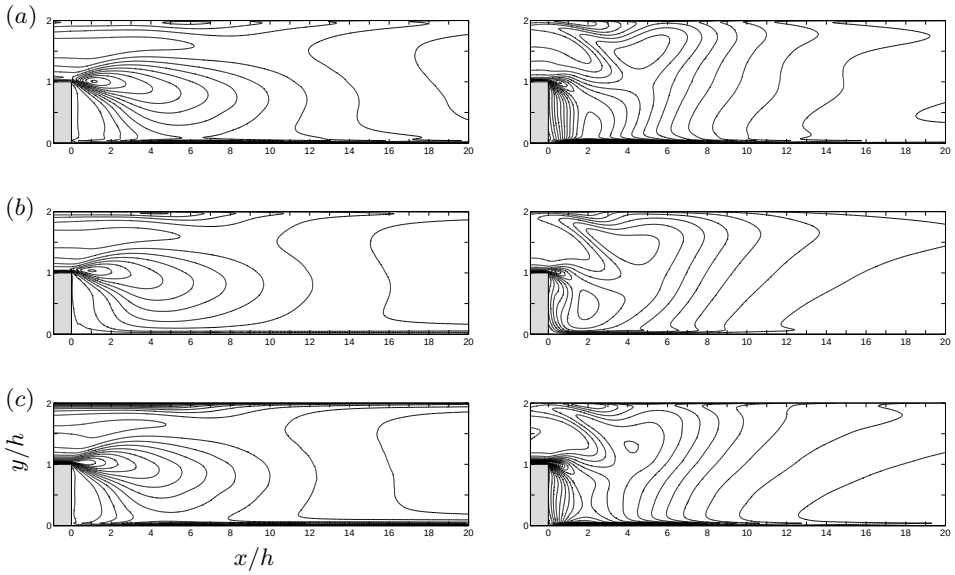

FIGURE 26. Root-mean-square vorticity fluctuations $\omega_{i_{rms}}$ for $Ro = 0.0$ (left) and $Ro = 0.4$ (right) scaled by u_τ^2/ν. Contour increment of 0.02 is used. (*a*) $\omega_{x_{rms}}$, (*b*) $\omega_{y_{rms}}$ and (*c*) $\omega_{z_{rms}}$.

can be further explored by examining the dominating terms in the contracted second-moment equation (2.5). In the present context, the stretching term $S5_{ij}$ is of particular concern. Tennekes & Lumley (1972) referred to this term as a mixed production term. In a rotating frame-of-reference, this is the only term in the second-moment vorticity budgets that explicitly includes the system rotation; see equation (A13) in the Appendix.

The enstrophy balance is readily obtained as the trace of equation (2.5), i.e. as the sum of the diagonal terms of the individual second-moments of the vorticity fluctuations. The rotational contribution to the stretching term $S5$ does not vanish when the indices are contracted in equation (2.5). However, in the zero absolute vorticity region where the vorticity ratio $S \approx -1.0$, the two parts $S5^I_{ij}$ and $S5^{II}_{ij}$ due to mean flow stretching and rotational stretching, respectively, cancel out as can be seen in figure 27(*e*). On the other hand, the stretching term $S5_{ij}$ plays a dominant in the cyclonic shear layer. It is noteworthy to recall that the enstrophy is an important indicator of regions with high energy dissipation levels. The enstrophy budget in figure 27 shows that the shear layers are the major contributors of enstrophy and energy dissipation.

7. Anisotropy invariant mapping

To further examine the anisotropy of the rotating Couette flow, anisotropy invariant maps (AIM) are presented in figure 28. Here, these are derived on the basis of the anisotropy tensors:

$$a_{ij} \equiv \frac{\overline{u_i u_j}}{2k} - \frac{1}{3}\delta_{ij} \tag{7.1}$$

$$d_{ij} \equiv \frac{\overline{\omega_i \omega_j}}{2\omega^2} - \frac{1}{3}\delta_{ij} \tag{7.2}$$

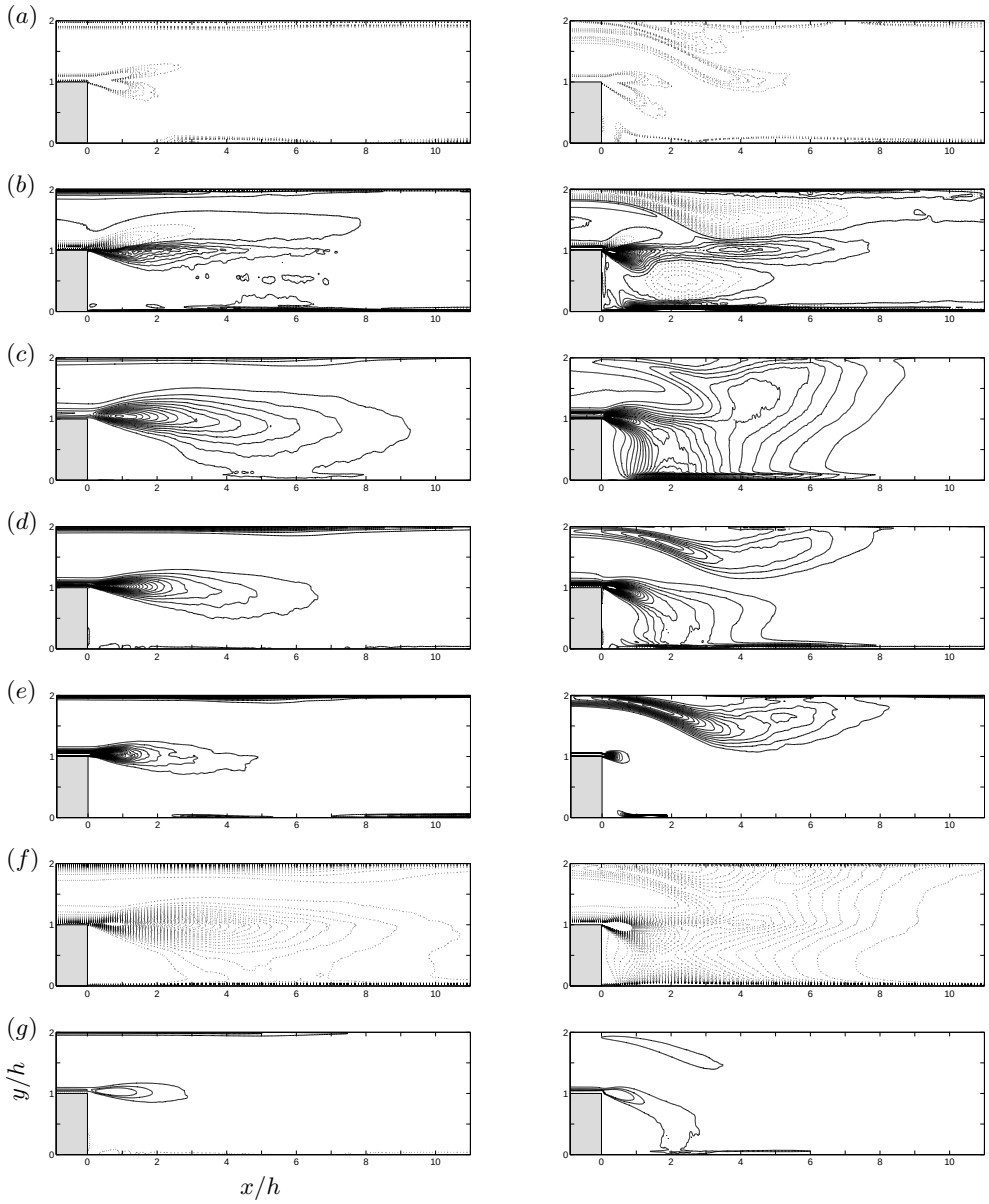

FIGURE 27. Enstrophy budget $\frac{1}{2}\overline{\omega_i\omega_i}$ for $Ro = 0.0$ (left) and $Ro = 0.4$ (right). The individual terms are scaled with $(u_\tau^2/\nu)^3$. Contour increment of 0.01 is used. (*a*) $T1_{ii}$, (*b*) $T2_{ii}$, (*c*) $S3_{ii}$, (*d*) $S4_{ii}$, (*e*) $S5_{ii}$, (*c*) $V7_{ii}$ and (*c*) $U_k\partial\overline{\omega_i\omega_i}/\partial x_k$.

The socalled Lumley triangle is drawn in the (-II, III)–plane where II and III are the second and third invariant of the anisotropy tensor, see Lumley & Newman (1977). However, all paths start somewhere at the upper boarder of the triangle, i.e. at the $1D$ branch where u_{rms} is the dominant turbulence intensity and ω_{zrms} exceeds the two other components of the fluctuating vorticity. This common feature shared by the non-rotating and the strongly rotating flows is somewhat surprising in view of the fact that the both

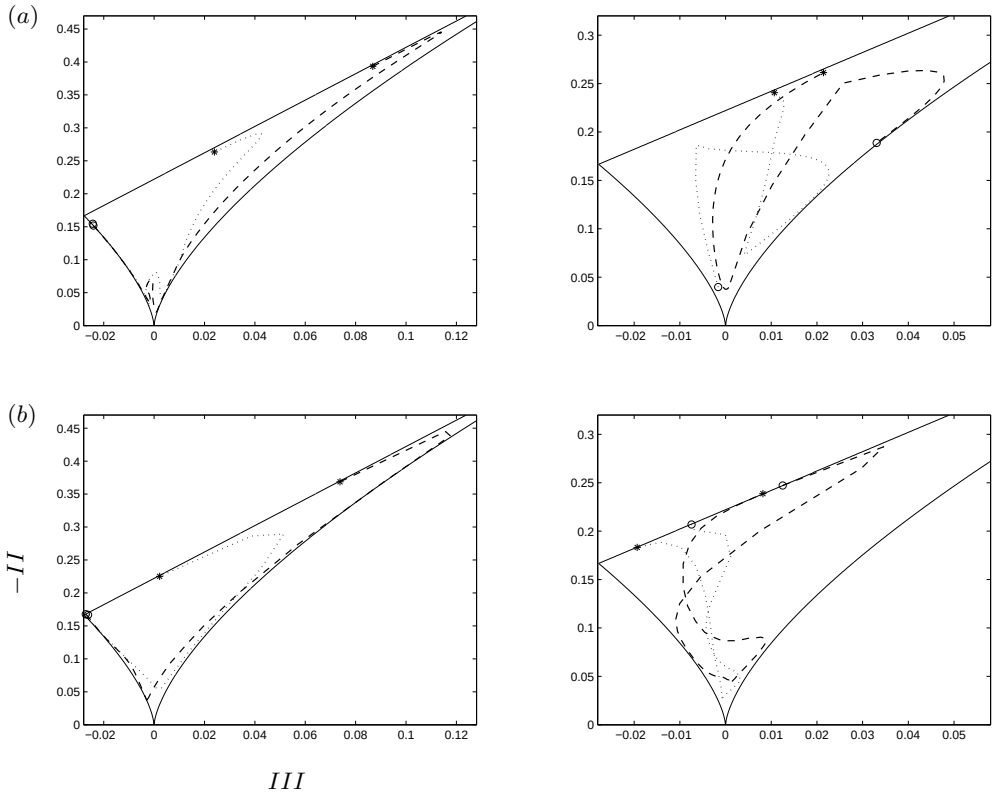

FIGURE 28. Anisotropy invariant maps for $Ro = 0.0$ (left) and $Ro = 0.4$ (right). (a) Reynolds stress ansotropy a_{ij} and (b) vorticity correlation anisotropy d_{ij}. $---$ and $\cdots$ are the center and the reattachment of the anti-cyclonic bubble, respectively. The straight wall (*) and the stepped wall (o).

paths start within the cyclonic separation bubble at the upper wall. Without rotation, the paths terminate near the left-hand corner of the triangle, which implies that the flow in the primary anti-clockwise separation bubble again approaches the $1D$ limit, but now with the two minor components being nearly equal; i.e. disk-like. For $Ro = 0.4$, on the other hand, the Reynolds stress tensor approaches a disk-like state just underneath the anti-cyclonic recirculation bubble and tends to an isotropic state at the reattachment point. The vorticity field behaves completely different and approaches a $1D$ state also at the stepped surface.

In the absence of system rotation, the paths followed by the anisotropy tensors in the AIM−maps in figure 28 exhibit roughly the same shapes. In the presence of strong system rotation, on the other hand, a_{ij} and d_{ij} follow rather different paths. It is particularly noteworthy that the anisotropy of the vorticity tensor behaves completely different from that of the Reynolds stress tensor.

8. Discussion and concluding remarks

The present computer experiments have demonstrated that the Coriolis force due to imposed system rotation gives rise to a number of different effects. The most readily accessible is the major alterations in the mean streamline pattern. The monotonic reduction of the primary separation bubble up to $Ro = 0.20$ is consistent with the experimental data provided by Rothe & Johnston (1979). The present $Ro = 0.40$ case, however, suggests that this tendency saturates at higher rotation rates (inaccessible in the apparatus used in the experimental study). The reduced separation distance from about 7 to 3 step heights is ascribed to the augmentation of the cross-stream turbulence intensity in the shear-layer formed between the bulk flow and the recirculating eddy due to the destabilizing influence of the Coriolis force. It is well established that the centrifugal force associated with streamline curvature exhibits similar effects on the turbulence field as the Coriolis force. The curvature of the free shear-layer emanating from the corner of the step would tend to reduce the turbulence relative to a parallel shear-flow. The observed amplification of the turbulence intensities demonstrates therefore that the Coriolis force dominates over the centrifugal force in the present flow cases.

Rothe & Johnston (1979) argued that the increased entrainment tended to reduce the base pressure, increase the streamline curvature, and thus reduce the reattachment distance. The base pressure is, however, increasing with increasing rotation rates, primarily due to the pressure rise required in order to balance the wall-normal component of the mean Coriolis force.

The spanwise-oriented vortex cells or roller-eddies found in non-rotating shear-layers were disrupted by the enhanced turbulence level, even at the lowest rotation number. This is in accordance with the observations reported by Rothe & Johnston (1979) on the basis of their flow visualizations and the pictures of anti-cyclonically rotating mixing-layers by Bidokhti & Tritton (1992).

Exceptionally high velocity fluctuations in the spanwise direction are observed in the vicinity of re-attachment zone behind the step. Inspections of instantaneous flow fields revealed the existence of longitudinal Taylor-Görtler-like roll-cells in the reattachment zone. Roll-cells, which result from a shear-Coriolis instability, have been observed before in rotating Poiseuille flows, both in laboratory experiments by Johnston *et al.* (1972) and computer simulations by Kristoffersen & Andersson (1993). Such longitudinal vortices were, however, not observed in the rotating free shear layer studied by Bidokhti & Tritton (1992) who therefore conjectured that the concurrent presence of the Kelvin-Helmholtz instability mechanism prevented Taylor-Görtler cells to occur. It is particularly noteworthy that the roll cells found in the present study are observed in the vicinity of the stagnation zone where the mean flow changes its direction.

The flow along the planar wall is subjected to an adverse pressure gradient induced by the sudden expansion. The stabilizing influence of the system rotation in this cyclonic shear layer tends to damp the turbulence and the flow becomes susceptible to flow separation. A substantial recirculation bubble is indeed observed at the higher rotation rates. The streamwise extent of this cyclonic bubble increases from about $3h$ at $Ro = 0.10$ to $6h$ at the highest rotating rate considered. Rothe & Johnston (1979) focused their attention

on the free shear layer and the reattachment zone at the stepped wall and did not report on the flow along the opposite side.

Flow separation effectively acts as an undesired blockage of the flow passage and may severely deteriorate the performance of a rotating device like a centrifugal impeller. In the present configuration, the meandering of the bulk flow caused by the blockage promotes the interactions between the anti-cyclonic shear layer at the stepped side and the cyclonic shear flow along the planar surface. These give rise to unexpectedly high turbulence levels at the cyclonic side in spite of the otherwise stabilizing influence of the Coriolis force.

A particular feature of the backward-facing step configuration considered herein is that the effective rotation number is four times higher downstream of the step than in the upstream, although the effective bulk flow Reynolds number remains the same. The flow field is statistically homogeneous in the spanwise direction and the mean flow and the turbulence statistics are therefore independent of z and time t. This makes the present flow configuration an attractive model problem for CFD codes aimed for turbo-machinery applications. The two-dimensionality of the mean fluid motion makes the mean strain rate $\partial U/\partial y + \partial V/\partial x$ different from the mean rotation rate $-\partial U/\partial y + \partial V/\partial x$ downstream of the sudden expansion. This distinction, which vanishes in uniform shear flows like the plane Poiseuille flow, becomes of relevance for instance in turbulence modelling where the mean shear rate rather than the mean rotation rate is affecting the Reynolds stress levels.

The support for this work from the Research Council of Norway through a research grant (contract no 171725/V30) and grants of computing time (Programme for Supercomputing) is gratefully acknowledged. Further access to the IBM p575+ distributed shared-memory (DSM) system was granted by the Research Programme in Computational Science and Visualization (BVV) at The Norwegian University of Science and Technology. Professor J.P. Johnston (Stanford University) kindly provided us with the tabulated reattachment-length data shown in figure 4.

Appendix. Second-moment transport equations in a rotating frame-of-reference

The transport equation (2.2) for the individual components of the second-moments $\overline{u_i u_j}$ of the velocity fluctuations is written in quasi-symbolic form. The various terms on the right-hand side are defined in Cartesian tensor notation as follows:

$$P_{ij} \equiv -\overline{u_i u_k}\frac{\partial U_j}{\partial x_k} - \overline{u_j u_k}\frac{\partial U_i}{\partial x_k} \tag{A 1}$$

$$G_{ij} \equiv -2\Omega_k^F(\overline{u_j u_m}\varepsilon_{ikm} + \overline{u_i u_m}\varepsilon_{jkm}) \tag{A 2}$$

$$D_{ij} = D_{ij}^T + D_{ij}^P + D_{ij}^V \tag{A 3}$$

$$\Pi_{ij} \equiv \overline{\frac{p}{\rho}\left(\frac{\partial u_i}{\partial x_j} + \frac{\partial u_j}{\partial x_i}\right)} \tag{A 4}$$

$$\varepsilon_{ij} \equiv 2\nu\overline{\left(\frac{\partial u_i}{\partial x_k}\frac{\partial u_j}{\partial x_k}\right)} \tag{A 5}$$

where the different parts of the diffusion are given by

$$D_{ij}^T \equiv -\frac{\partial}{\partial x_k}(\overline{u_i u_j u_k}) \tag{A 6}$$

$$D_{ij}^P \equiv -\frac{1}{\rho}\frac{\partial}{\partial x_k}(\overline{pu_i}\delta_{jk} + \overline{pu_j}\delta_{ik}) \tag{A 7}$$

$$D_{ij}^V \equiv \nu\left(\frac{\partial^2\overline{u_i u_j}}{\partial x_k \partial x_k}\right) \tag{A 8}$$

Here, ε_{ijk} is the permutation or *Levi-Civita* tensor. This organization of the terms in the second-moment transport equation follows Launder *et al.* (1987). The turbulent diffusion due to velocity (D_{ij}^T) and pressure (D_{ij}^P) fluctuations and the viscous diffusion (D_{ij}^V) are labeled collectively as a single diffusion term D_{ij}.

Similarily, the transport equation (2.5) for the individual components of the second-moments $\overline{\omega_i\omega_j}$ of the vorticity fluctuations was written in quasi-symbolic form, where the various terms on the right-hand side are defined as follows:

$$T1_{ij} \equiv -\overline{\omega_i u_k}\frac{\partial \Omega_j}{\partial x_k} - \overline{\omega_j u_k}\frac{\partial \Omega_i}{\partial x_k} \tag{A 9}$$

$$T2_{ij} \equiv -\overline{u_k\frac{\partial \omega_i\omega_j}{\partial x_k}} \tag{A 10}$$

$$S3_{ij} \equiv \overline{\omega_i\omega_k\frac{\partial u_j}{\partial x_k}} + \overline{\omega_j\omega_k\frac{\partial u_i}{\partial x_k}} \tag{A 11}$$

$$S4_{ij} \equiv \overline{\omega_j\omega_k}S_{ik} + \overline{\omega_i\omega_k}S_{jk} \tag{A 12}$$

$$S5_{ij} = S5_{ij}^I + S5_{ij}^{II} \equiv (\Omega_k + 2\Omega_k^F)(\overline{s_{ik}\omega_j} + \overline{s_{jk}\omega_i}) \tag{A 13}$$

$$V6_{ij} \equiv \nu\frac{\partial^2\overline{\omega_i\omega_i}}{\partial x_k \partial x_k} \tag{A 14}$$

$$V7_{ij} \equiv -2\nu\overline{\left(\frac{\partial \omega_i}{\partial x_k}\frac{\partial \omega_j}{\partial x_k}\right)} \tag{A 15}$$

Here, S_{ij} and s_{ij} denote the mean and fluctuation parts of the instantaneous strain-rate tensor. Notice that $\mathbf{\Omega}^F$ denotes the constant angular velocity of the steadily rotating

frame-of-reference whereas $1/2\boldsymbol{\Omega}$ is the mean angular velocity associated with the fluid motion, i.e. half the mean vorticity $\nabla \times \boldsymbol{U}$. The stretching term $S5_{ij}$ has been split in two parts in order to distinguish between the roles played by mean fluid rotation ($S5^I$) and system rotation ($S5^{II}$). By contraction of the indices i and j in the above terms the enstrophy budget equation is recovered. The notion of transport (T), stretching (S), and viscous (V) terms follows Lamballais *et al.* (1996), whereas the numbering refers to the order of the terms in Antonia & Kim (1994), which in turn referred to equation (3.3.38) and the accompanying discussion in Tennekes & Lumley (1972).

REFERENCES

Antonia, R. A. & Kim, J. 1994 Low-Reynolds-number effects on near-wall turbulence. *J. Fluid Mech.* **276**, 61–80.

Barri, M. & Andersson, H. I. 2009 Computer experiments on rapidly rotating plane Couette flow. *Commu. Comput. Phys., DOI: 10.4208/cicp.2009.09.068* .

Barri, M., El Khoury, G. K., Andersson, H. I. & Pettersen, B. 2009a Inflow conditions for inhomogeneous turbulent flows. *Int. J. Numer. Meth. Fluids* **60**, 227–235.

Barri, M., El Khoury, G. K., Andersson, H. I. & Pettersen, B. 2009b DNS of backward-facing step flow with fully turbulent inflow. *Int. J. Numer. Meth. Fluids, DOI: 10.1002/fld.2176* .

Bech, K. H. & Andersson, H. I. 1997 Turbulent plane Couette flow subject to strong system rotation. *J. Fluid Mech.* **347**, 289–314.

Bidokhti, A. A. & Tritton, D. J. 1992 The structure of a turbulent free shear layer in a rotating fluid. *J. Fluid Mech.* **241**, 469–502.

Brethouwer, G. 2005 The effect of rotation on rapidly sheared homogeneous turbulence and passive scalar transport. Linear theory and direct numerical simulation. *J. Fluid Mech.* **542**, 305–342.

Cambon, C., Benoit, J.-P., Shao, L. & Jacquin, L. 1994 Stability analysis and large-eddy simulation of rotating turbulence with organized eddies. *J. Fluid Mech.* **278**, 175–200.

Gartling, D. K. 1990 A test problem for outflow boundary conditions-flow over a backward-facing step. *Int. J. Numer. Meth. Fluids* **11**, 953–967.

Grundestam, O., Wallin, S. & Johansson, A. V. 2008 Direct numerical simulation of rotating turbulent channel flow. *J. Fluid Mech.* **598**, 177–199.

Iida, O., Tsukamoto, Y. & Nagano, Y. 2008 The tilting mechanism of a longitudinal vortical structure in a homogenous shear flow with and without spanwise shear. *Flow, Turbulence Combust.* **81**, 17–37.

Jeong, J. & Hussain, F. 1995 On the identification of a vortex. *J. Fluid Mech.* **285**, 69–94.

Johnston, J. P. 1998 Effects of system rotation on turbulence structure: a review relevant to turbomachinery flows. *Int. J. Rotating Machin.* **4**, 97–112.

Johnston, J. P., Halleen, R. M. & Lezius, D. K. 1972 Effects of spanwise rotation on the structure of two-dimensional fully developed turbulent channel flow. *J. Fluid Mech.* **56**, 533–557.

Kasagi, N. & Matsunaga, A. 1995 Three-dimensional particle-tracking velocimetry measurment of turbulent statistics and energy budget in a backward facing flow. *Int. J. Heat Fluid Flow* **16**, 477–485.

Kim, J., Moin, P. & Moser, R. 1987 Turbulence statistics in fully developed channel flow at low Reynolds number. *J. Fluid Mech.* **177**, 133–166.

Kristoffersen, R. & Andersson, H. I. 1993 Direct simulations of low-Reynolds-number turbulent flow in a rotating channel. *J. Fluid Mech.* **256**, 163–197.

Lamballais, E., Lesieur, M. & Métais, O. 1996 Effects of spanwise rotation on the vorticity stretching in transitional and turbulent channel flow. *Int. J. Heat Fluid Flow* **17**, 324–332.

Lamballais, E., Métais, O. & Lesieur, M. 1998 Spectral-dynamic model for large-eddy simulation of turbulent rotating channel flow. *Theoret. Comput. Fluid Dynamics* **12**, 149–177.

Launder, B. E., Tselepidakis, D. P. & Younis, B. A. 1987 A second-moment closure study of rotating channel flow. *J. Fluid Mech.* **183**, 63–75.

Le, H., Moin, P. & Kim, J. 1997 Direct numerical simulation of turbulent flow over a backward-facing step. *J. Fluid Mech.* **330**, 349–374.

Liu, N.-S. & Lu, X.-Y. 2007 A numerical investigation of turbulent flows in a spanwise rotating channel. *Comput. Fluids* **36**, 282–298.

Lumley, J. L. & Newman, G. R. 1977 The return to isotropy of homogeneous turbulence. *J. Fluid Mech.* **82**, 161–178.

Manhart, M. 2004 A zonal grid algorithm for DNS of turbulent boundary layers. *Comput. Fluids* **33**, 435–461.

Métais, O., Flores, C., Yanase, S., Riley, J. J. & Lesieur, M. 1995 Rotating free-shear flow. part2. numerical simulations. *J. Fluid Mech.* **293**, 47–80.

Nakabayashi, K. & Kitoh, O. 1996 Low Reynolds number fully developed two-dimensional turbulent channel flow with system rotation. *J. Fluid Mech.* **315**, 1–29.

Nakabayashi, K. & Kitoh, O. 2005 Turbulence characteristics of two-dimensional channel flow with system rotation. *J. Fluid Mech.* **528**, 355–377.

Orlandi, P. 1997 Helicity fluctuations and turbulent energy production in rotating and non-rotating pipes. *Phys. Fluids* **9**, 2045–2056.

Orlanski, I. 1976 A simple boundary condition for unbounded hyperbolic flows. *J. Comp. Physics* **21**, 251–269.

Rothe, P. H. & Johnston, J. P. 1979 Free shear layer behavior in rotating systems. *J. Fluids Eng.* **101**, 117–120.

Salhi, A. & Cambon, C. 1997 An analysis of rotating shear flow using linear theory and DNS and LES results. *J. Fluid Mech.* **347**, 171–195.

Tennekes, H. & Lumley, J. L. 1972 *A First Course in Turbulence*. MIT Press.

Yanase, S., Tanaka, M., Kida, S. & Kawahara, G. 2004 Generation and sustenance mechanisms of coherent vortical structures in rotating shear turbulence of zero-mean-absolute vorticity. *Fluid Dyn. Research* **35**, 237–254.

Paper 11

Turbulent flow in a sudden-expansion channel. Part II: Effects of cyclonic system rotation

Barri, M. & Andersson, H. I.

Manuscript to be submitted to *Journal of Fluid Mechanics*.

Turbulent flow in a sudden-expansion channel. Part II: Effects of cyclonic system rotation

MUSTAFA BARRI AND HELGE I. ANDERSSON

Fluids Engineering Division, Department of Energy and Process Engineering
Norwegian University of Science and Technology (NTNU), 7491 Trondheim, Norway

(Received 14 September 2009)

Turbulent flow in a sudden-expansion channel subject to system rotation around the spanwise axis is explored by means of direct numerical simulations. The effect of Coriolis force is often said to be stabilizing at the cyclonic recirculation regions (and destabilizing on the anti-cyclonic regions). The present computer experiments reveal a more subtle influence of the cyclonic system rotation on sudden-expansion flows while the anti-cyclonic effect was presented in Part I. The backward-facing step configuration is rotated cyclonically about the spanwise axis. The upstream flow is a fully-developed plane channel flow subjected to orthogonal-mode rotation, which detaches from the step corner and eventually reattaches further downstream. The size of the resulting separation bubble significantly increases with low-moderate rotation rates and the reattachment distance is increased by factor of two. This is ascribed to the reduction of the cross-stream turbulence intensity in the shear-layer due to the stabilization effect of the Coriolis force. Further increasing in the rotation rate leads to a valuable reduction in the size of the recirculation bubble. In this particular rotation range, the flow downstream of the step is almost two-dimensional since variations along the span have been quenched.

1. Introduction

The effects of system rotation are known to have important impact on the turbulent flow pattern in various engineering and geophysical applications. The Coriolis force which arises from the system rotation gives rise to fascinating flow phenomena both in wall-bounded and free shear flows.

Wall-bounded shear flows subjected to system rotation have been extensively investigated in laboratory and computer experiments. The thorough experimental measurements of rotating channel flow by Johnston *et al.* (1972) were complemented by direct numerical simulations by Kristoffersen & Andersson (1993). These and other studies showed that the mean velocity profile was distorted by the system rotation and tended to develop a localized region in which the mean flow vorticity balanced the system rotation. In the rotating channel flow, the turbulence was damped adjacent to the *cyclonic*

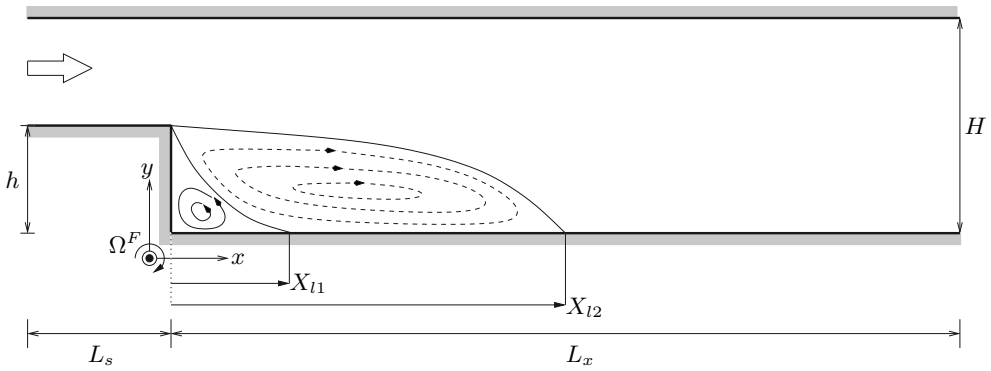

FIGURE 1. Schematic of spanwise rotating sudden-expansion flow (BFS). The system is rotating with constant angular velocity $-\Omega^F$ about the spanwise $z-$axis.

side where the mean flow vorticity vector is parallel to the rotation vector whereas the turbulent agitation was enhanced near the *anticyclonic* side where the mean flow vorticity is anti-parallel with the imposed rotation. Anticyclonic rotation gave also rise to a secondary-motion in the cross-sectional plane. Rotating channel flows are inevitably exposed simultaneously to cyclonic and anticyclonic rotation.

In free shear flows, the rotating wake is exposed simultaneously to cyclonic and anticyclonic rotation, whereas the rotating mixing-layer is subjected only to cyclonic or anticyclonic rotation. The illuminating experimental investigation of rotating backward-facing step by Rothe & Johnston (1979) is of great impact to our understanding about separated-reattached flows subjected to system rotation. Bidokhti & Tritton (1992) confirmed the existence of Kelvin-Helmholtz rollers in all cyclonic cases (and high anti-cyclonic rotation rates) where the three-dimensionality of the turbulent flow is suppressed. The direct and large-eddy simulations by Métais *et al.* (1995) confirmed the two-dimensionalization effect of cyclonic and rapid anti-cyclonic rotation.

The effect of system rotation on detached, reattached and massive recirculated flows is still not well understood. The anti-cyclonic system rotation effect on sudden-expansion channel is studied in Part I. The aim of the present manuscript is to explore the effects of cyclonic rotating frame-of-reference on turbulent flow in separated-reattached configuration. To this end the plane backward-facing step, which has been used in Part I, will be considered.

The present investigation is a natural continuation of our work in Part I. To this end, we consider the turbulent flow over a backward-facing step subjected to cyclonic rotation in the free shear-layer ,i.e. the flow along the stepped wall, and anti-cyclonic along the opposite planar surface, as illustrated in figure 1. The primary recirculation bubble is also cyclonic whereas the secondary corner-eddy, if any, is anti-cyclonic. The major aim of the present work is to study the effect of cyclonically rotating frame-of-reference on the shear layer downstream of the step and the recirculation bubbles. The result will be compared with the experimental data for the reattachment distance by Rothe & Johnston (1979).

The turbulence level is known to be enhanced along the anti-cyclonic side of a rotating channel. Therefore, no separation can be expected on the planar wall in contrast with the observation found at the cyclonic-planar-wall in Part I.

2. Flow configuration and governing equations

Let us consider the turbulent flow in an infinitely long planar channel geometry with a one-sided sudden expansion, i.e. the so-called *backward-facing step* configuration depicted in figure 1. All the details kept to be the same as in Part I except the direction of rotation which is here anti-parallel to the spanwise axis. The expansion ratio $ER = H/(H-h)$ is taken to be 2 at a Reynolds number $Re = \rho U_b(H-h)/\mu$ of about 5600 based on the upstream bulk velocity U_b and the upstream channel height $H-h$. The amount of system rotation is expressed in terms of the upstream rotation number $Ro = \Omega^F(H-h)/U_{bo}$, where U_{bo} denotes the upstream bulk velocity in the absence of rotation. Only cyclonic rotation, i.e. $\Omega^F < 0$, will be considered in the present article whereas results for anti-cyclonic rotation were presented in a companion paper (Part I).

The incompressible flow of a Newtonian fluid in a constantly rotating frame-of-reference is governed by the conservation equations for mass and momentum:

$$\nabla \cdot \boldsymbol{u} = 0 \tag{2.1a}$$

$$\frac{\partial \boldsymbol{u}}{\partial t} + \boldsymbol{u} \cdot \nabla \boldsymbol{u} = -\frac{1}{\rho}\nabla p + \nu \nabla^2 \boldsymbol{u} - 2\boldsymbol{\Omega}^F \times \boldsymbol{u} \tag{2.1b}$$

where ν is the kinematic viscosity μ/ρ. The last term on the right-hand side of equation (2.1b) is the Coriolis force due to system rotation, whereas centrifugal effects are absorbed in the effective pressure p.

The instantaneous velocity components u_i and pressure p can be decomposed into mean (U_i, P) and fluctuating (u_i, p) parts to facilitate both the presentation and interpretation of the outcome of the simulations. The mean flow becomes two-dimensional $(U, V, 0)$ and the mean pressure P serves to drive the flow through the stepped channel configuration and at the same time to balance the wall-normal component of the Coriolis force. The transport equation for the individual second-moments can be written as follows:

$$\frac{D\overline{u_i u_j}}{Dt} = P_{ij} + G_{ij} + D_{ij} + \Pi_{ij} - \varepsilon_{ij} \tag{2.2}$$

The right-hand-side terms, which are responsible for production due to mean shear (P_{ij}), production due to rotation (G_{ij}), viscous and turbulent diffusion (D_{ij}), pressure-strain redistribution (Π_{ij}), and viscous energy dissipation (ε_{ij}), are defined in the Appendix.

3. Computer simulations

Direct numerical simulations of turbulent flow over a backward-facing step were performed for a wide range of upstream rotation numbers ($Ro = 0$, -0.05, -0.10, -0.20, -0.30, -0.40, -0.50 and -0.60). The upstream bulk Reynolds number $Re \approx 5600$ in the present simulations is only marginally below the Reynolds number ≈ 5900 in the

simulations by Kristoffersen & Andersson (1993). Irrespective of the rotation number considered in the present study, the wall-friction $Re_\tau = \rho u_\tau (H-h)/\mu$ was kept equal to 360, i.e. exactly the same value as in the plane Poiseuille flow simulations of Kim *et al.* (1987) and marginally lower than $Re_\tau = 388$ in the rotating channel flow simulations by Kristoffersen & Andersson (1993).

The simulations were performed with the second-order accurate finite-volume code MGLET; see Manhart (2004). Coriolis body force terms were implemented into the discretized momentum equations. The three-dimensional governing equations (2.1) were integrated forward in time until a statistically steady state was reached. The results for the non-rotating case $Ro = 0$ compared perfectly well with the accurate PIV data provided by Kasagi & Matsunaga (1995) from an $ER = 1.5$ set-up at a slightly lower step Reynolds number Re_h. Both mean velocity profiles and turbulent statistics in the separated zone, near reattachment, and in the recovery region were compared by Barri *et al.* (2009b). The results for the anti-cyclonic simulations $Ro > 0$ have been studied in the previous paper (Part I).

3.1. *Computational domain and grid resolution*

The length of the computational domain was $L_x + L_s = 32h + 6h = 38h$ in streamwise direction, $L_y = H = 2h$ in the wall-normal direction and $L_z = 6.28h$ in the spanwise direction. The upstream length L_s before the sudden expansion was taken as $6h$. The grid resolution was kept the same for all different simulation cases where the number of grid points was $864 \times 256 \times 200$ in the $x-$, $y-$ and $z-$directions, respectively. The computational domain size and the grid resolution were kept to be the same as in the anti-cyclonic rotation in Part I.

Precursor simulations of fully developed Poiseuille flow subjected to cyclonic system rotation about the spanwise axis have been used in order to establish realistic fully developed inflow boundary conditions at the entrance region of the cyclonically rotating backward-facing step. The duration t_s of each finite-length time series was $2h/u_\tau$, which is twice as long as recommended by Barri *et al.* (2009a) to assure representative inflow conditions comprising a wide range of time and length scales. Separate precursor simulations were run for each of the eight rotation numbers. On the other hand, the convective boundary condition has been used as outflow condition. Provided that the exit boundary is sufficiently downstream of the step, the influence of the streamwise component of the mean Coriolis force has become vanishingly small and can therefore be ignored.

4. Mean flow pattern and primary turbulence statistics

The attention of this section is focused on the mean flow just downstream of the expansion, which encompasses the shear layer which develops from the sharp corner as well as the zones with separated and reattaching flow. The results in the far downstream of the step will generally not be shown. Throughout the presentation and discussion of the results, negative rotation rates $-\Omega^F < 0$ (i.e. clockwise rotation in figure 1) will be

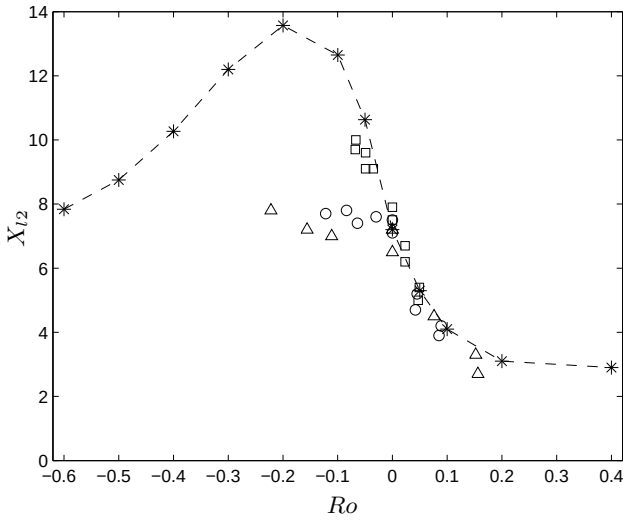

FIGURE 2. Positions of mean flow reattachment X_{l2}, as defined in figure 1. △, ∘ and □ are experimental data from Rothe & Johnston (1979) for Reynolds numbers 3000, 5500 and 10000, respectively. – ∗ – X_{l2}.

referred to as *cyclonic* since the system rotation is parallel to the mean flow rotation along the stepped wall upstream of the sudden expansion.

4.1. *Mean flow pattern*

The location of the reattachment point of the primary cyclonic bubble in the eight different flow cases is summarized in figure 2. The experimental data points by Rothe & Johnston (1979) for $Re = 3000$ and 5000 indicate a roughly constant reattachment distance X_{l2} about $7.5h$. On the other hand, the present simulations show approximately a linear region for rettachment distance for low-moderate rotation rates. The reattachment point is increased and reaches it maximum value at rotation number about $Ro = -0.2$. Further increase in the system rotation changes the trend of increasing the bubble size and instead the reattachment point is reduced and reach a value of $8h$ at the highest rotation case $Ro = -0.6$.

Mean velocity profiles $U(x, y)$ are presented in figure 3 at some characteristic streamwise locations. The strongest backflow ($U < 0$) is observed in the core of the primary recirculation bubble. The strong effects of rotation can be observed from the mean velocity profiles $24h$ downstream of the step. In the non-rotating case the profile compares surprisingly well with the fully-developed flow profile from the DNS of Kim *et al.* (1987). For the two lowest rotation numbers $Ro = -0.05$ and -0.10, comparisons are made with the profiles of Kristoffersen & Andersson (1993) for $Ro = -0.20$ and -0.50, respectively (data for $Ro = -0.40$ is not available). The mean velocity profiles seem to be far from being re-developed into those of a fully-developed rotating channel.

The variation of the local skin-friction coefficient $C_f = \tau_w(x)/\rho u_\tau^2$ downstream of the expansion is shown in figure 4. The multiple zero-crossings of C_f at low rotation rates

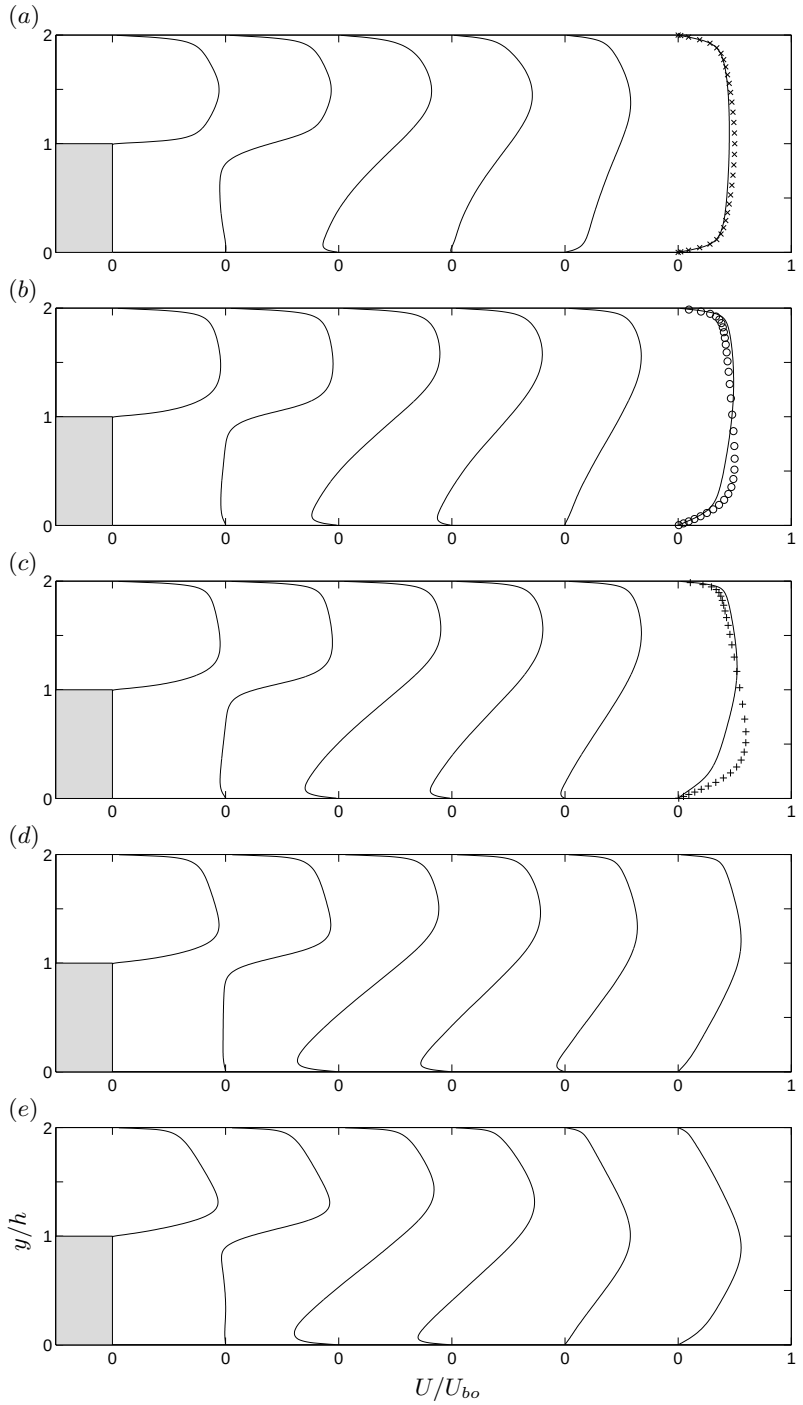

FIGURE 3. Mean streamwise velocity distribution at different streamwise locations $x/h = 0, 1, 2, 4, 7$ and 24. (a) $Ro = 0.0$, (b) $Ro = -0.05$, (c) $Ro = -0.1$, (d) $Ro = -0.2$ and (e) $Ro = -0.4$. $\times$ is DNS data for non-rotating plane Poiseuille flow from Kim *et al.* (1987), $\circ$ and $+$ are DNS data from Kristoffersen & Andersson (1993) for $Ro = -0.2$ and -0.5, respectively.

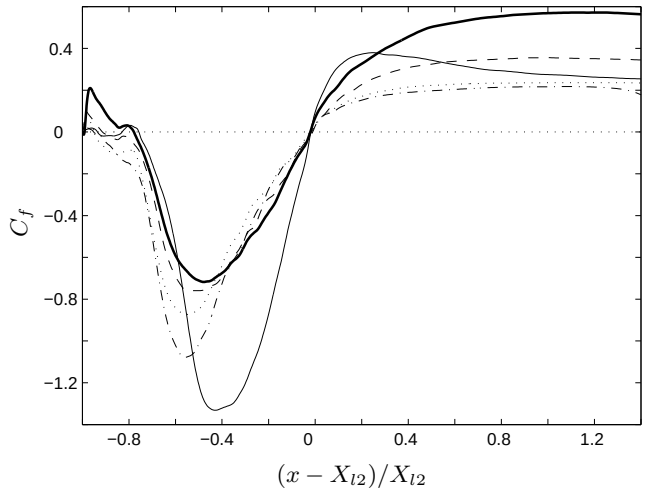

FIGURE 4. Variations of the skin friction coefficient C_f along the stepped wall. (bold line) $Ro = 0.0$, – – – $Ro = -0.05$, $\cdots$ $Ro = -0.1$, – · – $Ro = -0.2$, —— $Ro = -0.4$.

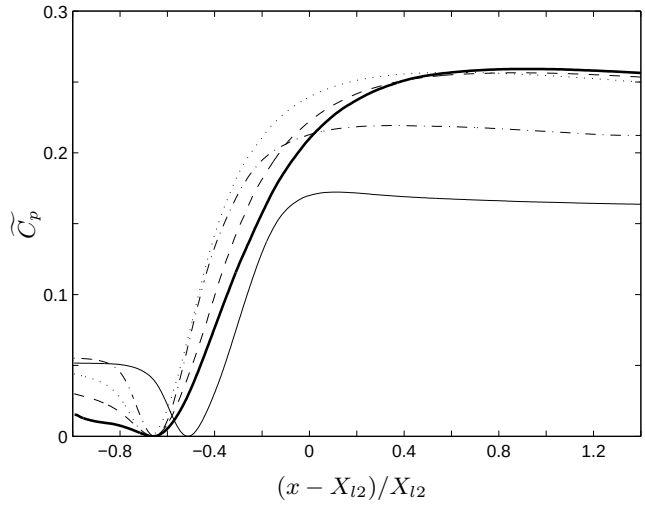

FIGURE 5. Variations of the pressure coefficient $\widetilde{C_p}$ along the stepped wall. (bold line) $Ro = 0.0$, – – – $Ro = -0.05$, $\cdots$ $Ro = -0.1$, – · – $Ro = -0.2$, —— $Ro = -0.4$.

confirm the existence of the primary ($C_f < 0$) and secondary ($C_f > 0$) separation bubbles at the lower wall. At higher rotation rates, the C_f curves show that the crossing point for the secondary corner-bubble is almost disappers. This means either the small bubble is quenched or, maybe, lifted up from the lower wall. The local skin-friction coefficient gradually approaches a constant level in the re-development zone. However, a complete recovery has not been attained even at $x = 30h$. A nearly complete symmetry between the two sides has been reached in the non-rotating case. C_f at the cyclonic side of the channel shows a monotonic decrease with increasing rotation.

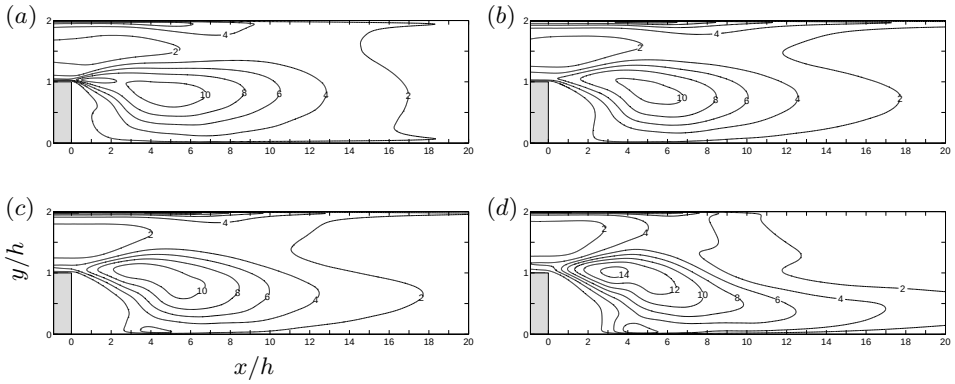

FIGURE 6. Streamwise Reynolds stress $\overline{uu}$ scaled with u_τ^2. (*a*) $Ro = 0.0$, (*b*) $Ro = -0.1$, (*c*) $Ro = -0.2$ and (*d*) $Ro = -0.4$.

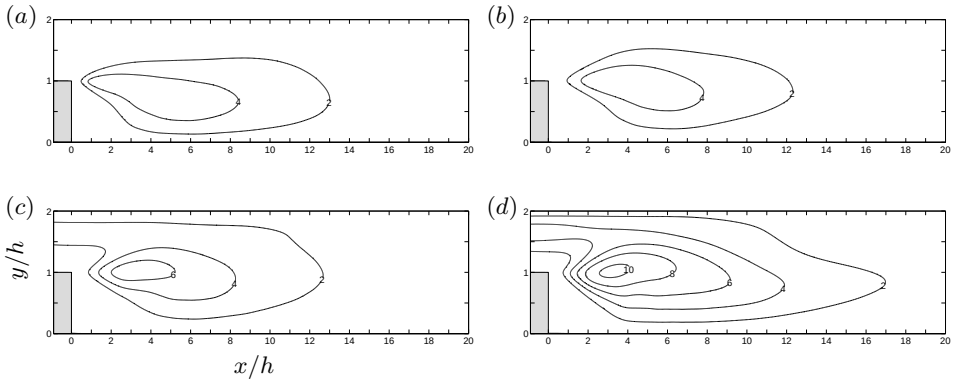

FIGURE 7. Wall-normal Reynolds stress $\overline{vv}$ scaled with u_τ^2. (*a*) $Ro = 0.0$, (*b*) $Ro = -0.1$, (*c*) $Ro = -0.2$ and (*d*) $Ro = -0.4$.

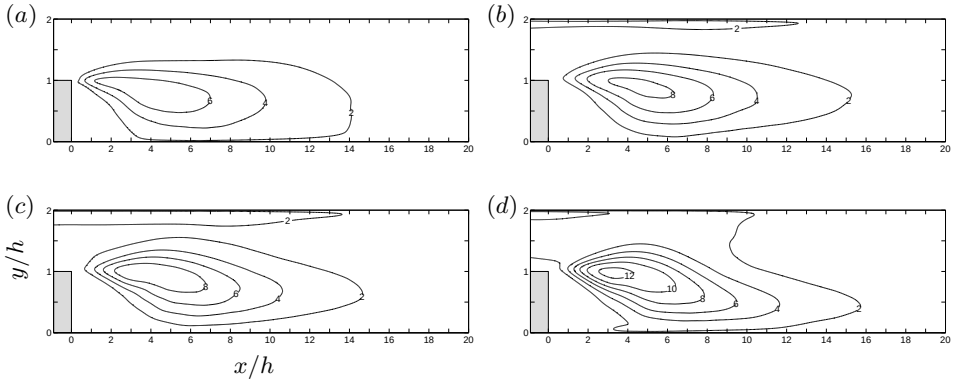

FIGURE 8. Spanwise Reynolds stress $\overline{ww}$ scaled with u_τ^2. (*a*) $Ro = 0.0$, (*b*) $Ro = -0.1$, (*c*) $Ro = -0.2$ and (*d*) $Ro = -0.4$.

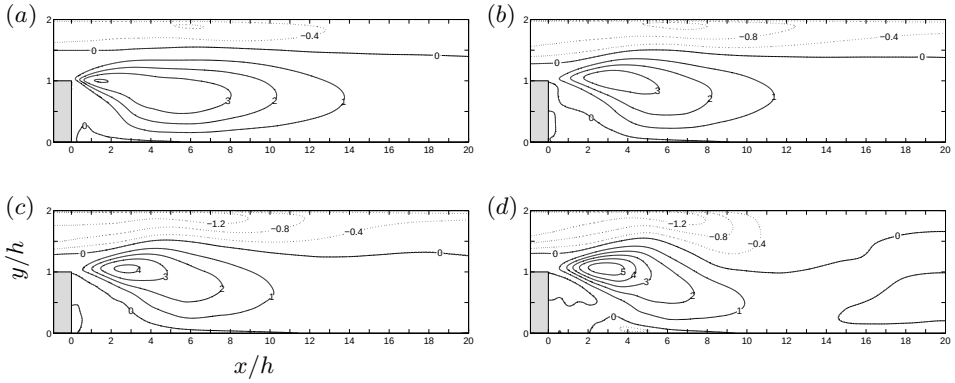

FIGURE 9. Reynolds shear stress $-\overline{uv}$ scaled with u_τ^2. (*a*) $Ro = 0.0$, (*b*) $Ro = -0.1$, (*c*) $Ro = -0.2$ and (*d*) $Ro = -0.4$.

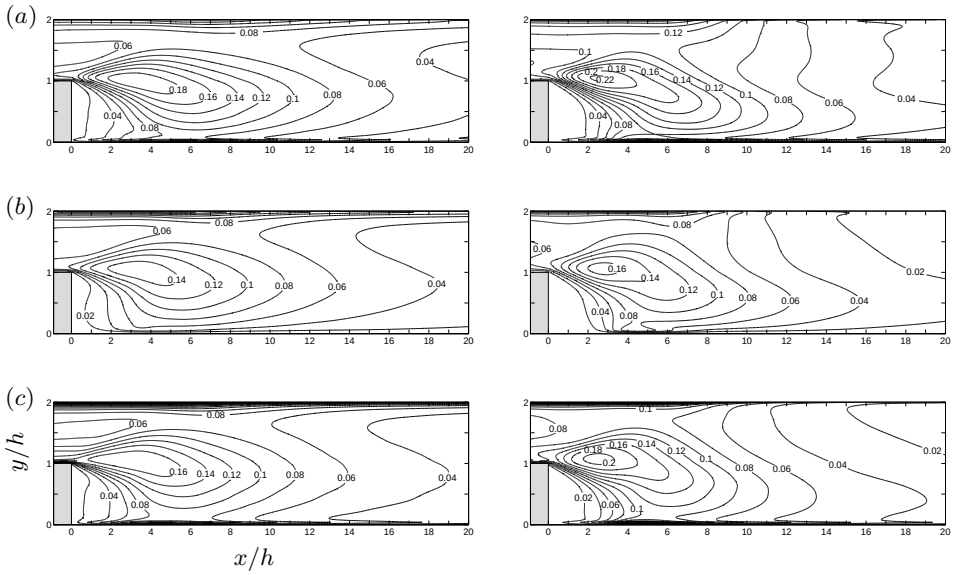

FIGURE 10. Root-mean-square vorticity fluctuations ω_{irms} for $Ro = -0.1$ (left) and $Ro = -0.4$ (right) scaled by u_τ^2/ν. Contour increment of 0.02 is used. (*a*) ω_{xrms}, (*b*) $\omega_{y_{rms}}$ and (*c*) ω_{zrms}.

The local wall pressure coefficient is defined as $\widetilde{C_p} = (C_p - C_{p_{min}})/(1 - C_{p_{min}})$, where $C_p = (P - P_o)/\frac{1}{2}\rho U_{bo}^2$ and $C_{p_{min}}$ is the minimum value of C_p. The reference pressure P_o and the bulk velocity U_{bo} are taken at the inflow section of the non-rotating case. In figure 5, C_p exhibits a local minimum close to the position of maximum backflow, i.e. beneath the core of the primary anti-cyclonic separation bubble. The pressure then recovers and attains a local maximum somewhat downstream of reattachment. Downstream of the recovery region, the mean pressure exhibits a linear variation with streamwise location x. This reflects that the constant and favourable streamwise pressure gradient required to drive the flow further downstream has been established.

4.2. *Primary turbulence characteristics*

The different second-moments of the velocity fluctuations, i.e. $\overline{u_i u_j}$, are shown in figures 6−9. Even though the turbulent kinetic energy is not directly affected by the imposed rotation, both the turbulence level and the anisotropy of the turbulence are severely changed.

The streamwise fluctuations $\overline{uu}$ in the cyclonic mixing-layer just downstream of the step is lower for $Ro = -0.1$ than in the non-rotating case. At higher rotation rates, the velocity fluctuations are slightly increased at $Ro = -0.2$ whereas a substantial enhancement occurs for $Ro = -0.4$. The low levels of streamwise fluctuations observed for low rotation rates cannot be explained by the rotational term $G_{xx} = 4\Omega^F \overline{uv}$.

The wall-normal fluctuations shown in figure 7 reduced at low-moderate rotation rates in the primary cyclonic separation bubble downstream of the step. This reduction can directly be associated with the Coriolis term $G_{yy} = -4\Omega^F \overline{uv}$ which acts as a gradually increasing source term. Even the velocity fluctuations in the spanwise direction are affected by the rotation, as seen in figure 8. However, neither the mean shear nor the Coriolis force tend to alter this velocity component (both P_{zz} and G_{zz} are zero) and the changes in $\overline{ww}$ in figure 8 are therefore due to other mechanisms. Pressure-strain interactions are known to be a primary source of spanwise velocity fluctuations in parallel shear flows which, possibly, can explain such changes in the spanwise component.

The Reynolds shear stress $-\overline{uv}$ in figure 9 changes sign across the stepped channel just as in a planar channel flow. The magnitude of $-\overline{uv}$ reduces with low-moderate rotation rates in the cyclonic shear-layer region. This reduction seems to be correlated with the wall-normal velocity fluctuations. The lower levels of the wall-normal fluctuations will tend to promote the mean shear production P_{xy}, whereas the Coriolis production $G_{xy} = -2\Omega^F(\overline{uu} - \overline{vv})$ makes a negative contribution to $-\overline{uv}$ along the cyclonic side.

The root-mean-square values of the fluctuating vorticity components are shown in figure 10. The only resemblance with conventional wall-flow behaviour is that the wall-normal vorticity goes to zero at the wall simply as a result of the no-slip condition. A distinct and anomalous anisotropy prevails with ($\overline{\omega_x^2} \approx \overline{\omega_z^2} > \overline{\omega_y^2}$) has been noticed in the cyclonic region. The anisotropy of the vorticity tensor resembles that downstream of the step in the non-rotating simulation.

5. Second-moment budgets

The major contributions to the budgets of the Reynolds stress components at low and high rotation rates are shown in figures 11-13. The mean shear production P_{xx} and the Coriolis production G_{xx} are positive in cyclonic shear layer whereas the Coriolis production G_{xx} inevitably attains the same sign as $\overline{uv}$, cf figure 11(a) and figure 12(a). The system rotation thus tends to increase $\overline{uu}$ in the shear layer. As already noticed, however, the streamwise velocity fluctuations are enhanced for $Ro = -0.20$ and $Ro = -0.40$ in figure 6.

The rotational production $G_{yy} = -4\Omega^F \overline{uv}$ becomes negative, thereby reducing the

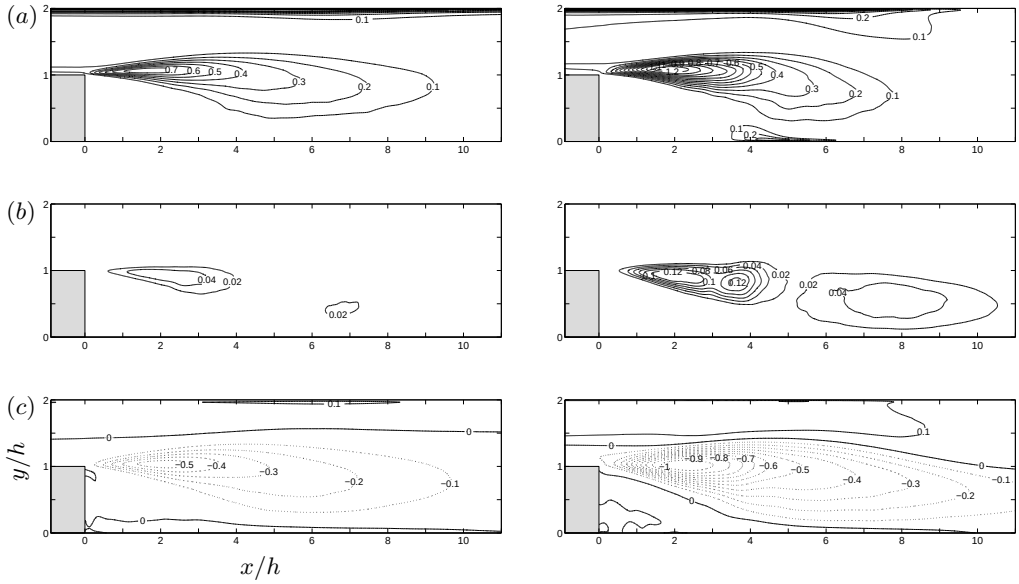

FIGURE 11. Mean shear production term P_{ij} scaled with u_τ^4/ν for $Ro = -0.1$ (left) and $Ro = -0.4$ (right). (*a*) P_{xx}, (*b*) P_{yy} and (*c*) P_{xy}.

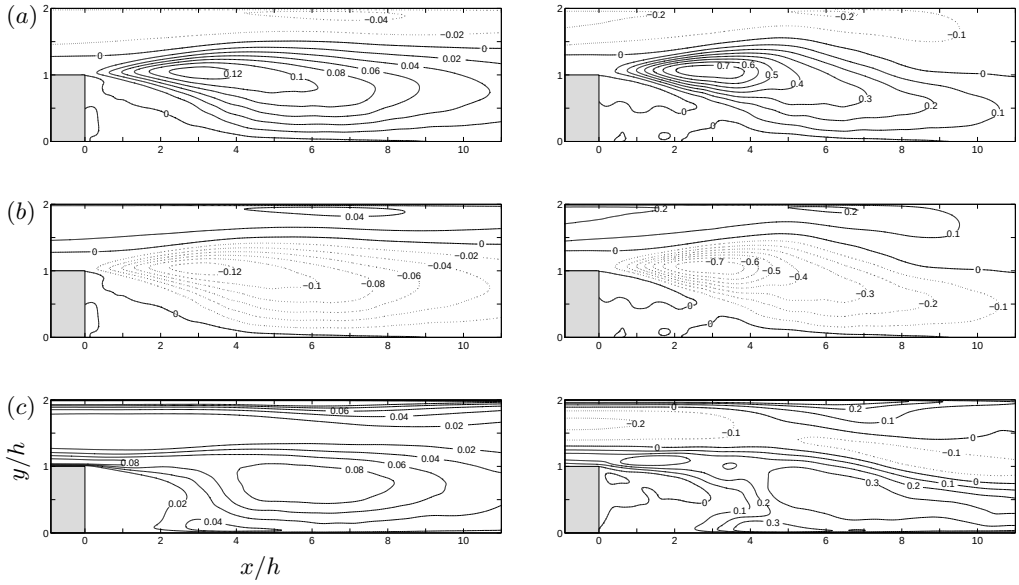

FIGURE 12. Rotational production term G_{ij} scaled with u_τ^4/ν for $Ro = -0.1$ (left) and $Ro = -0.4$ (right). (*a*) G_{xx}, (*b*) G_{yy} and (*c*) G_{xy}.

wall-normal fluctuations $\overline{vv}$ in figure 7(*b*) in comparison with the non-rotating case. By reducing the wall-normal fluctuations the magnitude of the shear production P_{xy} is also reduced, and the shear stress level $-\overline{uv}$ is further reduced by the rotational production $G_{xy} = -2\Omega^F(\overline{uu} - \overline{vv})$. The increase of turbulence intensity at higher rotation rates

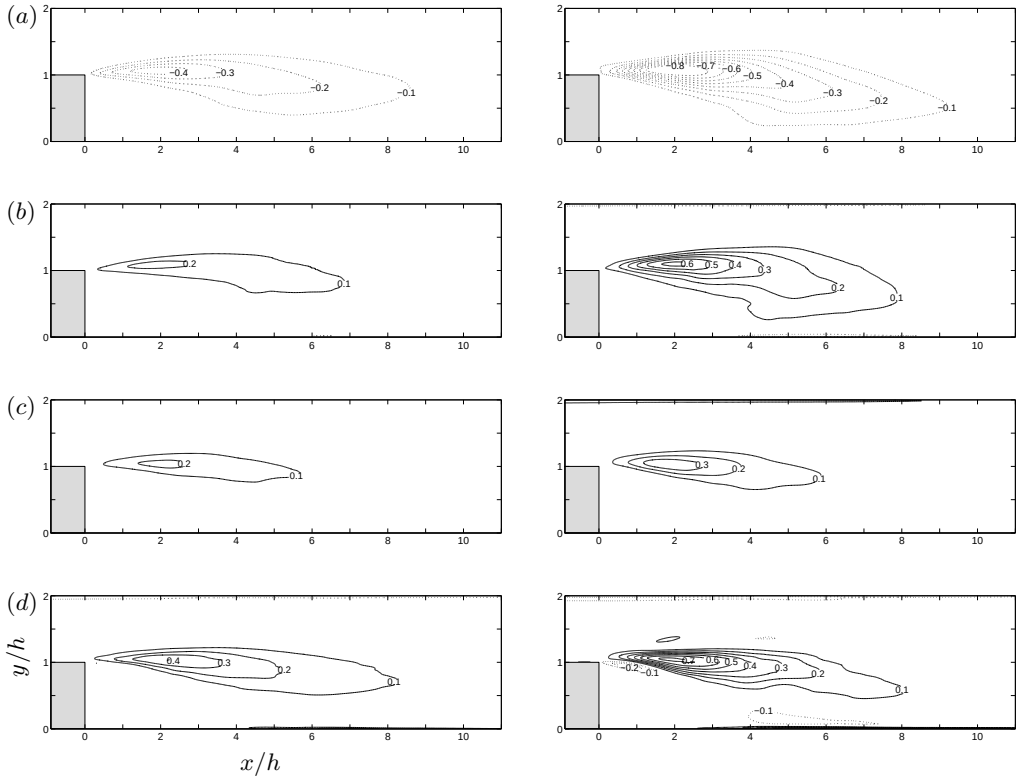

FIGURE 13. Pressure-strain term Π_{ij} scaled with u_τ^4/ν for $Ro = -0.1$ (left) and $Ro = -0.4$ (right). Contour increment of 0.1 is used. (*a*) Π_{xx}, (*b*) Π_{yy}, (*c*) Π_{zz} and (*d*) Π_{xy}.

cannot explained in similar way. Therefore, another mechanism should influence the turbulence level at such rotation rates.

The pressure-strain interaction terms Π_{ij} are known to play an important role in shear-flow turbulence. For example, Π_{zz} is the only source of spanwise fluctuations in a planar mean flow since both production terms are identically zero. Normally, turbulent energy is being transferred from the mean flow direction to the two other components of the fluctuating velocity vector, i.e. $\Pi_{xx} < 0$ whereas Π_{yy} and Π_{zz} are positive. This is indeed the situation also in the cyclonic shear layer in the present case, as shown in figure 13. At high rotation rates, the increase in the energy transfer to the wall-normal and spanwise directions compare to the low rotation cases can, probably, explain the increase in the wall-normal and spanwise turbulence intensities in figures 7 and figure 8, respectively.

6. Flow structures

In this section we focus on the instantaneous features of strong cyclonically rotating turbulent flow over a backward-facing step. To this end, the highest rotation rate $Ro = -0.60$ has been investigated. A snapshot of the flow field is shown in figure 14 where contours of streamwise and wall-normal velocities are plotted. The turbulent flow is

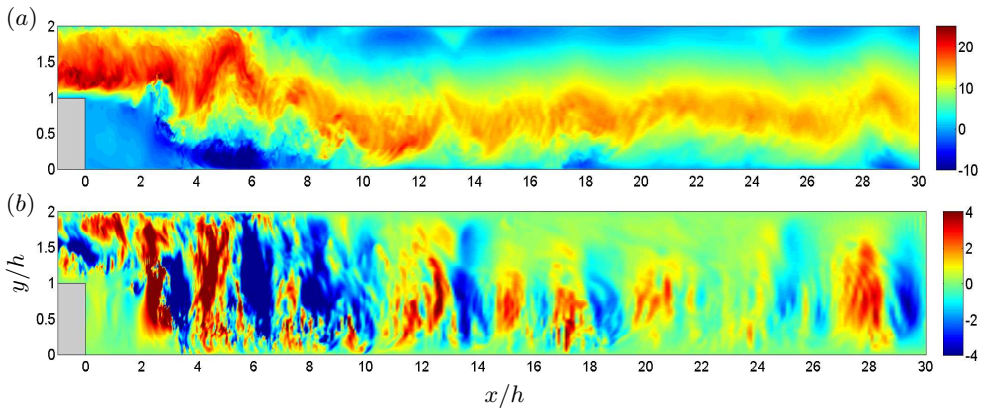

FIGURE 14. Instantaneous velocity field in $(x, y)-$plane for $Ro = -0.6$ taken at the center of the channel at $t = 14h/u_\tau$. (a) streamwise velocity u/u_τ and (b) wall-normal velocity v/u_τ.

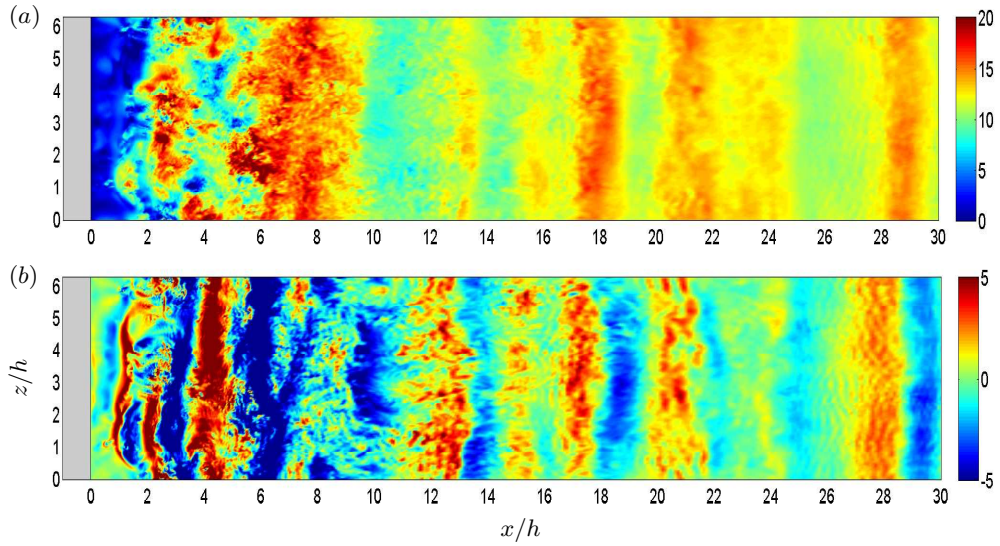

FIGURE 15. Instantaneous velocity field in $(x, z)-$plane for $Ro = -0.6$ taken at the center of the channel at $t = 14h/u_\tau$. (a) streamwise velocity u/u_τ and (b) wall-normal velocity v/u_τ.

almost laminarized in the region upstream of the step along the cyclonic (stepped) side, whereas the turbulent augmentation is increased along the anti-cyclonic (planar) side. The flow topology in figure 14(a) shows large streamwise flow structures downstream of the reattachment and close to the cyclonic (stepped) wall. This can explain the behavior in the recovery region which has been shown in figure 3. The present large scale structures prohibit the turbulent flow to recover to a fully-developed rotating Poiseuille flow. On the other hand, these structures show a kind of waviness in the streamwise direction which, maybe, related to inertial waves reported previously in rotating flows by different authors. The contour plot in figure 14(b) shows alternating positive and negative values

downstream of the step for the wall-normal velocity component. This is an indication of possible large structures elongated in the spanwise direction.

Further investigations are shown in the contour plots of figure 15. The results show no alternations of the turbulent flow along the spanwise direction. The three dimensionalization of the turbulent flow is suppressed and the fully turbulent flow has become almost two-dimensional since the variations along the span have been quenched. The present two-dimensionalization effect can also been seen in the shear layer region where quasi-two-dimesional behavior is persist. This observation is consistent with the previous works on rotating shear layers by Rothe & Johnston (1979), Bidokhti & Tritton (1992) and Métais *et al.* (1995).

7. Discussion and concluding remarks

Direct numerical simulations have been performed with the view to explore the influence of the system rotation on the turbulent flow in a sudden-expansion channel. The present article concern the cyclonically rotating backward-facing step while the effect of anti-cyclonic system rotation is covered in the previous part of the same title (Part I). The monotonic increase of the primary separation bubble up to $Ro = -0.20$ indicates a linear relationship between the rotation number and the reattachment length in the range of low-moderate rotation rates ($-0.20 < Ro < +0.20$). At higher rotation rates the reattachment length is saturated for anti-cyclonic background rotation, see Part I. On the other hand, the effect of high cyclonic rotation ($Ro < -0.2$) is to reduce the reattachment length. It is noteworthy to mention that the experimental data provided by Rothe & Johnston (1979) show a saturation effect on the reattachment length at cylonic rotation rates which inconsistent with the current DNSs.

The increased separation distance from 7 to 14 step hights is ascribed to the reduction of the cross-stream turbulence intensity in the shear-layer due to the stabilisation influence of the Coriolis force. The reduction in the reattachment length from $14h$ at $Ro = -0.20$ to around $8h$ at $Ro = -0.60$ is due an increase in the turbulence intensities at higher rotation rates. More investigations are needed in order to explain such unexpected reduction in the reattachment distance. Rothe & Johnston (1979) observed that stabilizing rotation suppressed the three-dimensional motion in the shear-layer to the point that the flow was laminar-like. Similar behavior has been noticed at the highest rotation rate where the flow is two-dimensional and spanwise elongated structures are clear to be observed.

The flow along the planar wall is subjected to an adverse pressure gradient by the sudden expansion. The destabilizing influence of the system rotation at this anti-cyclonic wall tends to increase the turbulence level at low-moderate rotation rates. Therefore, the separation along the planar wall is unlikely to happened in this range of rotation rates. At higher system rotation, the destabilization take place at the anti-cyclonic wall and the turbulence is reduced. This can assist the shear-layer to separate at the planar wall in the region downstream of the step, see figure 14(a).

The support for this work from the Research Council of Norway through a research grant (contract no 171725/V30) and grants of computing time (Programme for Supercomputing) is gratefully acknowledged. Further access to the IBM p575+ distributed shared-memory (DSM) system was granted by the Research Programme in Computational Science and Visualization (BVV) at The Norwegian University of Science and Technology. Professor J.P. Johnston (Stanford University) kindly provided us with the tabulated reattachment-length data shown in figure 2.

Appendix. Second-moment transport equations in a rotating frame-of-reference

The transport equation (2.2) for the individual components of the second-moments $\overline{u_i u_j}$ of the velocity fluctuations is written in quasi-symbolic form. The various terms on the right-hand side are defined in Cartesian tensor notation as follows:

$$P_{ij} \equiv -\overline{u_i u_k}\frac{\partial U_j}{\partial x_k} - \overline{u_j u_k}\frac{\partial U_i}{\partial x_k} \tag{A 1}$$

$$G_{ij} \equiv -2\Omega_k^F(\overline{u_j u_m}\varepsilon_{ikm} + \overline{u_i u_m}\varepsilon_{jkm}) \tag{A 2}$$

$$D_{ij} = D_{ij}^T + D_{ij}^P + D_{ij}^V \tag{A 3}$$

$$\Pi_{ij} \equiv \overline{\frac{p}{\rho}\left(\frac{\partial u_i}{\partial x_j} + \frac{\partial u_j}{\partial x_i}\right)} \tag{A 4}$$

$$\varepsilon_{ij} \equiv 2\nu\overline{\left(\frac{\partial u_i}{\partial x_k}\frac{\partial u_j}{\partial x_k}\right)} \tag{A 5}$$

where the different parts of the diffusion are given by

$$D_{ij}^T \equiv -\frac{\partial}{\partial x_k}(\overline{u_i u_j u_k}) \tag{A 6}$$

$$D_{ij}^P \equiv -\frac{1}{\rho}\frac{\partial}{\partial x_k}(\overline{pu_i}\delta_{jk} + \overline{pu_j}\delta_{ik}) \tag{A 7}$$

$$D_{ij}^V \equiv \nu\left(\frac{\partial^2 \overline{u_i u_j}}{\partial x_k \partial x_k}\right) \tag{A 8}$$

Here, ε_{ijk} is the permutation or *Levi-Civita* tensor. This organization of the terms in the second-moment transport equation follows Launder *et al.* (1987). The turbulent diffusion due to velocity (D_{ij}^T) and pressure (D_{ij}^P) fluctuations and the viscous diffusion (D_{ij}^V) are labeled collectively as a single diffusion term D_{ij}.

REFERENCES

Barri, M., El Khoury, G. K., Andersson, H. I. & Pettersen, B. 2009a Inflow conditions for inhomogeneous turbulent flows. *Int. J. Numer. Meth. Fluids* **60**, 227–235.

Barri, M., El Khoury, G. K., Andersson, H. I. & Pettersen, B. 2009b DNS of backward-facing step flow with fully turbulent inflow. *Int. J. Numer. Meth. Fluids, DOI: 10.1002/fld.2176* .

Bidokhti, A. A. & Tritton, D. J. 1992 The structure of a turbulent free shear layer in a rotating fluid. *J. Fluid Mech.* **241**, 469–502.

Johnston, J. P., Halleen, R. M. & Lezius, D. K. 1972 Effects of spanwise rotation on the structure of two-dimensional fully developed turbulent channel flow. *J. Fluid Mech.* **56**, 533–557.

Kasagi, N. & Matsunaga, A. 1995 Three-dimensional particle-tracking velocimetry measurment of turbulent statistics and energy budget in a backward facing flow. *Int. J. Heat Fluid Flow* **16**, 477–485.

Kim, J., Moin, P. & Moser, R. 1987 Turbulence statistics in fully developed channel flow at low Reynolds number. *J. Fluid Mech.* **177**, 133–166.

Kristoffersen, R. & Andersson, H. I. 1993 Direct simulations of low-Reynolds-number turbulent flow in a rotating channel. *J. Fluid Mech.* **256**, 163–197.

Launder, B. E., Tselepidakis, D. P. & Younis, B. A. 1987 A second-moment closure study of rotating channel flow. *J. Fluid Mech.* **183**, 63–75.

Manhart, M. 2004 A zonal grid algorithm for DNS of turbulent boundary layers. *Comput. Fluids* **33**, 435–461.

Métais, O., Flores, C., Yanase, S., Riley, J. J. & Lesieur, M. 1995 Rotating free-shear flow. part2. numerical simulations. *J. Fluid Mech.* **293**, 47–80.

Rothe, P. H. & Johnston, J. P. 1979 Free shear layer behavior in rotating systems. *J. Fluids Eng.* **101**, 117–120.

Paper 12

On the stabilizing effect of the Coriolis force on the turbulent wake of a normal flat plate

Khaledi, H. A., Barri, M. & Andersson, H. I.

Accepted for publication in *Physics of Fluids.*

The present manuscript is an extended version of the paper titled as **Asymmetric vortex shedding in the turbulent wake of a flat plate in rotating fluid**. The paper is printed In *Advances in Turbulence XII, Proceedings of the 12th EUROMECH European Turbulence Conference, Springer–Verlag, pp.301–304, 2009.*

On the stabilizing effect of the Coriolis force on the turbulent wake of a normal flat plate

Hatef A. Khaledi, Mustafa Barri and Helge I. Andersson

Fluids Engineering Division
Department of Energy and Process Engineering
Norwegian University of Science and Technology
7491 Trondheim, Norway

The turbulent Karman vortex street behind a flat plate in a rotating fluid is explored by means of direct numerical simulations. The effect of the Coriolis force is often said to be stabilizing on the cyclonic side of the wake and destabilizing on the anticyclonic side. The present computer experiments reveal a more subtle influence of the system rotation. The turbulence is suppressed at the cyclonic side of the wake at Rossby numbers of about unity whereas the cyclonic Karman roller eddies persist. The anticyclonic vortex cells which are blurred by the enhanced turbulence level are scarcely visible. The Strouhal number of this asymmetric vortex shedding is slightly higher than in the absence of rotation. At even higher rotation rates, the three-dimensional turbulence is suppressed also along the anticyclonic side of the wake and a nearly symmetric vortex street is observed at Rossby number 0.16 with the Strouhal number significantly lower than for the non-rotating wake. At this rotation rate, the anticyclonically shed cells appeared as high-pressure zones. At even lower Rossby numbers, not only the turbulence but also the periodic vortex shedding is suppressed, in accordance with the demarcation line in a Rossby – Ekman number flow regime map.

Key words: rotating wakes; free shear layers; Coriolis forces; asymmetric vortex shedding; turbulence; stability.

I INTRODUCTION

Rotating shear flows have received considerable attention due to their numerous occurrences both in geophysical and industrial fluid dynamics. The Coriolis force which arises from the system rotation gives rise to fascinating flow phenomena both in wall-bounded and free shear flows. A rotating flow of a homogeneous fluid is normally a two-parameter problem described in terms of two of three dimensionless dynamical parameters: the Rossby number, the Ekman number, and the Reynolds number. The Rossby number, which is a measure of the relative importance of the inertial and Coriolis forces, varies considerably from one flow problem to another. For Jupiter's great red spot, for instance, the Rossby number is about 0.02, for atmospheric island wakes ≥ 1, and for tornados of the order 10^3. Different orientations of the fluid vorticity vector relative to the rotation vector give rise to rather different implications of the Coriolis force. In geophysical problems, the projection of the Earth's rotation along the local vertical is normally aligned with the vorticity vector of the

flow. In engineering applications, however, the vorticity vector may either be aligned with or perpendicular to the rotation axis. The latter situation occurs, for instance, in a rotating pipe. In this investigation, however, only the former situation will be investigated. The wake behind a flat plate perpendicular to an oncoming stream will be considered in a rotating frame-of-reference where the axis of rotation is aligned with the axis of the plate.

A. Shear layers in rotating fluids

Wall-bounded shear flows subjected to system rotation have been extensively investigated in laboratory and computer experiments. The thorough experimental measurements of rotating channel flow by Johnston *et al.*[1] were complemented by direct numerical simulations by Kristoffersen and Andersson[2]. These and other studies showed that the mean velocity profile was distorted by the system rotation and tended to develop a localized region in which the mean flow vorticity balanced the system rotation. In the rotating channel flow, the turbulence was damped adjacent to the *cyclonic side* where the mean flow vorticity vector is parallel to the rotation vector whereas the turbulent agitation was enhanced near the *anticyclonic* side where the mean flow vorticity is anti-parallel with the imposed rotation. Anticyclonic rotation gave also rise to a secondary-motion in the cross-sectional plane. Rotating channel flows are inevitably exposed simultaneously to cyclonic and anticyclonic rotation. The rotating Couette flow, on the other hand, is either exposed entirely to cyclonic or anticyclonic rotation. Barri and Andersson[3] reported that the distinct secondary flows observed by Bech and Andersson[4] were quenched and the turbulence damped when a plane Couette flow was subjected to strong anticyclonic rotation. The rotational destabilisation is therefore only present in a certain interval of anticyclonic rotation rates and the flow is otherwise being stabilised. A further exposition of rotational-induced flow phenomena of particular relevance to turbomachinery applications can be found in the review by Johnston[5] and in chapter 7 of the text book by Greitzer *et al.*[6]

Similar to the wall-bounded shear flows, free shear flows are also differently affected by system rotation. A rotating wake is exposed simultaneously to cyclonic and anticyclonic rotation, whereas a rotating mixing-layer is subjected only to cyclonic or anticyclonic rotation. An early flow visualisation study of the mixing-layer emanating from the corner of a backward-facing step was performed by Rothe and Johnston[7]. They observed that the position at which the flow reattached to the channel wall downstream of the step, i.e. the reattachment point, was crucially dependent on the sense of rotation and the rotation rate. In short, the reattachment length increased with increasing cyclonic rotation and diminished with higher anticyclonic rotation. In the latter case, the turbulence in the shear layer was promoted and the excess mixing enhanced the spreading rate of the mixing layer. Cyclonic rotation, on the other hand, tended to damp the turbulence and the spanwise-oriented coherent flow structures were strengthened. The rotating mixing-layer was further investigated by Bidokhti and Tritton[8] albeit in a rather different apparatus. They showed that the flow was stabilized when the imposed system vorticity was parallel with the mean shear vorticity vector (i.e. in the cyclonic regime) whereas the flow was first destabilized and subsequently restabilized when the system rotation vector was anti-parallel to the vorticity vector (i.e. anticyclonic rotation). Measurements of the Reynolds-stress components at higher rotation rates indicated that the destabilization occurred in an early stage of the mixing-layer development and subsequent two-dimensionalization took place further downstream. They also confirmed the existence of a roller-eddy pattern (Kelvin-Helmholtz rollers) in all cyclonic cases whereas the flow was completely disrupted by the destabilisation at even weak anticyclonic rotation.

Boyer[9] investigated the variety of flow patterns that may occur in the wake of a circular cylinder in a rotating water tunnel. Extensive experimental measurements in the cylinder wake were provided by Boyer and Davies[10]. They were mostly concerned with the variation of the wake length and its asymmetry due to system rotation. A time-sequence of photographs revealed a distinct unsteadiness on the cyclonic side of the wake whereas the anticyclonic side remained steady. In an accompanying satellite photo of the cloud pattern in the lee wake behind Guadelupe Island, the asymmetry of the vortex street is evident with a distinct dominance of the cyclonic eddies. Measurements of turbulent quantities in the wake of a cylinder in a rotating fluid were probably presented for the first time by Witt and Joubert[11]. Since the two sides of the wake are differently affected by rotation, so were the turbulence intensities and thereby the moment defect. The streamwise intensity was damped whereas the normal intensity was increased on the anticyclonic (i.e. leading) side of the wake. The reorientation of the turbulence intensities eventually resulted in a large Reynolds shear stress on the anticyclonic side as compared to the cyclonic side of the wake. While Witt & Joubert[11] were able to measure all three turbulence intensities using x-wire anemometers, Koyama & Ohuchi[12] used only a single-wire to measure the mean velocity profile and the streamwise turbulence intensity in the rotating wake downstream of a circular cylinder. Their measurements also showed distinct asymmetries when the cylinder axis was aligned with the rotation axis, whereas the wake turned out to remain symmetric when the cylinder axis was oriented perpendicular to the axis of rotation.

Chabert d'Hières *et al.*[13, 14, 15] were primarily concerned about measurements of the oscillating lift and drag forces caused by the alternating vortex shedding over a range of Rossby and Ekman numbers. The mean total lift coefficient and the mean total drag coefficient were found to increase with increasing rotation rates and this was ascribed to wake asymmetries. Indeed, their photo of the vortex street downstream of their cylinder exhibits the same qualitative features as the satellite photograph referred to above. At the lower Reynolds numbers they also observed that the Strouhal number increased with the imposed rotation rate. In the vortex shedding regime, the shed cyclonic vortices were stronger than their anticyclonic counterparts.

Métais *et al.*[16] performed direct and large-eddy simulations of a planar mixing-layer and a planar wake flow subjected to solid-body rotation. Their simulations were concerned with the time evolution from an initial mean flow profile (a hyperbolic-tangent form for the mixing-layer and a Gaussian profile for the wake) and periodicity was assumed in the streamwise direction. They superimposed both quasi-two-dimensional and three-dimensional perturbations separately on the basic shear flow and studied the effect of different Rossby numbers on cyclonic and anticyclonic shear flow regimes. Their simulations confirmed the two-dimensionalization effect of cyclonic rotation and rapid anticyclonic rotation. At higher Rossby numbers, a destabilization was observed in the anticyclonic regime.

Quantitative PIV measurements, supplemented by dye visualisations, in the rotating vortex street behind a circular cylinder were performed by Stegner *et al.*[17] They observed that the symmetry between the cyclonic and the anticyclonic vortices in the lee of the obstacle was broken when the local Rossby number exceed unity. They furthermore found a modest tendency of the measured Strouhal number to decrease with increasing Rossby numbers.

In almost all laboratory experiments on rotating wakes, the wake is formed in the lee of a circular cylinder. The only investigation of the wake formed by a normal flat plate in a rotating frame-of-reference is the computational study by Becker[18]. The system rotation vector was oriented along the axis of the plate whereas the oncoming flow was perpendicular to the plate. She was only concerned with low-Rossby-number flows in which the geostrophic balance applied and the flow became steady and two-dimensional.

B. Stability of rotating shear flows

In laminar and turbulent shear flows subjected to solid body rotation, the impact of the Coriolis force depends crucially on the orientation of the system rotation vector relative to the mean vorticity vector. In other words, the effect of the rotation on a shear layer such as wall-bounded flows, mixing-layers and wake flows depends on the sense of rotation. The system rotation can thus be either cyclonic or anti-cyclonic depending on whether the rotation vector is aligned with or anti-parallel with the mean flow vorticity. In channel flow investigations, it has become the prevailing practice to define a *global* rotation number based on a bulk flow mean vorticity, see e.g. Refs. 1 – 4. Cambon *et al.*[19] pointed out the importance of distinguishing between the background flow, large-eddy structures and the turbulence in order to pinpoint rotational effects on individual cyclones and anticyclones. They considered the non-dimensional parameter

$$N = \frac{2\Omega_i}{\omega_i} = \frac{2\Omega_i}{\left|\nabla \times \vec{V}\right|_i}, \tag{1}$$

which is a *local* rotation number. Here, Ω_i is the angular velocity of the rotating reference frame about the x_i-axis and ω_i is the local vorticity associated, for instance, with a large-scale flow structure. Bradshaw[20] demonstrated that a uniform shear flow subjected to constant system rotation was unstable when $N(N + 1) < 0$ and otherwise stable. Thus, both $N = 0$ and $N = -1$ correspond to neutral situations whereas $N = -\frac{1}{2}$ is the most unstable case. Lesieur *et al.*[21], however, argued that maximum destabilisation occurred at $N = -1$. This controversy motivated Cambon *et al.*[19] to further explore this issue. Bradshaw's criterion emerged from a simple displaced-particle analysis in which pressure effects were ignored. They therefore made a rigorous linear stability analysis, rapid-distortion theory (RDT) computations and full three-dimensional simulations of the development of initially two-dimensional Taylor-Green vortices. Their results consistently supported the outcome of Bradshaw's simple analysis, namely that maximum destabilisation of a vortex structure occurs for $N = -\frac{1}{2}$, i.e. maximum tilting vorticity, whereas stability is obtained for $N = -1$. The latter situation is that of zero absolute vorticity, i.e. the imposed system vorticity exactly outweighs the flow vorticity. Cambon *et al.*[19] furthermore emphasized that although neutral stability is suggested both for $N = -1$ and for $N = 0$ according to the Bradshaw-Richardson criterion, the flow field will be fundamentally different in the two cases. Yanase *et al.*[22] examined the instability properties of both planar wakes and mixing layers subjected to rigid-body rotation by means of linear stability analysis. The outcome of their analysis is in qualitative agreement with the considerations of Cambon *et al.*[19] and furthermore seems to confirm the criterion of zero tilting vorticity, i.e. $N = -\frac{1}{2}$, for maximum destabilization.

The outcome of the rotating mixing-layer experiments by Bidokhti & Tritton[8] was generally in accordance with the above stability considerations. Their rotation number was, however, based on an average shear-rate across the mixing layer and not on the vorticity of the individual Kelvin-Helmholtz vortices. In practice they approximated ω_i in eq. (1) as $(U_+ - U_-)/2\delta_m$ where U_+ and U_- are the high and low velocities upstream of their splitter plate and δ_m is a measure of the local width of the mixing layer. Thus, since the mixing layer thickens with downstream distance x, the local rotation number N also increases with x. Bidokthi and Tritton[8] pointed out that since the Kelvin-Helmholtz rollers are essentially two-dimensional, they will not be suppressed by stabilizing, i.e. cyclonic, rotation. What will be suppressed are

the three-dimensional motions that lead to distortions of the large eddies. They therefore anticipated that stabilizing rotation tends to make the roller eddies more robust.

The direct and large-eddy simulations by Métais *et al.*[16] are, at least qualitatively, consistent with the above criterion. For instance, they showed that cyclonic rotation of the mixing layer inhibited the growth of three-dimensional perturbations, regardless of rotation rate and initial conditions. This inhibition was also observed for strong anticyclonic rotation, whereas a severe destabilization was found at moderate anticyclonic rotation rates. In spite of the inevitable fact that the wake flow is simultaneously exposed to cyclonic and anticyclonic rotation, the highest rotation rates rendered the wake flow two-dimensional. At moderately high rates of rotation, on the other hand, the cyclonic side of the wake was composed of regular Karman vortices whereas the large-eddy pattern was quenched on the anticyclonic side due to the three-dimensionalisation and longitudinal rib-like vortices appeared.

More recent computer simulations of rotating homogeneous turbulence have shown that there are more cyclones than anti-cylones, e.g. van Bokhoven *et al.*[23] and references therein. Sreenivasan and Davidson[24] suggested that these observations could arise if anti-cyclones are less likely to form. Such results that are concerned with cyclones and anticyclones in homogeneous turbulence may have some relevance also for vortex dynamics in shear flows submitted to solid-body rotation.

C. Present investigation

The objective of the present investigation is to explore the wake formed in the lee of a flat plate normal to the incoming stream in a rotating system. The focus is on the eddy shedding regime with the particular view to study the asymmetric vortex shedding. Direct numerical simulations (DNSs) of the three-dimensional flow field enable detailed inspections of the velocity and vorticity field in the rotating wake. This study is a sequel to the computational investigation of the wake flow behind a flat plate by Narasimhamurthy & Andersson[25]. The Reynolds number in that study (Re = 750) was sufficiently high to assure that the wake was fully turbulent in the absence of rotation. In the present investigation, the Reynolds number remains the same, while background rotation is imposed in order to explore the impact of the Coriolis force both on the shed Karman rollers and the underlying turbulence field. This investigation is apparently the first DNS study ever of the asymmetric turbulent vortex shedding behind a bluff body in a rotating fluid.

The paper is organized as follows. Following the introductory section, in which earlier investigations are summarized and different global and local stability criteria are discussed, the present flow problem and the computational approach are presented in Section II. In Section III, the observed wake topology and the vortical flow structures are shown for a variety of Rossby numbers and the observed asymmetries will be explained, before conclusions are drawn in Section IV.

II. FLOW CONFIGURATION AND COMPUTER EXPERIMENTS

The flow in the wake behind a flat plate in a rotating system will be considered. The Reynolds number based on the uniform inflow velocity U_0 and the constant width of the plate d will be taken sufficiently high to assure that even the near-wake is turbulent, at least in the absence of rotation. The incoming flow is directed perpendicular to the plate whereas the axis of rotation is parallel with the axis of the plate, as shown in Figure 1. The flow is conveniently described

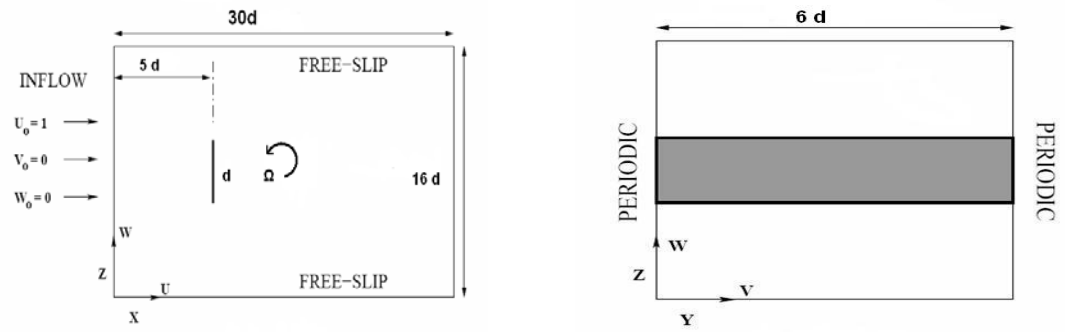

(a) (b)

Figure 1 Sketch of the computational domain and the Cartesian coordinate system (not to scale). The computational domain is rotated with angular velocity Ω. a) Side view. The y-axis points inwards and counter-clockwise rotation implies that $\Omega < 0$. b) Rear view.

in a Cartesian coordinate system with the x-axis in the direction of the inflow, the y-axis aligned with the axis of rotation, and the z-axis directed across the flow.

The flow will be observed from a frame-of-reference which rotates with a constant angular velocity vector $\vec{\Omega}$ about the y-axis, as indicated in Figure 1(a). The motion of the incompressible fluid is then governed by the Navier-Stokes and the continuity equations:

$$\frac{\partial \vec{\tilde{u}}}{\partial \tilde{t}} + \vec{\tilde{u}} \cdot \nabla \vec{\tilde{u}} = -\frac{1}{\rho} \nabla \tilde{\pi} + \frac{\mu}{\rho} \nabla^2 \vec{\tilde{u}} - 2\vec{\Omega} \times \vec{\tilde{u}}; \qquad \nabla \cdot \vec{\tilde{u}} = 0. \tag{2}$$

Here, $\vec{\tilde{u}}$ is the velocity vector relative to the rotating frame and $\tilde{\pi}$ is the *effective* pressure which includes the potential of the centrifugal force, i.e.

$$\tilde{\pi} = \tilde{p} - \rho \Omega^2 \tilde{r}^2 / 2 . \tag{3}$$

The distance from the axis of rotation is denoted $\tilde{r}$ and the tilde (˜) identifies dimensional variables.

The constant plate width d and the uniform inflow velocity U_o are the only imposed length and velocity scales in the present problem. Let us therefore recast equations (2) into dimensionless form by means of these two scales:

$$\frac{\partial \vec{u}}{\partial t} + \vec{u} \cdot \nabla \vec{u} = -\nabla \pi + \frac{1}{\mathrm{Re}} \nabla^2 \vec{u} - \frac{1}{Ro} \vec{e}_\Omega \times \vec{u}; \qquad \nabla \cdot \vec{u} = 0. \tag{4}$$

Here, $\vec{e}_\Omega$ is the unit vector in the direction of the axis of rotation. The dimensional time $\tilde{t}$ has been normalized by the time scale d/U_o. The two dimensionless parameters

$$\mathrm{Re} \equiv \rho d U_o / \mu; \qquad Ro \equiv U_o / 2|\Omega| d \tag{5}$$

are the Reynolds number and the Rossby number, respectively. Re is a measure of the importance of the inertia terms relative to the viscous terms while Ro measures the relative importance of the inertia terms as compared with the Coriolis terms.

The flow problem under consideration is a two-parameter problem. In geophysical fluid dynamics, the Ekman number

$$Ek = Ro / \mathrm{Re} = \mu / \rho 2|\Omega| d^2 \qquad (6)$$

is routinely used to signify the relative importance of the fluid viscosity rather than the Reynolds number Re. A variety of different definitions of the controlling parameters appear in the literature. The above definitions are identical to those used by Boyer[9] in their experimental study of wake flow regimes in the lee of a circular cylinder with diameter *d*.

Direct numerical simulations are performed with the finite-volume solver MGLET due to Manhart[26]. The three-dimensional Navier-Stokes equations are approximated on a staggered Cartesian grid system. In order to simulate flows in a rotating frame-of-reference, however, Coriolis force terms are implemented in the discretized momentum equations whereas the effects of the centrifugal force are embedded into the effective pressure π defined in eq. (3). A 3rd-order explicit Runge-Kutta scheme is employed to march the solution forward in time and a 2nd-order accurate central-differencing scheme is used to approximate the spatial derivatives. An iterative SIP (Strongly Implicit Procedure) solver is used for the Poisson equation. The direct-forcing immersed boundary method described by Peller *et al.*[26] transforms the no-slip and impermeability conditions at the plate surface into internal boundary conditions at the nodes of the Cartesian grid. The internal boundary condition values were determined by 3rd-order accurate least-square interpolations. The same Navier-Stokes solver has recently been used in a companion study by Narasimhamurthy & Andersson[25] to simulate the turbulent wake behind a flat plate in a non-rotating environment and by Khaledi *et al.*[28] and Narasimhamurthy *et al.*[29] to investigate the wake characteristics behind tapered plates at low and moderately high Reynolds numbers, respectively.

In the present study, the size of the computational domain was $L_x = 30d$, $L_y = 6d$ and $L_z = 16d$ in the streamwise, spanwise and lateral (cross-stream) directions, respectively. The plate was located 5d from the inflow boundary and the thickness of the plate was 0.02d. The number of grid points in each coordinate direction was $N_x = 512$, $N_y = 60$, and $N_z = 384$ with non-uniform grid spacing in the streamwise and lateral directions. A uniform inflow velocity without any disturbances was prescribed at the inlet boundary at X = 0 together with a Neumann-condition for the pressure. Free-slip boundary conditions were used along the 'side-walls' of the computational domain to reduce the blockage effect, whereas periodic boundary conditions were used in the spanwise direction in order to mimic an infinite aspect ratio, i.e. spanwise statistical homogeneity.

III. RESULTS AND DISCUSSIONS

In order to explore the effect of system rotation on the wake behind the flat plate, some different rotation rates were considered while the Reynolds number was maintained at Re = 750, i.e. the same as in the study of the non-rotating wake by Narasimhamurthy & Andersson[25]. The sense of rotation about the y-axis was consistently negative, which implies counter-clockwise rotation in Figure 1. The Rossby number range covered was from 0.16 to 2.5 together with the infinitely high Ro in the non-rotating case.

In the course of the present study, it turned out that the wake flow remained in the 'eddy shedding' regime for all Rossby numbers, i.e. eddies are being shed from both sides of the wake according to the classification of Boyer[9]. Some additional simulations were therefore performed at lower Rossby and Reynolds numbers in order to pass the demarcation

line between the 'eddy shedding' and the 'unsteady eddy system' in Boyer's[9] flow regime map. Table 1 shows that the present parameter values are fairly close to the parameter ranges studied by Boyer[9] and Boyer & Davies[10], whereas the cases reported by Witt & Joubert[11] and Koyama & Ohuchi[12] were for substantially higher Rossby and Ekman number values.

Author(s)	**Year**	**Ro**	**$10^4 \cdot$ Ek**	**Re**
Boyer[9, #]	1970	≥ 0.05	4.3	~ 120
Boyer & Davies[10, §]	1982	0.05	1.7	350
Witt & Joubert[11]	1985	62.5	550	575
Koyama & Ohuchi[12]	1987	180	1800	1 000
Present simulations	2009	0.16 – 2.5	2.1 - 40	750
Present low-Ro cases	2009	0.0714	8.4 - 14	85 - 50

Table 1. Earlier experimental studies of rotating wakes behind circular cylinders

[#]Boyer[9] considered a wide range of Ro and Ek numbers. The entry in the table is for the flow visualization photos shown in their paper. [§]The entries are for their figure 13.

The variety of different wake topologies, supplemented with some primary flow statistics, will be presented in the following sub-sections. Although the length of the computational domain was 30d (see Figure 1a), the flow visualisations and the statistics are from the first 20d in order to eliminate any adverse effects from the downstream boundary. The present length 30d compares favourably with our earlier computational studies of wakes behind uniform[25] and tapered[28, 29] flat plates in which domain lengths of 25d and 20d were used.

A. Wake topology and shedding frequency

Perspective views of the complex vortex structures in the wake are shown in Figure 2. The wake topology is visualized by iso-contours of instantaneous λ_2-values. Following Jeong & Hussain[30] λ_2 corresponds to the second largest eigenvalue of the symmetric tensor $S_{ij}S_{ij} + \Omega_{ij}\Omega_{ij}$ where S_{ij} and Ω_{ij} represent the symmetric and anti-symmetric parts of velocity gradient tensor, respectively. Negative values of λ_2 are associated with low-pressure zones normally found in the vortex cores in the absence of system rotation. The Reynolds number Re = 750 is sufficiently high for the non-rotating wake to be fully turbulent with characteristic Karman cells embedded in the distinctly three-dimensional flow field. The primary shedding frequency f, deduced from a Fourier spectrum of the cross-stream velocity component, yields a Strouhal number $St = fd/U_o = 0.1678$. A further description of the non-rotating wake has been provided by Narasimhamurthy & Andersson[25].

It is immediately observed from Figure 2 that the vortex shedding found in the non-rotating case prevails throughout the Rossby number range considered. The wake topology, however, is substantially affected by the presence of the Coriolis force. At the moderate Rossby numbers the wake becomes distinctly asymmetric. The cyclonic vortex cells shed from the lower part of the plate become gradually clearer with decreasing values of Ro whereas the anticyclonic cells shed from the upper part of the plate are hardly discernible due to the turbulent stirring which does not decay until Ro is reduced below unity. The characteristic braids of streamwise vorticity, which tend to connect consecutive Karman-

rollers, vanish. The rapidly rotating wake flow in Figure 2e exhibits again an apparent symmetry between cyclonic and anticyclonic cells, but the wake topology has nearly evolved into a purely two-dimensional flow pattern.

In order to check if the λ_2-criterion[30] for vortex identification is applicable also for the vigorously turbulent wake with distinct vortex cells, we also considered the Q-criterion which is an alternative local vortex identification scheme; see e.g. the recent analysis and comparisons of the most popular point-wise methods for vortex identification by Chakraborty *et al*.[31] The resulting vortex structures deduced by the Q-criterion were almost indistinguishable from the λ_2-contours in Figure 2 for all Rossby numbers considered and are therefore not included in this paper.

The instantaneous isocontours of the spanwise vorticity in Figure 3 are taken at the same instants of time as the λ_2-contours in Figure 2. The alternating Karman rollers are identifiable both in the lower and upper sides of the wake. Although rather blurred by the turbulence, anticyclonic cells are distinguishable in the upper part of the wake also at the intermediate Rossby numbers. The global features of the wake pattern observed for Rossby numbers of the order unity, i.e. Ro = 2.5 and Ro = 1.0, are strikingly similar to the photography of a rotating vortex street shown by Chabert d'Hières *et al*.[13] in their figure 1. Their photo was for a flow at a substantially higher Reynolds number (Re = 30 000) and Ro = 2.39. The cyclonic eddies showed sharply-defined forms with clearly recognizable cores, while the anticyclonic counterparts had diffuse structures and were difficult to discern. The Skylab photography reproduced by Boyer & Davies[10] in their figure 14 also revealed an asymmetric vortex street cloud pattern with dominance of cyclonic vortices in the lee of the Guadalupe Island. However, the asymmetry of atmospheric vortex streets is probably caused by other effects than rotation, for instance by stratification, the Ekman boundary layer or by asymmetries of the island itself. With a typical wind speed of 5-10 m/s and an island diameter of 10-20 km the Rossby number is of the order of 2-10. The Coriolis force does therefore not play a dominant role, although wake asymmetries are discernible even at Ro = 2.5 in Figure 2b. In the ocean, on the other hand, the current speed is typically $1/10^{th}$ of the atmospheric wind speed and the oceanic Rossby number is thus always below unity and rotation becomes an essential influence.

The observed scenario depicted in Figures 2 and 3 exhibits a number of different flow phenomena. When the Re = 750 wake is subjected to *weak* rotation, both cyclonic and anticyclonic vortex cells are shed from the plate but once shed they are differently affected by the Coriolis force. The absolute value of the non-dimensional parameter N defined in eq. (1) is below unity and the Bradshaw-Richardson number N(N + 1) suggests that the cyclones are stabilized ($N > 0$) and the anticyclones are destabilized ($N < 0$). This is indeed what we observe at the global Rossby number Ro = 2.5 in Figure 2b and 3b. At this fairly modest rotation rate the wake responds to rotation in accordance with linear analysis in which the Bradshaw-Richardson number is the controlling parameter; e.g. Bradshaw[20], Yanase *et al*.[22] and Cambon *et al*.[19] The authors in the latter reference pointed out the importance of choosing a physically relevant measure of the local fluid vorticity ω_i in the determination of N. In the present context, $\pm U_o/d$ is apparently a reasonably good estimate for the vorticity ω_y of the Karman cells. For Rossby number 2.5 this gives $N = \pm 1/Ro = \pm 0.4$ where the plus and minus signs apply for cyclones and anticyclones, respectively. These results are in qualitative agreement with the Taylor-Green vortices simulated by Cambon *et al*.[19] They found that the anticyclonic vortices were severely attenuated for N = - ½ whereas the cyclonic vortices were somewhat 'scrambled'. Let us recall that N = - ½ corresponds to the lowest possible value - ¼ of the Bradshaw-Richardson number N(N + 1), i.e. maximum destabilization or zero tilting vorticity.

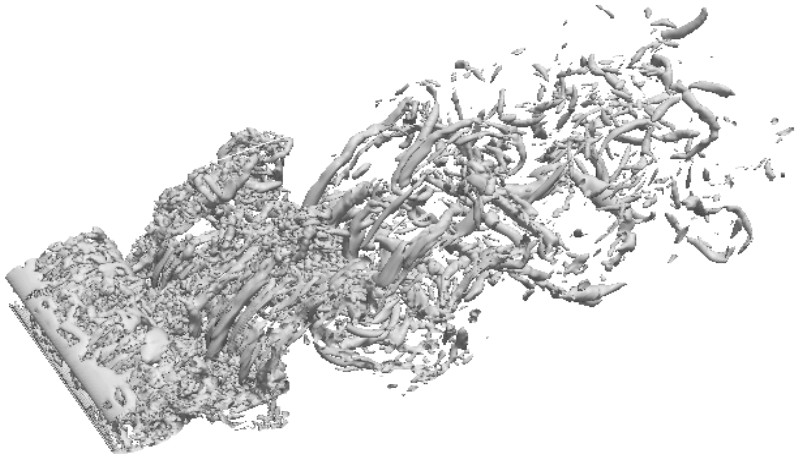

(a) $Ro = \infty$

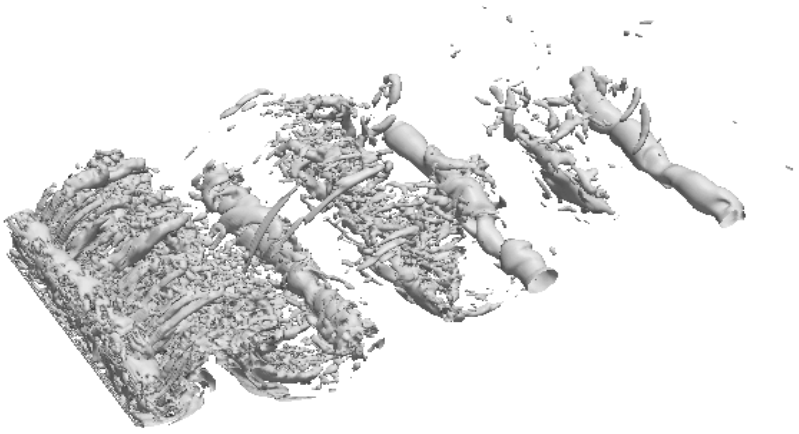

(b) $Ro = 2.5$

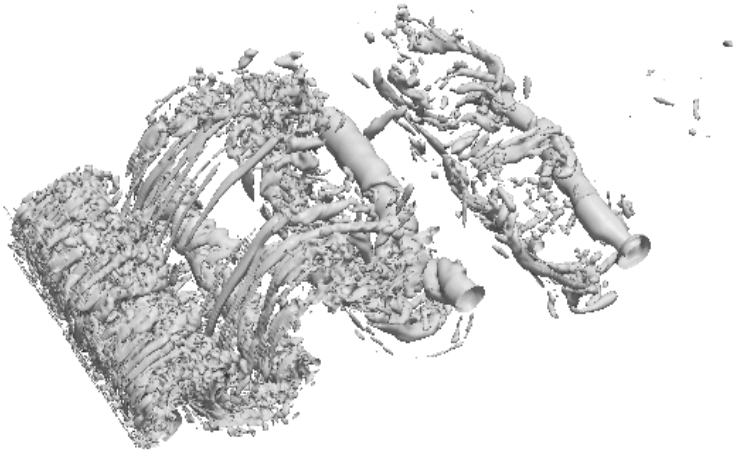

(c) $Ro = 1.0$

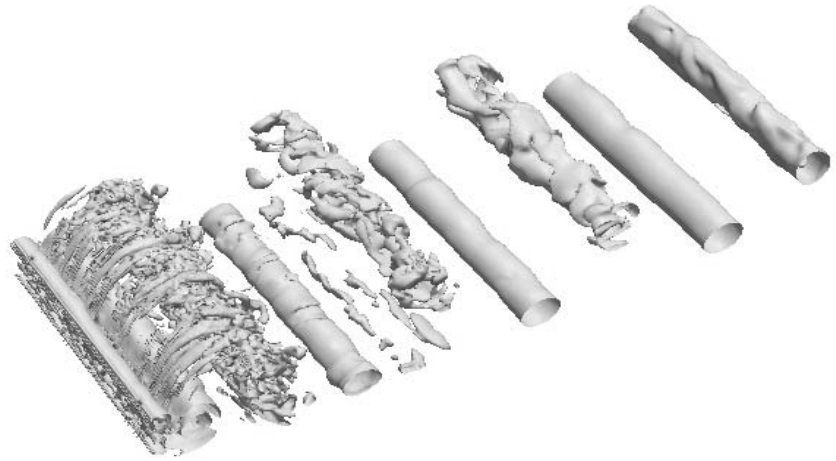

(d) $Ro = 0.33$

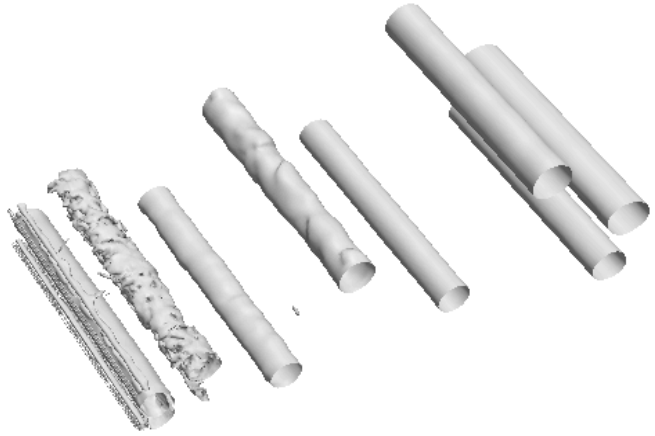

(e) $Ro = 0.16$

Figure 2: Perspective view on iso-surfaces of $-\lambda_2$ at $\tilde{t} = 120d/U_0$ at various Rossby numbers. The plate is in the lower left part of each frame and the primary flow direction is towards the upper right corner. The Reynolds number is fixed as Re = 750 whereas the system rotation increases from top to bottom. The contour level shown is the same in all parts of the figure. (a) $Ro = \infty$; (b) $Ro = 2.5$; (c) $Ro = 1.0$; (d) $Ro = 0.33$; (e) $Ro = 0.16$.

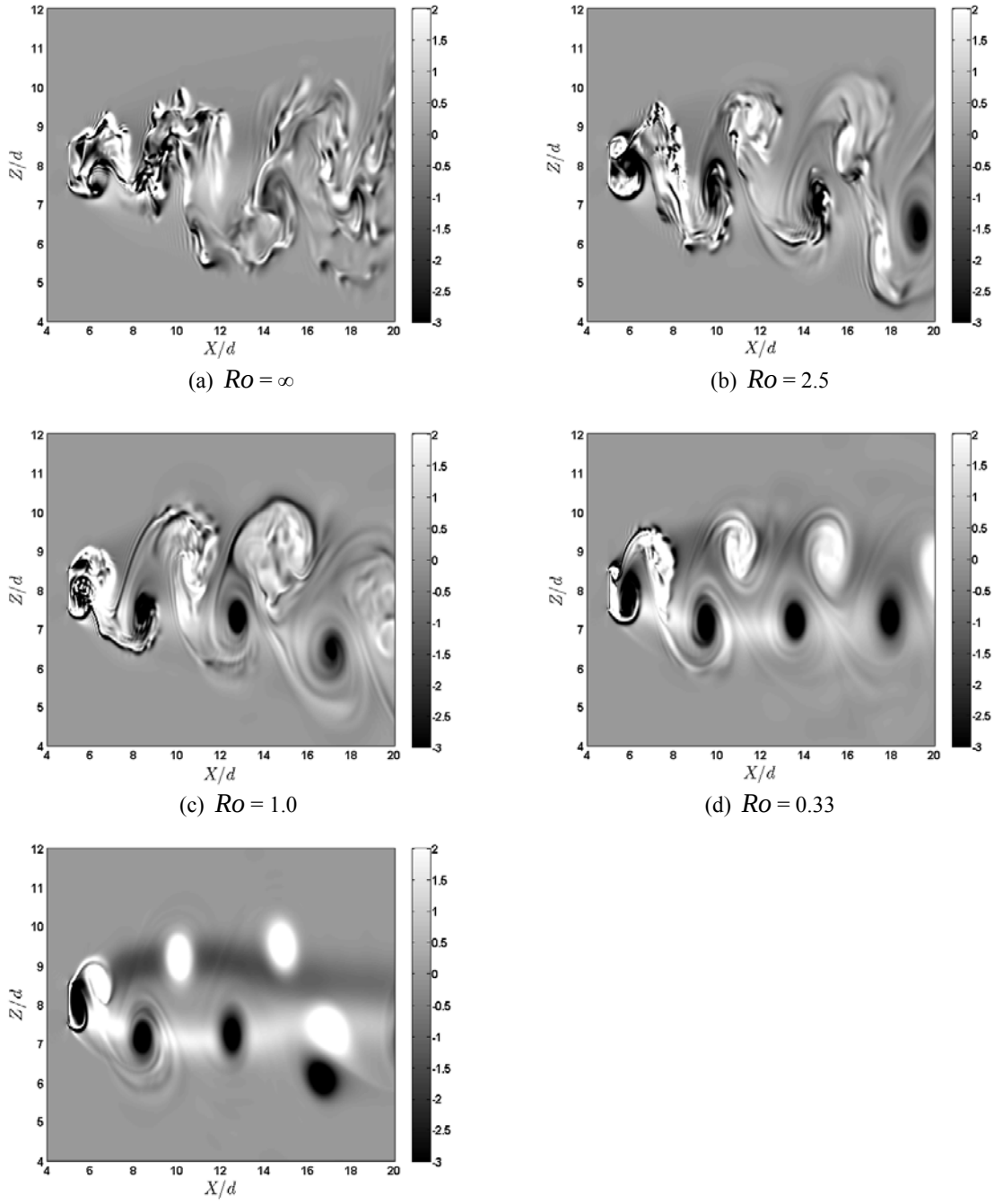

(a) $Ro = \infty$ (b) $Ro = 2.5$

(c) $Ro = 1.0$ (d) $Ro = 0.33$

(e) $Ro = 0.16$

Figure 3: Contours of instantaneous spanwise vorticity ω_y in an (x, z) - plane at $\tilde{t} = 120d/U_0$. The light colours represent positive values, i.e. $\omega_y > 0$, and thereby anticyclonic rotation, whereas the dark colours represent negative values ($\omega_y < 0$) and signify cyclonic vortices. The contour level shown is the same in all parts of the figure. The Reynolds number is Re = 750. (a) $Ro = \infty$; (b) $Ro = 2.5$; (c) $Ro = 1.0$; (d) $Ro = 0.33$; (e) $Ro = 0.16$.

In the simulation of a temporarily developing wake Métais *et al*.[16] reported that the anticyclonic Karman vortices disappeared at an intermediate Rossby number. Their wake did not originate from a bluff body, however, and streamwise homogeneity was imposed. Although substantially blurred, the anticyclones were not quenched in the present spatially developing wake flow. These qualitatively different findings can also be due to the higher Reynolds number, i.e. Re = 750 in the present work as compared to ≈ 400 in Ref. 16.

At *higher* rotation rates and lower Rossby numbers, i.e. Ro < 1, the cyclones are further stabilized in the sense that the turbulence is completely suppressed and only the columnar vortices remain. The anticyclones are, however, gradually less destabilized with increasing rotation rates in this low-Ro regime. Eventually, the three-dimensional scrambling is quenched at Ro = 0.16 and distinct regular cells appear. Following the interpretation suggested by Cambon *et al*.[19], this implies that the rotation 2Ω is now dominant with respect to the local vorticity ω_y for all scales up to the dissipation range, which means that non-linear transfer mechanisms are shut off. An inspection of the rapidly rotating wake at Ro = 0.16 in Figures 2e and 3e shows that the anticyclonic cell just shed from the plate is somewhat destabilized. The anticyclones stabilize as they are convected downstream and almost perfectly regular vortex cells are observed 10d downstream of the plate. This can either be a result of viscous damping or an increasing stabilization with downstream distance from the plate. The linear stability analysis is probably no longer valid in this flow regime, but the local parameter N certainly remains a measure of the impact of rotation. The anticyclonic cells with N way below - ½ (maximum destabilization) are likely to be increasingly exposed to stabilizing rotation only if the magnitude of N increases downstream, i.e. if the local vorticity ω_y decays with x. Complete laminarization by anticyclonic rotation of an otherwise turbulent flow has been observed in computer experiments by Bech & Andersson[4] and laboratory investigations by Alfredsson & Tillmark[32] of rapidly rotating plane Couette flow.

In order to determine the shedding frequency of the Karman rollers, the time evolution of the instantaneous velocity components and pressure was sampled along a line parallel to the axis of the plate. The sampling line was located 3d downstream of the plate and offset 0.5d towards the cyclonic side of the wake, i.e. flush with the edge of the plate. The total sampling time was $120d/U_0$, i.e. comprising nearly 20 shedding cycles. The present sampling time seems to be long enough for the results to converge. Here, only the time traces of the cross-stream velocity W are shown in Figure 4(a) for Ro = 1.0 and the accompanying power spectrum is presented in Figure 4(b). The spatio-temporal variation of W in Figure 4(a) demonstrates that the vortices are shed parallel with the plate. Power spectra were obtained by fast Fourier transforms of the velocity signals. The sample spectrum in Figure 4(b) shows that the most energetic frequency corresponds to a Strouhal number 0.1755. This Strouhal number is higher than that in the non-rotating case. This increase is consistent with the earlier observations by Chabert d'Hières *et al*.[15] who found a similar increase in St in the low-end of their Reynolds number range and with the more recent experimental data by Stegner *et al*.[17] for Re ~ 150.

At even higher rotation rates, however, the shedding frequency and thus St reduces with decreasing Rossby numbers and St at Ro = 0.16 is way below the Strouhal number in the absence of rotation (see Table 2). The flow visualizations in Figures 2 and 3 suggest that the wake is becoming increasingly asymmetric when system rotation is imposed and gradually increased until the Rossby number is of order unity. The flow on the cyclonic side of the wake is stabilized and the cyclonic cells are rendered two-dimensional whereas the anticyclonic cells are destabilized and remain fully three-dimensional. When the rotation rate is further increased, i.e. Ro decreases below unity, the three-dimensional scrambling of the anticyclonic vortices seizes and the wake topology tends again to a nearly symmetric state. The relatively

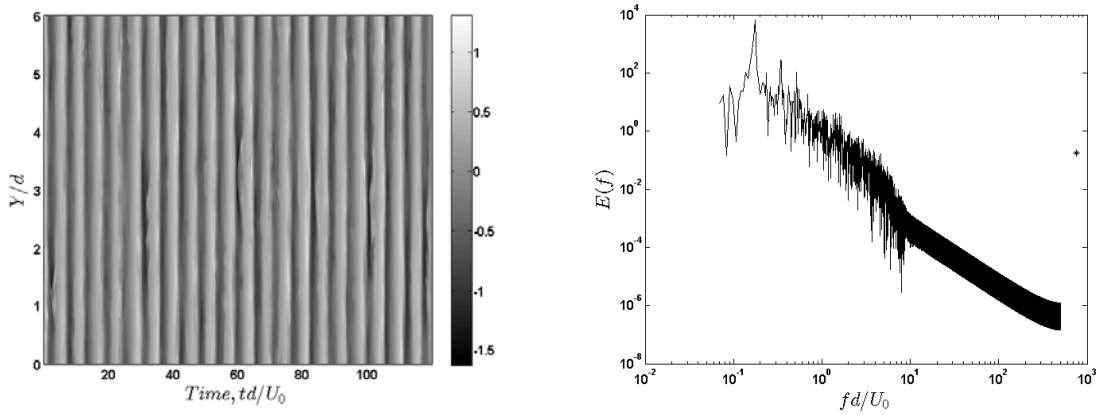

(a) (b)

Figure 4: Vortex shedding at the cyclonic side of the wake for Ro = 1.0 and Re = 750.
(a) Time-traces of the cross–stream velocity component W along the entire span. The sampling line is located at X/d = 3.0 and Z/d= -0.5 (measured from the axis of plate); (b) Power spectrum exhibiting a dominant shedding frequency at fd/U_0=0.1755.

Ro	∞	***2.5***	***1.0***	***0.33***	***0.16***
St = fd/U₀	***0.1678***	***0.1708***	***0.1755***	***0.1526***	***0.145***

Table 2: Strouhal number deduced from a power spectrum obtained at the cyclonic side of the wake (see e.g. Figure 4(b)). The Reynolds number is Re = 750.

high Strouhal number observed for Ro = 1 is believed to be associated with the wake asymmetry in that Ro-range.

The non-monotonous variation of the shedding frequency with rotation rate has not been reported elsewhere. Although the wake topology is symmetric both at the low Rossby number 0.16 and in the non-rotating case, the distinctly lower Strouhal number in the former case is undoubtedly due to the complete laminarization whereas the wake is fully turbulent in absence of system rotation. The laminarized wake flow at Ro = 0.16 is nevertheless distinctly different from a low-Reynolds-number wake in the absence of rotation. The recent in-house simulations at Re = 62.5 reported by Khaledi *et al.*[28] showed vortex shedding with a Strouhal number 0.1704. In this low-Re regime, however, viscous effects are coming into play. The remarkably low St-number observed in the present study is undoubtedly associated with the strong system rotation. As the three-dimensional motions are suppressed by the strong Coriolis force, the decay mechanism of the vortex cells is weakened and high levels of spanwise vorticity persist in Figure 3(e). The Reynolds number is more than a tenfold higher than that considered by Khaledi *et al.*[28] and viscous effects are almost negligible.

The Karman cells being shed from a bluff body are normally low-pressure regions. The instantaneous isobars displayed in Figure 5, however, show that the anticyclonic cells in

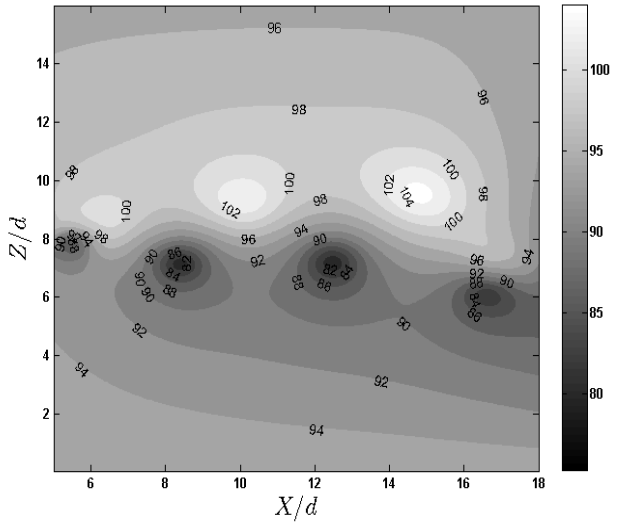

Figure 5: Contours of the instantaneous reduced pressure in an (x, z) - plane for $Ro = 0.16$ at $\tilde{t}$ = 120d/U_0. The effective pressure field is obtained by adjusting the effective pressure $\tilde{\pi}$ defined in eq. (3) for the rotational-induced cross-stream pressure gradient $2\Omega U_0$. The light colours represent high-pressure zones whereas the dark colours represent low-pressure zones.

the rapidly rotating wake are high-pressure zones. This is consistent with the simulations by Métais *et al.*[16] of a temporarily developing wake and by Lesieur *et al.*[21] of temporarily developing mixing-layers. Aristegui *et al.*[33] more recently detected elevations and depressions of the isotherms downstream of Cran Canaria as evidence of cyclonic and anticyclonic eddies. The rapidly rotating wake (Ro = 0.16) exhibits both low-pressure cyclones and high-pressure anticyclones that are clearly distinguishable in the λ_2-contour plot in Figure 2(e) and in the pressure contour plot in Figure 5. This observation implies that the inward Coriolis force more than outweighs the outward centrifugal force associated with the anticyclonic vortices. An outward pressure force is therefore established to aid the centrifugal force in balancing the Coriolis force. High vortex core pressures are therefore considered as a signature of the dominance of the system rotation. It is noteworthy that also the high-pressure anticyclones are identifiable by the λ_2-scheme, which traditionally[30, 31] is considered as a means of detecting localized pressure minima (i.e. a vortex core).

B. Primary flow statistics

Turbulent wakes are often described by means of Reynolds-averaged statistics, notably the mean velocity components and Reynolds-stresses. Reynolds-averaging of a turbulent Karman street implies that the fluctuations, i.e. the deviations from the mean values, comprise not only the three-dimensional turbulent fluctuations but also the essentially two-dimensional Karman-rollers. The present statistics are averaged in time over nearly 20 shedding cycles (corresponding to a time interval of 120d/U_0) as well as in the statistically homogeneous spanwise direction. The profiles of the streamwise mean velocity component $\overline{U}$ and the Reynolds shear stress $\overline{u'w'}$ are shown in Figure 6 for three distinctly different Rossby numbers. The mean velocity profiles for Ro = 2.5 and Ro = 0.33 are almost indistinguishable

from the profiles for Ro = 1.0 and Ro = 0.16, respectively, and are therefore not included here.

The mean velocity profiles are symmetric about the mid-plane of the wake (z/d = 8.0) in the non-rotating case and the shear stress profiles are consistently anti-symmetric. The velocity deficit, i.e. the momentum defect, and the Reynolds shear stress gradually reduce with downstream distance. For Ro = 1.0, however, the mean velocity distribution becomes highly asymmetric far downstream, apparently as a result of the distinct differences between the cyclonic and anticyclonic cells at this Rossby number. A more substantial velocity deficit is observed for even higher rotation rates (Ro = 0.16) in which case the turbulent mixing is gradually hampered with downstream distance. The modest asymmetries of $\overline{U}$ observed in the very-near wake tend to vanish further downstream and the wake becomes gradually symmetric again in the far field. The Karman vortices tend to weaken as they are convected downstream and the local rotation number N in eq. (1) is therefore slowly increasing in the x-

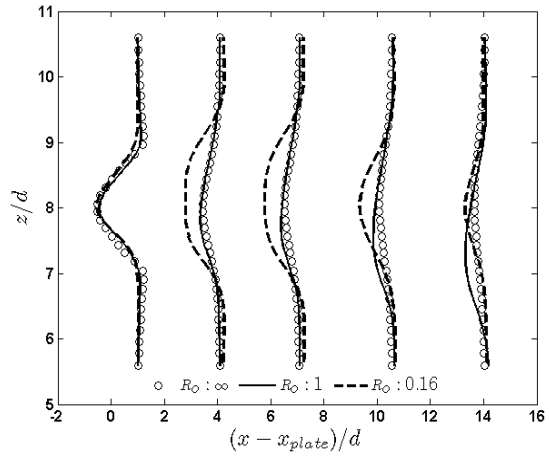

(a)

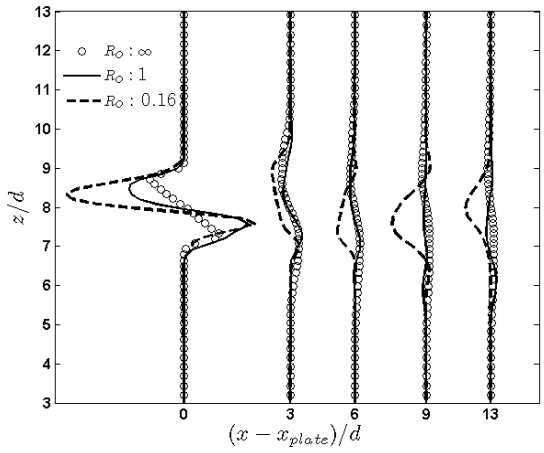

(b)

Figure 6: Time-averaged mean velocity (a) $\overline{U}/U_0$ and (b) Reynolds shear stress $\overline{u'w'}$ at different locations downstream of the plate for three different Rossby numbers and Re = 750.

direction, i.e. the imposed system vorticity $2\Omega_y$ becomes gradually more important relative to the local eddy vorticity ω_y.

The substantial wake deficit for Ro = 0.16 is undoubtedly associated with the suppression of the three-dimensional scrambling due to the strong background rotation which in turn tends to promote the Karman rollers. The mostly negative $\overline{u'w'}$ observed in the downstream part of the wake at the highest rotation rate does not represent conventional turbulence but rather the shearing effect of the nearly 2D vortex street. It is particularly noteworthy that although the mean velocity profile becomes symmetric again in the presence of sufficiently strong rotation, i.e. at Ro = 0.16, the shear stress profile exhibits a symmetric variation about the mid-plane rather than the typically anti-symmetric variation observed in the absence of rotation. For the rapidly rotating wake, i.e. when Ro < 1, the x-component of Reynolds-averaged Navier-Stokes equations becomes essentially a balance between the shearing term $\partial(-\overline{u'w'})/\partial z$ and the Coriolis force $-2\Omega W$ where W denotes the mean velocity across the wake. The observed symmetry of $\overline{u'w'}$ thus assures the anti-symmetry of the shearing term required to balance the streamwise component of the Coriolis force.

Etling[34] summarised findings from experiments with three-dimensional obstacles and emphasized that rotation increases the effective obstacle diameter due to steering effects which result in an increased lateral extent of the vortex-street wake. This is, at least qualitatively, in accordance with the increased momentum deficit for Ro = 0.16 observed in Figure 6(a). A larger momentum deficit is directly linked to a higher drag coefficient, which in turn is associated with a reduced shedding frequency; see e.g. Roshko.[35] If a mean recirculation region is defined by averaging over several shedding periods, see e. g. Williamson,[36] an extraordinarily long 'bubble' of length $L_w \approx 10.2d$ is obtained for Ro = 0.16, whereas $L_w < 2d$ in the non-rotating cases at both Re = 750 and Re = 62.5.[25] This tends to explain the reduction in Strouhal number when the rotation rate is further increased beyond Ro = 1.0; see Table 2.

C. **Wake pattern regimes**

Boyer[9], by means of flow visualization studies in a rotating water tunnel, identified five qualitatively different regimes of the wake flow behind a circular cylinder. As the Rossby number was gradually increased for a given Ekman number, the flow pattern evolved from that of a fully attached flow at the lowest Ro via unsteady wake regimes to the eddy shedding regime at lower rotation rates (higher Rossby numbers). For an Ekman number of $4.3\cdot10^{-4}$, for instance, eddy shedding was observed when Ro reached about 0.20. The outcome of these flow visualizations was summarized in a flow regime map in which the different wake regimes were separated by lines $Ro \sim Ek^{1/2}$. The present direct numerical simulations were performed with Re fixed as 750 while Ro was varied. Inevitably also the Ekman number varied in accordance with eq. (6). The Rossby-Ekman number map in Figure 7 shows that the numerically simulated wake flows at Re = 750 fall above the demarcation line between the eddy shedding regime and the unsteady eddy system. Indeed, the plots of the instantaneous λ_2 and spanwise vorticity ω_y in Figures 2 and 3 show beyond any doubt that these wakes are all in the eddy shedding regime.

In an attempt to pass the demarcation line in the Ro-Ek map, several attempts were made to further reduce the Rossby number while maintaining Re at 750. These attempts unfortunately failed and we instead reduced Ro to 0.0714 by increasing Ω and increasing the kinematic viscosity ν for the sake of increasing the stability of the numerical computations. The periodic vortex shedding was then suppressed and an unsteady non-shedding wake was

observed, as shown in Figure 8. The suppression of the eddy shedding accordingly occurred at Re=50. The topology of the wake at this Rossby number is surprisingly similar to the wake pattern observed behind a linearly tapered plate at Re_{local} = 32 by Khaledi *et al.*[28] This Reynolds number range is just where the near-wake of a uniform plate undergoes a Hopf bifurcation and becomes unsteady; see e.g. Saha[37]. Although the Reynolds number is way above 32 for the wake depicted in Figure 8, periodic vortex shedding does not occur. As one of the main results from laboratory experiments on homogeneous rotating flows, Etling[34] stated that vortex shedding from a cylinder is suppressed for rotation rates corresponding to a Rossby number Ro < 0.1. The observed suppression of the Karman-street in Figure 8 is foremost associated with the low Rossby number, but also the relatively low Reynolds number is not without influence. The demarcation line $Ro \sim Ek^{1/2}$ in the flow regime map of Boyer[9] and in the present Figure 7 can readily be recast as $Ro \sim Re^{-1}$ by replacing Ek by Ro/Re in accordance with eq. (6). This is indeed in keeping with earlier observations by Aristegui *et al.*[33] that background rotation delays the occurrence of vortex shedding to higher Reynolds number values.

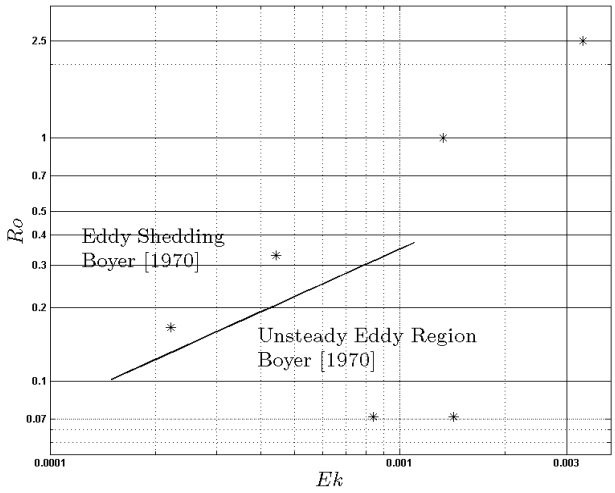

Figure 7: Rossby-Ekman number flow regime map. The straight demarcation line $Ro \sim Ek^{1/2}$ is adapted from Boyer[9] and passes through Ro = 0.20 and $Ek = 4.3 \cdot 10^{-4}$. The symbols show the present DNS.

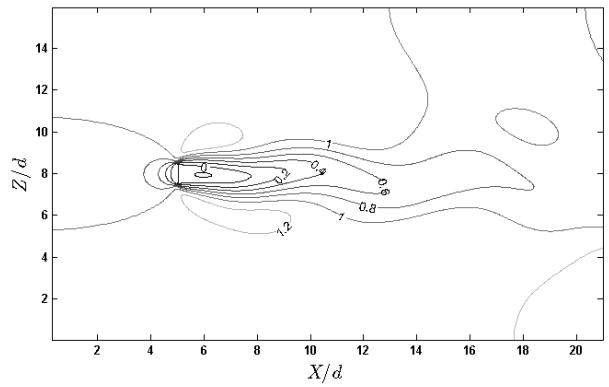

Figure 8: Side view of the wake topology at Rossby number Ro = 0.0714. The flow is visualized by means of iso-contour lines of the instantaneous streamwise velocity. The Ekman number is $Ek = 1.42 \cdot 10^{-3}$ and the Reynolds number is 50.

IV. CONCLUDING REMARKS

Direct numerical simulations have been performed with the view to explore the influence of the Coriolis force on the turbulent wake behind a normal flat plate. Lee-wake asymmetries have been observed before, both meso-scale vortex shedding from large islands and downstream of circular cylinders in rotating laboratory-scale apparatuses. The present investigation is apparently the first DNS study ever of the asymmetric turbulent vortex shedding behind a bluff body in a rotating fluid. The parameter range consider herein gives rise to a variety of non-linear flow phenomena as compared to the steady and symmetric wake flow investigated in the only earlier computational study of flat plate wakes (Becker[18]).

A distinguishing feature of the wake behind a flat plate is that the flow detaches and free shear layers form from the sharp edges of the plate, i.e. the separation points are fixed. The wake behind a flat plate becomes unstable and eventually fully turbulent at substantially lower Reynolds numbers than wakes in the lee of circular cylinders. In spite of these major differences, the rotating Karman vortex streets investigated in the present study share many of the salient features of the cylinder wakes observed in earlier laboratory studies, including the distinct asymmetries for Rossby numbers of the order of unity when the turbulence in the cyclonic cells has been suppressed while the anticyclones remain fully turbulent. This wake asymmetry is accompanied with a modest increase in the Strouhal number. The pronounced drop (about 20%) in the Strouhal number at even higher rotation rates has, however, not been reported before. In this particular parameter range the otherwise fully turbulent wake has become almost perfectly two-dimensional since variations along the span have been quenched as a result of the suppression of non-linear transfer mechanisms; see e.g. Cambon *et al*.[19]

The impact of the system rotation on the wake topology has been explained in terms of the local rotation number N defined in eq. (1), where the magnitude of N can be estimated as the inverse of the global Rossby number Ro defined in eq. (5). It is noteworthy that Ro can be interpreted as the ratio between the Coriolis length scale (or Rossby radius) $l_c \sim U_o/\Omega$ and the diameter of a vortex cell. Thus, with cell diameter ~ d this ratio becomes $U_o/\Omega d = 2Ro$. Two-dimensionalization of a vortex cell thus occurs when the Rossby radius l_c reduces to the cell diameter d.

The present study bears some resemblance with the wake flow simulations reported by Métais *et al*.[16] While they considered a temporarily evolving wake developing from an initially Gaussian mean velocity profile the present study addressed the spatially developing wake formed behind a bluff body, i.e. the flat plate. This approach enabled us to demonstrate how the influence of the background rotation increased downstream as the local fluid vorticity decayed, i.e. the local Rossby number N^{-1} decreased.

The numerical simulation results presented herein have served to illustrate the subtle effects of background rotation upon the wake topology. The importance to distinguish between the influence of the Coriolis force on the two-dimensional Karman rollers and on the three-dimensional turbulence became evident.

Acknowledgments

The financial support from The Research Council of Norway is gratefully acknowledged. This work has also been supported through grants of computing time from The Research Council of Norway (Program for Supercomputing) and the Norwegian University of Science and Technology (Program for Computational Science and Visualisation). The authors are indebted to Prof. Thomas Mc Climans for helpful discussions on the results and to Dr. Henri Didelle for kindly making the articles by Chabert d'Hiéres *et al*.[13 - 15] available to us. The revised paper benefited from the insightful comments of the anonymous reviewers.

REFERENCES

[1]J.P. Johnston, R.M. Halleen, and D.K. Lezius, "Effects of spanwise rotation on the structure of two-dimensional fully developed turbulent channel flow," J. Fluid Mech. **56**, 533-557 (1972).

[2] R. Kristoffersen and H.I. Andersson, "Direct simulations of low-Reynolds-number turbulent flow in a rotating channel," J. Fluid Mech. **256**, 163-197 (1993).

[3] M. Barri and H.I. Andersson, "Computer experiments on rapidly rotating plane Couette flow," Comm. Comp. Phys. DOI: 10.4208/cicp.2009.09.068

[4] K.H. Bech and H.I. Andersson, "Turbulent plane Couette flow subject to strong system rotation," J. Fluid Mech. **347**, 289-314 (1997).

[5] J.P. Johnston, "Effects of system rotation on turbulence structure: a review relevant to turbomachinery flows," Int. J. Rotating Machin. **4**, 97-112 (1998).

[6] E. Greitzer, C.S. Tan and M.B. Graf, Internal Flow: Concepts and Applications (Cambridge University Press, 2004).

[7] P.H. Rothe and J.P. Johnston, "Free shear layer behavior in rotating systems," ASME J. Fluids Eng. **101**, 117-120 (1979).

[8] A.A. Bidokhti and D.J. Tritton, "The structure of a turbulent free shear layer in a rotating fluid," J. Fluid Mech. **241**, 469-502 (1992).

[9] D.L. Boyer, "Flow past a right circular cylinder in a rotating frame," ASME J. Basic Eng. **92**, 430-436 (1970).

[10] D.L. Boyer and P.A. Davies, "Flow past a circular cylinder on a β-plane," Phil. Trans. R. Soc. Lond. A **306**, 533-556 (1982).

[11] H.T. Witt and P.N. Joubert, "Effect of rotation on a turbulent wake," In: *Proc. 5th Symposium on Turbulent Shear Flows*, Ithaca, pp. 21.25 – 21.30 (1985).

[12] H.S. Koyama and M. Ohuchi, "Wakes behind circular cylinder fixed in a rotating rectangular channel," In: *Proc. 6th Symposium on Turbulent Shear Flows*, Toulouse, pp. 13.7.1 -13.7.6 (1987).

[13] G. Chabert d'Hières, P.A. Davies, and H. Didelle, "Laboratory studies of pseudo-periodic forcing due to vortex shedding from an isolated solid obstacle in a homogeneous rotating fluid," in *Mesoscale/Synoptic Coherent Structures in Geophysical Turbulence*, edited by J.C.J. Nihoul and B.M. Jamart (Elsevier, Amsterdam, 1989), pp. 639-653.

[14] G. Chabert d'Hières, P.A. Davies, and H. Didelle, "A laboratory study of the lift forces on a moving solid obstacle in a rotating fluid," Dyn. Atmos. Oceans **13**, 47-75 (1989).

[15] G. Chabert d'Hières, P.A. Davies, and H. Didelle, "Experimental studies of lift and drag forces upon cylindrical obstacles in homogeneous, rapidly rotating fluids," Dyn. Atmos. Oceans **15**, 87-116 (1990).

[16] O. Métais, C. Flores, S. Yanase, J.J. Riley, and M. Lesieur, "Rotating free-shear flow. Part 2. Numerical simulations," J. Fluid Mech. **293**, 47-80 (1995).

[17] A. Stegner, T. Pichon, and M. Beunier, "Elliptical-inertial instability of rotating Karman vortex streets," Phys. Fluids **17**, 066602 (2005).

[18] A. Becker, "Flow past a normal flat plate in a rotating frame," Q. J. Mech. Appl. Math. **45**, 451-468 (1992).

[19] C. Cambon, J.-P. Benoit, L. Shao, and L. Jacquin, "Stability analysis and large-eddy simulation of rotating turbulence with organized eddies," J. Fluid Mech. **278**, 175-200 (1994).

[20] P. Bradshaw, "The analogy between streamline curvature and buoyancy in turbulent shear flows," J. Fluid Mech. **36**, 177-191 (1969).

[21] M. Lesieur, S. Yanase, and O. Métais, "Stabilizing and destabilizing effects of solid-body rotation upon quasi-two-dimensional shear layers," Phys. Fluids A **3**, 403-407 (1991).

[22] S. Yanase, C. Flores, O. Métais, and J.J. Riley, "Rotating free-shear flows. I. Linear stability analysis," Phys. Fluids A **5**, 2725-2737 (1993).

[23] L.J.A. van Bokhoven, C. Cambon, L. Liechtenstein, F.S. Godeferd, and H.J.H. Clercx, "Refined vorticity statistics of decaying rotating three-dimensional turbulence," J. Turbul. **9**, N6 (2008).

[24] B. Sreenivasan and P.A. Davidson, "On the formation of cyclones and anticyclones in a rotating fluid," Phys. Fluids **20**, 085104 (2008).

[25] V.D. Narasimhamurthy and H.I. Andersson, "Numerical simulation of the turbulent wake behind a normal flat plate," Int. J. Heat Fluid Flow (final version August 2009).

[26] M. Manhart, "A zonal grid algorithm for DNS of turbulent boundary layers," Comput. Fluids **33**, 435-461 (2004).

[27] N. Peller, A. Le Duc, F. Tremblay, and M. Manhart, "High-order stable interpolations for immersed boundary methods," Int. J. Num. Meth. Fluids **52**, 1175-1193 (2006).

[28] H.A. Khaledi, V.D. Narasimhamurthy, and H.I. Andersson, "Cellular vortex shedding in the wake of a tapered plate at low Reynolds numbers," Phys. Fluids **21**, 013603 (2009).

[29] V.D. Narasimhamurthy, H.I. Andersson, and B. Pettersen, "Cellular vortex shedding in the wake of a tapered plate," J. Fluid Mech. **617**, 355-379 (2008).

[30] J. Jeong and F. Hussain, "On the identification of a vortex," J. Fluid Mech. **285**, 69-94 (1995).

[31] P. Chakraborty, S. Balachandar, and R.J. Adrian, "On the relationships between local vortex identification schemes," J. Fluid Mech. **535**, 189-214 (2005).

[32] P.H. Alfredsson and N. Tillmark, "Instability, transition and turbulence in plane Couette flow with system rotation," In: *Laminar Turbulent Transition and Finite Amplitude Solutions*, edited by T. Mullin and R.R. Kerswell (Springer, 2005), pp. 173-193.

[33] J. Aristegui, P. Tett, A. Hernandez-Guerra, G. Basterretxea, M.F. Montero, K. Wild, P. Sangra, S. Hernandez-Leon, M. Canton, J.A. Garcia-Braun, M. Pacheco, and E.D. Barton, "The influence of island-generated eddies on chlorophyll distribution: a study of mesoscale variation around Gran Canaria," Deep-Sea Research **44**, 71-96 (1997).

[34] D. Etling, "Mesoscale vortex shedding from large islands: a comparison with laboratory experiments of rotating stratified flows," Meteorol. Atmos. Phys. **43**, 145-151 (1990).

[35] A. Roshko, "Experiments on the flow past a circular cylinder at very high Reynolds number," J. Fluid Mech. **10**, 345-356 (1961).

[36]C.H.K. Williamson, "Vortex dynamics in the cylinder wake," Annu. Rev. Fluid Mech. **28**, 477-539 (1996).

[37] A.K. Saha, "Far-wake characteristics of two-dimensional flow past a normal flat plate," Phys. Fluids **19**, 128110 (2007).